MEASUREMENT OF A WEAK POLARIZATION SENSITIVITY TO THE BEAM ORBIT OF THE CEBAF ACCELERATOR

BY

JOSEPH MICHAEL GRAMES

B.S., Stevens Institute of Technology, 1992
M.S., University of Illinois at Urbana-Champaign, 1994

THESIS

Submitted in partial fulfillment of the requirements
for the degree of Doctor of Philosophy in Physics
in the Graduate College of the
University of Illinois at Urbana-Champaign, 2000

Urbana, Illinois

MEASUREMENT OF A WEAK POLARIZATION SENSITIVITY
TO THE BEAM ORBIT OF THE CEBAF ACCELERATOR

Joseph Michael Grames, Ph.D.
Department of Physics
University of Illinois at Urbana-Champaign, 2000
Douglas H. Beck, Charles K. Sinclair, Co–Advisors

An accelerator-based experiment was performed using the CEBAF accelerator of the Thomas Jefferson National Accelerator Facility to investigate a predicted sensitivity of the beam polarization to the vertical betatron orbit in the recirculation arcs. This is the first measurement of any such effect at CEBAF, and provides information about the polarized beam delivery performance of the accelerator. A brief description of the accelerator is given, followed by the experimental methods used and the relevant issues involved in measuring a small ($\sim 10^{-2}$) change in the beam polarization. Results of measurements of the polarization sensitivity parameters and the machine energy by polarization transport techniques are presented. The parameters were obtained by measurement of the strength of the effect as a function of orbit amplitude and spin orientation, to confirm the predicted coupling between the spin orientation and the quadrupole fields in the beam transport system. This experiment included characterizing the injector spin manipulation system and 5 MeV Mott polarimeter, modeling of the polarization transport of the accelerator, installation of magnets to create a modulated orbit perturbation in a single recirculation arc, and detailed studies of the Hall C Møller polarimeter.

Acknowledgments

Looking back at the path that brings me to this point, the largest contribution to this work are the people whom I have known along the way. I am happy to have had the opportunity to work in a dynamic environment, alongside many bright and interesting people. Commensurate with the hard work and long hours during the past seven years of graduate school are many experiences and memories which go with me toward my future.

Foremost along this path is my family. My mother showed me at an early age why it is so much fun to wonder how the world works, and how dear the rewards of pursuing your dreams can be. She showed her strength, by example, that when you love what you do, happiness will follow. My sister Janis, grandmother Rose, and Uncle Mike have reached me in special ways during my life. I think these lessons, more than anything, gave me reason to pursue my dreams.

As a graduate student I have had an unique opportunity to be advised by three very good, hard-working scientists. Douglas Beck, my co-advisor at the University of Illinois, has continually supported my work to complete my graduate training. In some way, the incredible amount of energy he has for his own work has hopefully rubbed-off over the years. However difficult it has been to supervise a student more than 1000 miles from campus, he has guided me to think critically and showed me how to stand on my own feet as a physicist. Charlie Sinclair, my co-advisor at Jefferson Laboratory, has been an example of what I can strive to be as a physicist. I admire his academic integrity and professionalism, and I have tried to learn much from his experience and keen insight. He has thoroughly supported making my thesis

experiment a reality. Finally, I am indebted to the commitment Larry Cardman has maintained for me since I have come to the laboratory. He has guided me from the initial stages of proposing and drafting this experiment, through the years of preparation. He has continually been an example of how to take complicated problems and then find the essential points. I sincerely appreciate the many hours of valuable time each has spent trying to teach me about physics.

While a high school and college student I was given an excess of latitude and opportunity to pursue my interests, particularly those in science and mathematics. I thank Jim Smith, John St. Clair and Jim Burne for showing me why they had so much fun teaching science. As an undergraduate at Stevens Institute of Technology, I was lucky to be assigned Edward Whittaker as my advisor, Veneta Tsoukala my thesis advisor, and thank the late Timothy Hart for recognizing both my talents and my failings. Michael Sheldon trusted me with the responsibility for learning to teach others, an incredibly rewarding experience.

After my first class at the University of Illinois I realized that while I was still a student, most of what I had expected had changed. Often stressed by the amount of work and general high caliber of the department, I realized I was a smaller fish in a larger sea. However, I had the good fortune to meet an interesting group of people that gave balance to the struggle. The group at Feynman House, where I lived during my two years in Urbana, made the snow-covered corn fields much more bearable. The memories and friendships I cast there continue with me today. They include Chris Bochna, Bart Terburg, Dan and Lisa McLaughlin, Johann Beda, Rachel Wortis, Andrew Dalke, Nathan Yanasak, and Kathy McCormick.

The preparation and coordination for this experiment was much more than I ever realized it would be. I have gained some invaluable experiences and expect they will serve me well. I would like to thank specific groups at the laboratory that supported my work. Foremost are the Injector Group and Hall C Møller Polarimeter Group. Their own respective hard work made my job so much easier. From the Injector Group I would like to thank Scott Price for taking a personal interest in my graduate

work and teaching me how to appreciate some of the finer points of polarized beam measurements; Matt Poelker for teaching an often impatient graduate student (me) to keep his cool under pressure; John Hansknecht and Tony Day for their technical advice and support, and for teaching me about electronics and suggesting how to improve upon my designs; Phil Adderley for explaining vacuum systems and technology; and Reza Kazimi for showing me how to steer the beam through the first few meters of the injector. I thank the Polarimeter Group for providing me with the right tool for the job; an exceptional polarimeter. Joe Mitchell and Beni Zihlmann have been part of this thesis project for many years. I appreciate their encouragement, support, and the long nights they have given toward the experiment. I will never forget the night we *traded* experimental asymmetries, verifying the first polarized beam delivered to a CEBAF end station. Simply, Beni made the polarimeter work for this experiment. His (expletive) approach for getting software to run is precious. I would also like to thank Marko Zeier for the contributions he made, particularly to the polarimeter software used for the experiment and analysis. I am indebted to the Techs who often saved my rear in the polarimeter alcove; Mark Hogerel, Paul Hood, and Steve Knight.

Seeking an identity among the many experiments vying for approval at accelerator scheduling meetings, I urged the experiment name *Spin fX* at some point years ago. The efforts of those who joined this collaboration and volunteered their knowledge, insights, and humor are sincerely appreciated. Without their support this endeavor surely would have failed. The Spin fX Collaboration is Chris Armstrong, Dave Barkhuff, Doug Beck, Roger Carlini, Rolf Ent, Ken Garrow, Paul Gueye, Larry Cardman, Peter Hartmann, Reza Kazimi, Dave Meekins, Bob Michaels, Joe Mitchell, Hamlet Mkrtchyan, Mark Pitt, Matt Poelker, Charlie Sinclair, Michael Steigerwald, Raphael Tieulent, Bill Vulcan, Steve Williamson, Rhett Woo, Marko Zeier, and Beni Zihlmann.

I appreciate all of the efforts the Operations Group made to this experiment, in many cases, far beyond the call of duty. The majority of my time inside the accelerator fence was spent at the Machine Control Center (MCC). While on site,

it was my second home. I appreciate the support and access they gave me to the accelerator (and their cuisine). For example, I will not forget when Jacque Ludwig kept the injector running on his own time to bring the injector polarimeter DAQ on-line. Nor will I forget the last minute changes Michele Erb made to the Mott polarimeter software controls for my experiment. Finally, I would like to thank that guy from Canada who knows the value of skipping out of PAC'99 to see Wayne Gretzky break the all-time scoring record. Chris Payne has contributed a very good deal to developing code to meet goals for this experiment, helping me out of software pickles, and generally being a good friend. He is also the only person I know that can rival my complaints of Newport News.

Working in an active environment, where *my* research lab and a world class accelerator and nuclear physics facility are one in the same, has given me excellent opportunities and evolved me as a scientist. To all of those whom I have spoken or communicated with during this adventure, thank you. Particularly, Dave Douglas, whose discussion, advice, and keen wit I always looked forward to; to Valeri Lebedev, Alex Bogacz, Byung Yunn, Michael Tiefenback, and Leigh Harwood for many useful discussions about the accelerator. Jeff Karn, Al Guerra, and Danny Machie have given me a large amount of hardware and technical support for the magnet systems. A special thanks goes to Simon Wood and Scott Higgins for making sure every last deflection magnet cable and look-up table was ready, even on the shortest of notice. I have had many teachers during this research project; Tim Siggins showed me how I can turn a chunk of steel into a mirror, Marie Keesee taught me how delve behind the panels of MEDM, and Valerie Bookwalter put me on the road to programming using Tcl. Another special thank you goes to Steve Suhring who has emptied his tools on the office floor more than once when I was desperate.

I was given an excellent opportunity when invited to the first planning meeting of the 5 MeV Mott polarimeter. This project became my thesis project away from thesis projects. The experiences there have taught me a great deal about experimental physics and polarized beam measurements. I learned much from the original group;

Charlie Sinclair, Dave Mack, Ketevi Assamagan, Scott Price, Philippe Piot, and Phil Adderley; and later, from Paul Rutt and Michael Steigerwald.

The Bldg. 90 mezzanine has been my second home. I was both fortunate and unfortunate to have shared an office with another UIUC graduate student for about half of this time. Fortunate because Dave Engwall is an interesting guy to have worked alongside; a capable accelerator physicist and someone who largely softened my initial impact so far from campus. Unfortunate because our cubicle measured only $7' \times 11'$. I don't recall when I first met Jack Segal, but his friendship goes back as far as we have shared a common office wall. Jack has been a buddy, with whom I have had many opportunities to share daily war-stories with, and to generally make life at work a little less about work.

I am simply thankful to have had Penny Sigler and Gaylon Reeves on the other end of the phone in the managing office of the Nuclear Physics Laboratory at UIUC. Their patience and support has made my student life *in absentia* much less painful than it would have otherwise been; only they and I know how well this is true.

It is ironic that my best friend since grade–school, Chris Bochna, ended up at the same graduate school with the same advisor. Chris is a competent physicist and has taught me quite a few things of nuclear physics which I doubt to have otherwise appreciated. I am lucky that he spent part of his graduate school at Jefferson Lab, feeling a bit more as if we were at home in New Jersey. Having pursued similar studies has been one of the pleasures of being a graduate student.

Lastly, I thank Maud, for her strength, her smile, and her love. She has been a very bright spot for me during the toughest times of this thesis. For this, I am a very lucky guy.

This material is based on work supported by the National Science Foundation under grant NSF PHY 89-21146, NSF PHY 92-57057, NSF PHY 93-10871, and NSF PHY 94-20787, and by the United States Department of Energy under contract DE–AC05-84ER40150.

Contents

List of Tables

List of Figures

Chapter 1

Introduction

1.1 History

The use of beams of polarized particles in nuclear and high energy physics experiments provides an important degree of freedom in understanding fundamental interactions. In particular, the spin structure of nucleons can be probed using a beam of polarized electrons in conjunction with either a polarized target or recoil polarimetry, or by parity violation experiments. However, a balance has historically been struck between the desirability of this additional degree of freedom for physics experiments and the effort required to produce polarized beams and to characterize and control them in accelerators [Mo84].

In this way, the domain of accelerator physics, or beam physics, involving the development of polarized beam sources and the underlying transport phenomena of polarized beams and their dependence on the beam energy, orbit, charge delivered, and the accelerator magnetic lattice design parameters is important. Specifically, the ensemble of particle spins, which constitute the polarization of such beams, depend upon their trajectories in accelerators. This significance of the particle spin in accelerators is better understood by first considering the development of the concept of spin.

In 1925, Uhlenbeck and Goudsmit introduced the idea [Uh25] that a free electron retained an angular momentum, separate from its bound orbital angular momentum,

to describe the anomalous Zeeman effect. They proposed an intrinsic angular momentum, or electron spin $\vec{s}$, which could take only quantized values of $\pm\hbar/2$ projected along a quantization axis. The spin is related to the magnetic moment of the electron, $\vec{\mu}$, by

$$\vec{\mu} = \frac{ge}{2m_e c}\vec{s}, \tag{1.1}$$

where e and m_e are the electronic charge and mass, and c is the speed of light. The interaction potential of the two spin states of an orbital electron in a magnetic field result in the observed energy splittings. Their explanation made use of an empirical gyromagnetic factor (g) shown in Equation 1.1. Using $g = 2$ they explained the anomalous Zeeman effect (multiplet splittings), but not the observed fine structure splitting size. The cause of their discrepancy was uncovered in 1926 following work by Thomas [Th26]. He was prompted to investigate the precession of an electron with a magnetic moment orbiting a hydrogen atom relativistically. He showed that a purely kinematic precession arises which when properly included gave both the Zeeman effect and the multiplet splittings, while retaining the value $g = 2$. Later, the Dirac equation provided an exact relativistic solution of quantum mechanics, predicting the existence of spin-$\frac{1}{2}$ particles (and anti-particles), and independently predicting $g = 2$. Higher order quantum electrodynamic (QED) corrections to the electron interaction modifies this value, resulting in the theoretically calculated value [Ki81] of the gyromagnetic factor of an electron,

$$\left(\frac{g-2}{2}\right)_{thy} = (1159652460 \pm 202) \times 10^{-12}. \tag{1.2}$$

Experimentally, the value has been measured [Co87],

$$\left(\frac{g-2}{2}\right)_{exp} = (1159652193 \pm 10) \times 10^{-12}, \tag{1.3}$$

providing excellent agreement with theory.

Others had considered the spin motion of an electron in traversing electromagnetic fields, but in 1959 Bargmann, Michel, and Telegdi [Ba59] re-cast Thomas' equation of spin motion by applying the theorem of Ehrenfest to the quantum mechanical

spin operator. This theorem states that the expectation value of an observable to a quantum mechanical solution should follow the classical limit. In this way, the well-known BMT equation (discussed in Section 2.1.1) was developed, solving the classical equation of spin motion for a particle moving relativistically in an electromagnetic potential.

This description for the motion of a spin-$\frac{1}{2}$ particle found direct use in understanding the polarization, or ensemble average, for a large collection of particle spins found in accelerator beams. Two historical examples demonstrate this point. In 1959, Froissart and Stora [Fr60] found that the polarization of a proton beam stored in a synchrocyclotron accelerator was lost. The effect was explained by treating the motion of the proton spins of the particle beam through field inhomogeneities of the magnets. Their work prompted further investigation, beginning the study of what are now known as depolarization resonances. This phenomena is necessarily analyzed in the design, and then routinely tested in the practice, of particle storage rings. In 1964, Sokolov and Ternov [So64] described the self-polarizing effect of an electron beam in a storage ring by the emission of synchrotron radiation. This effect prompted the design and construction of polarimeters to measure the polarization of an electron beam in a storage ring. In this way, spin motion has been studied in storage rings, designed to produce high energy beams of polarized electrons, over the past 30 years. Conversely, linear accelerator designs, for which there is no self-polarization of the electron beam, attracted less interest for studying their spin transport properties. However, advances of polarized electron sources began to meet the requirements for producing accelerator quality beams in the early 1970's. Consequently, linear accelerator facilities have been built and are proposed with the capability to support requirements for nuclear and high energy polarized beam experiments. These facilities require testing of their polarization transport properties.

Returning to the fundamental issue, it is important to recognize that the tools for treating the spin motion of electrons transported through accelerators is rooted in the basic understanding of the motion of the quantum mechanical spin of an electron

moving (relativistically) in electromagnetic fields. Whether the accelerator fits in a university laboratory or spans many kilometers and adjoining countries, the integration of the classical equation of motion of the electron spin in the electromagnetic fields it encounters along its trajectory uniquely determine its spin motion.

1.2 Motivation

The physics of transporting a polarized electron beam in an accelerator has been largely studied for storage rings. In this case, the electron spin is rapidly precessing in the bending dipole magnetic fields along the ring. Imperfections in the stable beam orbit, magnetic field inhomogeneities, and finite beam size during many revolutions of the accelerator can result in strong depolarization resonances. However, when transporting a polarized beam through an accelerator a single time (linear transport system) or a few circuits (recirculation transport system) the effects of the beam orbit $(\vec{r}, \vec{p})$, energy (E), energy spread $(\frac{\Delta E}{E})$, beam size (σ_x or σ_y), and accelerator imperfections are different. In a linear transport system the storage time is significantly reduced (microseconds compared with hours). While the magnetic system may still have periodic magnetic errors, the recirculation number is very low (single or few-pass compared with $\gg 10^6$ turns of the storage ring or between 10^3 and 10^6 turns for a pulse stretcher ring). Yet, the effects of transporting a polarized beam in a linear or recirculation accelerator can be significant.

The development and progress of semiconductor photoemission polarized electron sources now plays a role in the design of such accelerators. Electron sources of this sort can deliver high quality beams of polarized electrons which can be directly injected into an accelerator without the need to store the beam in a circular accelerator to build-up the beam polarization. An example, which is the focus of investigation for this work, is the CEBAF (Continuous Electron Beam Accelerator Facility) accelerator located at the Thomas Jefferson National Accelerator Facility in Newport News, Virginia. A simple description of this accelerator is shown in Figure 1.1. A

more detailed description of the accelerator and its components is given in Chapter 2 and Chapter 3. The concept of this accelerator is straight forward. A polarized

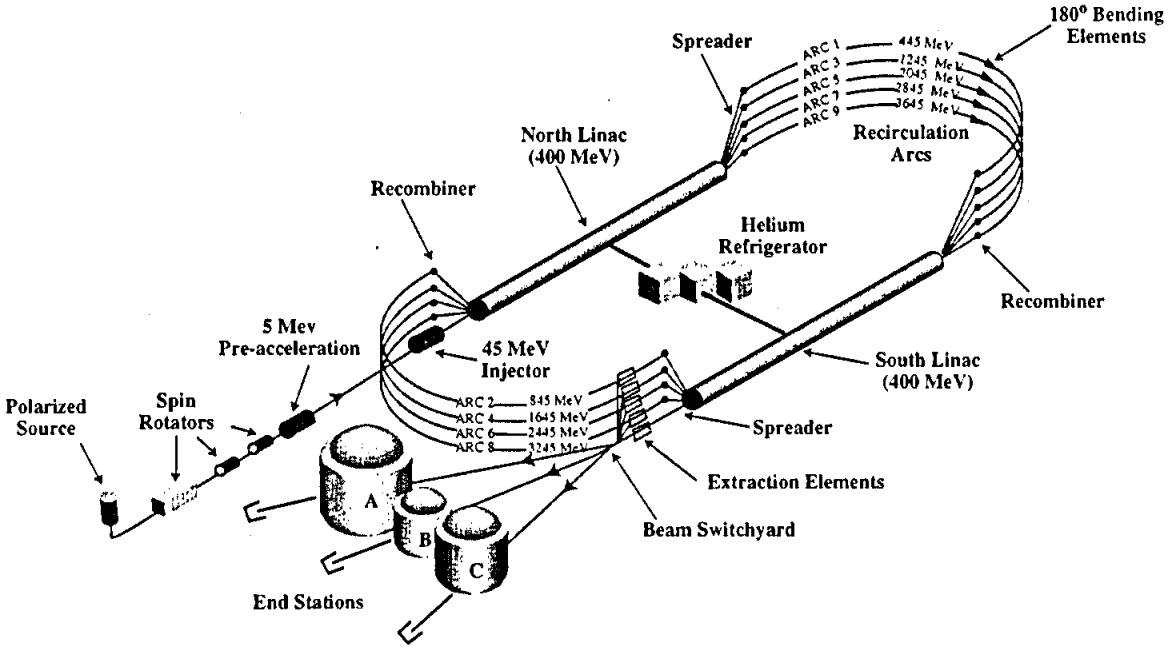

Figure 1.1: Layout of the injector, recirculating accelerator and experimental end stations. The view not shown to scale. Figure courtesy of M. Stewart.

electron gun produces a continuous series of electron bunches at the characteristic radiofrequency (RF) of the accelerator, 1497 MHz. The polarized gun source is based on photoemission, by an incident circularly polarized laser beam, from semiconductor photocathodes (gallium arsenide type). This continuous beam of electron bunches is accelerated to 45 MeV and then injected into the main accelerator (north linac) at relativistic speed ($v_{electron} \approx c$). As the beam passes through the linac it sees a repeating pattern of magnets and superconducting accelerating cavities. The cavities are the basic accelerating structures, and the magnets focus and steer the beam. As the beam is transported through the north linac it gains a nominal energy of 400 MeV. The beam then exits the linac and enters a recirculation arc which transports it to the entrance of the south linac (another 400 MeV gain); at the end of the south linac a similar arc transports the beam to the entrance of the north linac. Electrons can

make as many as five full circuits of the accelerator this way.

Since the beam is continuous, there can be electrons at five discrete energies simultaneously in each linac because of the recirculation process. Exiting each linac, these beams of different energy are separated by a *spreader*, a series of magnets, which separate the different energy beams vertically into different beamlines. This is necessary because beams of different energy require different magnets to bend through the same *arc*. At the end of the arc, but preceding the next linac segment, a *recombiner* merges the beams vertically for the next acceleration. Each recirculation arc is composed of a group of magnets which steer and focus the beam it contains, along with beam diagnostics.

The electron bunches, which are at an energy corresponding to between one (845 MeV) and five (4.045 GeV) passes, can be extracted from the accelerator and directed to the experimental areas by RF separators (time–domain beam deflectors) just downstream of the spreader following the south linac. These devices, operating at the third subharmonic of the accelerator RF frequency, can extract every third bunch of electrons, so a beam of the desired energy is diverted to an experimental area while the remaining bunches in the beam continue to the next recirculation arc for further acceleration. The extracted beams are directed through a *beam switchyard* and transport arcs by additional magnets to the appropriate experimental area.

In an ideal situation, a beam with point–like width follows the reference orbit of an accelerator, central to magnets and acceleration fields with ideal symmetry. For CEBAF, the ideal beam only interacts with the longitudinal electric fields of the acceleration cavities and the transverse magnetic fields of dipole bending magnets. Here, the electron spin direction remains constant in the longitudinal acceleration fields, and the magnetic fields precess the electron spin relative to the momentum of the beam. As one might expect, however, the trajectories of the electrons in an accelerator can be complicated and imperfections of the electric and magnetic fields exist. The finite size of the beam and non–ideal particle motion therefore cause the precession of the electron spin to be different than nominally expected.

Such a case for non–ideal particle motion was observed [Li93] in the single–pass transport arc of the Stanford Linear Collider (SLC). It was characterized at first as a very strong sensitivity of the beam polarization orientation at the SLC target location to the position of the electron beam entering a 1200 m transport arc. Studies there indicated that vertical orbit oscillations induced by a beam position offset of 0.5 mm resulted in the polarization of the beam rotating, ending completely transverse to the desired orientation at the target. This effect was characterized by a relation between the beam polarization precession frequency and the oscillation frequency of the component of the beam orbit which is perpendicular to the plane of precession. The strength of this sensitivity in their single–pass magnetic lattice was surprising, and had not been previously studied. A methodology to correct for the undesired polarization rotation had to be devised, using a complex orbit–dependent spin correction technique.

To investigate this effect at CEBAF, Chapter 2 introduces the basic tools for studying the spin motion of particle beams in electromagnetic fields, and then presents the nominal spin transport of the accelerator. The depolarization phenomena due to the finite beam size is also considered. Electromagnetic fields in the accelerator vary little over the scale of the beam profile, and the effect of the beam size for full recirculation of the accelerator is estimated to be small ($< 10^{-4}$). To measure depolarization in a linear accelerator the beam polarization is measured at separate locations by indepedent polarimeters. Therefore, systematic uncertainty in the absolute knowledge of the beam polarization at each polarimeter determine the total uncertainity in measuring beam depolarization. Within the systematic uncertainties of a few percent in the polarimeters at the injector and experimental halls a small loss in polarization ($< 5\%$) is not measurable.

A study of the sensitivity of the beam polarization to the beam orbit of the accelerator is presented. Simulations of spin motion in the recirculation arcs predict the same sensitivity observed at the SLC exists at CEBAF and is due to the action of quadrupole magnetic fields on the beam polarization. The effect is a small rotation

of the average direction of the beam polarization ($\leq 0.05°$) at each quadrupole. The size of the rotation depends upon the beam energy, the strength of the quadrupole magnetic field, and the beam location in the quadrupole. Generally, the effect of the quadrupoles on the beam polarization averages to zero, even if individual rotations are relatively large. However, a coherence condition can exist between the spin precession frequency and the oscillation frequency of the beam orbit that results in the small spin rotations adding. Although the net effect is still rather small, simulations show the effect exists and is of the order of a few degrees.

1.3 Experiment and Results

Chapter 3 describes our experiment to measure the effect of the beam orbit in a recirculation arc on the beam polarization. The choice of the arc was determined by simulation results. The strongest effect (which depends on beam energy) was found to be in arc 7 (2.845 GeV) for the nominal accelerator energy . The experiment provides a method to verify the interaction of the beam polarization with the accelerator transport. Further, because all 9 recirculation arcs were designed with similar transport optics, this measurement can be used as a model description for the remainder of the machine.

A polarized electron gun, based on photoemission from a semiconductor, produced a longitudinal polarized electron beam ($\approx 70\%$). The longitudinal polarization could be reversed by reversing the optical polarization of the laser beam used to cause the photoemission. The electron beam polarization at the injector could be oriented by a series of spin rotators, and measured by a Mott polarimeter before being injected into the main accelerator. The injector spin rotators provided beam polarization orientations transverse to the bending plane of the accelerator. The uncertainty in the setting of each spin rotator was characterized to better than 2°. Perturbations to the nominal beam orbit were introduced locally in recirculation arc 7 by a series of deflecting magnets, while maintaining the beam position stable to $\leq 200\,\mu$m in the

remainder of the accelerator. This was required to systematically measure the small polarization effect. A Møller polarimeter and beam diagnostics measured the final beam parameters at the exit of the accelerator.

Chapter 4 describes the conditions and results for the experiment. A small polarization sensitivity to the beam orbit in recirculation arc 7 was successfully measured. The beam energy was determined from measurements of the total spin rotation through the accelerator. This measurement is consistent (at the level of 0.1%) with beam momentum and elastic electron–proton scattering measurements of the final beam energy in the experimental halls. The operation of the injector spin manipulation system, as measured by the Mott polarimeter, agreed to better than $\pm 5^\circ$ with measurements made at the Møller polarimeter.

The strength of the sensitivity of the beam polarization on the quadrupole fields in arc 7 is consistent with the prediction for linear scaling with beam orbit amplitude. However, simulations of the measurements performed, as described by an accelerator model and calculated with a spin tracking program, underestimate the measured effect. The dependence of the sensitivity on the orientation of the beam polarization has the predicted azimuthal dependence about the momentum direction.

Finally, in Chapter 5, conclusions from this experiment and a discussion of the implications of the results for this and other accelerators is made.

Chapter 2

Theory and Simulation

The formalism for describing the spin motion of an electron moving in electromagnetic fields and a description of the ensemble of electron spins which constitute a polarized beam are discussed in Section 2.1. The CEBAF accelerator is described in terms of a spin transport model. The spin transport results for the nominal accelerator design are given in Section 2.2. Finally, simulations describing depolarization phenomena and the predicted polarization sensitivity to the beam orbit are given in Section 2.3.

2.1 Electron Spin and Beam Polarization

The formalism of the interaction of the spin of a relativistic electron with an electromagnetic field is described in Section 2.1.1. In Section 2.1.2 the ensemble of electrons forming a polarized beam is discussed.

2.1.1 Interaction of EM Fields with Electron Spin

In 1959, Bargmann, Michel, and Telegdi used a set of relativistically covariant *classical* equations of motion to solve the spin motion of a relativistic particle interacting with electromagnetic (EM) fields [Ba59, Ja75]. The spin motion of a single electron in an accelerator (or other electromagnetic system) is a consequence of the interaction of its magnetic moment with the EM fields it encounters along its trajectory. This

interaction causes the spin vector, $\vec{s}$, to undergo rotations described by

$$\frac{d\vec{s}}{dt} = \vec{s} \times \vec{\Omega}, \tag{2.1}$$

where

$$\vec{\Omega} = \frac{e}{m}\left[\left(\frac{g}{2} - 1 + \frac{1}{\gamma}\right)\vec{B} - \left(\frac{g}{2} - 1\right)\frac{\gamma}{\gamma+1}\left(\vec{\beta}\cdot\vec{B}\right)\vec{\beta} - \left(\frac{g}{2} - \frac{\gamma}{\gamma+1}\right)\vec{\beta}\times\frac{\vec{E}}{c}\right]. \tag{2.2}$$

Here e and m are the electron charge and mass. The gyromagnetic factor g is given by Equation 1.2. In this equation the spin direction is evaluated in the rest frame of the electron, while all other quantities are expressed in the laboratory frame. Ω is the angular velocity of the spin precession, $\vec{E}$ and $\vec{B}$ are the electric and magnetic fields encountered along the particle trajectory, $\vec{v}$ is the velocity, $\vec{\beta} = \vec{v}/c$, and γ is the Lorentz factor $1/\sqrt{1-\beta^2}$.

The coordinate system used throughout this thesis and for all of the beam simulation programs described is the standard TRANSPORT [Br77] notation. The polar angles θ and ϕ describe the orientation of the beam polarization vector, $\vec{P}$, relative to the beam direction, as shown in Figure 2.1. In this coordinate system the $\hat{z}$ unit vector always points in the beam direction.

By applying Equation 2.2 to time–independent electric and magnetic fields the precession of the electron spin along a specific trajectory is easy to construct. Some examples for elements found in an accelerator are given here. Most common is the case of the transverse magnetic field ($\vec{B} = B_y\hat{y}$) as seen by the electron in a dipole magnet. In this case, the angular precession frequency reduces to

$$\vec{\Omega} = \frac{eB_y}{m\gamma}\begin{pmatrix} -a(\gamma-1)x'y' \\ (1+a\gamma) - a(\gamma-1)y'^2 \\ -a(\gamma-1)y' \end{pmatrix}, \tag{2.3}$$

where $a = \frac{g-2}{2}$, and x' and y' are the ratios of the transverse to longitudinal particle momenta, $x' = \frac{p_x}{p_z}$ and $y' = \frac{p_y}{p_z}$. To determine the precession angle of the electron spin (relative to the beam momentum), $\vec{\eta}$, the change in the beam direction along the

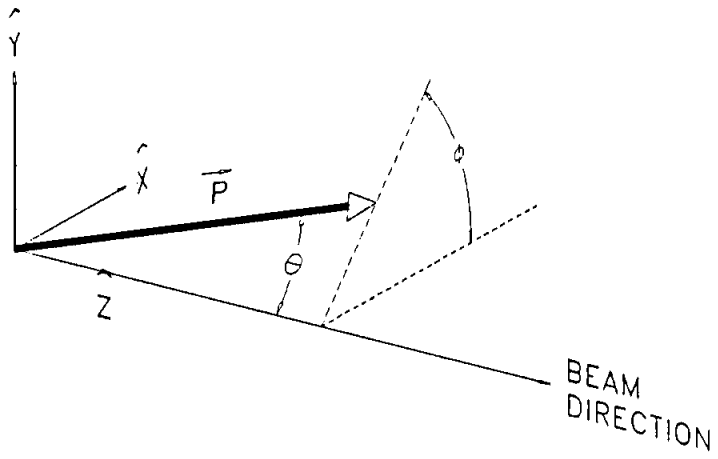

Figure 2.1: The coordinate system used for describing the beam, and the polar angles (θ, ϕ) that describe the orientation of the polarization vector, $\vec{P}$, relative to the beam direction.

trajectory must be accounted for by

$$\vec{\eta} = \vec{\Omega}\frac{l}{v} - \vec{\theta}_b. \tag{2.4}$$

Here l and v are the path length and velocity along the trajectory of the particle, and their quotient determines the interval of time the electron spin is precessing. θ_b is the angle through which a reference orbit ($x = x' = y = y' = 0$) particle is deflected and is given by $\frac{el_0B_y}{p_0}$, where l_0 and p_0 are the reference orbit path length and electron momentum, respectively. Combining these yields

$$\vec{\eta} = \frac{elB_y}{m\gamma v}\begin{pmatrix} -a(\gamma-1)x'y' \\ (1+a\gamma) - a(\gamma-1)y'^2 \\ -a(\gamma-1)y' \end{pmatrix} - \frac{el_0B_y}{p_0}\begin{pmatrix} 0 \\ 1 \\ 0 \end{pmatrix}. \tag{2.5}$$

A useful result (and one often used in this thesis) is for the case of the reference orbit.

Here, Equation 2.5 reduces to

$$\vec{\eta} = \begin{pmatrix} 0 \\ a\gamma\theta_b \\ 0 \end{pmatrix}, \tag{2.6}$$

which states that the spin of an electron deflected by a magnetic dipole field through an angle θ_b will precess by an amount $\eta_y = a\gamma\theta_b$ about the dipole field. The sense of rotation is given by the right-hand rule. Thus, since $a > 0$, the electron spin always rotates more than the electron momentum in a deflecting magnetic field.

Another example is the precession of an electron spin in a solenoid magnet where the magnetic field is longitudinal ($\vec{B} = B_z\hat{z}$). In this case Equation 2.4 becomes

$$\vec{\eta} = \frac{elB_z}{m\gamma v} \begin{pmatrix} -a(\gamma-1)x' \\ -a(\gamma-1)y' \\ 1+a \end{pmatrix}. \tag{2.7}$$

Because of the azimuthal symmetry of the solenoid we find the expected result that $\eta_x = \eta_y$. More importantly, we find that for the reference orbit (and most beams of interest) that the precession of the electron spin is given by

$$\vec{\eta} = \begin{pmatrix} 0 \\ 0 \\ \frac{geB_z l}{2mv\gamma} \end{pmatrix}, \tag{2.8}$$

where $B_z l$ is the integral of the solenoid axial field, $\int B_z dl$.

Finally, the case for a transverse electric field ($\vec{E} = E_x\hat{x}$) is given,

$$\vec{\eta} = \frac{elE_x}{m\gamma v} \begin{pmatrix} 0 \\ (a+\frac{1}{\gamma+1})\frac{\gamma v}{c^2} \\ (a+\frac{1}{\gamma+1})\frac{\gamma v}{c^2}y' \end{pmatrix}. \tag{2.9}$$

which describes spin precession in a type of spin rotator called a Wien filter, discussed later. Again, considering the reference orbit, the precession angle reduces to a rotation about the $\hat{y}$ axis. This is sensible because the transverse electric field in the laboratory

reference frame becomes, in the rest frame of the electron by the appropriate Lorentz transformation, a transverse electric field and transverse magnetic field about which the electron spin precesses,

$$\vec{\eta} = \begin{pmatrix} 0 \\ \frac{el_0 E_x}{p_0}\left(\frac{g}{2\gamma} - a\gamma\right) \\ 0 \end{pmatrix}. \tag{2.10}$$

For example, a spin manipulation system [En93] previously operated at CEBAF required electrostatic deflectors to precess the electron beam polarization by 90° which, for a 100 keV beam, required the bending angle to be 107.7°.

2.1.2 Description of a Polarized Beam

The motion of charged particles in an accelerator is determined by solving the dynamical equations of motion for particles in the presence of electromagnetic fields. Each particle is identified by two 3–dimensional variables; position and momentum $(\vec{r}, \vec{p})$. Thus, an ensemble of particles occupies a 6–dimensional phase volume. If the forces acting on the particles are conservative a theorem of Liouville states that the total 6–dimensional volume containing the particles is conserved.

The concept of a particle beam, as in an accelerator, has the condition that the momentum of the particles in a common direction (defined by the motion of a reference particle in an accelerator), usually p_z, is much greater than the momentum components transverse to this direction, p_x or p_y. It is often useful to project the transverse components of the 6-dimensional volume into each of two 2-dimensional transverse phase space areas defined by (x, x') and (y, y'), where $x' = \frac{p_x}{p_z}$ and $y' = \frac{p_y}{p_z}$.

Two simplifying assumptions of this concept of a beam are implied. The first is that the longitudinal and transverse motions are uncoupled by the nature of acceleration in the longitudinal direction. The second is that the transverse motions, x and y, are uncoupled, providing for independent solutions to the orthogonal motion. The longitudinal motion gives the central trajectory. The transverse motions are described

with respect to the central trajectory. Consequently, each of the two transverse phase space areas are useful quantities for characterizing the beam in an accelerator. The area of the transverse phase space (x, x') is the unnormalized emittance and is defined by

$$\epsilon_x = \frac{1}{\pi} \int \int dx dx', \tag{2.11}$$

and similarly for ϵ_y. Another useful quantity describing the emittance of a beam of particles undergoing acceleration is the normalized emittance given by

$$\epsilon_n = \beta\gamma\epsilon, \tag{2.12}$$

which describes how the phase space containing the particles scales with the central energy of the distribution. The utility of a normalized emittance is a consequence that during acceleration, the momenta of the particles in the direction of the acceleration, p_z, increases while the transverse momentum, p_x and p_y, do not change. Consequently, x' and y' decrease, ϵ_x and ϵ_y decrease, yet the total number of particles in the beam is still conserved. The ϵ_n, alternatively, are constant during longitudinal acceleration characterized by changing β and γ.

To discuss a beam of particles with spin we describe the beam polarization. The spin of a single particle can be described by the eigenvalue equations

$$\begin{aligned} \mathbf{S}^2\chi &= \hbar^2 s(s+1)\chi \\ \mathbf{S}_z\chi &= m_s\chi, \end{aligned} \tag{2.13}$$

where $s = \frac{1}{2}$ for an electron spin and $\chi = \binom{a_1}{a_2}$ is thus a two component (spinor) wave function. These equations may also be written in terms of the Pauli matrices $\vec{\sigma}$ defined by $\vec{S}\chi = \frac{\hbar}{2}\vec{\sigma}$. An explicit representation of these matrices is

$$\sigma_x = \begin{pmatrix} 0 & 1 \\ 1 & 0 \end{pmatrix}, \qquad \sigma_y = \begin{pmatrix} 0 & -i \\ i & 0 \end{pmatrix}, \qquad \sigma_z = \begin{pmatrix} 1 & 0 \\ 0 & -1 \end{pmatrix}. \tag{2.14}$$

The wave function is normalized to unity by the condition

$$\langle\chi|\chi\rangle = \left((a_1^*, a_2^*), \begin{pmatrix} a_1 \\ a_2 \end{pmatrix}\right) = 1. \tag{2.15}$$

The spinor wave function can also be described by the real-space polar coordinates (θ, ϕ) on the unit sphere. This relation is made by projecting, by use of the Pauli matrices, the spinor wave function onto the unit vector $\hat{e} = (\sin\theta\cos\phi,\ \sin\theta\sin\phi,\ \cos\theta)$, through

$$(\vec{\sigma}\cdot\hat{e})\chi = \lambda\chi. \tag{2.16}$$

Consequently, the wave function can be written

$$\chi = +\frac{\hbar}{2}\begin{pmatrix}\cos\frac{\theta}{2}\\ \sin\frac{\theta}{2}e^{i\phi}\end{pmatrix} - \frac{\hbar}{2}\begin{pmatrix}\sin\frac{\theta}{2}\\ -\cos\frac{\theta}{2}e^{i\phi}\end{pmatrix}, \tag{2.17}$$

and the expectation value of this wave function (describing a single spin direction) is

$$\vec{P} = \langle\chi|\vec{\sigma}|\chi\rangle. \tag{2.18}$$

As expected,

$$\begin{aligned} P_x &= \sin\theta\cos\phi, \\ P_y &= \sin\theta\sin\phi, \\ P_z &= \cos\theta. \end{aligned} \tag{2.19}$$

Note the magnitude of the polarization, $P = \sqrt{P_x^2 + P_y^2 + P_z^2} = 1$.

A realistic beam, however, is not perfectly polarized, but rather is a statistical mixture of the spin states of the constituent particles. The expectation value of the beam polarization is computed as the weighted average of the polarization, P_n, of the n constituent pure spin states, χ_n, forming the particle beam

$$\vec{P} = \sum_n w_n P_n = \sum_n w_n \langle\chi_n|\vec{\sigma}|\chi_n\ \rangle. \tag{2.20}$$

The factor w_n is the contribution of the n^{th} pure spin state to the system and is computed by

$$w_n = \frac{N_n}{\sum_n N_n}, \tag{2.21}$$

where N_n is the number of electrons in state χ_n. Exactly as before, the expectation value of the spinor wave functions with the Pauli matrices yields the polarization of

the beam of particles. The only difference is that the expectation value is now the weighted sum of n wave functions. The density matrix operator, ρ, is defined to be

$$\rho = \sum_n w_n |\chi_n\rangle\langle\chi_n|. \tag{2.22}$$

The polarization is calculated as $\mathbf{P} = tr(\rho\sigma)$, or explicitly,

$$\begin{aligned} tr(\rho\sigma_x) &= tr\left(\sum_n w_n \begin{pmatrix} a_{1,n}a_{2,n}^* & |a_{1,n}|^2 \\ |a_{2,n}|^2 & a_{1,n}^* a_{2,n} \end{pmatrix}\right) = P_x, \\ tr(\rho\sigma_y) &= P_y, \\ tr(\rho\sigma_z) &= P_z. \end{aligned} \tag{2.23}$$

The density matrix can then be written compactly,

$$\rho = \frac{1}{2}\begin{pmatrix} 1+P_z & P_x - iP_y \\ P_x + iP_y & 1-P_z \end{pmatrix} = \frac{1}{2}(1 + \mathbf{P}\cdot\vec{\sigma}). \tag{2.24}$$

As an example, consider measuring the polarization of a beam of particles whose spin states are along the beam momentum direction, p_z. Using the convention $\uparrow = +\frac{\hbar}{2}$ and $\downarrow = -\frac{\hbar}{2}$, the probability of measuring spin states with value $+\frac{\hbar}{2}$ is $\frac{1}{2}(1+P)$ and physically corresponds to counting the total number of spin states in the direction $\hat{z}$, $N_\uparrow$, over the total $N_\uparrow + N_\downarrow$. Likewise, the probability of measuring the $N_\downarrow$ electron spin states with value $-\frac{\hbar}{2}$ corresponds to a probability $\frac{1}{2}(1-P)$, therefore,

$$\begin{aligned} \frac{N_\uparrow}{N_\uparrow + N_\downarrow} &= \frac{1}{2}(1+P), \\ \frac{N_\downarrow}{N_\uparrow + N_\downarrow} &= \frac{1}{2}(1-P). \end{aligned} \tag{2.25}$$

Combining these yields the polarization as is physically observed in experimental systems used to measure the beam polarization,

$$P = \frac{N_\uparrow - N_\downarrow}{N_\uparrow + N_\downarrow}. \tag{2.26}$$

This result will be used to describe the extraction of the beam polarization from both Mott and Møller polarimetry used for this thesis.

2.2 Calculations for Spin Transport and CEBAF

This section includes the method and calculations for the polarization phenomena expected for the nominal beam transported at the Continuous Electron Beam Accelerator Facility (CEBAF). This includes a description of the accelerator necessary for calculating spin transport quantities in Section 2.2.1, and the method underlying the injector spin manipulation system and basic spin rotation results in Section 2.2.2. An estimate of the effect of the linacs on the spin transport is given in Section 2.2.3.

2.2.1 Spin Model for CEBAF

To calculate the motion of the beam polarization through the CEBAF accelerator a number of factors need to be considered. Refer to Section 1.2 for details and a layout of the accelerator. The dominant factors are the beam energy and beam bending angle, which determine how the spin precesses in each arc. The spin dynamics of a zero emittance beam, which are identical to those of a single electron, can be calculated easily to leading order by making three approximations: (a) the linacs do not rotate the spin; (b) the dipole fields of the arcs and transport channel precess the spin; and (c) the spreaders and recombiners do not give any net precession. With this model of CEBAF, the effective spin transport becomes a series of drift sections and 180° bending sections. The precession angle of the spin, θ_{spin}, for a relativistic electron in the bend plane of the dipole field is again, simply related to the bending angle, θ_{bend}, by

$$\theta_{spin} = \frac{g-2}{2}\gamma\theta_{bend}. \tag{2.27}$$

The leading contribution to the precession is the guiding dipole fields in the accelerator. Large dipole fields are located in the spreader, recirculator, recombiner, beam switchyard, and experimental hall magnet systems referred to in Figure 1.1.

The spreader and recombiner systems are symmetrical in that each serves to bend the beam orbit from one momentum direction to another which is parallel, but translated from the first, as shown in Figure 2.2. For example, the polarization at location

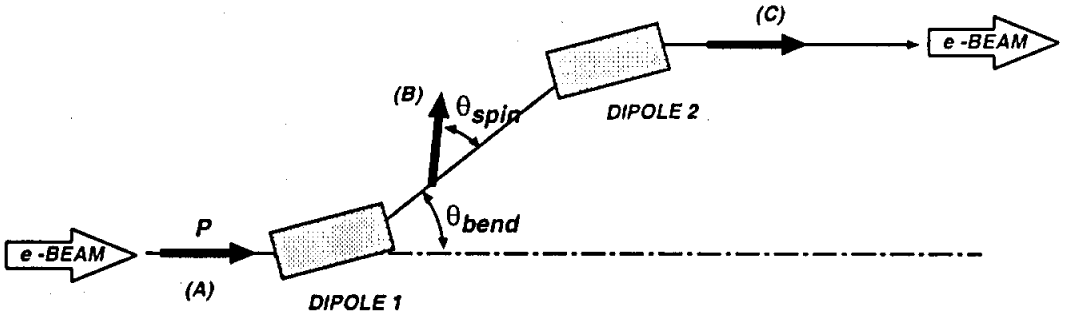

Figure 2.2: A magnetic *chicane* used to translate the beam to a parallel axis preserves the beam polarization orientation. This type of magnetic system is found in the spreader and recombiner sections of the CEBAF accelerator.

A is longitudinal to the beam momentum. When the beam momentum direction is changed by an amount θ_{bend} by *Dipole-1* the spin is precessed an amount θ_{spin}, and is no longer parallel with the beam momentum direction at location B. However, when the beam momentum direction is again changed by *Dipole-2* an amount $-\theta_{bend}$ the polarization rotates back, and at location C has its original orientation. Consequently, the net bend angle is zero and the beam polarization orientation, although rotated by each dipole magnet, is ultimately returned and preserved to the initial orientation.

The recirculator and beam switchyard magnets, however, are not compensated in this way and contribute to a net precession of the polarization. The net precession in each arc depends on the beam energy through the factor γ. All recirculation arcs have the same bending angle $\theta_{bend} = \pi$. A useful quantity for describing the precession of the polarization is the *spin tune*, ν_s, defined to be

$$\nu_s = \frac{\theta_{spin}}{2\pi}, \tag{2.28}$$

the number of revolutions the spin precesses relative to the beam momentum. The nominal beam energy and spin tune for each arc is given in Table 2.1.

The polarization precesses in the transport arcs which are used to deliver the beam from the accelerator to each of three experimental halls. The bend angles to reach the Hall A and Hall C experimental areas are nominally equal and opposite to one

Recirculation Arc	1	2	3	4	5	6	7	8	9
Beam Energy (MeV)	445	845	1245	1645	2045	2445	2845	3245	3645
Spin Tune (ν_s)	.505	.959	1.41	1.87	2.32	2.77	3.23	3.68	4.14

Table 2.1: Spin tune, ν_s, for the nine recirculation arcs of CEBAF for the design energy ($E_{injector} = 45\,MeV$ and $E_{linac} = 400\,MeV$).

another at the elevation of the accelerator beamline. The Hall B experimental hall is at an elevation above the accelerator beamline. As with the spreader and recombiner geometries, the Hall B beamline is parallel to the prior beamline, and consequently, the net rotation of the beam polarization between the accelerator and Hall B is zero. The bend angles to each transport arc and the corresponding spin tune per GeV (ν_s'), depending upon the number of recirculations, are listed in Table 2.2.

Experimental Area	Hall A	Hall B	Hall C
Transport Arc Bend Angle (θ_{bend})	+37.50°	+0°	−37.52°
ν_s' [GeV^{-1}]	+0.2363	0	−0.2364

Table 2.2: The spin tune per GeV (ν_s') in the transport arcs between the accelerator and each of the three experimental areas. ν_s' is used because the beam energy depends upon the number of recirculations prior to extraction.

2.2.2 Spin Manipulation Approach

Photoemission polarized electron sources produce beams with longitudinal polarization. In the transport from the injector to the experimental hall the electron spin precesses relative to the beam momentum. For example, referring to Table 2.1, the total precession of a beam accelerated to 4 GeV is more than 20 revolutions. Many experiments proposed at Jefferson Laboratory require a stable high polarization beam of electrons with the polarization oriented along the beam momentum at the scatter-

ing target. To meet this need a spin rotator is located in the injector to orient the polarization to be longitudinal at the experimental target.

A spin rotator is a sequence of magnets or electrostatic components which provide for the control of the spin orientation of a beam while leaving the outgoing orbit unaffected. Accelerators of various design employ different spin rotators to either preserve or orient the beam polarization. For example, in polarized beam storage rings, spin rotators termed *snakes* are employed to reverse the orientation of the beam polarization upon each revolution for the purpose of removing polarization errors which could otherwise coherently add to depolarize the beam. In a linear transport system such as CEBAF or the SLC a *snake* is unnecessary. In these accelerator designs the spin rotator is used to rotate the beam polarization orientation such that it satisfies a condition somewhere in the accelerator, typically that it be longitudinal at the target location of an experiment.

The spin transport model of the accelerator indicates that the net precession at CEBAF remains in the horizontal plane. However, if the accelerator has imperfections (as all do) it is sensible to have a device which can rotate the polarization by some amount out of the accelerator bend plane. Indeed, this experiment requires several such polarization orientations (including transverse to the bend plane).

It is worthwhile to explore a few levels of sophistication that can be employed to preserve longitudinal polarization at the experimental halls, leading to the approach used at CEBAF.

Without a spin manipulation system the final polarization orientation at the experimental halls can still be chosen by judiciously setting the linac and injector energy gains, E_{linac} and $E_{injector}$, respectively. The beam energy is then determined in each of the recirculation and transport arcs. The net precession for a given beam delivery configuration (number of recirculations and choice of experimental hall) determine the total precession between the electron gun and the experimental target. For p passes of the accelerator and a final bend $\hat{\theta}_{hall}$ to the experimental hall (in units of

π), the net accelerator precession is given by

$$\psi_{Total} = \frac{a\pi E_{linac}}{m_e c^2}\left(2p^2 - p(1-2\alpha-2\hat{\theta}_{hall}) - \alpha(1-\hat{\theta}_{hall})\right). \tag{2.29}$$

Here, $\alpha = 0.1125$, a fixed scaling factor between the injector and linac energy gain. The derivation of Equation 2.29 is given in Appendix A. The requirement for longitudinal polarization at the experimental area sets the condition that $\psi_{Total} = l\pi$, where l is an integer. Finally, the allowable linac energies are given by

$$E_{linac} = \frac{l m_e c^2}{a\left(2p^2 - p(1-2\alpha-2\hat{\theta}_{hall}) - \alpha(1-\hat{\theta}_{hall})\right)}. \tag{2.30}$$

The restriction of this method is that only specific final beam energies are allowed.

A more useful approach is to employ a spin rotator somewhere in the accelerator. The spin rotator can in principle be located anywhere in the accelerator. However, if the spin transport is well understood it is more practical to locate the rotator at a position where the beam energy is smallest. For example, a solenoid field integral of 0.0175 kG m is required to precess an 100 keV (electron gun energy) beam polarization by 90 °, however, to do this at the maximum design energy of 4 GeV the required field is $\frac{(\gamma\beta)_{4GeV}}{(\gamma\beta)_{100keV}}$ larger, or 209.2 kG m.

The approach at CEBAF is to locate two types of rotators in the 100 keV section of the injector shortly following the polarized electron gun. The first type of spin rotator, called a Wien filter, is discussed in Section 3.2.1. It produces a rotation of the spin direction in the Wien filter electric field plane (η_y). The second type of spin rotator is a solenoid magnet, discussed in Section 3.2.2, which produces a rotation about the longitudinal magnetic axis (η_z). To produce the required rotations for this experiment one Wien filter and two solenoid magnets are used in series.

The product of the rotations of the three spin manipulators transforms the polarization vector at the electron gun, $\vec{P}_{Gun}$, to a polarization vector exiting the spin manipulation system, $\vec{P}_{SM}$, like

$$\vec{P}_{SM} = R_z(\phi_{Solenoid_2}) \cdot R_z(\phi_{Solenoid_1}) \cdot R_y(\theta_{Wien}) \cdot \vec{P}_{Gun}, \tag{2.31}$$

where $R_x(\theta)$, $R_y(\theta)$, and $R_z(\theta)$ are the usual rotation matrices (defined in Appendix B). Because the rotations in the two solenoid magnets are about the same axis, and are in series, they commute, where $\phi_{S_{12}} = \phi_{Solenoid_1} + \phi_{Solenoid_2}$, giving

$$\vec{P}_{SM} = R_z(\phi_{S_{12}}) \cdot R_y(\theta_{Wien}) \cdot \vec{P}_{Gun}. \tag{2.32}$$

The condition for setting the rotation angles of the spin manipulator involve choosing $(\theta_{Wien}, \phi_{S_{12}})$ such that a final polarization, $\vec{P}_{final}$, is reached in an experimental hall. The final polarization is determined by the spin precession following the spin manipulators, but prior to the final location. All of the intervening spin rotations (about 3 possible axes) are due to the precession of the beam polarization in the accelerator. The final polarization can be written as the product of N rotations

$$\vec{P}_{final} = \prod_{j=1}^{N} ((R_i)_j(\theta_j)) \cdot \vec{P}_{SM}, \tag{2.33}$$

where the j^{th} rotation is due to a precession θ_j about the i^{th} axis. If the simple spin transport model for the accelerator is correct then this product of rotations due to the recirculation and transport arcs are all about the same $\hat{y}$ axis. In this case, all of the rotations commute and add simply giving

$$\vec{P}_{final} = R_y(\Theta) \cdot \vec{P}_{SM}, \tag{2.34}$$

where $\Theta = \sum_{j=1}^{N} \theta_j$ is the net bending angle through which the beam momentum is deflected in the accelerator.

The most trivial solution is for the case where the final polarization is to be longitudinal at the experimental hall ($\vec{P}_{final} = \pm P_0 \hat{z}$). The solution then shows that $\phi_{S_{12}} = 0$ (polarization is preserved to the bend plane of the accelerator) and $\theta_{Wien} = -\Theta$ (modulo 2π). A detailed derivation and the more general result of Equation 2.33 is given in Appendix C.

The most flexible approach is achieved by combining the above two methods. A linac energy is chosen such that the *difference* in net precession to any two experimental halls is a multiple of π. In this way, the reference spin direction can be adjusted

at the injector (one location) and the resultant beam polarization can be longitudinal in two or three end stations simultaneously. Calculation of linac energies using this method have been made by Sinclair [Si96] for two hall simultaneous operation.

Although this approach is preferable, it does not always satisfy the requirements for an experiment. It is often the case that the simultaneous experimental programs in the three halls cannot find a common linac energy (experimental schedule or unanticipated hardware failure) to provide exact multiples of π spin precession. In this situation, a compromise in the longitudinal polarization and beam current required for an experiment are helpful to optimize the efficient setup of the accelerator.

To describe the quality of a polarized beam for an experiment, a figure of merit relating the beam current and polarization is useful. The figure of merit is made by the basic relationship between a spin–dependent process, S, that can produce a measurable asymmetry, ϵ, from a preferentially polarized beam of polarization P,

$$\epsilon = S \cdot P. \tag{2.35}$$

The statistical uncertainty in the measurement of the spin–dependent process, ΔS, is proportional to $\Delta\epsilon/P$, where $\Delta\epsilon \sim 1/\sqrt{N}$. N is the number of events measured to determine the asymmetry, which is proportional to the beam current I. Combining these yields the figure of merit, IP^2. Obviously, there are only two orientations where the polarization is either parallel or anti–parallel to the beam momentum at the experimental hall. Consider the case where the polarization orientation is within some tolerance of being longitudinal, rather than being exactly longitudinal at the experimental area. For this case, assume the figure of merit can be reduced by at most 10% because another experimental hall requires some amount of the same beam current and polarization. This corresponds to reducing the longitudinal component of the beam polarization to $\leq$ 95% of its maximum value; or orienting the same polarization at an angle within $\theta = \cos^{-1}(0.95) = \pm 18^\circ$ of being longitudinal.

2.2.3 Estimate of Linac Effects

The estimate for the effect of the linac on the polarization of the electron beam is made by considering separately the magnetic and electric fields as seen by the beam. Quadrupoles, to focus and maintain the beam in the linac, and correction dipoles, to steer the beam along the reference orbit, are used in the linacs; there are no net bend dipoles and consequently the precession of the reference orbit electron due to magnetic fields is zero. The RF cavities produce the accelerating gradient, $\vec{E}$, which near the axis of the linac is longitudinal, or nearly parallel to the beam motion, $\vec{\beta}$. In this case $\vec{\beta} \parallel \vec{E}$ and the only term in the BMT equation containing the electric field, proportional to $\vec{\beta} \times \vec{E}$, is zero. The extent to which the electron spin experiences transverse electric fields away from the cavity axis is small for two reasons. First, the coefficient of the term proportional to the electric field, $(\frac{g}{2} - \frac{\gamma}{\gamma+1})$, is the difference between two nearly equal values, which for beam energies between 400 MeV and 4 GeV is in the range of (2.5 to 1.3) $\times 10^{-3}$. Second, the geometry of the acceleration cavity RF couplers introduce transverse electric fields of alternating sign to the passing beam, thus tending to cancel.

2.3 Simulation of Spin Transport at CEBAF

This section describes results for the simulation of spin transport, and specifically for the sensitivity of the beam polarization to the beam orbit. Concepts and definitions used to describe beam motion are given in Section 2.3.1. The spin simulation program used for spin motion analysis is described in Section 2.3.2. Results of simulations for finite beam size depolarization phenomena are given in Section 2.3.3, and the sensitivity of the beam polarization to the beam orbit is discussed in Section 2.3.4. Finally, a description and simulation results for the proposed experiment is given in Section 2.3.5.

2.3.1 Betatron Motion

The need for focusing charged particles in an accelerator is a fundamental part of its design. Without some type of focusing particles with even a small initial transverse momentum would eventually reach the walls of the accelerator chamber or beampipe and be lost. To overcome this problem accelerators are designed with magnetic elements which provide a restoring force to stabilize the divergent motion. For example, in the low energy ($\leq 500\,\mathrm{keV}$) section of the CEBAF injector beamline solenoid magnets are used for their focusing properties, similar to an optical lens. In the remainder of the CEBAF accelerator, sequences of focusing (and defocusing) quadrupole magnets accomplish the same goal. The general equation of motion for particles in these restoring force magnetic fields is that of a simple harmonic oscillator,

$$u''(s) + \omega^2 u(s) = 0, \tag{2.36}$$

where u represents either x or y transverse displacement along a reference orbit in the direction s. The particle moving through the accelerator performs oscillations about the reference orbit with some amplitude, $\hat{u}$, and a frequency ω. Because this type of motion was discovered in connection with particle motion in the Betatron developed by Kerst and Serber [Ke41], the motion is referred to as a *betatron oscillation.* Stable solutions of Equation 2.36 are sinusoidal and trajectories are often classified as sine–like or cosine–like for this reason, as depicted in Figure 2.3. Consequently, the general solution can be made as a superposition of sine and cosine –like orbits.

This is, of course, an oversimplification. In reality, the magnetic focusing scheme is a series of distributed elements. Between each element is a *drift space*, where the beam continues undeflected (we neglect the Earth's magnetic field). Rather than the *classical* oscillation described above the real beam receives a series of localized deflections from quadrupole magnets. Formally, the amplitude and phase advance of the betatron oscillation is determined by the distribution of focusing elements referred to as the magnetic lattice. Consider two examples which are of consequence. Imagine an actual beam were to follow the ideal reference orbit of an accelerator. The

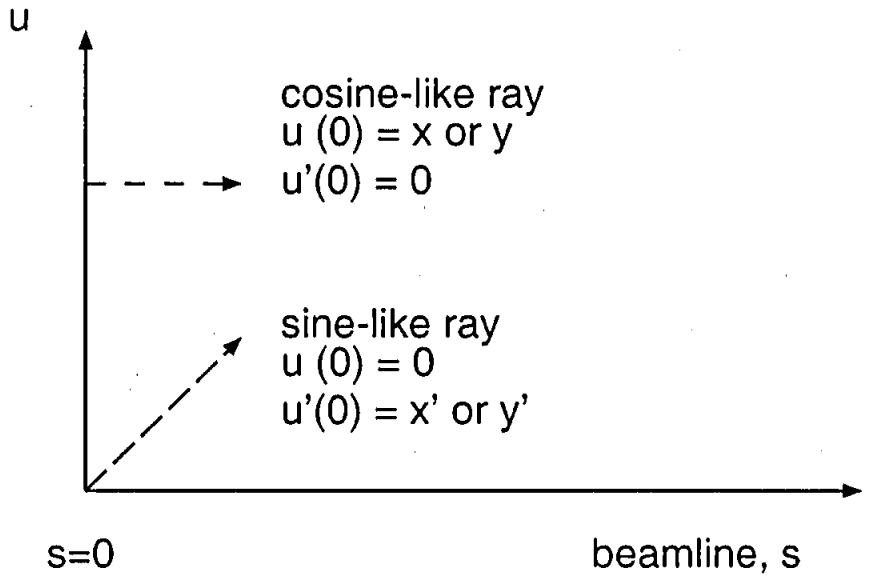

Figure 2.3: Trajectories are described by sine–like and cosine–like rays according to the conditions which describe the amplitude and angle of the particle motion.

finite transverse size of the beam results in particles at the edge of the beam profile undergoing betatron oscillations (with amplitudes comparable to the beam size) about the reference orbit. Extending this concept, if the beam itself were displaced from the reference orbit, or moving at an angle to the reference orbit, the entire beam would execute a betatron oscillation. The oscillation would be about the reference orbit, with some characteristic frequency dependent upon the magnetic focusing. The particle motion within the beam profile, described above, would be superposed with the betatron motion of the entire beam. A useful expression characterizing the number of oscillations a particle or beam makes in traversing a region of an accelerator is the *betatron tune*, denoted by ν_x (horizontal motion) or ν_y (vertical motion).

2.3.2 MURTLE SPIN22 Spin Tracking Code

The single particle spin tracking program MURTLE SPIN22 [Fi95], written at the Stanford Linear Accelerator Center to understand the spin transport of the Stanford Linear Collider, was used to simulate spin transport at CEBAF. The program, written in

standard Fortran, numerically integrates the equations of motion to second order to calculate the trajectory through an accelerator model. The accelerator model is a sequential list of the elements along the beamline as defined in the input standard of TRANSPORT [Br77], a first- and second- order matrix multiplication computer program intended for the design of magnetic beam transport systems. A typical simulation takes as input the accelerator model (description of beamline), and the initial position (x, y), initial angles (x', y'), spin orientation $(\vec{s_0} = s_x, s_y, s_z)$, and energy (E) of a single electron. The simulation output includes a list of the particle position and spin orientation along the length of the beamline. Also included is a spin transport matrix (STM) which maps an initial spin vector, $\vec{s}_{initial}$, to the final point of the beamline,

$$\begin{pmatrix} s_x \\ s_y \\ s_z \end{pmatrix}_{final} = \begin{pmatrix} S_{xx} & S_{xy} & S_{xz} \\ S_{yx} & S_{yy} & S_{yz} \\ S_{zx} & S_{zy} & S_{zz} \end{pmatrix} \begin{pmatrix} s_x \\ s_y \\ s_z \end{pmatrix}_{initial} . \tag{2.37}$$

The accelerator model used for the spin tracking simulations is based on the design model for the CEBAF accelerator. The design model is defined in terms of the standard input for DIMAD [Br85], a second-order particle tracking program which has been well-tested and is used in the design of circular accelerators and beamlines. To perform spin transport studies the design model of the recirculation arcs of the accelerator was converted from the DIMAD input standard to the TRANSPORT input standard. The conversion between standards was checked for equality before any of the spin simulations were performed. Minor modifications were made to the original spin tracking program to streamline the output and allow for scaling recirculation arc models to arbitrary energies. However, the simulation program is otherwise entirely based on MURTLE SPIN22.

One limitation of the spin tracking program is that the particle energy cannot be incremented in the accelerator model to include linac energy gains. Rather, to compute the spin tracking for elements separated by a linac requires simulating the region before and after the linac and then combining the results in a meaningful way.

This is done by successively multiplying the spin transport matrices and assuming the spin transport matrix for each linac is **1**.

Another limitation is that only single particle tracking is performed. To simulate spin effects related to the finite size of the beam many simulations of single particle tracking were performed with initial conditions that sampled the beam profile. The typical time required to compute the spin transport matrix for a recirculation arc on a moderately busy Hewlett-Packard 9000 workstation is 60 seconds.

2.3.3 Depolarization in Recirculation Arcs

Spin tracking simulations were performed for each recirculation arc to determine the extent to which spin motion would differ for electrons which originated from different locations in the beam profile. The differences in the spin motion are due to the non-uniformity of the electromagnetic fields over the extent of the beam profile. The average of these differences over the beam profile provides an estimate of the depolarization a beam of uniform spin orientation would incur traversing a recirculation arc. The simulations were performed for electrons exiting a linac and entering a spreader, and then tracked through elements until the end of the recombiner, before entering the next linac. The initial position and momenta of the electrons were chosen to sample the center and extrema of the accelerator unnormalized phase space ($\epsilon_{x,y} = \epsilon_n/\beta\gamma$) for each recirculation arc as shown in Figure 2.4, using the CEBAF normalized design emittance, $\epsilon_n = 3.916 \times 10^{-6}\,\mathrm{m\,rad}$ (4σ). For each trajectory a different spin transport matrix is computed. For a set of trajectories the maximum difference in the spin orientation between two electrons at the end of the arc, given the same initial spin orientation at the entrance, was determined. The difference in the final spin orientation between two trajectories is determined from the inclusive angle between the final spin vectors, $\vec{s}_1$ and $\vec{s}_2$, given by

$$\delta = \frac{\vec{s}_1 \cdot \vec{s}_2}{|\vec{s}_1||\vec{s}_2|}. \tag{2.38}$$

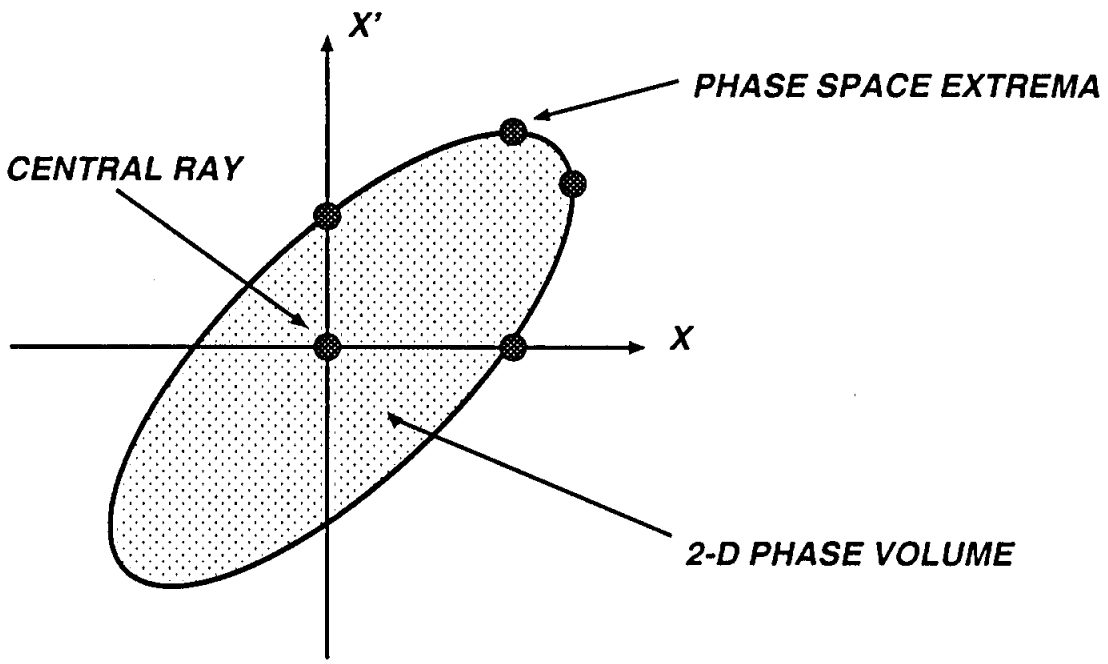

Figure 2.4: Diagram indicates locations in the transverse phase space used for sampling initial trajectory conditions for simulating depolarization effects due to the finite size of the electron beam.

The results, shown in Table 2.3, are twice the maximum inclusive angle as determined from the simulation for each recirculation arc. The factor of two arises because the simulation was performed for only half of the symmetrical phase space area. The linearity of the fields over the small beam profile ($\sim 100\,\mu$m) make this assumption reasonable. The results indicate that the nominal depolarizing effect from the finite beam emittance is modest, incoherently adding (an upper bound) to 0.72° for all 9

Arc	1	2	3	4	5	6	7	8	9
Beam Energy (MeV)	445	845	1245	1645	2045	2445	2845	3245	3645
δ_{max} (deg)	.016	.028	.022	.198	.036	.096	.256	.074	.150

Table 2.3: The maximum inclusive angle, δ_{max}, for all nine recirculation arcs at the nominal design energies.

recirculation arcs. This maximum angle is not a practical quantity to use. However,

a depolarization, or difference from the nominal polarization is useful. Assuming the EM fields vary linearly over the beam profile, the maximum difference angle simply bounds a space linearly filled with spin components that vary between 1 and $\cos(\delta_{max})$. In the same way that $\int \cos^2(\theta) d\theta$ over a period is $\frac{1}{2}$, the average of the spin components relative to the central ray can be computed. Orienting the final spin vector for the reference orbit along the $\hat{z}$ direction, as a point of reference, the components which differ by an angle δ have length $\cos(\delta)$ along the $\hat{z}$ direction. The average over all of the spin directions in the phase space is then simply

$$\overline{s}_z = \frac{\int \cos(\delta) d\delta}{\int d\delta}, \tag{2.39}$$

and the result is

$$\overline{s}_z = \frac{\sin\left(\frac{\delta_{max}}{2}\right)}{\left(\frac{\delta_{max}}{2}\right)}. \tag{2.40}$$

The depolarization for the 9 recirculation arcs using $\delta_{max} = 0.72°$ results in an average depolarization of $\sim 10^{-3}$ % ! In fact, to produce a 1% beam depolarization requires $(delta_{max} = 28°$.

Presently, the systematic uncertainties in the beam polarimeters limit the relative uncertainty in measuring the difference in polarization between the injector and experimental halls to $\leq 5\%$. Consequently, the level of depolarization estimated from the effect of the finite beam size is not measurable. A future accelerator might have 5–10 larger beam energy and 20–50 larger normalized emittance. In this case, the effects are larger and may be measurable.

2.3.4 Polarization Sensitivity

The largest spin transport effect at CEBAF is the precession of the beam polarization about the bending magnetic dipole fields which guide the beam along the reference orbit of the accelerator. Spin transport simulations for orbits undergoing betatron oscillations about the reference orbit in the recirculation arcs show a striking connection to the precession frequency of the electron. The effect originates because

the quadrupole magnetic fields act on the beam polarization in a regular way. The net effect is largest when the spin tune ν_s is close to the betatron tune in the plane perpendicular to the plane of spin precession. For the case of the recirculation arcs (horizontal spin precession) the relevant orbit is the betatron oscillation in the vertical plane (ν_y). Actual accelerator operations include beam orbit errors and/or instabilities of the magnetic fields that cause the betatron oscillations. To explain these points a series of spin transport simulations of a vertical betatron oscillation in the CEBAF recirculation arcs is presented.

A plot of a cosine-like ($y = y_0, y' = 0$) vertical plane betatron oscillation is shown in Figure 2.5. Here the electron is introduced with a vertical offset ($y = 1\,\text{mm}$) at

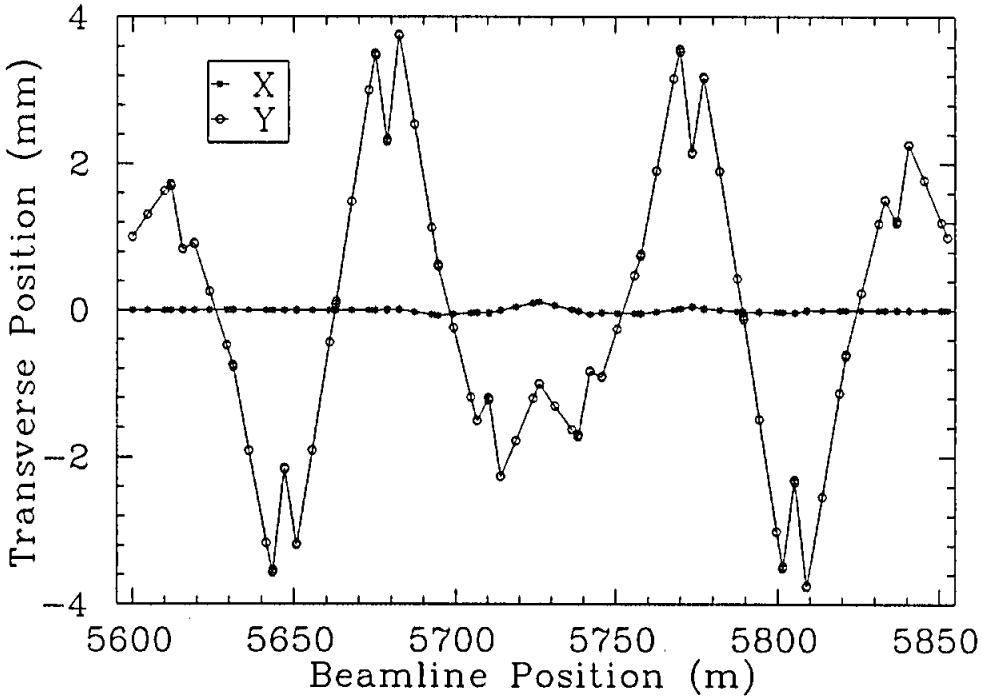

Figure 2.5: Characteristic betatron motion in arc proper for a vertical orbit displacement.

the end of the spreader of arc 9 with no horizontal or angular offset. The resulting horizontal and vertical trajectories are plotted through the arc. Quadrupole magnets are at the locations where the slope of the trajectory changes. The π bend for each of the nine recirculation arcs is designed with nominally identical betatron tunes. Each

has a horizontal betatron tune $\nu_x = 5$ and a vertical betatron tune $\nu_y = 3$. The latter can be counted by tracing the number of periods in Figure 2.5. As a consequence of the similar optics, equal initial conditions result in identical betatron motion for each arc. The x and y motions are clearly uncoupled. The ratio of the amplitudes for the vertical and horizontal trajectories is $\approx \frac{4\,\mathrm{mm}}{100\,\mu\mathrm{m}}$, or 40:1.

The spin transport simulation results of three recirculation arcs (1, 7, 9) is discussed for the vertical betatron oscillation described. The results are shown in Figure 2.6 through Figure 2.8. By studying these plots it becomes clear that when $\nu_s \approx \nu_y$ the difference between the spin motion of the perturbed electron orbit and the spin motion of the reference electron orbit increases. Characteristically, the effect is a rotation of the spin vector about the $\hat{x}$ axis ($R_x(\theta)$).

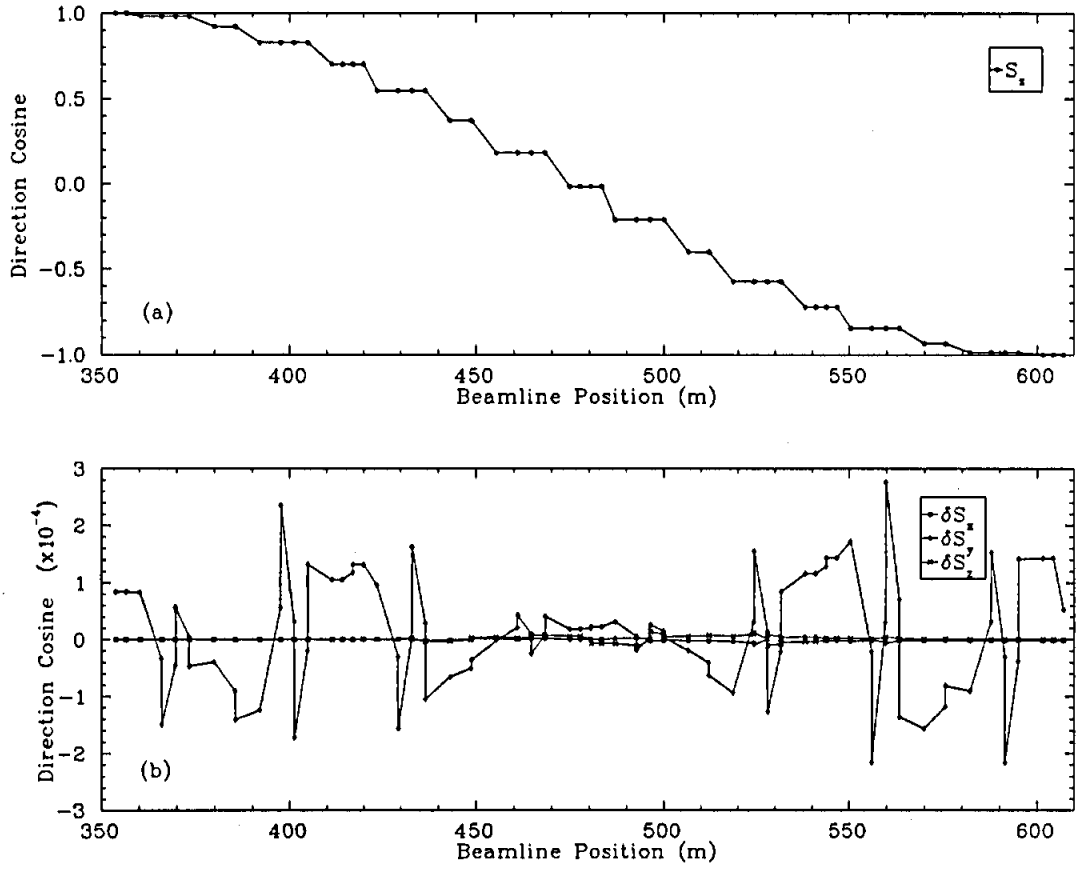

Figure 2.6: Arc 1 spin tune (a); and differences (b) between the spin components of a vertical betatron orbit and the reference orbit.

The simulation results for arc 1 ($E = 445\,\mathrm{MeV}$) are shown in Figure 2.6. The initial spin direction is $\vec{s}_i = +\hat{z}$. The upper plot of Figure 2.6 shows the s_z component of the spin motion for the reference orbit. The change in s_z (direction cosine of the spin angle) is due to precession caused by dipole magnetic fields along the beamline. The region of the plot where the spin direction is constant indicate that the electron spin is not interacting with a magnetic field. While traversing the arc, the spin direction cosine changes from $+1$ to -1 indicating that as the particle momentum is bent through π in the arc the spin rotates $\approx 2\pi$ to a new orientation.

The spin motion for the orbit shown in Figure 2.5 is then calculated. The lower plot shows, component-by-component, the *differences* between the spin motion for the perturbed and reference orbits, where

$$\delta s_j = (s_j)_{perturbation} - (s_j)_{reference}, \tag{2.41}$$

$j \in (x, y, z)$. During the betatron oscillation for the perturbed orbit the electron spin interacts with EM fields not seen on the reference orbit, such as the quadrupole fields which are non-zero away from the quadrupole magnetic axis. These interactions add additional spin rotations to the perturbed electron orbit, resulting in a difference in the spin motion. Because the dipole magnetic fields are essentially constant over the vertical motion, the s_x and s_z components are equally affected during the vertical betatron oscillations. Note that both δs_x and δs_z are less than 2×10^{-5} in this simulation.

In contrast, s_y is sensitive to the horizontal component of the quadrupole magnetic fields, which increase linearly as a particle moves vertically away from the reference orbit. It is evident from the plot that the accumulated spin rotations which differ from the reference orbit due to vertical excursions into the horizontal quadrupole fields show larger, non-zero spin rotations. However, they tend to cancel and δs_y never becomes larger than 3×10^{-4}. This results because the precession frequency varies slowly compared with the frequency of the vertical orbit motion. In other words, the quadrupole magnetic fields are effectively sampled by the electron spin as

it slowly precesses in the bend plane. In this way, the additional spin rotations tend to systematically cancel in the same way that, for example,

$$\int_0^1 dx \cos(2\pi\nu_s x) \cos(2\pi\nu_y x) \approx 0, \tag{2.42}$$

when $\nu_s \neq \nu_y$. In arc 1 $\nu_s = 0.505$ and $\nu_y = 3.0$.

Simulation results for a similar study of arc 7 ($E = 2845\,\mathrm{MeV}$) are shown in Figure 2.7. The upper plot shows s_z along the reference orbit of arc 7. Again,

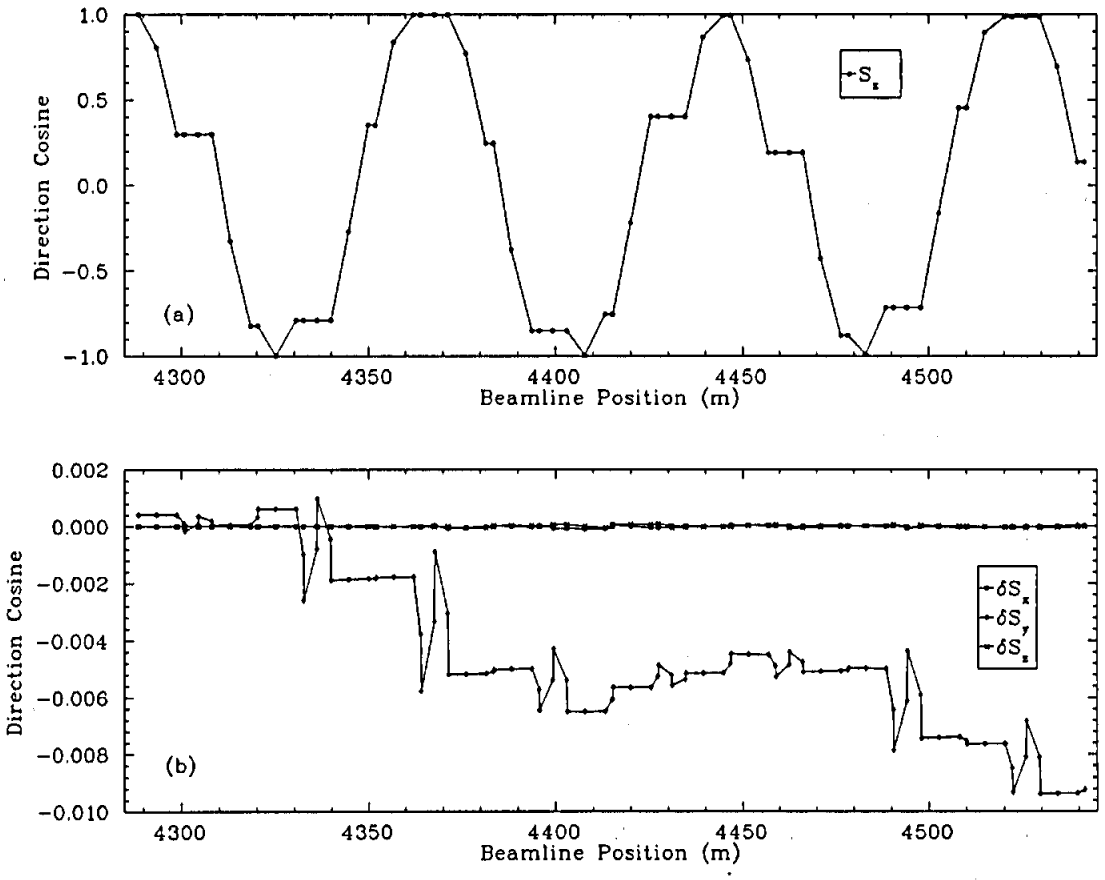

Figure 2.7: Arc 7 spin tune (a); and differences (b) between the spin components of a vertical betatron orbit and the reference orbit.

$\vec{s}_i = +\hat{z}$. The precession rate is larger in arc 7 than arc 1 because γ is larger by the ratio of the beam energies of the two arcs, $\frac{E_7}{E_1} \approx 6$. The spin tune for arc 7 is $\nu_s = 3.25$. The betatron tune ν_y and the spin tune ν_s have nearly identical phase along the arc.

Again, the spin motion for the perturbed orbit is calculated. The lower plot in the figure shows, component–by–component, the *differences* between the spin motion for the perturbed and reference orbits. Again, $\delta s_x \approx 0$ and $\delta s_z \approx 0$ for both of the trajectories because the vertical fields along each of the trajectories is nearly identical. However, s_y does change significantly due to the horizontal component of the quadrupole magnetic fields encountered by the electron spin over the vertical orbit motion. These interactions coherently add to precess the spin in the same direction along the length of the arc. This is because when the electron is at the top of a betatron oscillation the horizontal component of the quadrupole fields add, for example, a small negative vertical spin component. Then, later in the arc at the bottom of the betatron oscillation, the particle interacts with a reversed horizontal quadrupole magnetic field. Because the horizontal components of the spin have precessed by $\approx \pi$ at this point, the spin has also reversed direction, and another small negative vertical spin rotation is generated.

Finally, the simulations results for arc 9 ($E = 3645\,\mathrm{MeV}$) are shown in Figure 2.8. These indicate that some coherence between the vertical betatron oscillation and the spin tune still exists. The upper plot indicates that the spin orientation is now rotating faster than the betatron oscillation, accumulating more periods than the precession frequency over the length of the arc. Because of this, the phase difference between the two oscillations increases along the length of the arc. The difference between the spin orientation of the perturbed electron orbit and reference electron orbit, shown in the lower plot, is again explained by considering the accumulated spin rotations in the quadrupoles. The initial positive spin growth observed is due to the similarity in the periodic structure of the betatron oscillation and the spin tune. However, roughly half-way along the arc the mis-match in phase causes the spin rotations due to excursions in the quadrupole fields to begin accumulating in the opposite direction, leading to a peak in the vertical spin component followed by a reduction.

This investigation (and its interpretation) was checked by performing an element–by–element analytical calculation which considered the vertical position, spin orienta-

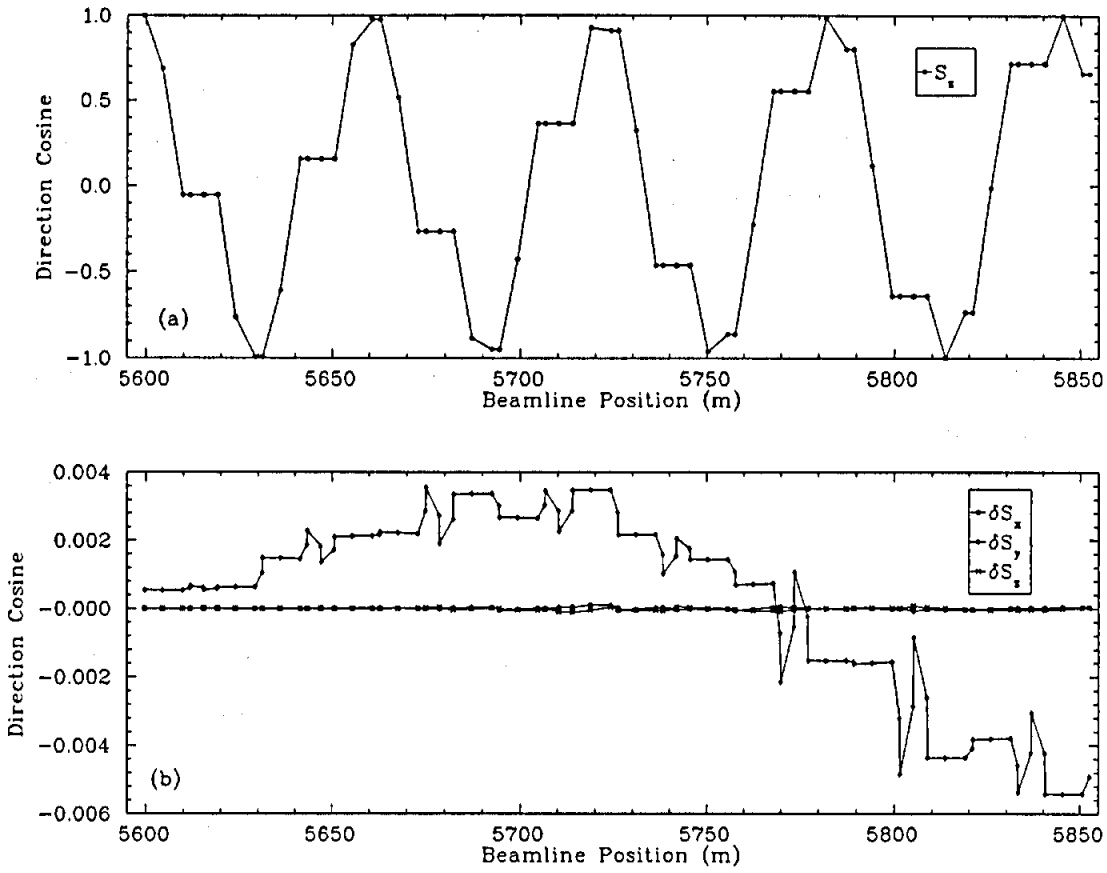

Figure 2.8: Arc 9 spin tune (a); and differences (b) between the spin components of a vertical betatron orbit and the reference orbit.

tion, and quadrupole locations along arc 9. By summing the net spin rotations along the arc a good fit to the lower plot shown in Figure 2.8 was obtained. The results from the simulations indicate that the spin rotations are due to excursions into the quadrupole fields.

These simulations predicted the sensitivity of the spin direction to vertical betatron oscillations to be the strongest in arc 7. Further simulations were performed for two trajectories which were injected at the entrance to arc 7 with the same initial spin direction, but which followed different orbits. This was done to determine the inclusive angle between the final spin directions of the two orbits as a function of the initial spin direction at the beginning of arc 7. The calculated inclusive angle, ΔS, is plotted in Figure 2.9 as a function of the initial spin direction for the case

where one orbit was introduced with a vertical displacement of 1 mm and the second orbit was introduced with a vertical displacement of -1 mm. Two significant pieces

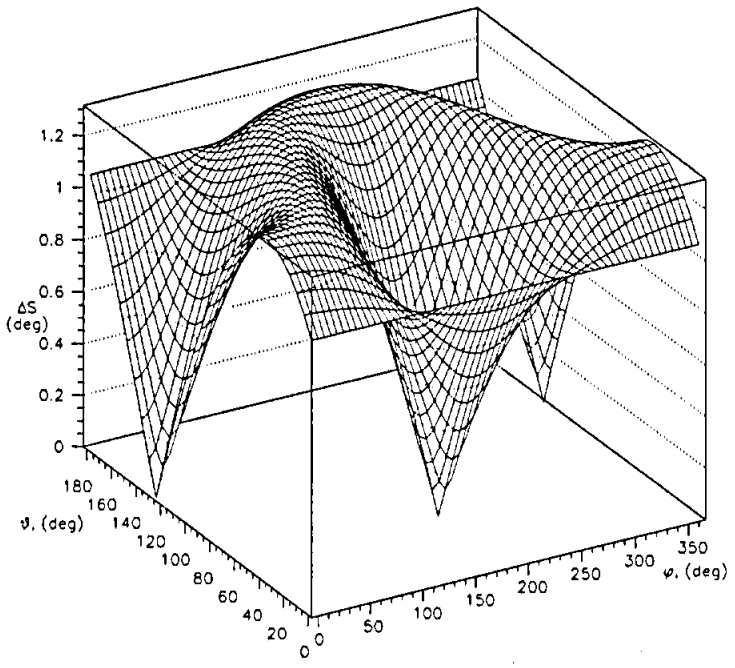

Figure 2.9: Inclusive angle, ΔS, between final spin vectors at the end of arc 7 of two different orbits as a function of the initial spin direction at the beginning of arc 7.

of information are extracted from this plot. First, the largest relative spin angle difference, ΔS, is roughly 1.3°. Second, there are specific initial spin orientations which have identical final spin orientations (indicated by the zeros in the plot). Both of these features are due to the beam polarization–quadrupole coupling introduced by the orbit perturbations.

These features can be understood by writing the spin transport matrix (STM) for both trajectories in terms of the sum of two matrices: (1) the reference orbit matrix; and (2) the difference orbit matrix showing the additional precession contribution due to the orbit perturbation. In this form, the precession effects due to orbits different

than the reference orbit becomes more obvious. The matrices are listed here;

$$STM_{ref} = \begin{pmatrix} +0.13656 & +0.00000 & -0.99063 \\ +0.00000 & +1.00000 & +0.00000 \\ +0.99063 & +0.00000 & +0.13656 \end{pmatrix} \tag{2.43}$$

$$STM_{y=+1mm} = STM_{ref} + 10^{-2} \begin{pmatrix} +0.005 & -0.821 & +0.004 \\ -0.683 & -0.007 & -0.923 \\ -0.003 & +0.803 & -0.002 \end{pmatrix}_{difference} \tag{2.44}$$

$$STM_{y=-1mm} = STM_{ref} + 10^{-2} \begin{pmatrix} +0.005 & +0.821 & +0.004 \\ +0.683 & -0.007 & +0.923 \\ -0.003 & -0.803 & -0.002 \end{pmatrix}_{difference} \tag{2.45}$$

First, note that in *each difference matrix* the elements which couple s_y with s_x and s_y with s_z are approximately equal. These matrix elements describe the rotation of the bend plane spin components (s_x or s_z) into the vertical direction (s_y). This precession is the result of the interaction between the bend plane spin components and the horizontal quadrupole magnetic fields. It is important to consider that these matrices are not for a single quadrupole magnet, but rather for a collective set of magnets which can act on all three components of the beam polarization simultaneously. If we studied a single quadrupole magnet then the expected coupling of s_x with s_y would be zero . However, because the dipole bending magnets mix the s_x and s_z components by rotating the beam polarization in the bend plane, the quadrupole interaction becomes apparent in all the S_{xy}, S_{yx}, S_{yz}, and S_{zy} matrix elements, which are roughly two orders of magnitude larger than the other matrix elements. Note the sign change of these matrix elements between the spin transport matrices of the two trajectories. This sign changes are because the two trajectories are symmetric to one another about the horizontal bend plane. The direction of the quadrupole fields, however, is anti-symmetric about the horizontal bend plane (required for beam focusing). Therefore, the spin orientation along the two trajectories show equal and opposite spin rotations with respect to one another.

Finally, we note that the remaining elements in both *difference* matrices are approximately equal. The value of these elements mainly causes the bend plane spin components to rotate $\sim 0.001°$ more than the central orbit. Each of these matrix elements have the same sign which indicates that the effect is not related to the quadrupoles (which are anti-symmetric between perturbations). The value of these matrix elements may be related to path length difference in the arc.

2.3.5 The Proposed Experiment

For different spin orientations a study of the sensitivity of the spin transport to vertical betatron oscillations in the 180° bend of arc 7 is proposed. A measurement of the spin transport associated with either a reference or perturbed orbit in arc 7 requires transporting the beam, following arc 7, through the recombiner, south linac, extraction region, beam switchyard, and Hall C transport channel. The Møller polarimeter is located there. Because the CEBAF Møller polarimeter [Ro94] is designed to measure only the longitudinal component of the beam polarization it is necessary to study the spin rotation sensitivities in terms of the final s_z component of the beam polarization.

Analogous to the spin transport matrices presented earlier for arc 7, the cumulative spin transport matrices for two perturbed trajectories: (1) a vertical offset of $y = +1$ mm into arc 7 followed by the reference orbit from the end or arc 7 to the Møller polarimeter and (2) a vertical offset of $y = -1$ mm into arc 7 followed by the reference orbit from the end of arc 7 to the polarimeter, are presented here in terms of the cumulative reference orbit matrix,

$$STM_{reference} = \begin{pmatrix} -0.97009 & -0.00001 & -0.24276 \\ -0.00001 & +0.99999 & -0.00000 \\ +0.24276 & +0.00000 & -0.97009 \end{pmatrix} \tag{2.46}$$

$$STM_{y=+1mm} = STM_{reference} + 10^{-2} \begin{pmatrix} +0.004 & -0.887 & +0.002 \\ -0.683 & -0.007 & -0.923 \\ +0.004 & -0.730 & +0.004 \end{pmatrix}_{difference} \tag{2.47}$$

$$STM_{y=-1mm} = STM_{reference} + 10^{-2} \begin{pmatrix} +0.004 & +0.887 & +0.002 \\ +0.683 & -0.007 & +0.923 \\ +0.004 & +0.730 & +0.004 \end{pmatrix}_{difference} \tag{2.48}$$

A plot showing the difference in the s_z components, δS_z, of the beam polarization at the polarimeter for the two trajectories is shown in Figure 2.10. The plot shows that the sensitivity of the longitudinal polarization component to the two trajecto-

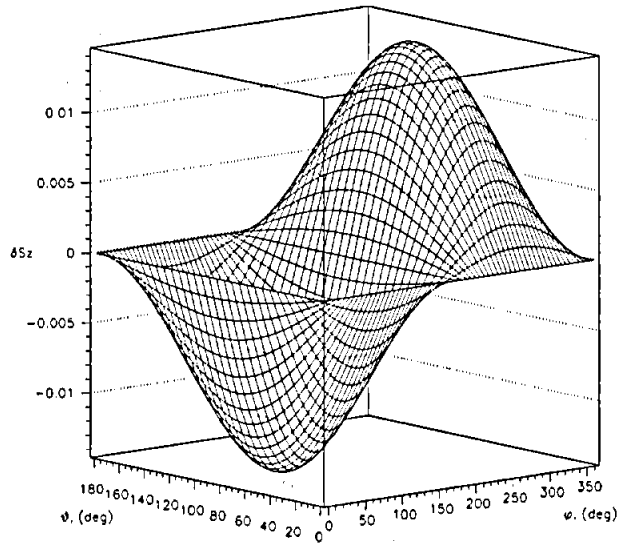

Figure 2.10: δS_z for Arc 7 to Møller polarimeter.

ries which differ vertically by ± 1 mm about the reference orbit in arc 7 is a small, but measurable quantity. Because we are examining the s_z component of the beam polarization at the Møller polarimeter we only compare the differences between the contributions of the matrix elements $S_{zj}, j \in (x, y, z)$, of the two spin transport matrices.

Of these matrix elements, as in the earlier simulations, the quadrupole coupled matrix element, S_{zy}, is dominant (S_{zx} and S_{zz} are $\sim 10^{-2}$ times smaller than S_{zy}) in the final spin transport matrix because of the perturbation in arc 7. Because it is this matrix element which is the dominant contribution to the final s_z component of the beam polarization, we see a surface which is $\sim \sin(\theta)\sin(\phi)$. Recall that S_{zy} couples to s_y and that for our simulations we have been writing the initial spin in terms of θ and ϕ, i.e.,

$$\begin{aligned} s_x &= \sin(\theta)\cos(\phi) \\ s_y &= \sin(\theta)\sin(\phi) \\ s_z &= \cos(\theta). \end{aligned} \tag{2.49}$$

Because the orbit perturbations in arc 7 are equal and opposite we find that the value of S_{zy} changes sign between the two spin transport matrices. Thus the amplitude of the surface shown in Figure 2.10 is equal to $(S_{zy})_{y=+1mm} - (-(S_{zy})_{y=-1mm})$, i.e., twice the value of S_{zy} or -0.0146.

In the end, the measurable polarization effect at the Møller polarimeter is caused by the strength of the cumulative coupling to the quadrupole fields as given by S_{zy}, and is particularly sensitive to the extent to which the beam polarization entering arc 7 is vertical.

Chapter 3

The Experiment

The goal of this experiment is to characterize the predicted sensitivity of the spin transport to the beam orbit in a CEBAF recirculation arc. This is the first measurement of this effect at CEBAF. The results provide information on the polarized beam delivery performance of this latter accelerator and for future accelerators of this type, such as the proposed Electron Laboratory for Europe (ELFE). This accelerator would be similar to the CEBAF accelerator, but operate at beam energies up to 25 GeV, where γ is greater, so the effects may be greater.

The experiment relies on the operation of many sub-systems of the accelerator. A simplified schematic of the accelerator showing only elements necessary for the experiment is shown in Figure 3.1. The experiment was performed at a beam energy 5% higher than the nominal design energy of the accelerator. The photoemission electron source described in Section 3.1 provides the polarized electron beam for the experiment. A spin manipulation system described in Section 3.2 can orient the beam polarization over a solid angle $\approx 2\pi$. The beam is then accelerated to an energy of 5 MeV and diverted to a Mott polarimeter (see Section 3.3) where the transverse components of the beam polarization are measured. For the energy configuration of the accelerator for this experiment, the beam bypasses the polarimeter and is accelerated to an energy of 47.3 MeV before injection into the main accelerator. Two parallel linacs joined by beam transport arcs allow the beam to pass multiple times through the accelerator, or *recirculate*. The beam recirculates 3.5 times in the accelerator

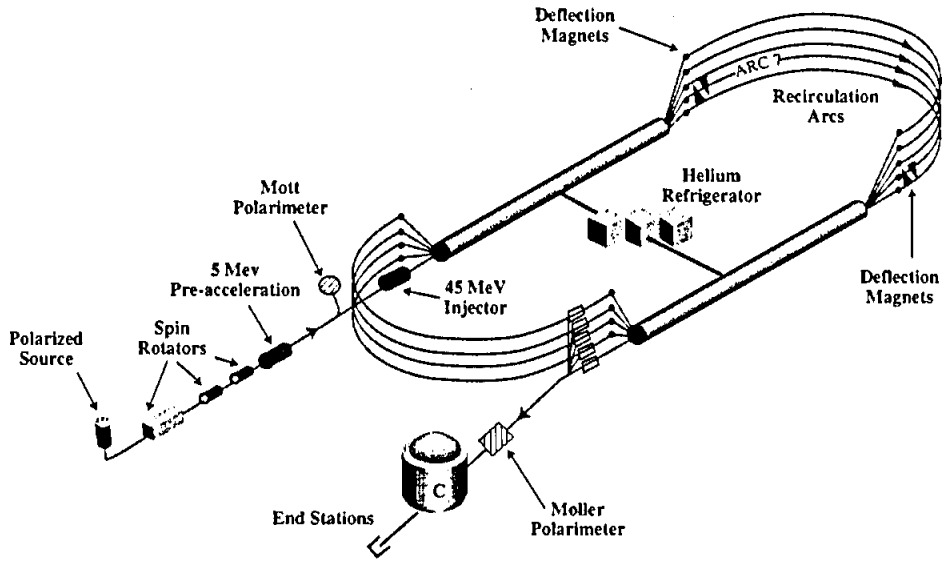

Figure 3.1: Layout of the accelerator systems used for this experiment. The triangles in the recirculation arc represent vertical deflection magnets. Figure courtesy of M. Stewart.

to an energy of 2.989 GeV. In arc 7 a pair vertical deflecting magnets perturb the nominal beam orbit. The resulting large amplitude ($\approx$ 15 mm peak-to-peak) vertical betatron oscillation propagates through the recirculation arc. The orbit perturbation is removed by a second pair of magnets at the end of the arc. In this way, the effect of the perturbation on the beam orbit is contained within the arc. The beam orbit requirements and the design, construction, and installation of the deflection magnets used for the experiment are described in Sections 3.4 and 3.5, respectively. After arc 7 the beam is accelerated once more and extracted from the accelerator to the Hall C experimental area at 3.407 GeV. Here, a Møller polarimeter described in Section 3.6 measures the longitudinal component of the polarization of the beam. The effect of the beam orbit on the beam polarization is extracted by performing measurements of the final longitudinal beam polarization component for different orbit perturbations and polarization orientations. Finally, the beam feedback systems and accelerator controls are discussed in Section 3.7 and Section 3.8, respectively.

3.1 Polarized Electron Source

The polarized electron source [Du93] is a 100 keV electron gun. The polarized beam is produced by photoemission from a gallium arsenide (GaAs) cathode described in Section 3.1.1. The laser system and optical transport system are discussed in Section 3.1.2. The dependence of the electron and optical beam polarization on the laser system and polarizing optics are discussed in Section 3.1.3.

3.1.1 Photocathode Physics

The development of photoemission electron guns to create polarized electron beams for accelerator applications using GaAs photocathodes has been discussed extensively [Ca92, Si88]. The operation of these sources is based upon the excitation of electrons between well defined states in the valence and conduction bands of GaAs using circularly polarized photons of energy just above the minimum band gap. An examination of the band structure of GaAs (Figure 3.2) indicates how it is possible to

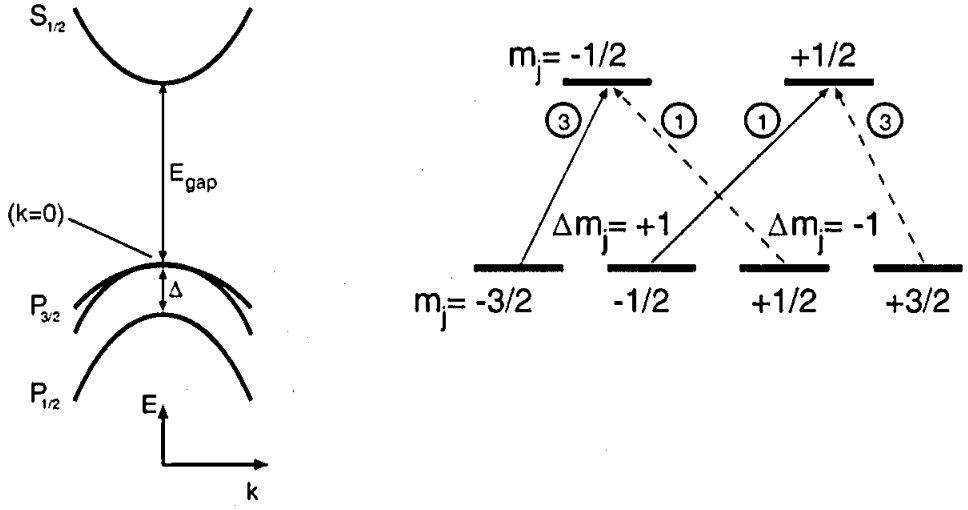

Figure 3.2: GaAs band structure (a) and energy level diagram (b).

develop electron spin polarization. GaAs is a semiconductor with a direct band gap transition energy of $E_{gap} \approx 1.4\,\text{eV}$. The wavefunction of an electron at the band gap

minimum is p–like in the valence band and s–like in the conduction band. Spin–orbit coupling splits the p–like states into $p_{1/2}$ and $p_{3/2}$ where the $p_{1/2}$ state has an energy of about $\Delta = 0.33\,\text{eV}$ below the $p_{3/2}$ state. Photoadsorbtion of light with photon energy between E_{gap} and $E_{gap} + \Delta$ excites electrons from $p_{3/2}$ to $s_{1/2}$.

The selection rules for the adsorption of *right* (σ^+) and *left* (σ^-) circularly polarized light are $\Delta m_j = +1$ and $\Delta m_j = -1$, respectively. The relative transition probabilities for σ^+ and σ^- Photoadsorbtion are given by the Clebsch-Gordon coefficients. For example, σ^+ photons of the correct energy will preferentially excite electrons ($\Delta m_j = +1$) to the conduction band in the ratio of 3 ($m_j = -\frac{1}{2}$) to 1 ($m_j = +\frac{1}{2}$). Consequently, applying Equation 2.26, the electron polarization created in the conduction band of GaAs is $P = \frac{1-3}{1+3} = -50\%$.

The conduction band is separated from the vacuum level (known as electron affinity) by about 4 eV as shown in Figure 3.3. The photons necessary to selectively

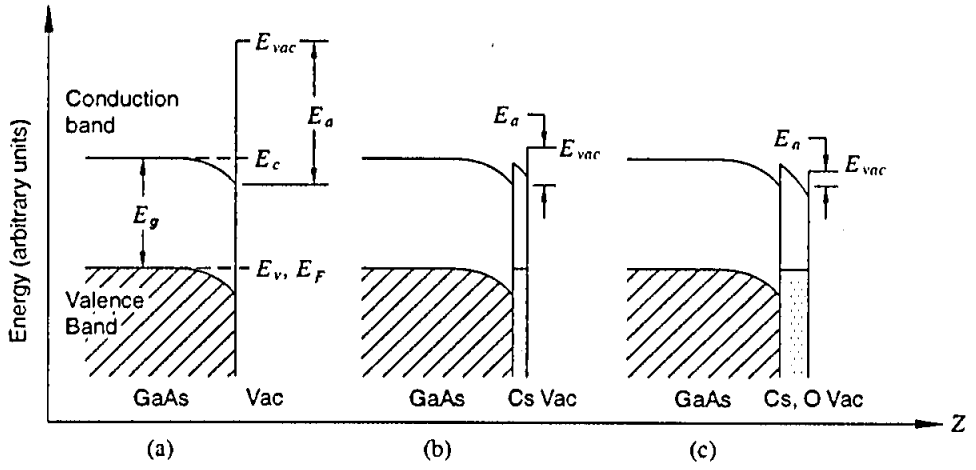

Figure 3.3: The band structure of GaAs near its surface: (a) p–type GaAs; (b) p–type GaAs with a cesiated surface; and (c) p–type GaAs with a layer of Cs and O on its surface. The energy of a free electron is shown as E_∞ (from [Pi76]).

polarize the conduction band are near the band gap energy and therefore the electrons which reach the conduction band do not have enough excess energy to overcome the potential barrier and pass to the vacuum. The standard approach to remove this barrier is to apply a monolayer of cesium to the GaAs surface. The electron affin-

ity is then reduced to almost zero. Oxidation of that layer using NF_3 or O_2 lowers the electron affinity further until the vacuum level is *below* the conduction level in the bulk semiconductor. Such a surface is said to have a negative electron affinity (NEA). Electrons at the conduction band minimum are energetically allowed to leave the crystal. They are formed into a beam by an accelerating potential applied to the cathode.

Although the theoretical polarization limit of the beam is expected to be $\pm 50\%$, the measured polarization is less because of depolarization processes, such as spin relaxation, as the electrons diffuse through the GaAs and exit the surface. Progress has been made by using thin crystals of GaAs which limit this process. Bulk GaAs photocathodes used at CEBAF provide a beam polarization of $\leq 42\%$.

Higher polarization gallium arsenide photocathodes have been developed [Ca92]. This is accomplished by first growing GaAsP atop GaAs, and then forming a final thin layer of GaAs atop the GaAsP. The mis-match of the GaAs lattice to the smaller lattice constant of GaAsP at the interface to the GaAs results in an approximate uniform compressive strain in the GaAs. This is equivalent to a uniaxial strain normal to the crystal surface. This perturbation to the crystal potential removes the degeneracy of the valence band in the GaAs. Consequently, the theoretical 50% limit for bulk GaAs is removed, and by choosing the correct photon energy to excite only one non-degenerate electron state higher polarization is produced. Strained GaAs photocathodes used at CEBAF provide a beam polarization of $\leq 80\%$.

The yield of electrons from a photocathode is specified by its quantum efficiency. This is the number of photoelectrons generated per incident photon. The photocurrent therefore depends upon the incident optical power (number of photons) and the energy of the photons (wavelength) which can excite electrons to the conduction band. In general, as the quantum efficiency of a prepared photocathode increases, the polarization of the extracted electrons decreases. An increase in quantum efficiency means a larger fraction of final state electronic transitions are able to populate the conduction band, and consequently the resulting conduction band polarization is re-

duced. Separately, contamination of the photocathode can degrade the NEA surface and reduce the quantum efficiency.

The lifetime of a photocathode is defined as the time required for the quantum efficiency to fall by $1/e$. The lifetime is therefore related to the extent the photocathode has become contaminated or damaged during operation. Studies reveal that ion back–bombardment of the cathode is the major process in determining the photocathode lifetime in the CEBAF gun. Ion back-bombardment results from ionization of the residual gas atoms in the ultra–high vacuum (UHV) environment by beam electrons. Ions generated in the cathode–anode gap are accelerated back toward the photocathode by the accelerating potential. The ions strike and damage the photocathode surface and bulk. Consequently, the lifetime of photocathodes are observed to depend upon the number of ions formed in the cathode–anode gap which is proportional to the total charge extracted from the photocathode.

This experiment measures a small effect ($\sim 10^{-2}$) on the beam polarization. To acquire the statistical precision in the scheduled run period required maximizing the figure of merit ($I \cdot P^2$) of the polarized source. The beam current for the experiment is limited to $\leq 4\,\mu$A by target heating considerations at the Møller polarimeter. Consequently, the experiment was run using a higher polarization strained GaAs photocathode to increase the figure of merit. The beam polarization during this experiment was $\approx 70\%$.

3.1.2 Laser System and Optical Transport

The laser system [Po95] creates a train of circularly polarized optical pulses to extract polarized electrons from the photoemission gun. The system is comprised of three lasers, one dedicated to each experimental area. Each laser is composed of a gain switched diode seed laser and a single–pass optical amplifier. Each diode seed laser is pulsed with a repetition rate at the third subharmonic (499 MHz) of the accelerator frequency. The train of optical pulses from each laser is combined by an optical

transport system shown in Figure 3.4 to a common axis, to produce the 1497 MHz

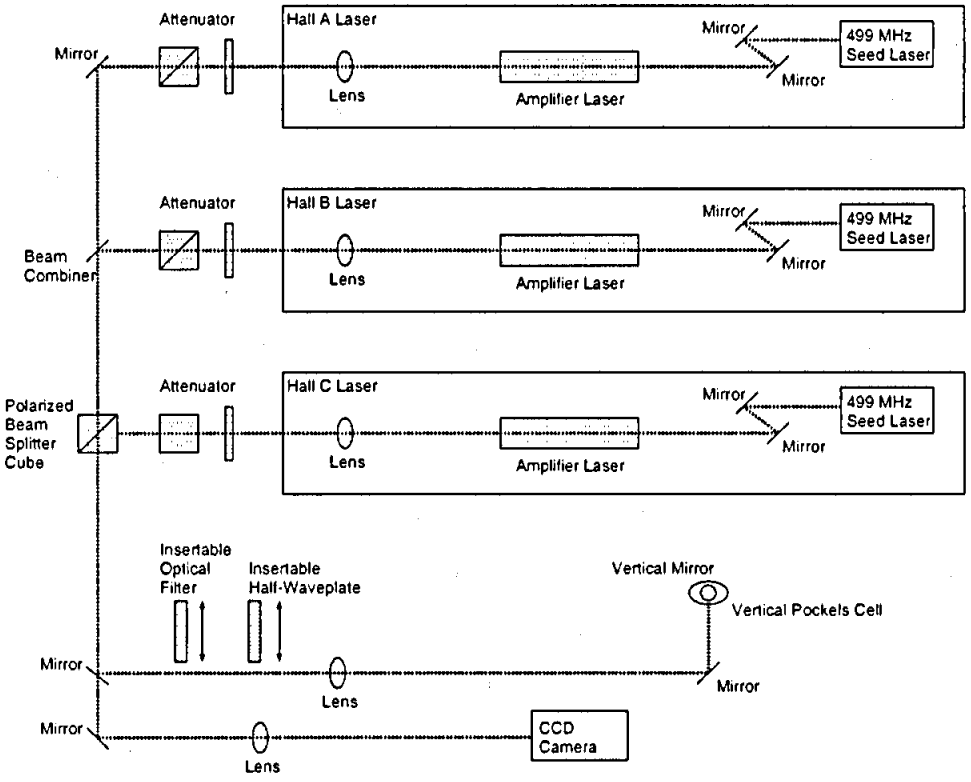

Figure 3.4: Plan view layout of the laser system and polarizing optics. The laser beams are transported in the plane of the optical table. They are reflected upward by the vertical mirror and then pass through the Pockels cell and electron gun vacuum window to the photocathode. Figure courtesy of M. Poelker.

microstructure of the accelerator. This pulse train is transported by mirrors and optical polarizers to the photocathode. The polarizers set the optical helicity (σ^+ or σ^-) of the beam.

Each laser produces optical pulses of $\approx$ 55 ps duration (30° RF). These pulses propagate through the injector and are accelerated in the linacs. Because the photocathode quantum efficiency decays at a rate proportional to the total charge extracted, this choice improves the efficiency of the electron gun by a factor of 18 for 499 MHz operation compared to that of a gun driven by a DC operated laser. No appreciable cathode decay was noticed during the 4 day run period of the experiment.

3.1.3 Polarization Stability

The electron beam polarization depends upon the optical beam polarization in two ways. First, the degree of electron beam polarization depends upon the degree of the optical circular polarization exciting the electronic states. For example, an electron beam resulting from a linearly polarized optical beam will have zero polarization. This is because a linearly polarized optical beam is equally composed of σ^+ and σ^- circularly polarized photons. The optical circular polarization of a laser beam can be determined by measuring the intensity of the beam as analyzed by a linear polarizer. The degree of circular polarization is given by

$$P_{circ} = \frac{2\sqrt{I_{max} I_{min}}}{I_{max} + I_{min}}, \tag{3.1}$$

where I_{min} and I_{max} are the minimum and maximum optical power passed through a linear polarizer rotated through 360°. P_{circ} was typically in excess of 99.9%. Second, the helicity of the *electron* beam polarization depends upon the sense of the *optical* beam polarization (helicity of the photons) incident on the photocathode. The measurement of the beam polarization by Møller polarimetry relies upon a comparative measurement of scattering rates between the two helicity states of the electron beam. To accomplish this, the helicity of the optical beam is reversed at 1 Hz. An important component of this experiment is to precisely and reliably reverse the optical helicity in a regular and repeatable manner. This is accomplished with a Pockels cell.

The Pockels effect [He90], after Friedrich Carl Alwin Pockels, is a linear electro-optic effect in a class of crystals exhibiting an induced birefringence with applied electric field. The unique characteristic of these crystals is that they lack a center of symmetry. There is no central point in the crystal through which every atom can be reflected into an identical atom. The property of birefringence is characterized by a difference in the index of refraction, and therefore the propagation velocity of light, along two axes orthogonal to one another and an optical axis. The two axes are commonly referred to as *fast* and *slow* to distinguish the relative propagation velocities. Consider the example shown in Figure 3.5 of a linearly polarized optical

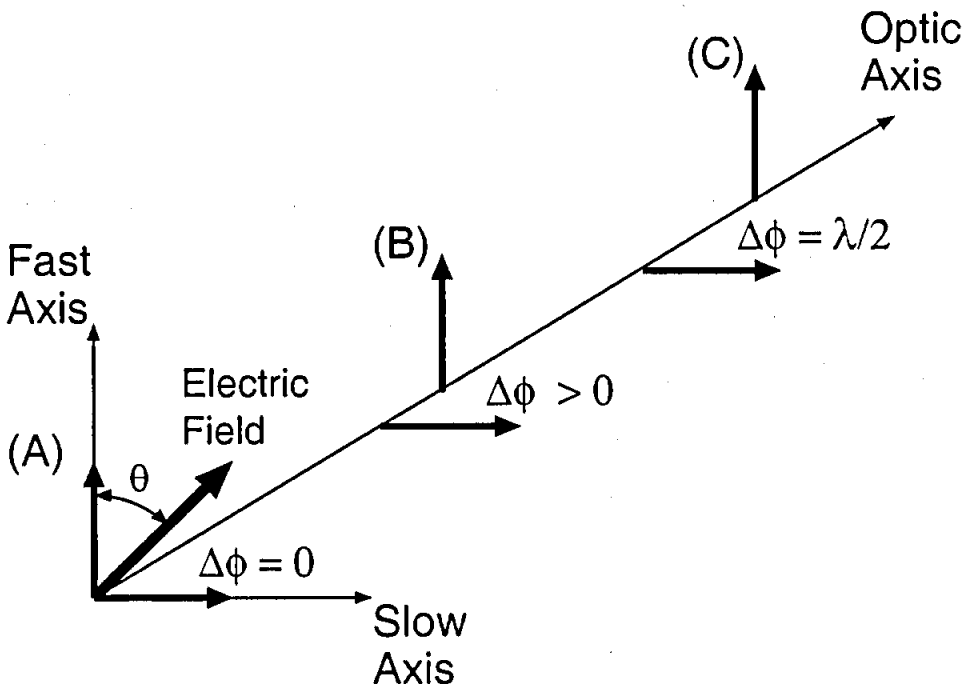

Figure 3.5: The two components of the incident electric field propagate at different velocities along the *fast* and *slow* axes. A net distance, or phase $\Delta\phi$, between originally equal wave-fronts occur.

beam incident along the optic axis of a birefringent crystal at position A, at some angle θ to the fast axis. The angle θ determines the amplitude of the electric field along the fast and slow axes. The component of the incident electric field along the fast axis propagates more quickly than along the slow axis, generating a net phase difference between the two components at point B. If the amplitudes of the electric field along the two axes are set equal ($\theta = 45°$) and the phase difference is adjusted to be 90° (corresponding to a quarter of a wavelength) then by the exit of the crystal at point C the resulting optical polarization will be circularly polarized.

Pockels cells are devices which house such a birefringent crystal and an electrode structure to apply the electric field. The crystals are typically uniaxial, or show little birefringence, $\Delta\phi_0$, with no applied field. Such crystals are mounted in situ with their optic axis closely parallel to the applied electric field. In this case the resulting

birefringent phase is

$$\Delta\phi = \frac{2\pi {n_0}^3 r_{63} V_c}{\lambda_0} + \Delta\phi_0, \tag{3.2}$$

where n_0 is the ordinary index of refraction, r_{63} is the electro-optic tensor coupling constant characteristic of this class of crystal structure [He90], V_c is the voltage applied across the crystal to produce the electric field, λ_0 is the laser wavelength, and $\Delta\phi_0$ is the residual birefringence of the crystal.

The Pockels cell used [LM] is a single crystal of potassium dideuterium phosphate (KD_2PO_4), or KD^*P. The crystal is housed in a cell with a 10 mm aperture immersed in an index matching fluid (FC-43) between the crystal and window surface. The windows are anti-reflection coated to avoid resultant beam satellites from the photocathode due to multiple optical reflections. The crystal is wedged at 30′ to avoid etalon effects. For this crystal, $n_0 \approx 1.52$ and $r_{63} \approx 23.310^{-12}$ m/V.

The laser used for this experiment was operating at a wavelength $\lambda_0 \approx 855$ nm. The quarter-wave retardation voltages are given by

$$V_{\pm\frac{\lambda}{4}} = \pm 2610\,\mathrm{V} - 29\,\tfrac{\mathrm{V}}{\mathrm{deg}} \cdot \Delta\phi_0. \tag{3.3}$$

By alternately applying these voltages across the Pockels cell the optical polarization and electron beam helicity are reversed. Optical polarization reversal by Pockels cells can be done rapidly ($\sim$ nanoseconds). Stability of the applied high voltage signal and decaying resonant modes of the optical polarization due to the electro-mechanical stresses on the crystal during the high voltage transition typically result in polarization instability lasting $\sim 100\,\mu$sec following a transition. Data are not taken during this period of instability. Typically $\approx 250\,\mu$s is allowed for the retardation of the Pockels cell to fully stabilize following a voltage reversal.

The planned helicity reversal frequency for this experiment was 30 Hz, to average line frequency related noise to zero. However, due to a component failure the Pockels cell high voltage switching electronics would not stabilize the applied cell voltage to better than 180 V for $\approx$ 25 ms following each transition making a 30 Hz reversal rate

impractical. A decision was made to reduce the reversal rate to 1 Hz and adjust the veto period following helicity reversal to 30 ms.

A characteristic of the laser system is that the laser wavelength may be tuned over a narrow range of wavelengths by adjusting the temperature of the laser. A change in laser wavelength can have two effects on the electron beam polarization. First, the degree of circular polarization relies on tuning the Pockels cell for a given wavelength. Second, the beam polarization depends upon the photon energy, $E_\lambda = \frac{hc}{\lambda}$, where h is Planck's constant, c is the speed of light, and λ is the laser wavelength. This temperature dependence, however, is adiabatic compared with the 1 Hz helicity reversal. In a test to determine the effect of varying the laser wavelength, the seed laser temperature was varied over a range ΔT =15 °C or, equivalently, a wavelength of $\Delta\lambda$ =4.5 nm. At a few seed laser temperatures the beam polarization, photocathode temperature, and beam current were measured. The results are shown in Figure 3.6. No significant dependence of the beam polarization over this temperature range was observed. Further, the seed laser temperature is stabilized to better than 0.5 °.

3.2 Injector Spin Manipulators

This section describes the spin manipulation system used in the injector, and modification to it made for this experiment. The requirements of the spin manipulation system for the accelerator are described in Chapter 2. The specific requirement for this experiment is that the beam polarization be oriented following the electron gun over a solid angle $\geq 2\pi$ of the unit sphere. This condition assures that a broad range of polarization orientations (or their reverse) can be reached at recirculation arc 7. In this way, the nominal polarization precession offset between the injector and arc 7 can be corrected. Two simple rotations accomplish this. The first rotation θ_{Wien} is determined by a spin rotator, named a Wien filter, described in Section 3.2.1. The second rotation $\phi_{S_{12}}$ is determined by a combination of two solenoid magnet spin rotators described in Section 3.2.2. Spin rotator calibration data for the devices is

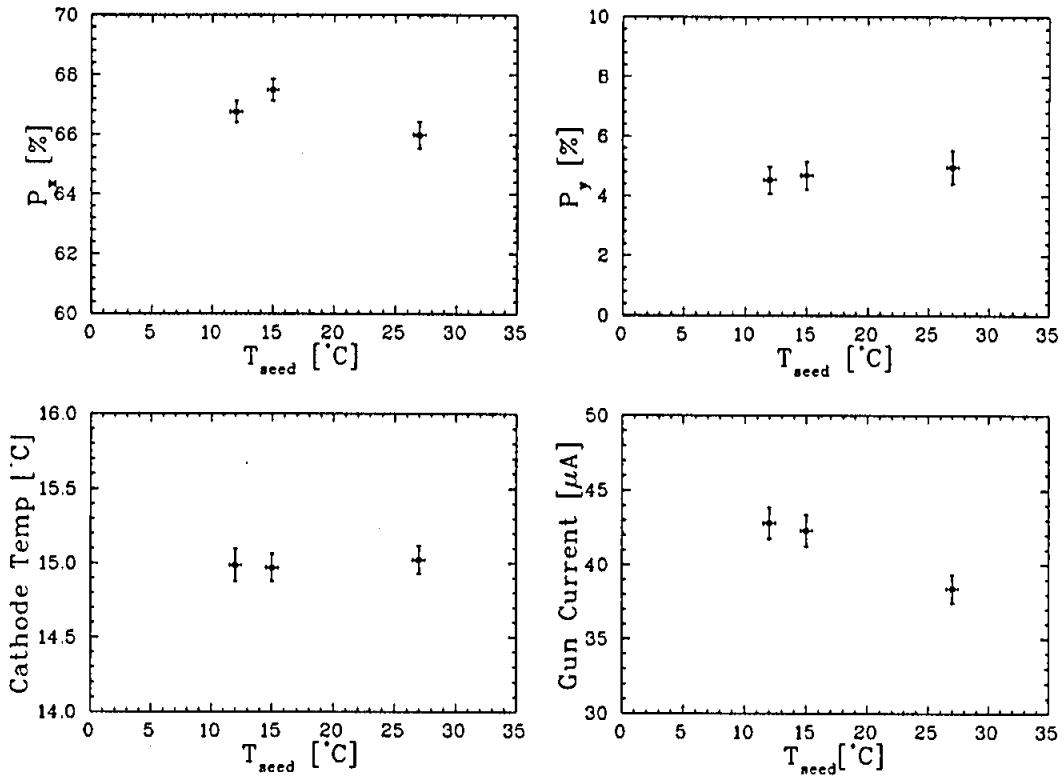

Figure 3.6: Varying the seed laser temperature shows no discernible effect on the beam polarization. Statistical error bars only shown. Systematic uncertainty in absolute polarization is approximately 5%.

given in Sections 3.3.7 and 3.3.8, respectively.

3.2.1 Wien Filter Spin Rotator

A Wien filter [Sa77] is a static electromagnetic device. It consists of crossed electric ($\vec{E}$) and magnetic ($\vec{B}$) fields transverse to the particle motion ($\vec{\beta}$) and each other as shown in Figure 3.7. The usefulness of a Wien filter is that the polarization of a beam passing through the device can be rotated without deflecting the outgoing central orbit. However, the device focuses in one plane, and is thus astigmatic. This is accomplished by two conditions. First, recall that the precession of an electron spin in the plane normal to a dipole field is given by $\eta_y = a\gamma\theta_b$ where $\theta_b = \frac{e}{p}\int B_y dl$. By adjusting $\int B_y dl$ the precession angle, η_y, can be controlled. However, the electrons

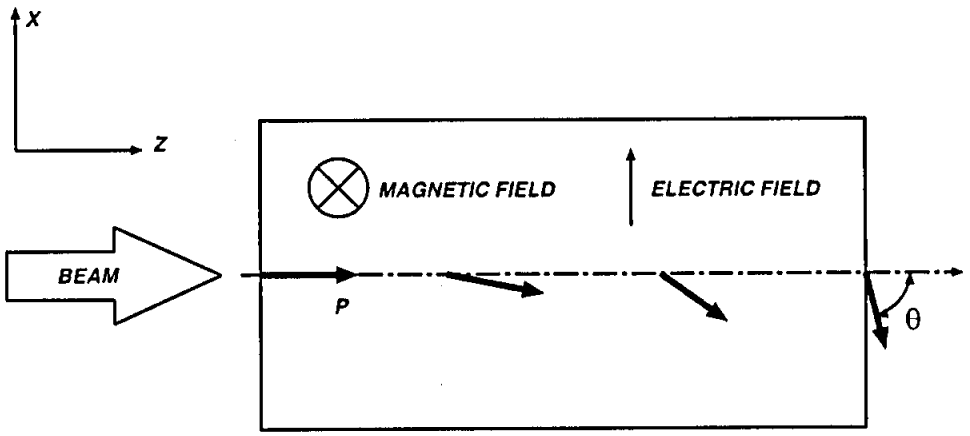

Figure 3.7: Diagram of Wien filter indicating the rotation of the beam polarization relative to the beam direction in crossed magnetic and electric fields ($\beta = \frac{E}{B}$).

also experience a deflecting force from the magnetic field. The second condition requires that an electric field be applied to just balance this deflecting force. The strength of the electric field is determined by considering that the net Lorentz force on the electron must be zero,

$$\vec{F} = q\left(\vec{E} + \frac{\vec{\beta}}{c} \times \vec{B}\right) = 0. \tag{3.4}$$

The second condition then requires that $\beta = \frac{E}{B}$.

3.2.2 Solenoid Spin Rotators

Solenoids are used in the low energy beamline to focus the beam. The inverse focal length of a solenoid lens in the paraxial approximation is given by [La77]

$$\frac{1}{f} = \left(\frac{q}{2p}\right)^2 \int B_z^2 dl, \tag{3.5}$$

where q and p are the particle charge and momentum, respectively, and $\int B_z^2 dl$ is the integral of the square of the axial component of the solenoid field taken along the central axis of the magnet. Recall from Equation 2.8 that the electron spin will precess about the axial solenoid field by an amount

$$\eta_z = \frac{ge \int B_z dl}{2p}, \tag{3.6}$$

where g is the electron gyromagnetic factor, $\int B_z dl$ is the integral of the axial component of the solenoid field taken along the central axis of the magnet, and the other quantities are already defined.

The solenoid magnets used for spin manipulation are constructed using two separate coils in one magnetic casing. If the number of turns in each coil is identical they can be connected in series to produce opposing fields and driven by a single power supply to provide focusing without a net polarization rotation ($(\eta_z)_{Coil_1} + (-\eta_z)_{Coil_2} = 0$). Alternatively, each coil in the magnet can be powered by a separate power supply to produce both the desired beam focusing and spin rotation conditions simultaneously. The details of the calculation for this configuration are given in Appendix B.

The injector beamline originally employed a single solenoid spin rotator capable of rotations of $\eta_z \approx \pm 47°$. However, this was insufficient for studying the desired angular dependence of the beam orbit on the beam polarization. Specifically, the beam polarization could not be oriented transverse to the beam momentum along the $\hat{y}$ direction. Another solenoid magnet located in the injector beamline was modified for this experiment to provide an additional rotation of $\eta_z \approx \pm 45°$. The focusing for each solenoid magnet, however, was kept constant for all spin rotation setpoints by adhering to the constraint that $\int B^2 dl$ remain constant.

3.3 Injector Mott Polarimeter

It is important to measure the electron beam polarization and orientation prior to injection into the main accelerator. This localizes the polarimetry near the electron source and eliminates the requirement for using the entire accelerator to measure the beam polarization. In this way photocathodes can be studied and the spin rotators calibrated, and the polarization of the beam for the nuclear physics experiments measured. An injector polarimeter based on Mott scattering was designed, constructed, and commissioned in parallel with this experiment.

The physics of Mott scattering is described in Section 3.3.1. The advantages of

conducting Mott polarimetry at higher energies are discussed in Section 3.3.2 and the design of a 5 MeV Mott polarimeter in Section 3.3.3. Discussion of the polarimeter and the analysis approach to extract the beam polarization from a measurement is presented in Section 3.3.4. Section 3.3.5 shows the calculation of the experimental asymmetry from the detected Mott scattering. Finally, results are presented in Section 3.3.6 for measuring the effective Sherman function for gold target foils of varying thickness (0.01 μm to 5 μm). A 1 μm target is used for this experiment.

3.3.1 The Physics of Mott Scattering

In the late 1920's N.F. Mott calculated the scattering of high energy electrons from the bare nucleus of atoms with a large nuclear charge [Mo29]. Classically, the large angle scattering in this case corresponds to a small impact parameter; the scattered electron experiences a magnetic field in its rest frame resulting from the motion of the electric field of the nucleus. The interaction of the orbital angular momentum (magnetic field) with the magnetic moment of the scattered electron (spin) leads to a spin–orbit coupling term in the scattering potential. The results in a term in the Mott cross-section which depends on the incident electron spin orientation. Referring to Figure 3.8 the cross section for the scattering angle θ is written as

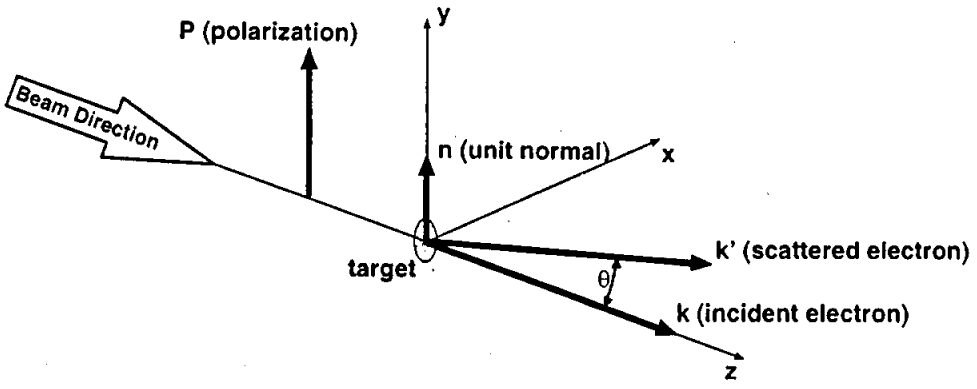

Figure 3.8: Diagram of Mott scattering from a target. In this diagram, the scattering angle θ is in the plane formed by $\hat{x}$–$\hat{z}$.

$$\sigma(\theta,\phi) = I(\theta)[1 + S(\theta)\vec{P}\cdot\hat{n}], \tag{3.7}$$

where $I(\theta)$ is the unpolarized cross section

$$I(\theta) = \left(\frac{Ze^2}{2mc^2}\right)^2 \cdot \frac{(1-\beta^2)(1-\beta^2\sin^2(\frac{\theta}{2}))}{\beta^4\sin^4(\frac{\theta}{2})}. \tag{3.8}$$

$S(\theta)$ is known as the Sherman function and $\vec{P}$ is the incident electron polarization. The unit vector $\hat{n}$ normal to the scattering plane is defined by

$$\hat{n} = \frac{\vec{k}\times\vec{k'}}{|\vec{k}\times\vec{k'}|}, \tag{3.9}$$

where $\hbar\vec{k}$ ($\hbar\vec{k'}$) is the incoming (outgoing) electron momentum.

The importance of the value of the Sherman function is that it determines the size of the scattering asymmetry, or how well the interaction distinguishes between the two spin states. The unpolarized part of the cross-section effectively averages over the initial spin state, whereas, the Sherman function contains the angular scattering amplitude which includes the initial spin state. Consider an electron beam with polarization $\vec{P}$ transverse to the scattering plane of a target, i.e., parallel or anti-parallel to $\hat{n}$. The target is typically a high atomic number material. This is done because the spin–orbit coupling increases with the nuclear charge. The number of electrons scattered through an angle θ to the right and detected, N_r, is proportional to $1 + PS(\theta)$ and the number scattered to left and detected, N_l, is proportional to $1 - PS(\theta)$. The scattering asymmetry is defined as the difference in the number of electrons scattered right versus left divided by their sum,

$$\epsilon = \frac{N_r - N_l}{N_r + N_l} = PS(\theta). \tag{3.10}$$

This formalism describes the scattering from a single atom where the Sherman function is calculated from the basic electron–nucleus cross section. It has been calculated with corrections for the effects of screening by the atomic electrons [Li63], and the finite distribution of nuclear charge [Ug70]. In reality, a target foil contains so many atoms that multiple and plural scattering also occurs, which tend to reduce

the intensity asymmetry between the left and right detectors. The measured asymmetry is then smaller than what would be expected from using the calculated single atom Sherman function. Consequently, it is the effective Sherman function which is measured,

$$\epsilon = \frac{N_r - N_l}{N_r + N_l} = PS_{eff}(\theta). \tag{3.11}$$

This depends upon the foil material (Z) and target thickness (density). The dilution of the Sherman function due to plural and multiple scattering can be as much as 44% [Du93] for a 100 keV beam striking a 0.1 μm gold foil. There are two distinct advantages of Mott polarimetry, however, at an energy of 5 MeV; the dilution by multiple scattering is smaller (a big effect due to the much lower cross section), and the value of the single atom Sherman function is larger ($\approx$ 20% effect).

The effective Sherman function can be determined. This is done by measuring the experimental asymmetries for a fixed polarization (known or unknown) for a variety of target thicknesses. The measured asymmetries are plotted versus target thickness and extrapolated to the zero target thickness to give A_0, the asymmetry expected for scattering from a single atom. The functional form of the fit is made assuming that the scattering rate depends to first and second order on the target thickness. The linear dependence carries the single elastic scattering dependence. The quadratic term carries no analyzing strength and corresponds to multiple scattering in the target.

$$N_{r,l} = (1 \pm PA_0) \cdot t + \alpha \cdot t^2. \tag{3.12}$$

By applying Equation 3.11 the resulting scattering asymmetry is determined

$$\epsilon \sim \frac{PA_0}{1 + \alpha t}. \tag{3.13}$$

In this way A_0 and α are determined. Using the single atom Sherman function $S(\theta)_{thy}$ the polarization of the beam is finally calculated

$$P = \frac{A_0}{S(\theta)_{thy}}. \tag{3.14}$$

Once the polarization is measured the effective Sherman function can be determined at different foil thicknesses by $S_{eff} = \epsilon_t / P$. An example is given for the Mott gold targets in Section 3.3.6.

3.3.2 5 MeV Mott Polarimeter

Low-energy Mott polarimeters ($E_k \leq 100\,\text{keV}$) based on elastic scattering from high-Z targets have been used in a variety of applications. However, multiple and plural scattering at low energies reduce the effective analyzing power even in very thin targets ($t \approx 100\,\text{nm}$). The large cross section at the maximum analyzing power scattering angle ($\theta = 120\,°$) limits the usable current to nanoamperes and requires thin targets. These targets are difficult to manage and their thickness difficult to measure. A variation of the low-energy Mott polarimeter has been developed and is installed at Jefferson Laboratory [Pr97]. It is located at the 5 MeV region of the injector, as shown in Figure 3.9. Mott scattering at this energy does not suffer the same dilution

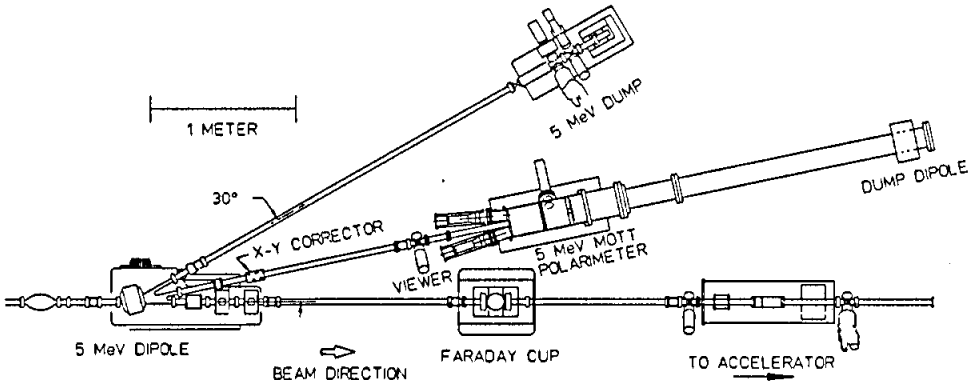

Figure 3.9: Drawing showing the location of the Mott polarimeter on a short beamline segment in the injector region. The 5 MeV dipole magnet field strength is adjusted to deliver the beam to the polarimeter. Figure courtesy of D. Machie.

of the analyzing power by plural and multiple scattering. The absolute analyzing power is larger and the cross section smaller than at $E_k = 100\,\text{keV}$, allowing for polarization measurements at microampere average beam currents. The RF structure of the beam makes monitoring the beam current (resonant cavity) and beam position

(tuned antenna) simpler along the beamline. The beam profile can be monitored at this energy and beam current through the use of transition radiation.

3.3.3 Design

The polarimeter design shown in Figure 3.10 is straight forward. A linear actuator is

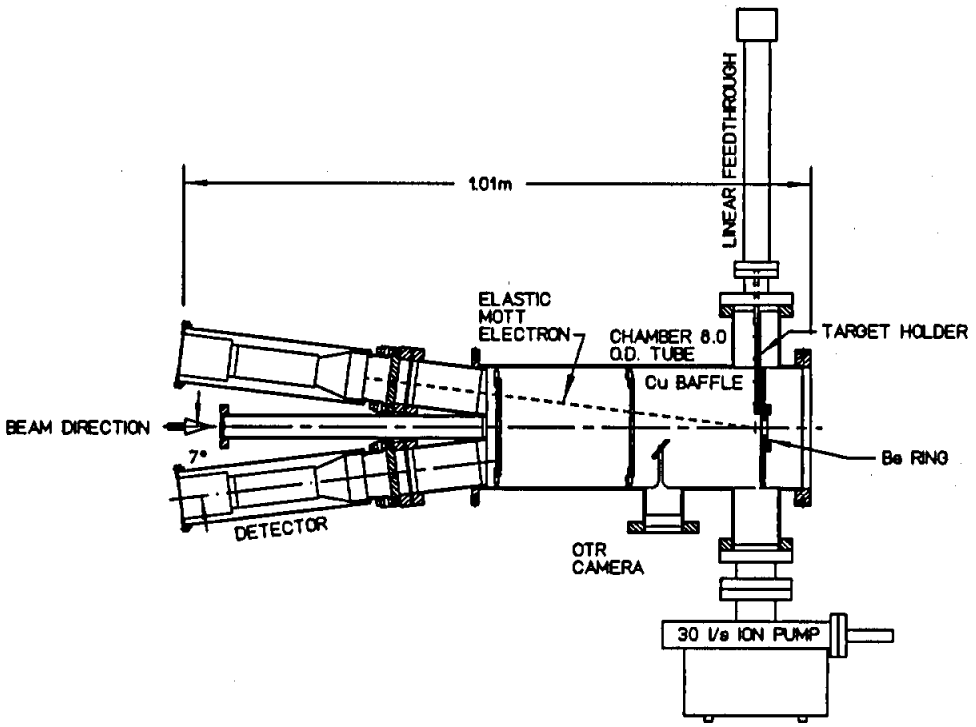

Figure 3.10: Schematic of the Mott scattering chamber with detectors. Figure courtesy of D. Machie.

mounted vertically on the scattering chamber, supporting an aluminum target ladder. The target ladder contains five targets in calibrated locations. Four locations are used for target foils, the fifth remains empty to measure the target ladder background. A 0.1 μm thick gold foil always remains as a standard target. The remaining target locations contain gold foils of different thickness (0.01 μm to 5 μm) for performing a target thickness extrapolation. A vacuum compatible stainless steel disk (1″ diameter) polished to a mirror surface is located inside the scattering chamber. This allows the target foil to be viewed by a CCD camera through a vacuum port. When the

electron beam impinges the target foil at 5 MeV, optical transition radiation (OTR) is produced [Pi96]. The OTR from the foil is imaged by the camera providing real-time monitoring of the beam intensity, profile and position at the target. This monitor, in principle, provides a diagnostic for helicity correlated beam motion. The intensity of the OTR is recorded using the CCD camera. Intensity profiles of the OTR in two transverse directions are shown in Figure 3.11. The spatial resolution, limited

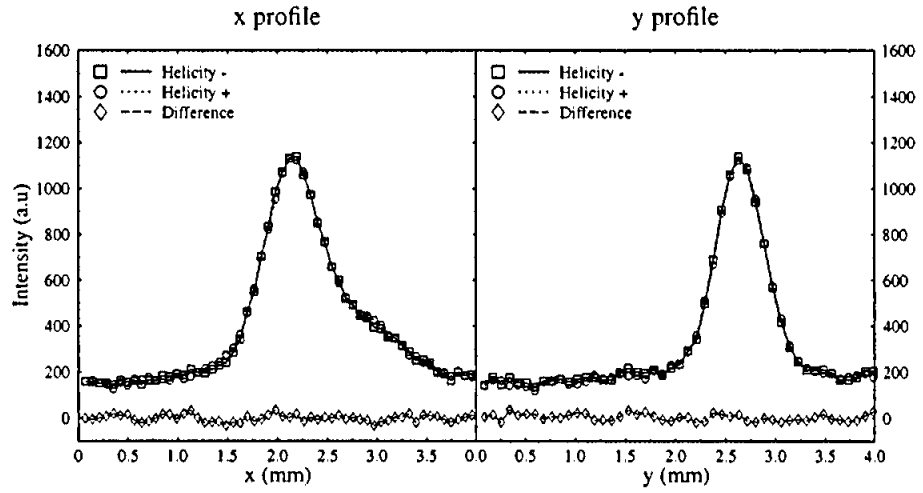

Figure 3.11: Horizontal (x) and vertical (y) beam profile using the Optical Transition Radiation (OTR) diagnostic at the Mott polarimeter. Figure courtesy of P. Piot.

by the camera, is 100 μm. From the profile it is clear that helicity correlations in the beam centroid or profile do not appear at a level approaching 10^{-3}. The OTR also provides a reference for monitoring the beam quality at the polarimeter. In Figure 3.11 the horizontal profile at the polarimeter target is broader than the vertical profile. The momentum spread of the beam, $\frac{\Delta p}{p}$, as dispersed by the 5 MeV dipole magnet (horizontal bend) can be considered as the cause. The energy spread and total beam energy at this dipole is $\Delta E \approx 9$ keV and $E \approx 5.52$ MeV, respectively. The corresponding spread in the beam momentum is $\frac{\Delta p}{p} = 0.165\%$. The spreading of the horizontal beam profile is calculated using the dipole bend angle $\theta = 12.5°$ and the

distance between the dipole and target foil $l = 170\,\mathrm{cm}$. The result is

$$\Delta x = \frac{\Delta p}{p} \cdot \theta \cdot l = 0.61\,\mathrm{mm}, \tag{3.15}$$

apparently consistent with the larger beam width in the horizontal beam profile.

Four electron detectors measure the backscattered electrons from the target foil. Two are in the horizontal (vertical) plane of the polarimeter to measure the left–right (up–down) asymmetry to determine P_y (P_x). The Sherman function for a range of kinetic energies is shown in Figure 3.12. The detectors are located at a mean

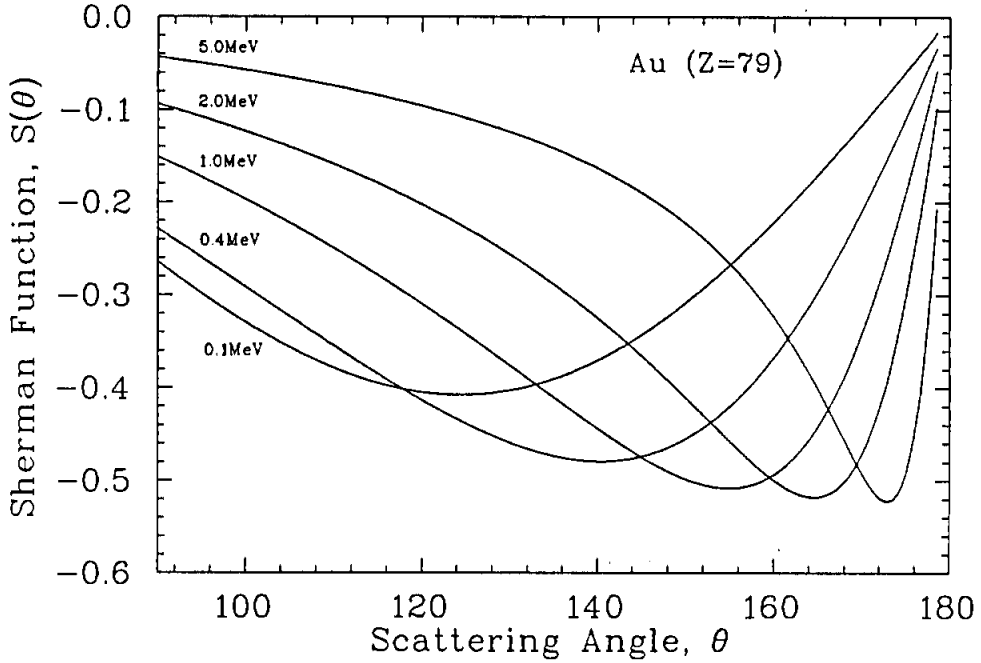

Figure 3.12: Sherman function $S(\theta)$ for scattering by gold at various kinetic energies.

backscattering angle $\overline{\theta} = 172.7°$, the calculated maximum of the Sherman function at 5 MeV.

The backscattered electrons pass through two baffles within the scattering chamber, to limit the inelastic background as seen by the detectors, and exit through a 0.20 mm thick aluminum vacuum window. In air, a pair of aluminum ($t = 12\,\mathrm{mm}$) and copper ($t = 6.4\,\mathrm{mm}$) apertures define the solid angle acceptance of the detector. Each detector is constructed from a 3″ diameter by 1.25″ thick disk of NE102a

plastic scintillator ($CH_{1.1}$). The scintillator is optically glued to a short conic light guide that mates to the face of a Thorn EMI 9807B phototube and divider base. The entire detector sits in a housing that is mounted behind the vacuum window. The defining acceptance, determined by the final copper aperture, is located $\approx 70\,\mathrm{cm}$ from the polarimeter target. The aperture is a hole 1 cm in diameter that subtends a solid angle $\Delta\theta = 0.819°$ and $\Delta\phi = 4.72°$. The acceptance of each detector is then $\Delta\Omega = 0.16\,\mathrm{msr}$. The energy loss of the detected electron in the plastic scintillator is determined by collisional (dominant at this energy) and radiative losses,

$$\left(\frac{dE}{dx}\right)_{tot} = \left(\frac{dE}{dx}\right)_{col} + \left(\frac{dE}{dx}\right)_{rad}$$

$$= (1.861\,\mathrm{g/cm^2})_{col} + (0.0665\,\mathrm{g/cm^2})_{rad} \tag{3.16}$$

The minimum energy loss (straight line path) in this thickness ($t = 3.175\,\mathrm{cm}$) of scintillator ($\rho = 1.032\,\mathrm{g/cm^3}$) is

$$\Delta E = \left(\frac{dE}{dx}\right)_{tot} \rho t \approx 6.3\,\mathrm{MeV}. \tag{3.17}$$

Therefore, the scintillator thickness is capable of fully stopping the most energetic electrons and the signal pulses for the elastic Mott electrons are proportional to the beam energy.

3.3.4 Pulse Height Spectra

The signals from the four detectors are processed by the chain of electronics shown in Figure 3.13. Event signals originate at the Mott detector. Events below $\approx 3\,\mathrm{MeV}$ are electronically discriminated against at the start of the chain. Below this energy the spectra have been shown to be mainly a photon background [St99] that carries no asymmetry due to the polarization of the beam. The integrated background rate (normalized to beam current and target thickness) below the electronic threshold is $\approx 1\,\mathrm{MHz}/(\mu\mathrm{A} - \mu\mathrm{m})$. Events above the threshold are counted in a scaler array and

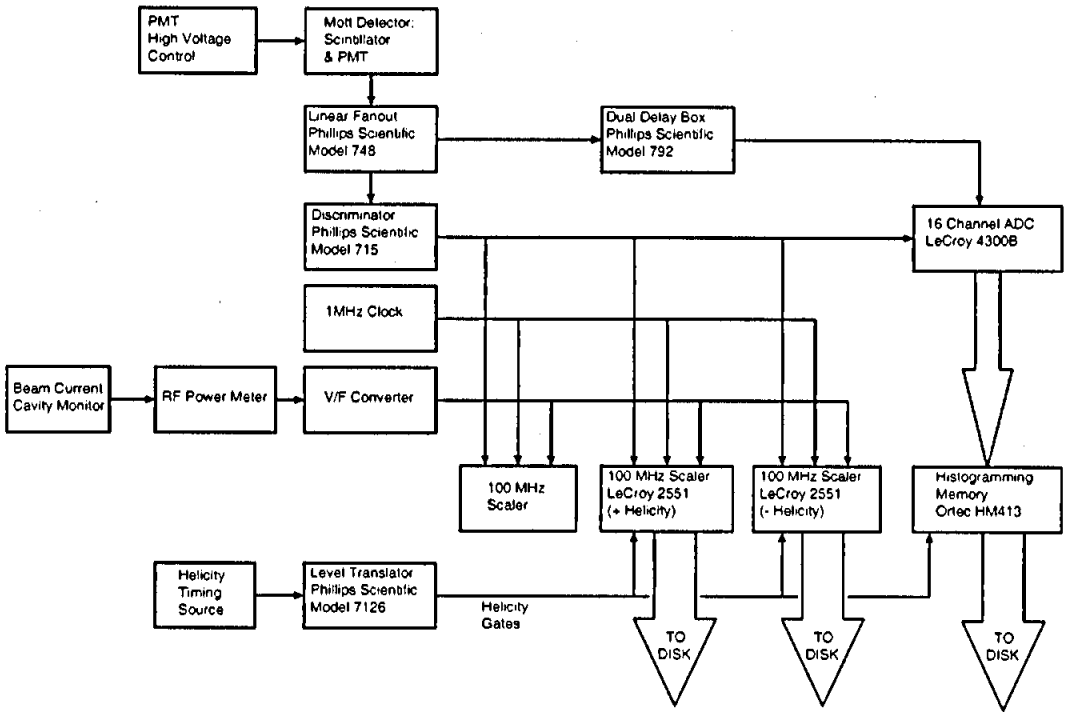

Figure 3.13: The electronics chain for the 5 MeV Mott polarimeter is shown. Signals originating at the Mott detector are discriminated against in energy. Valid events are charge–digitized in an ADC and stored in a histogramming memory. In parallel, valid events are counted by scalers. A time reference and proportional beam current signal are counted by scalers for normalizing the measured experimental asymmetry to the total charge delivered per helicity state. All events are separated according to detector and helicity.

integrated in a charge sensitive analog to digital converter (ADC). The ADC signal is directly binned to a histogramming memory component for each detector. The beam current is measured using a resonant cavity monitor and associated electronics to produce a frequency signal which is proportional to the beam current. This signal and a 1 MHz clock signal for time normalization purposes are sent to scalers as well. All of the recorded signals are separated according to the electron helicity state during which they were measured. A typical set of pulse height spectra for the four detectors (separated by helicity) is shown in Figure 3.14. The discrimination against signals $\leq$ 3 MeV is apparent near channel 440. The elastic peak (5 MeV) occurs at about channel 785. Recall that the scattering asymmetry occurs for the component of the

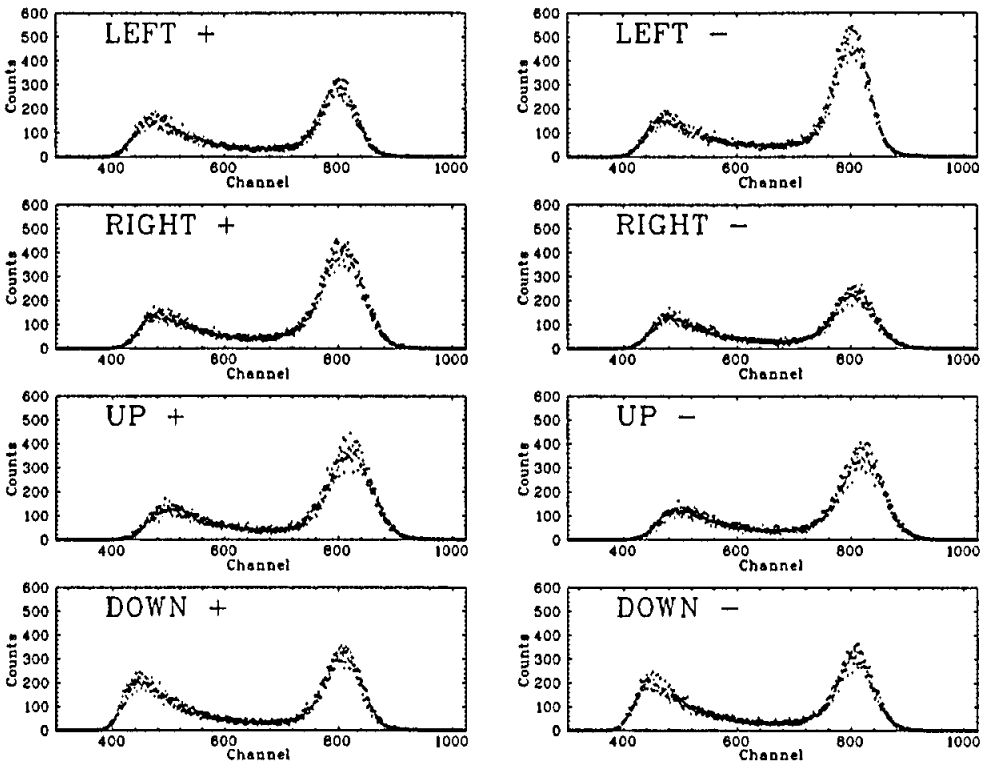

Figure 3.14: Pulse height spectra for the four Mott detectors is shown. The difference of the *left* and *right* spectra for the two helicity states indicate a large vertical polarization. The similarity of the *up* and *down* spectra for the two helicity states indicate no horizontal polarization.

polarization normal to the scattering plane. Comparison of the spectra for each detector reveals the scattering asymmetry and polarization. The difference in the *left* and *right* profiles indicate a vertical beam polarization. However, the similarity of the *up* and *down* detector spectra indicate no horizontal polarization. A characteristic of the background is that it lacks an asymmetry. The lowest energy channels (photon) carry no information of the beam polarization, while singly scattered elastic electrons carry the full information. The extent to which these overlap between channels 500 and 700 is seen by computing the asymmetry for a single detector between helicity states. A plot of the asymmetry of the *left* detector as a function of the channel number is shown in Figure 3.15. The asymmetry is computed as

$$\epsilon = \frac{L^+ - L^-}{L^+ + L^-}, \tag{3.18}$$

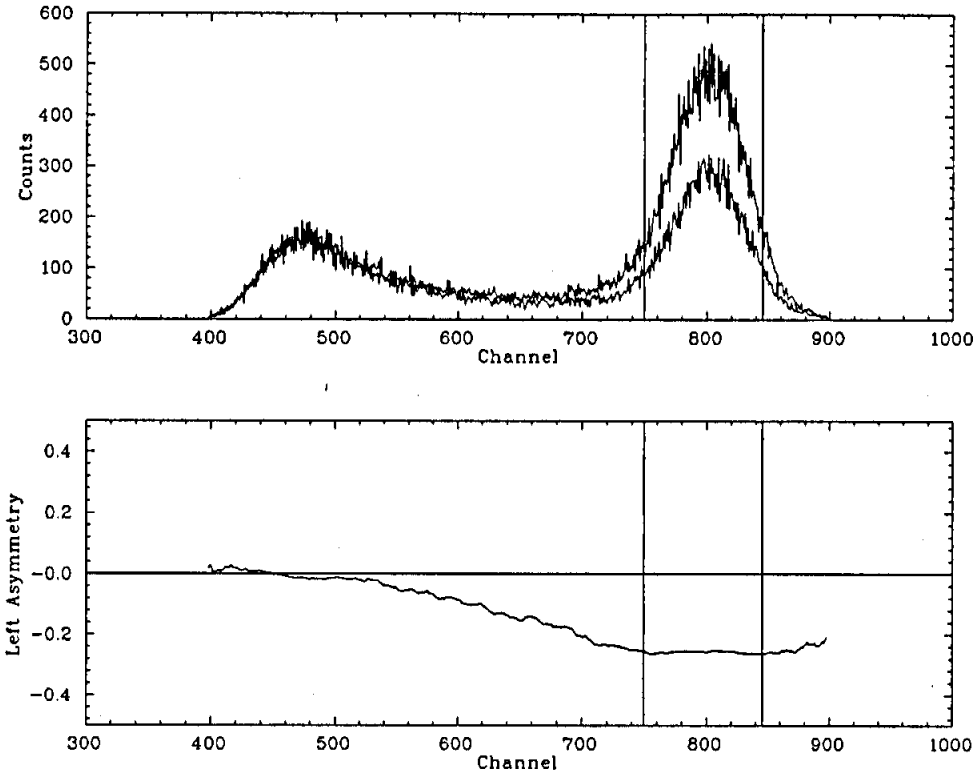

Figure 3.15: The *left* detector spectra for both helicities are shown in the upper plot. The asymmetry as calculated by Equation 3.18 is shown in the lower plot. A running average over 50 channels is used. Vertical bars delineate $\pm 1.5\sigma$

using a running average 50 channels wide. The lowest energy channels show no asymmetry. Lower threshold spectra show this zero asymmetry continues. The overlap region results from a combination of higher energy bremsstrahlung photons, medium energy inelastic scattering from the target chamber, and the radiative low-energy tail of the elastic peak. This tail is proposed to retain some asymmetry because the radiative losses are not expected to take away the asymmetry of the scattered beam. The asymmetry is clearly stable over $\approx \pm 1.5\sigma$ of the elastic peak.

The method for extracting the elastic cross section is to first perform cuts in each spectrum isolating a section of the background and elastic peak. The background and peak are then fit using a decaying exponential function and a Gaussian profile,

respectively. The form of the fit is

$$M(x) = e^{(p_1+p_2x)} + p_3 e^{-\frac{1}{2}\left(\frac{x-p_4}{p_5}\right)^2}. \tag{3.19}$$

The off-line analysis of Mott spectra is performed by a Fortran program. The algorithm for the fit uses the Levenberg-Marquardt [Pr92] method of non-linear least-squares minimization. The parameter p_1 scales the overall background rate (at threshold) and p_2 the characteristic background profile. As explained earlier p_1 and p_2 are helicity independent. The parameters p_3, p_4, and p_5 determine the amplitude, centroid, and width of the Mott signal. The amplitude p_3 varies in proportion to the beam polarization and therefore depends on the beam helicity. The centroid of the peak p_4 may shift by ≈ 1 channel due to detector pile-up effects with helicity state. This depends upon the overall rate (beam current and target thickness). The peak width, p_5, is characteristic of the detector energy resolution and therefore does not depend upon the beam helicity.

A fit of the *left* detector profile for a particular run for the negative helicity state (L^-) is shown in Figure 3.16. Preliminary cuts were made at channels 480 and 1000. The resulting fit parameters are $p_1 = 8.984$, $p_2 = -8.254 \times 10^{-3}$, $p_3 = 462.47$, $p_4 = 797.29$, and $p_5 = 31.857$. A typical χ^2 per degree of freedom (dof) of approximately 3 is obtained with this functional form. This results because of the poor representation of the fit function for the region of overlap between the inelastic background and low-energy Mott spectrum. For the example given $\chi^2/\text{dof} = 3.5$. Cuts at $\pm 1\sigma$ are used for extracting the Mott asymmetry. In this region the background ($\approx 3\%$) is subtracted before the asymmetry is computed. A statistical uncertainty of $< 0.5\%$ was obtained by performing polarimeter measurements lasting 6 minutes.

3.3.5 Determination of Mott Elastic Rate and Experimental Asymmetry

Consider as an example the *up* or *down* detector in Figure 3.14. Both represent the measurement a nominally unpolarized beam. The number of elastic events extracted

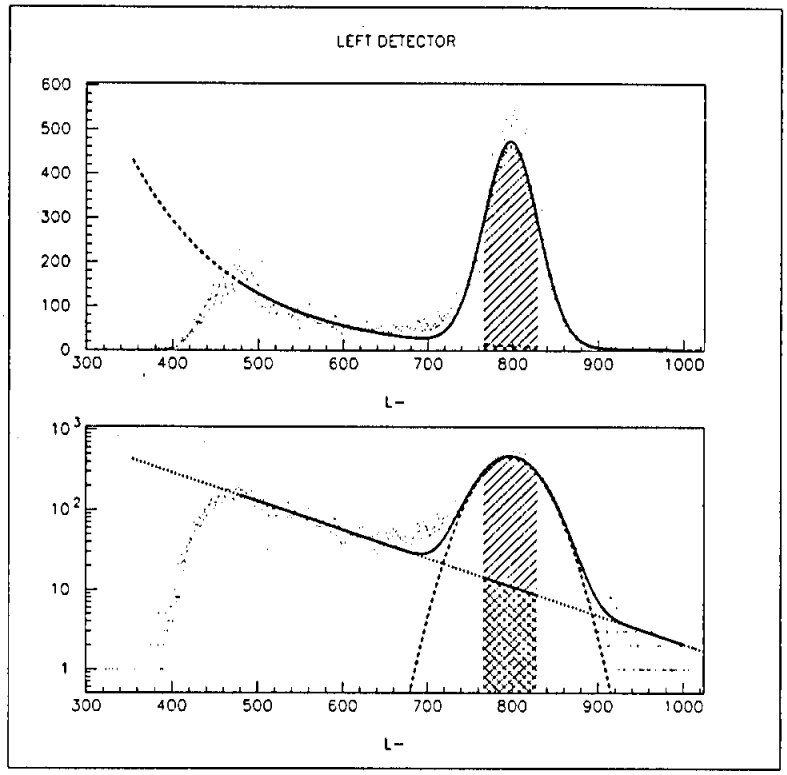

Figure 3.16: The upper plot is a pulse height spectrum with the total fit function shown in a linear scale. The lower plot is the same pulse height spectrum with the background and elastic fits shown separately in a logarithmic scale. The hatched region shows a cut at $\pm 1\sigma$ (within the $\pm 1.5\sigma$ region of asymmetry stability shown in Figure 3.15. Both cases shown are for the *left* detector.

from each spectrum is $\approx 30,000$. In this case, the target was the $1\,\mu$m gold foil, the beam current was $\approx 3.3\,\mu$A, and the measurement time was 120 seconds. Therefore, the normalized elastic rate measured is $R_{elastic} = 75\,\text{Hz}/(\mu\text{A}\cdot\mu\text{m})$. Alternatively, the normalized theoretical elastic rate for the detector is determined by calculating

$$R_{thy} = \sigma(\theta = 172.7°)\cdot\rho_{Au}\cdot t_{foil}\cdot\frac{N_A}{M_{Au}}\cdot\frac{i_{beam}}{e^-}\cdot\Delta\Omega\cdot S \approx 74.5\,\text{Hz}/(\mu\text{A}\cdot\mu\text{m}). \quad (3.20)$$

Here $\sigma(\theta = 172.7°) = 5.051\times10^{-26}$ cm^2/sr is the cross-section, $\rho_{Au} = 19.32\,$g/cm^3 is the density of gold at 20°C, $t_{foil} = 1\,\mu$m is the target thickness, $N_A = 6.022\times10^{23}\,\text{mol}^{-1}$ is Avagadro's number, $M_{Au} = 196.97\,$g/mol is the molecular mass of gold, $i_{beam} = 1\,\mu$A is the beam current, $e^- = 1.602\times10^{-19}\,$C is the electronic charge, $\Delta\Omega = 0.16\,$msr is the solid angle for a detector, and $S \approx 0.25$ is a correction factor for

multiple scattering in the aluminum vacuum window of the polarimeter. The multiple scattering results in a loss of $\approx 75\%$ of the Mott electrons at the final collimator. The multiple scattering angle (projected into a transverse plane of the defining collimator) has been calculated with the following formula [PDG98], which is accurate to within 11%,

$$\Theta_{MS} = \frac{13.6\,\mathrm{MeV/c}}{pc\beta}\sqrt{\frac{L}{L_{rad}}}\left(1 + 0.038\ln\left(\frac{L}{L_{rad}}\right)\right). \tag{3.21}$$

Here $p = 5.50\,\mathrm{MeV/c}$ is the electron momentum, $\beta = 0.996$, $L = 0.05\,\mathrm{cm}$ is the aluminum vacuum window thickness, and $L_{rad} = 8.9\,\mathrm{cm}$ is the radiation length for aluminum. The multiple scattering angle is then $\Theta_{MS} = 149\,\mathrm{mrad}$. Since the defining detector aperture is approximately 7 cm away from the vacuum window the beam spreads to a radius of 1.04 cm. The radius of the defining aperture is 0.5 cm. Consequently, the portion of the scattered electrons reaching the detector is proportional to $\left(\frac{r_{aperture}}{r_{electrons}}\right)^2 \approx 25\%$. Without the correction for the aluminum window the ideal Mott elastic rate for the detector acceptance would be 4 times larger, or $300\,\mathrm{Hz}/(\mu\mathrm{A}\cdot\mu\mathrm{m})$.

Although Equation 3.11 can be used to compute the experimental asymmetry, instrumental errors between the detectors introduce uncertainty in the measured polarization. These errors are introduced by inequalities in the pairs of detectors, or misalignments and inhomogeneities of the beam or target. Consider again the *up* and *down* detectors. Consider the case where the beam is aligned well and scatters into both detectors at an angle θ. The efficiencies (Q_u, Q_d) and solid angles ($\Delta\Omega_u$ and $\Delta\Omega_d$) of the detectors are different. For a beam of spin-up electrons the number of scattered elastic electrons detected are then

$$\begin{aligned} N_u^+ &= i^+\rho^+ Q_u \Delta\Omega_u I(\theta)[1 + PS(\theta)] \\ N_d^+ &= i^+\rho^+ Q_d \Delta\Omega_d I(\theta)[1 - PS(\theta)], \end{aligned} \tag{3.22}$$

where i^+ and ρ^+ is the beam current and target density for this spin state. If $Q_u\Delta\Omega_u \neq Q_d\Delta\Omega_d$ an experimental asymmetry due to the detectors exists. This can be eliminated by reversing the helicity of the electron beam. After reversing the

electron helicity (by reversing the optical helicity with a Pockels cell) the spin–down electrons are detected

$$\begin{aligned} N_u^- &= i^-\rho^- Q_u \Delta\Omega_u I(\theta)[1 - PS(\theta)] \\ N_d^- &= i^-\rho^- Q_d \Delta\Omega_d I(\theta)[1 + PS(\theta)], \end{aligned} \tag{3.23}$$

where i^- and ρ^- are the beam current and target density for this spin state. These two equations can be combined to produce

$$\begin{aligned} \sqrt{N_u^+ N_d^-} &= N^+ = \sqrt{i^+ i^- \rho^+ \rho^- Q_u Q_d \Delta\Omega_u \Delta\Omega_d} I(\theta)(1 + PS(\theta)) \\ \sqrt{N_u^- N_d^+} &= N^- = \sqrt{i^+ i^- \rho^+ \rho^- Q_u Q_d \Delta\Omega_u \Delta\Omega_d} I(\theta)(1 - PS(\theta)). \end{aligned} \tag{3.24}$$

The experimental asymmetry is then computed by calculating the super–ratio

$$\epsilon = \frac{N^+ - N^-}{N^+ - N^-} = PS(\theta), \tag{3.25}$$

which is independent of the beam current and target uniformity between helicity states (assuming no other helicity dependencies), and the detector solid angle and efficiencies. The experimental asymmetries for the Mott spectra like those shown in Figure 3.14 are calculated this way. First, the number of events in the elastic peak is determined by the fitting method and next the experimental asymmetry is calculated.

3.3.6 Mott Target and Analyzing Power

The analyzing power for a series of varying thickness gold (Z=79), silver (Z=47), and copper (Z=29) targets have been studied [Pr97] in the Mott polarimeter to determine their effective analyzing powers. The single–atom Sherman functions, $S(\theta)$, have been calculated as outlined in reference [Sh56] and are shown for these materials in Figure 3.17.

The Mott polarimeter scattering chamber detector geometry is optimized for the analyzing power maximum scattering angle for gold targets. The targets are routinely made with tenths of a micron thickness. The effective Sherman function for the

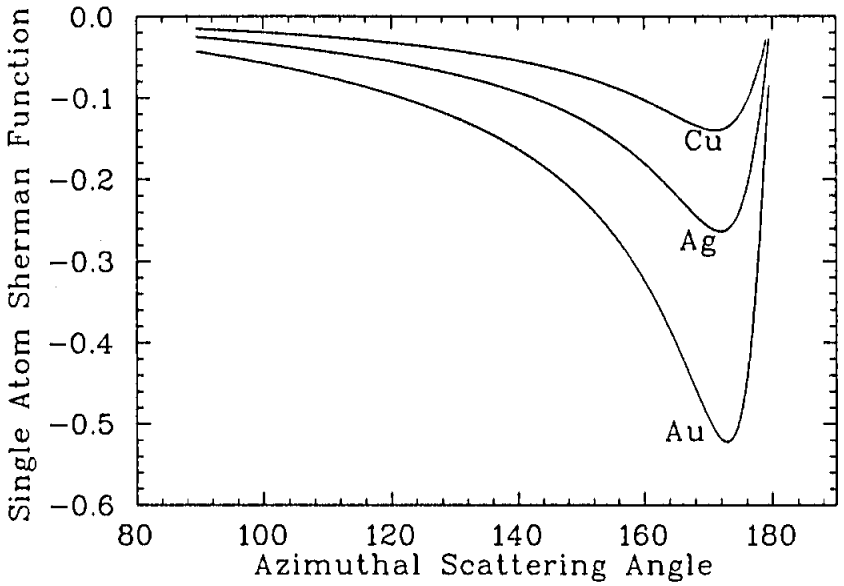

Figure 3.17: Sherman function calculated for copper (Cu), silver (Ag), and gold (Au) at a kinetic energy of 5 MeV.

0.1 μm gold foil is determined by the following procedure. First, the experimental asymmetries were measured for a series of gold target foils of varying thickness. The data shown in Figure 3.18 are fit with the functional form,

$$\epsilon_x = \frac{A_0}{1+\alpha t}. \tag{3.26}$$

The best fit values are $A_0 = 0.359 \pm 0.004$ and $\alpha = (0.316 \pm 0.012)\,\mu\text{m}^{-1}$.

The theoretical value of the Sherman function at this scattering angle has been calculated to be -0.522 with an uncertainty of 1% [Sh56] attributed to the degree of convergence in the method of calculation. An additional uncertainty of 0.5% is estimated due to electron screening effects of the outer shell electrons of the gold nuclei [Li63]. Including nuclear size corrections to the point-like nucleus scattering problem [Ug70, St99] *reduces* the Sherman function by $(1.3 \pm 0.4)\%$ and averaging the Sherman function over the detector acceptance further *reduces* the value by 0.4%. Combining the corrections and uncertainties results in the value -0.513 ± 0.013.

Using the zero–thickness extrapolation, the polarization of the beam for this measurement is $\frac{0.359 \pm (0.004)_{stat} \pm (0.011)_{sys}}{-0.513 \pm 0.013} = -0.700 \pm 0.034$. The effective Sherman function

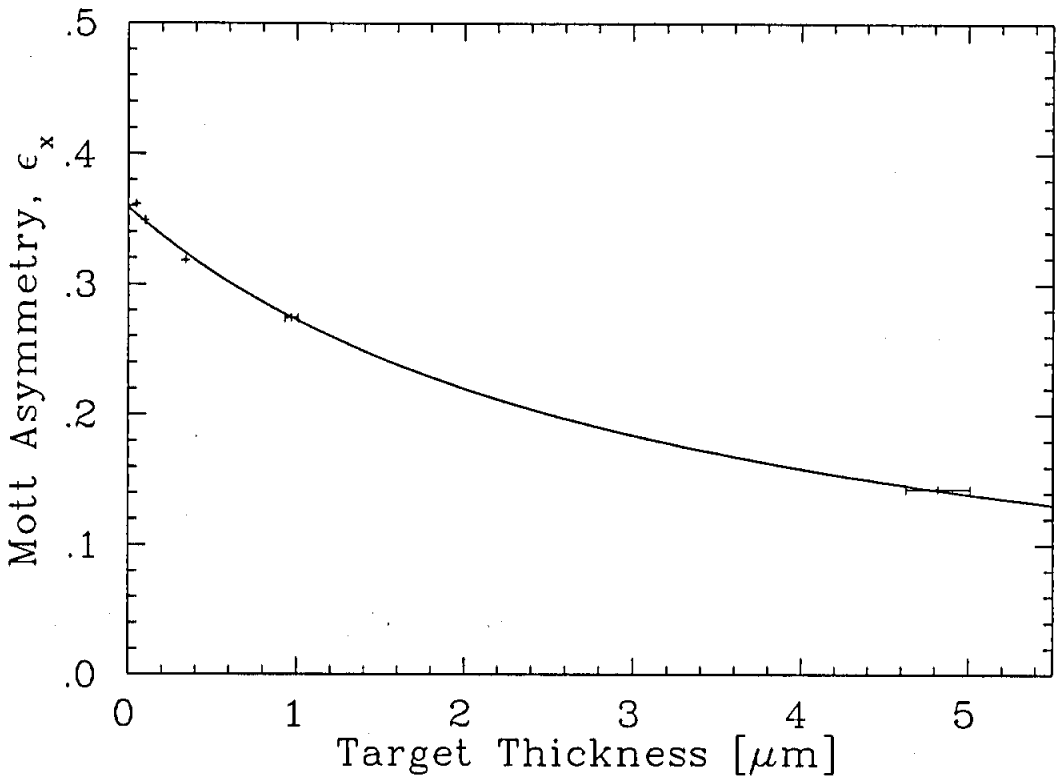

Figure 3.18: Data for gold foil target thickness extrapolation.

for the 1.0 μm gold target foil is then $\frac{0.274\pm(0.001)_{stat}\pm(0.008)_{sys}}{-0.700\pm0.034} = -0.391 \pm 0.023$. This value indicates a dilution of the Sherman function by $\approx 24\%$. Note that for the 0.1 μm gold target foil $S_{eff} = -0.506$ indicating dilution of this foil thickness by only 3.1%.

3.3.7 Wien Filter Calibration

A calibration of the Wien filter was performed using the 5 MeV Mott polarimeter [Pr97] (described in Section 3.3). The Wien magnet current (independent parameter) was set for 12 rotations spanning $\approx \pm 110°$ and the resulting polarization was measured at the polarimeter. In this configuration the Wien filter sets the polarization to 12 orientations which sweep out a circle in the x–z plane as depicted in Figure 3.19. The polarimeter measures the transverse components of the beam polarization and therefore resolves the corresponding sine-wave amplitude in the $\hat{x}$ direction. The data and a fit of the form $P_x = P_0 \sin(ki_{Wien} + \phi_0)$ is shown in Figure 3.20. The polariza-

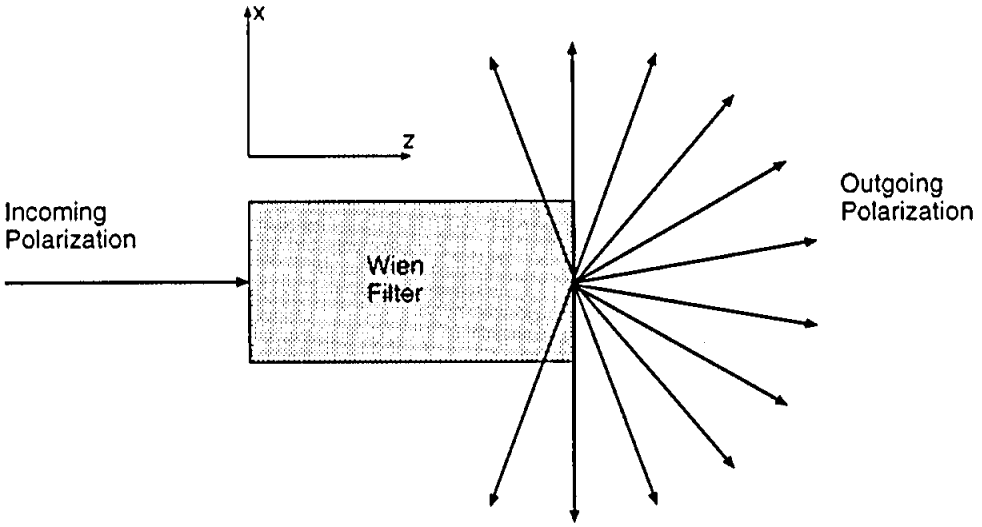

Figure 3.19: The Wien filter is calibrated by rotating the incoming polarization (parallel to the beam momentum) to 12 orientations within $\approx \pm 110°$. The outgoing polarization was then measured at the Mott polarimeter.

tion P_x is the measured experimental asymmetry divided by the effective Sherman function. The value of the Sherman function used is $S_{eff} = -0.391$ as measured for the $1\,\mu$m gold target foil (Section 3.3.6). The error bars are statistical only. The absolute uncertainty in the amplitude of the polarization is about 5%. The best-fit parameters are $P_0 = (-69.9 \pm 0.1)\%$, $k = (12.09 \pm 0.08)\,\frac{\text{deg}}{\text{A}}$, and $\phi_0 = (0.98 \pm 0.22)\,°$. The χ^2 of the fit is 1.09 per degree of freedom. A correction to the phase, ϕ_0, must be made to account for the polarization rotation incurred when the beam is steered by $(-12.5 \pm 0.4)\,°$ from the injector beamline to the polarimeter beamline. The total beam energy at this location is $5.52 \pm 0.10\,\text{MeV}$ ($KE = 5.01\,\text{MeV}$) and the correction to the measured precession is $(-0.156 \pm 0.005)\,°$. Consequently $\phi_0 = (1.14 \pm 0.21)\,°$.

3.3.8 Solenoid Spin Rotator Calibration

A calibration of the two solenoid spin rotators was performed using the Mott polarimeter. Using the calibration data for the Wien filter the beam polarization was oriented transversely prior to the solenoid magnets. For each solenoid the coil currents were set to produce 7 different precession angles. Each set of coil currents must

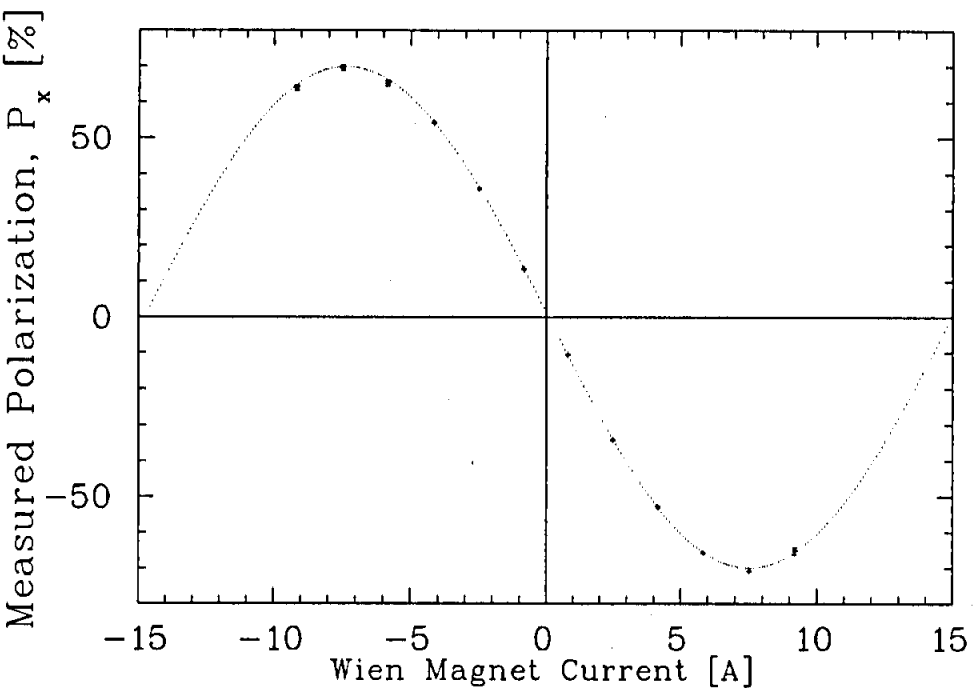

Figure 3.20: Wien filter calibration data and a sinusoidal fit to determine the spin rotation angle for the device setpoints. The error bars shown are statistical.

produce very similar focal lengths to transport the beam through the injector. The calculations made to produce the proper sets of coil currents is given in Appendix C. For these tests transmission of the electron beam through the injector was routinely successful indicating that the rotation angle could be set while maintaining the proper solenoid focal length. The 7 different precession angles were between $\approx \pm 50\,^\circ$ sweeping out an arc in the x–y plane as shown in Figure 3.21. The polarimeter measures both transverse components of the beam polarization, which can be written in terms of the polarization of the beam, P_0, and the rotation angle, ϕ,

$$\begin{aligned} P_x &= P_0 \cos(\phi) \\ P_y &= P_0 \sin(\phi). \end{aligned} \tag{3.27}$$

The rotation angle is then directly extracted from the two components using

$$\phi = \tan^{-1}\left(\frac{P_y}{P_x}\right). \tag{3.28}$$

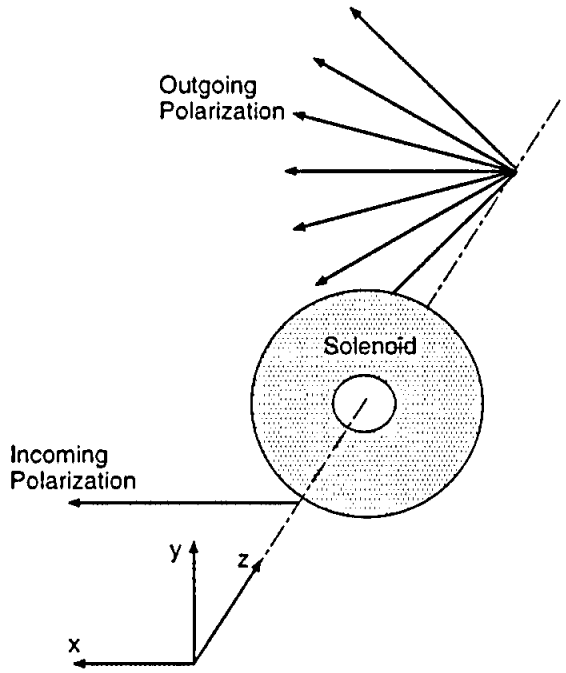

Figure 3.21: The solenoid spin rotators are calibrated by rotating the incoming polarization (transverse to the beam momentum) to 7 orientations within $\approx \pm 50°$. The outgoing polarization was then measured at the Mott polarimeter.

A plot of ϕ versus the difference in the coil setpoints, $i_B - i_A$, and a linear fit of the form $\phi = k_{S_1}(i_B - i_A) + \phi_{S_1}$ is shown in Figure 3.22 for the first spin rotator. The best fit yields $k_{S_1} = (0.0370 \pm 0.0003)\,\mathrm{deg/mA}$ and $\phi_{S1} = (1.48 \pm 0.19)\,°$. The second solenoid spin rotator is similarly calibrated and the results are shown in Figure 3.23. The linear best fit yields $k_{S_2} = (0.0323 \pm 0.0002)\,\mathrm{deg/mA}$ and $\phi_{S_2} = (0.96 \pm 0.19)\,°$.

The difference from zero of the phase offsets, ϕ_{S_1} or ϕ_{S_2}, may result from the residual field in the magnet. The uncertainties in the fit parameters result from the goodness of the fit.

3.4 Recirculation Arc

The recirculation arcs transport the electron beam from the end of one linac to the beginning of the next for successive acceleration. A description of the beam transport and basic optical properties of the recirculation arcs is given in Section 3.4.1.

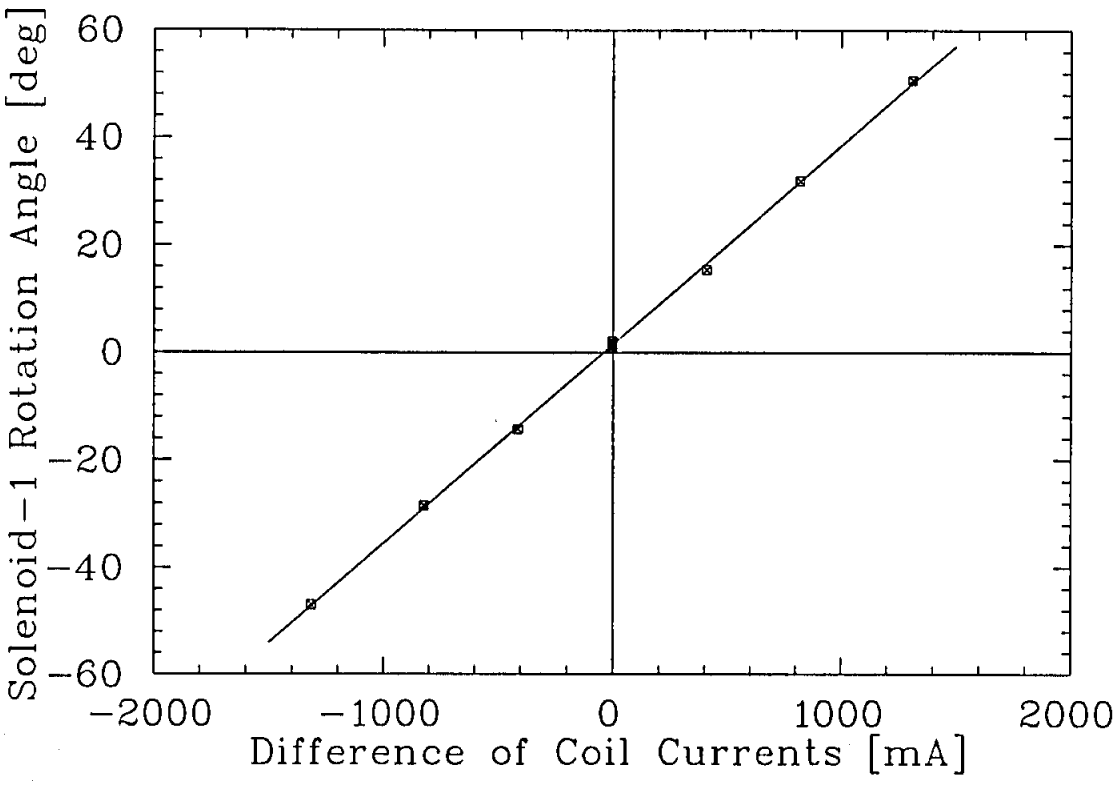

Figure 3.22: Solenoid spin rotator S_1 calibration results and a linear fit to determine the accuracy of the calculated coil current setpoints.

The beam orbit requirements for this experiment are described in Section 3.4.2. The approach for determining the deflecting magnet field strengths is discussed in Section 3.4.3.

3.4.1 Optical Properties

The optical setup for the recirculation system is that it not degrade the beam quality from one linac to the next. To do this, the recirculation arcs are designed to be (a) achromatic (final beam position and angle are energy independent); (b) imaging (beam profile exiting one linac enters the next linac unaffected); and (c) the reference orbit path length be an integral number of RF wavelengths (to maintain the beam in phase with the acceleration cavities). The achromaticity is accomplished with the transport optics by making sure the net dispersion (and first derivative of dispersion)

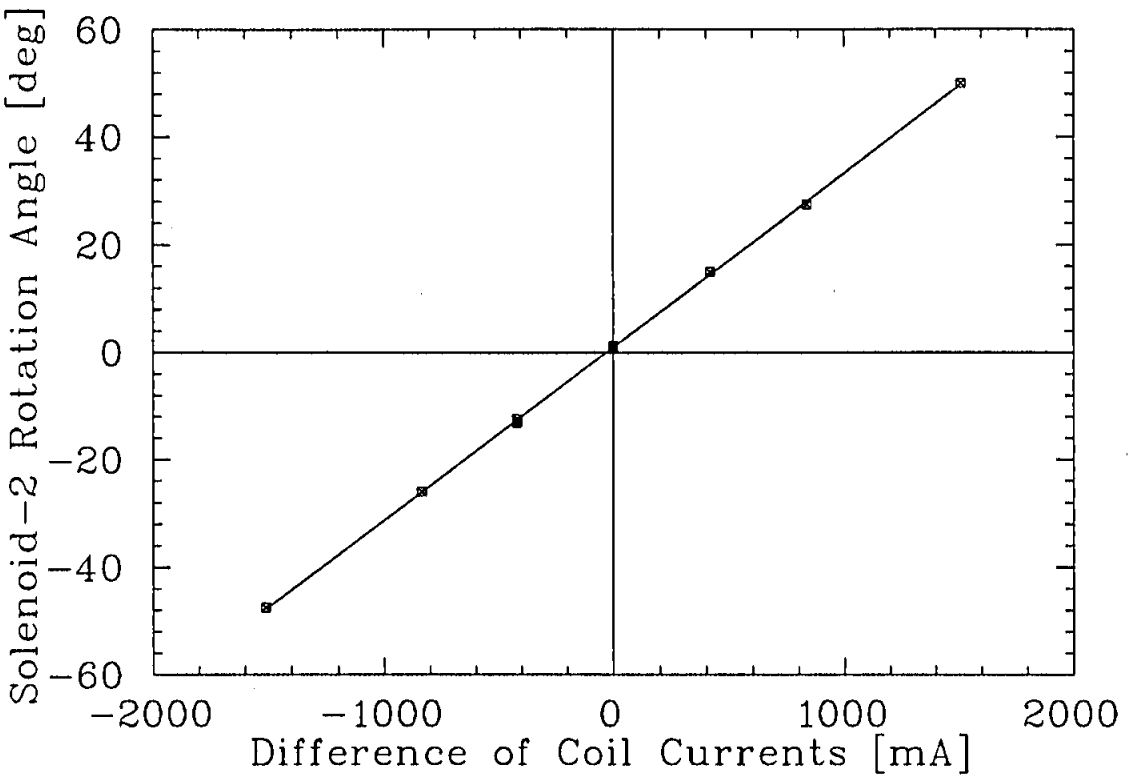

Figure 3.23: Solenoid spin rotator S_2 calibration results and a linear fit to determine the accuracy of the calculated coil current setpoints.

through the recirculation arc vanish at each linac exit and entrance. The imaging condition is met by choosing the quadrupole focusing such that the number of betatron oscillations in each arc is a whole or half-integer. For the π bending section the horizontal betatron tune $\nu_x = 5$ and the vertical betatron tune is $\nu_y = 3$. Including the spreader and recombiner, $\nu_x = 7$ and $\nu_y = 5$. The requirement for a multiple number of RF wavelengths is met by a segment of magnets outside of the arc. These magnets constitute what is called a *dogleg*. The doglegs provide for adjusting the path length of the entire orbit at either end of the accelerator, between each linac. The total magnetic adjustment at each dogleg can provide about 5% of an RF wavelength path length variation (≈ 8 mm) and keep the beam arrival time at the following linac in phase with the RF acceleration.

3.4.2 Orbit Perturbation Requirements

The experiment requires a series of measurements, each between two different perturbed orbits. In this way, the relatively small sensitivity to the beam polarization is easier to determine. An absolute measurement of the effect would increase the difficulty of the experiment unnecessarily. Each orbit perturbation is introduced at the entrance to arc 7 and removed at the exit of this arc. In the same way that parity violation experiments strive to change the electron beam helicity without changing other beam characteristics, this experiment aims to change the beam orbit without causing other effects. This approach aims to isolate the effect of the beam orbit perturbation on the beam polarization in the arc. It ensures that the beam position at the polarimeter target, for instance, is not correlated to the arc orbit effects. Commissioning tests demonstrated that while perturbing the reference orbit amplitude by as much as $\pm 8\,\mathrm{mm}$, the correlated motion at the polarimeter target could be kept below $\Delta x = 250\,\mu\mathrm{m}$ and $\Delta y = 150\,\mu\mathrm{m}$. Estimates of the effect of position motion at the polarimeter target are more fully discussed in Chapter 4.

The polarization effect is predicted to scale linearly with the perturbed orbit amplitude. This is because the mid-plane magnetic field of the quadrupole magnets in the arc grows linearly with displacement from the magnet center. Therefore, the orbit perturbation used is of variable amplitude to study this prediction. The maximum orbit amplitude is limited by the inner wall of the beampipe diameter. The narrowest apertures occur at the quadrupoles where the beampipe inner diameter is $\frac{7}{8}''$. The locations of the deflecting magnets and their field strengths should be capable of reaching this limit. Again, the perturbation of the reference orbit should only affect the vertical beam orbit. This is to say, the difference of the horizontal orbits between perturbations should be zero. This assures that the quadrupole fields are being sampled by the electron beam in the same vertical plane at each quadrupole for both orbit perturbations.

3.4.3 Orbit Calculations and Magnetic Field Requirements

To establish an orbit different than the reference orbit requires beam deflections. As pointed out in Chapter 2 the solution of betatron motion is oscillatory. The deflections of the beam orbit by magnets are simply initial conditions for this motion. To determine the beam orbit in one plane at some location (position and angle) requires two deflections. Therefore, to choose the amplitude and the slope of the beam orbit at the center of the arc and to remove the orbit motion at the end of the arc requires a total of four deflection magnets. A diagram of the arc and relevant locations are shown in Figure 3.24. The first condition requires that the orbit at

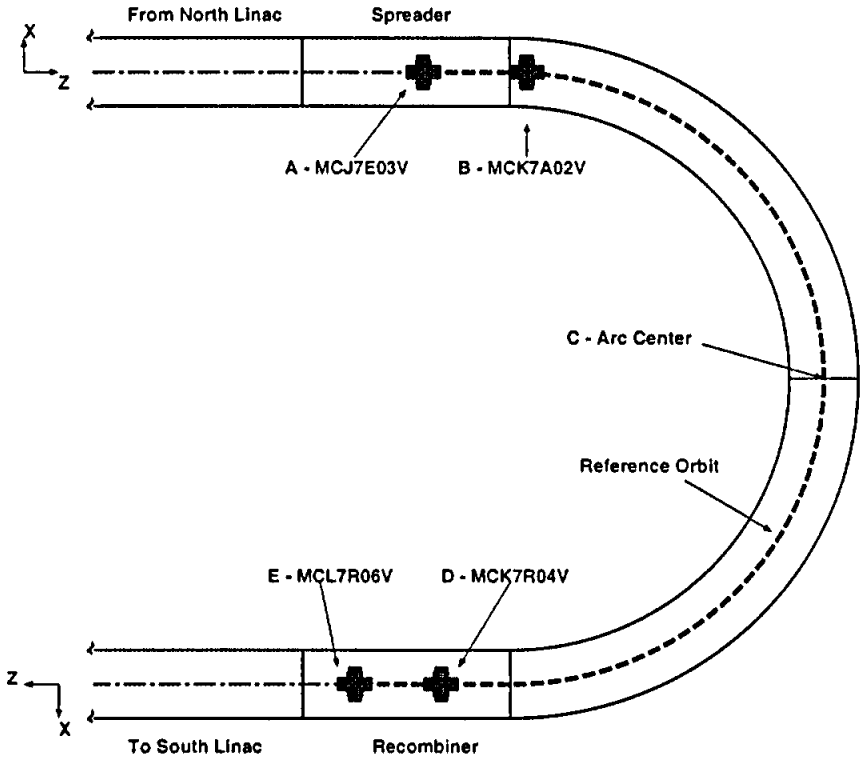

Figure 3.24: Layout of recirculation arc 7 indicating the locations and names of the vertical deflecting magnets used to perturb the nominal (reference) beam orbit.

location C have some some amplitude $y_c = \pm y_{max}$ and be flat, $y'_c = 0$. This ensures a symmetrical beam orbit about the center of the arc. The value of y_{max} is arbitrary and scales the amplitude of the perturbed orbit oscillation. The second condition

requires that the orbit exiting the arc be the reference orbit ($y_e = y'_e = 0$).

Using the matrix formalism for linear optics transport [Car92], and assuming the horizontal and vertical beam motion is uncoupled, the relation between the initial and final beam coordinates (x, x', y, y') can be written as

$$\begin{pmatrix} x \\ x' \\ y \\ y' \end{pmatrix}_f = \begin{pmatrix} M_{11} & M_{12} & 0 & 0 \\ M_{21} & M_{22} & 0 & 0 \\ 0 & 0 & M_{33} & M_{34} \\ 0 & 0 & M_{43} & M_{44} \end{pmatrix}_{i \to f} \begin{pmatrix} x_0 \\ x'_0 \\ y_0 \\ y'_0 \end{pmatrix}_i .$$

The M_{ij} are matrix elements which describe how the initial beam coordinates translate to the final position and angle of the beam. These matrix elements are determined from the nominal machine accelerator model as defined for DIMAD. The notation $i \to f$ is used and means the cumulative effect between locations i and f in the lattice. For example, $M_{34}^{B \to C}$ means the matrix element connecting the initial beam angle at location B (y'_B) with the final beam position at location C (y_C).

To meet the first boundary condition at location C (assuming $y_A = y'_A = 0$) the deflections at locations A and B are

$$\begin{aligned} y'_{A-kick} &= \pm \frac{y_{max} M_{44}^{B \to C}}{\Delta} \\ y'_{B-kick} &= \mp \frac{y_{max} M_{44}^{A \to C}}{\Delta}, \end{aligned} \tag{3.29}$$

where $\Delta = (M_{34}^{A \to C} M_{44}^{B \to C} - M_{34}^{B \to C} M_{44}^{A \to C})$. To meet the second boundary condition at location E the deflections at locations D and E are

$$y'_{D-kick} = \mp \frac{y_{max} M_{33}^{C \to E}}{M_{34}^{D \to E}} \tag{3.30}$$

$$y'_{E-kick} = \mp y_{max} M_{43}^{C \to E} \pm y_{max} \frac{M_{44}^{D \to E} M_{33}^{C \to E}}{M_{34}^{D \to E}}. \tag{3.31}$$

Once the angle y' is determined at each of the four deflection locations the magnetic field strength required to produce that deflection for a beam of momentum p_0 can be calculated as

$$\int B dl = \frac{2 p_0}{e} \sin\left(\frac{y'}{2}\right), \tag{3.32}$$

where e is the electronic charge. The recirculation arc energy proposed for this experiment was nominally 2.845 GeV, therefore the magnetic correction strength ($\int Bdl$) is calculated to be

$$\begin{aligned} \int Bdl &= \frac{2 \times 2845 \frac{\mathrm{MeV}}{c}}{e} \sin\left(\frac{y'}{2}\right) \left(\frac{1\,\mathrm{T\,m}}{299.79 \frac{MV}{c}}\right) \left(\frac{10^3\,\mathrm{kG\,cm}}{1\,\mathrm{T\,m}}\right) \\ &= 1.898 \times 10^4 \cdot \sin\left(\tfrac{y'}{2}\right) \mathrm{kG\,cm}. \end{aligned} \tag{3.33}$$

3.5 Deflection Magnets

The deflection magnets are required to produce, and subsequently remove, vertical orbit perturbations (betatron oscillations). The magnets must be capable of producing enough deflecting field strength, be reproducible, driven to their setpoints rapidly, and locatable in the beamline. Two of the four magnets are at locations routinely required by accelerator operations and must be capable of operating at deflections 15% greater than planned for this experiment. The criteria for selecting an air–core magnet design is presented in Section 3.5.1. The magnet modeling and design is described in Section 3.5.2. Fabrication and bench testing is described in Section 3.5.3 and Section 3.5.4, respectively. Finally, the magnet installation and controls are discussed in Section 3.5.5.

3.5.1 Air–Core Versus Iron–Core

An iron–core magnet is one with an iron return yoke to confine and strengthen the magnetic field of an electromagnet (magnetic field produced from a current in a coil of wire). Existing iron–core magnets in acceptable locations of the recirculation arc produce the required field strength and reproducibility. However, at the inception of this experiment it was considered advantageous to change the beam orbit, and magnet currents, at rates of 10 Hz. This can be accomplished, for instance, with

iron laminate type magnets, but not with the solid iron type magnets that exist in the accelerator. The inductive load, L, of the solid iron magnet geometry and coil inductance, combined with the resistive load, R, of the coil and electrical connections, limit the frequency response ($\tau_{rise} = \sqrt{L/R}$) of the magnet. The magnetic hysteresis of the iron also complicates the process for selecting magnet setpoints rapidly.

The alternative approach was to construct an air-core magnet; a magnet without an iron return yoke. The frequency response of an air-core magnet is limited by the inductance and resistance of the coil. Coils of this geometry typically have an inductance of order 10 mH and a resistance of order 1 Ohm. Consequently, $\tau_{rise} \sim 100$ ms is expected. Indeed, risetimes of about 100 ms were reproducible during bench testing. This is adequate for the orbit reversal rate finally selected for the experiment (once every 120 sec). The requirements to generate the required field strength (without iron), good magnetic uniformity over the beampipe aperture (low harmonic content), and a compact size to be located on the beamline were the driving factors in the final design.

3.5.2 Modeling

The prototype is based on a style of magnet used at various locations in the accelerator for correcting the beam orbit. The magnet is composed of two identical coils which are mounted symmetrically on either side of the beampipe. The two coils are powered in series to form a dipole field. A useful design model for the magnet is made from four wires spaced symmetrically around the beampipe as depicted in Figure 3.25. The model assumes longitudinal symmetry and neglects the end field effects of the coil.

If the two coils are driven in series by a single power supply the current in each of the design model wires is identical, and the field at the axis ($x = y = 0$) is simply given by

$$\vec{B}_{(axis)} = \sum_{i=4wires} \vec{B}_i(\vec{r}_i)$$

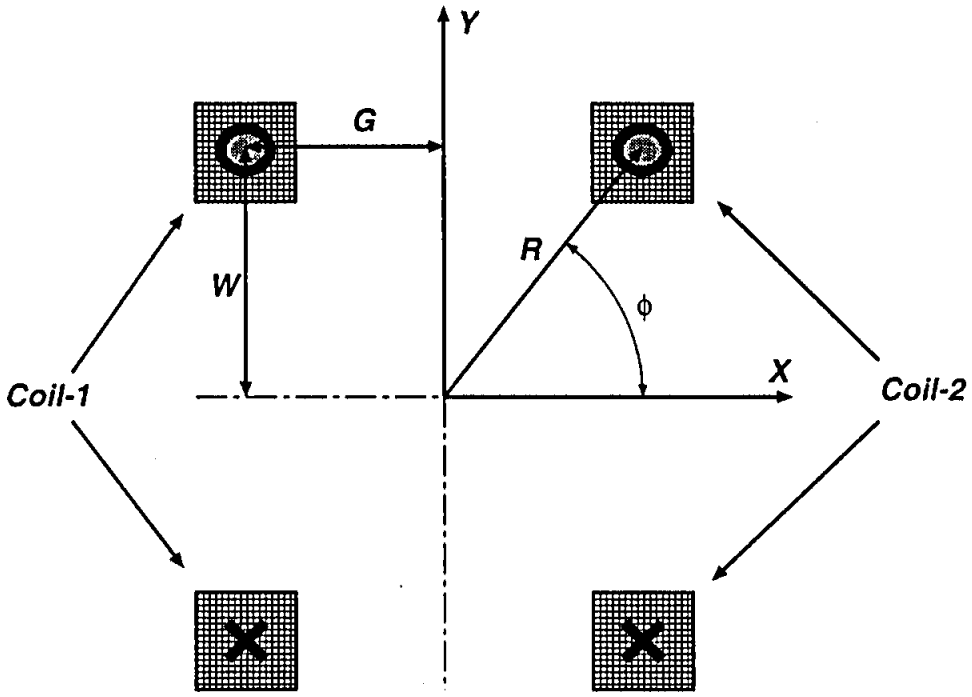

Figure 3.25: A four wire design model is used to estimate the magnet design parameters. The circle (cross) in each wire means the current is directed out of (into) the page.

$$= \frac{4\mu_0 I_{tot}}{2\pi} \cdot \frac{\sin\phi}{R}\hat{x}, \tag{3.34}$$

where μ_0 is the magnetic permeability of free space, $I_{tot} = Ni$, N is the number of turns of the coil and i is the current in the wire. ϕ and r, defined in Figure 3.25, set the geometry and spacing of the coils. By symmetry $B_y = B_z = 0$. This model does not consider the real distribution of the current in the coil package (coil diameter $< r_{coil}$) and it neglects the end field of the magnet, however, it does provide a good approximation for prototyping the magnet since the radial scale r is much less than the magnet length.

The beamline is compactly loaded with accelerator components, beamline diagnostics and other magnets so available space is a scarce commodity. To accommodate the space requirements and to reduce coupling of the magnetic field of the coils to nearby iron elements the end-to-end magnet length, L_{mag}, was limited to 30 cm.

Beam optics simulations of recirculation arc 7 (E_{beam} = 2.845 GeV) using DIMAD

were performed to determine the magnetic field strengths at possible installation locations for transporting large amplitude orbits without loss. The results indicate the minimum required field strength at location A (2″ beampipe) is $\approx$ 1000 Gauss cm and at locations B, C, and D (1″ beampipe) is $\approx$ 3300 Gauss cm. The first location requires a smaller field strength than the remaining three because it is followed by a large drift section (a large moment arm).

Magnets are often cooled to remove the heat load generated by the resistive heating of the current-carrying wire. To simplify the design and installation, the magnet was air cooled, rather than water cooled. The coil mass and material (copper) of the approximate magnet design determine the maximum operating current. Without additional cooling this magnet design operating in excess of 7 A would probably fail as a result of the epoxy binding the wire into a coil form melting ($\approx$ 250 °C). This constrained the design magnet current (and field integral) to a safe threshold of $\leq$ 5 A, producing $\approx$ 50% less resistive heating. The magnet constraints are summarized in Table 3.1.

Points	Available Space	Beampipe OD	$(\int Bdl)_{min}$	$(I_{coil})_{max}$
A	36.0 cm	2″	1000 G cm	5 A
B, D, E	36.7 cm	1″	3300 G cm	5 A

Table 3.1: The available beamline space, beampipe outer diameter (OD), minimum required magnetic field strength, and maximum coil current for the magnet design.

A magnet can be characterized by a few useful parameters; (a) the maximum magnetic field B_0 chosen along a suitable axis; (b) the field integral along this axis $(\int B \cdot dl)_{axis}$; and (c) the effective length defined by $L_{eff} = \frac{(\int B \cdot dl)_{axis}}{B_0}$. By measuring the dipole field on the axis of a magnet of similar geometry to the one considered here the ratio of the effective magnetic length to the total magnet length was determined to be $\frac{L_{eff}}{L_{mag}} = 0.93$. The effective length of the magnet being prototyped is then $L_{eff} = 30\,\text{cm} \cdot 93\% = 27.9\,\text{cm}$. The coil angle ϕ was chosen to be near 60° to provide

the best uniformity of the dipole field. The half-gap g and half-width h spacing was chosen to satisfy the beampipe diameter and coil angle. The number of turns was chosen to be large enough to produce the required magnetic field strength at currents less than 5 A. The effective length, beamline constraints, and allowing for 15% overhead in the required field strength, yield the magnet design requirements listed in Table 3.2.

Characteristic	1″ OD Magnet	2″ OD Magnet
Magnet Length	30.0 cm	30.0 cm
Half-Gap, g	1.270 cm	1.829 cm
Half-Width, h	2.222 cm	3.175 cm
Coil Angle, ϕ	60.25 °	60.06 °
Coil Turns, N	100	100

Table 3.2: The design values for deflection magnets as described in Figure 3.25.

3.5.3 Magnet Construction

The magnets were fabricated using the design values in Table 3.2 at the machine shop at Jefferson Laboratory. The fabrication process involved the following five steps:

1. A winding fixture was designed and then fabricated to provide the tool on which the magnet wire could be wound and formed into a coil.

2. For each of the two coil geometries 17 gauge kapton coated copper wire was wound under tension to produce $N = 100$ turns in 10 layers as depicted in Figure 3.26.

3. After the coil is wound on the fixture the ends of the coil are bent upward by an amount 60 ± 2.5 °. This reduces the strength of the field near the edge of

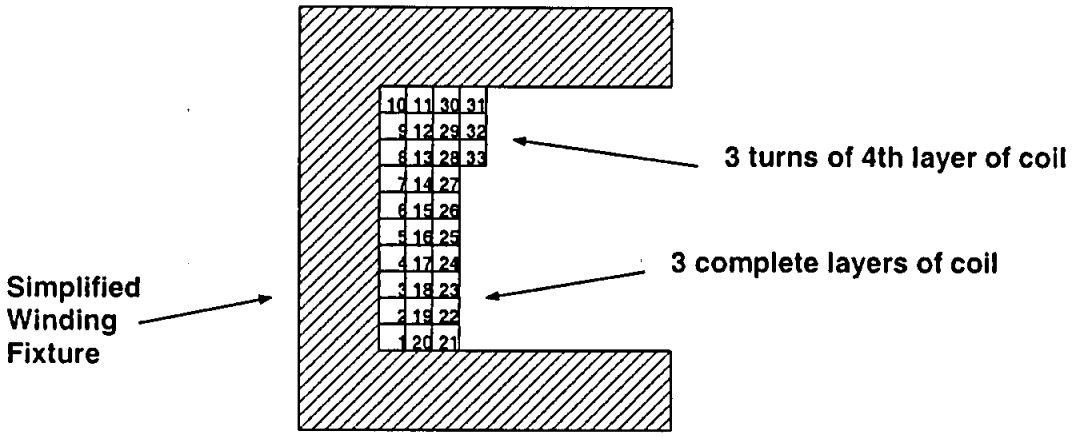

Figure 3.26: Simplified cross section of the fixture used to wind the magnet wire into a coil. Each coil is wound to 10 layers with 10 turns of wire per layer.

the magnet where the harmonic content is larger. It also allows for the magnet to straddle the beampipe at a closer radius. Bending the coil by more than 60° is mechanically difficult (the coil tends to deform) and was avoided.

4. The wound coil, still on the fixture, is dipped in a high temperature epoxy (HYSOL) which is cured in an oven. Two views of the completed coil (2″ OD beampipe design) are shown in Figure 3.27.

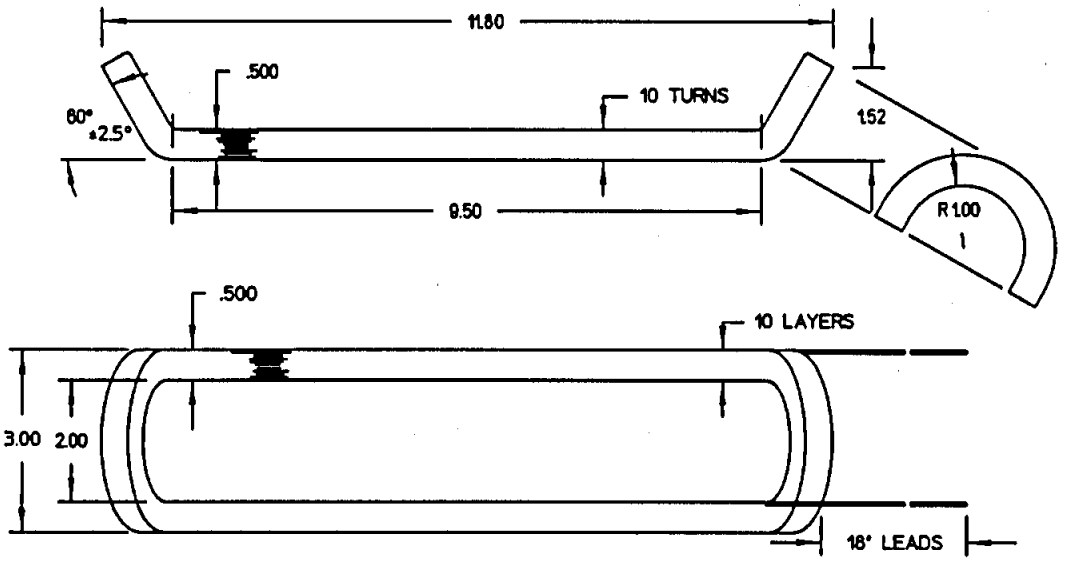

Figure 3.27: Two views of a magnet coil prior to assembly. Two coils are used together to create the dipole field for one magnet. Figure courtesy of D. Machie.

5. Two coils are assembled by capturing both with a pair of mounts fabricated from high density polyethylene to the beampipe to form the complete magnet. The mounts capture the outer diameter of the beampipe and are clamped together with tie wraps as shown in Figure 3.28.

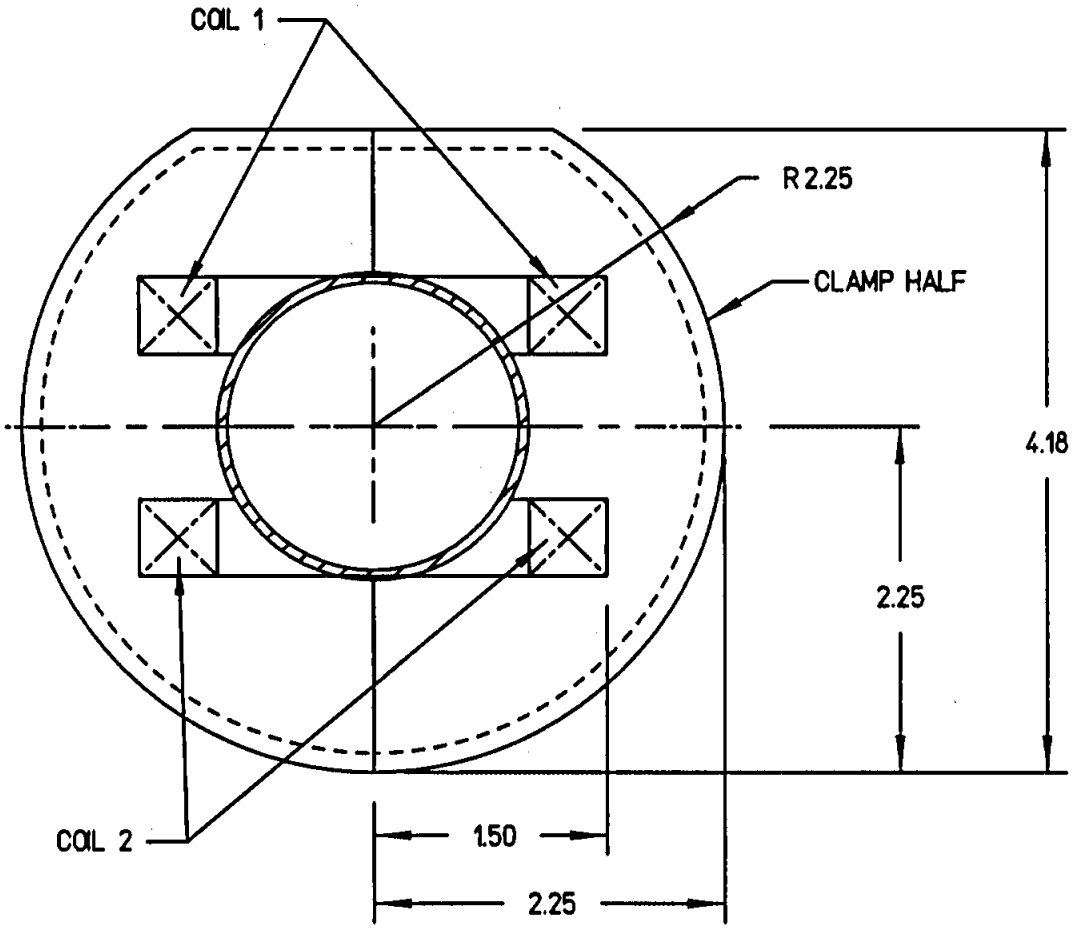

Figure 3.28: View showing two clamp halves symmetrically capturing two magnet coils to a 1" OD beampipe. Units are inches. Figure courtesy of D. Machie.

3.5.4 Bench Tests

Once fabricated each of the four magnets (three for 1″ diameter beampipe and one for 2″ diameter beampipe) was assembled with a set of mounts on a stock piece of beampipe as shown in Figure 3.29. Each was checked for continuity and proper

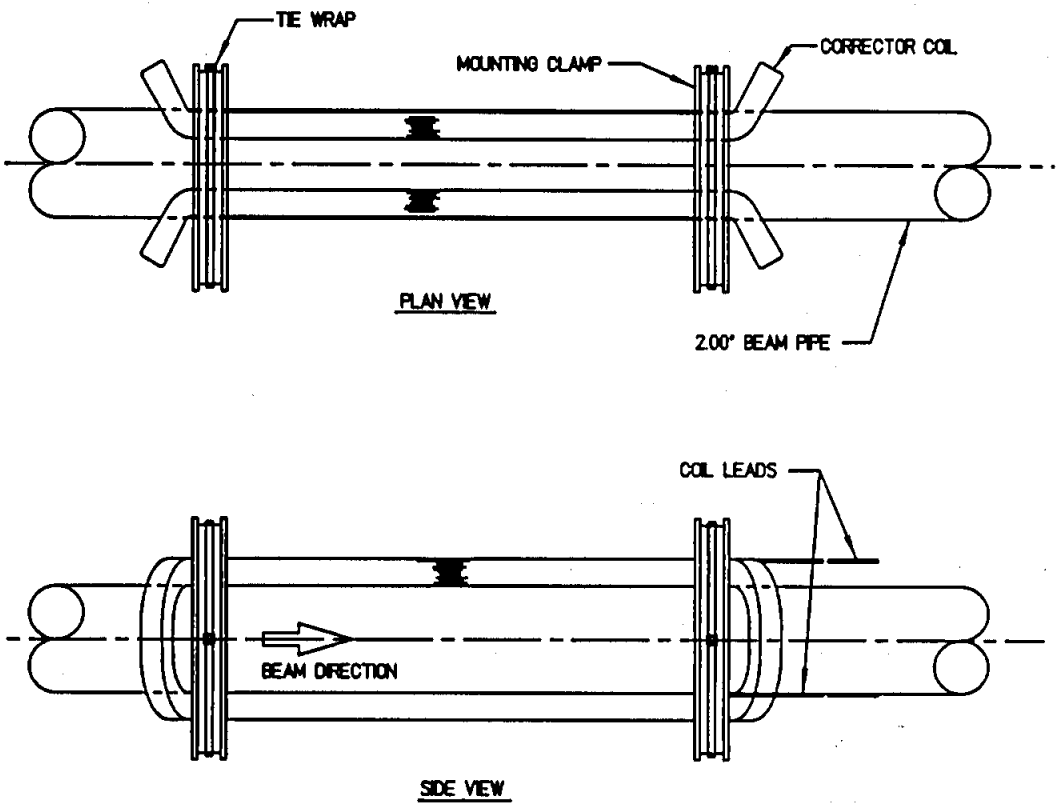

Figure 3.29: Assembly drawing of a deflecting magnet mounted to a section of beampipe. Figure courtesy of D. Machie.

wiring (a quadrupole field is created if the coils are mis-wired). The magnets are designed to operate between $\pm 5\,\mathrm{A}$. The first test verified operation of the magnet at 5 A while recording the coil surface temperature, and power supply current and voltage, as a function of time. This determines the operational resistivity of the coil. Plots of the coil surface temperature and resistivity are shown in Figure 3.30. The linear dependence of the coil resistance with temperature is described by the relationship [Ba78]

$$R = R_1 \left[1 + \alpha_1 (t - t_1)\right], \tag{3.35}$$

where $R_1 = 2.22\,\Omega$ is the resistance at temperature $T_1 = 20\,^\circ$ and $R_1 \cdot \alpha_1 = 0.0094\,\Omega/^\circ\mathrm{C}$; both values are extracted from the average intercept and slope, respectively, of the lower two plots. Consequently, $\alpha_1 = 0.0043\,/^\circ\mathrm{C}$, comparable to the handbook value $\alpha_1 = 0.0039\,/^\circ\mathrm{C}$.

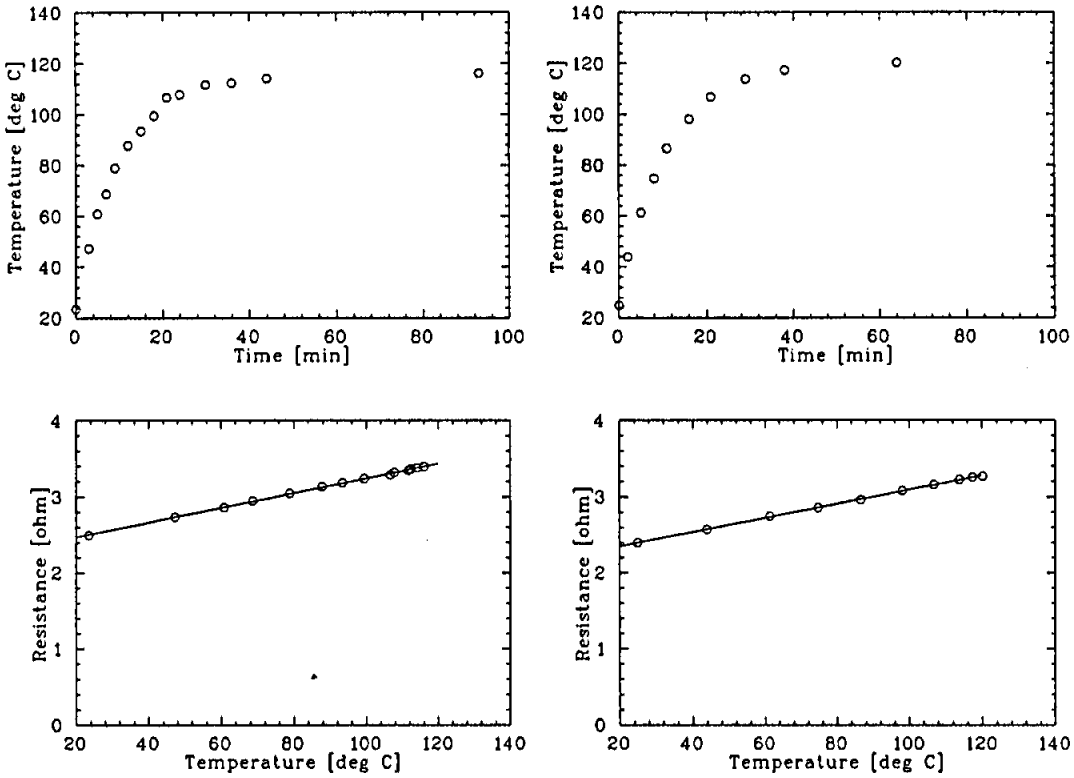

Figure 3.30: Coil surface temperature versus time and the magnet resistance versus coil temperature for the 1" (left) and 2" (right) OD magnets.

The next test involved measuring the transverse magnetic field along the axis of the magnet. The magnet is mounted on a test stand and a Hall probe is stepped along the beampipe axis in 0.5 cm increments. At each step the Hall probe location, transverse magnetic field, and power supply current is recorded.

Two profiles, measured for different magnet currents, are shown in the upper plot of Figure 3.31 for the 1″ beampipe magnet. The measured profile is the contribution of the Earth's field plus the magnet field (which scales linearly with the power supply current)

$$B_{Meas}(x) = B_{Earth} + i \cdot B_{Magnet}(x). \tag{3.36}$$

The contribution from the Earth's field can be determined and subtracted if this magnet profile is measured for two power supply currents, i_1 and i_2,

$$B_{Earth} = \frac{i_2 B_1 - i_1 B_2}{i_2 - i_1}. \tag{3.37}$$

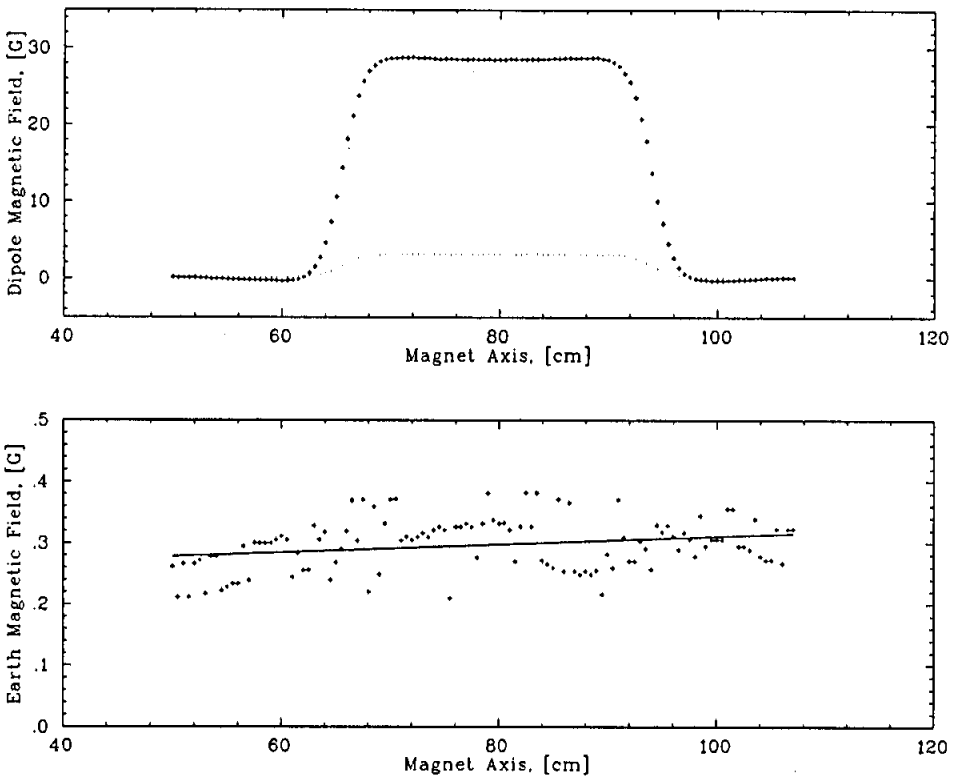

Figure 3.31: The measured dipole field profile along the 1" OD magnet is shown in the upper plot for (a) 1.0 Amp and (b) 0.1 Amp. The contribution of the Earth's magnetic field to the magnet profiles is shown in the lower plot.

The result is shown in the lower plot of Figure 3.31. A fit of the Earth's field along the measurement length yields $B_{Earth} = 0.246\,\text{Gauss} + 6.46 \times 10^{-4}\,\frac{\text{Gauss}}{\text{cm}} \cdot z$. The small slope is likely due to a mis-alignment between the Hall Probe path between measurements. The semi-discreet fluctuation in the data is likely attributed to the resolution of the probe used for the measurement. Using the value at the center of the magnet $B_{Earth} = 298\,\text{mG}$. The profile for the 2" beampipe magnet was also measured. A comparison of profiles for both magnets operating with a power supply current of 1 A is shown in Figure 3.32. Finally, the characteristic magnet parameters are determined from the field profiles. The maximum magnetic field along the central portion of the magnet axis, $(B_0)_{axis}$, is determined from the profile. The strength of the magnet, $(\int Bdl)_{axis}$, is determined by summing over the profile, $\sum B_i \Delta x_i$. The effective length, L_{eff}, is determined from the ratio of the strength to the maximum

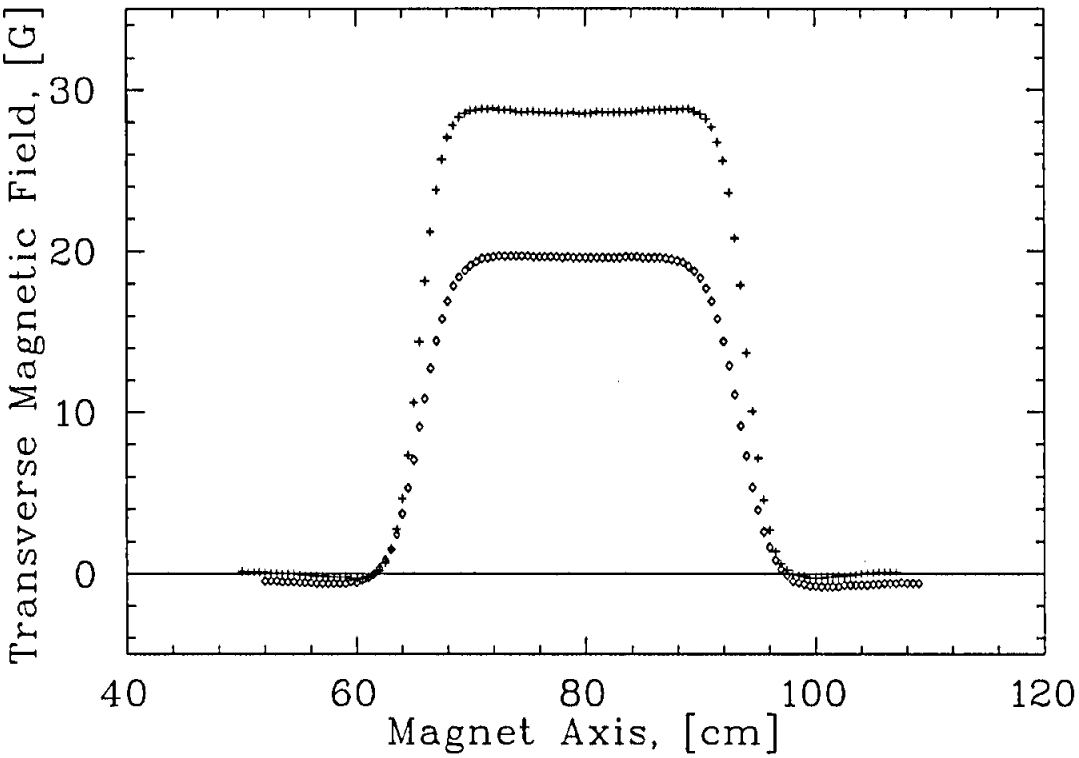

Figure 3.32: Transverse magnetic field profile on the axis of the 1″ (plus symbol) and 2″ (diamond symbol) OD magnets. Each magnet is powered by $i = 1$ Amp for this plot.

field. A comparison between the modeled and measured magnet parameters is shown in Table 3.3.

Characteristic	1″OD	1″OD	2″ OD	2″OD
	Design	Measured	Design	Measured
$(B_0)_{axis}$ (G/A)	27.3	28.4 ± 0.1	18.8	19.3 ± 0.1
L_{eff} (cm)	27.9	28.0 ± 3.0	27.9	26.3 ± 0.1
$\int(Bdl)_{axis}$ (Gcm/A)	761.7	795.0 ± 3.0	524.5	508.1 ± 3.0

Table 3.3: Comparison of modeled and measured characteristic magnet parameters for the 1″ and 2″ OD magnets.

3.5.5 Magnet Installation and Control

To install the four magnets at the desired beamline locations, existing iron-core magnets were removed and the new air-core magnets were mounted. They were mounted to the beampipe using pairs of high density polyethylene disks cut to capture the magnet coils to the beampipe. The magnets are oriented so their dipole field is horizontal. Mounting the coils proved difficult because of flexing of the semi-hard polyethylene mounts. Shims were used to square the coil pairs. Their final arrangement was measured and all coils were oriented with a precision of 0.5° respect to plumb. Each magnet is powered by a DC power supply (with a ±5 A limit) which can be controlled either remotely through accelerator software controls (EPICS) or locally by a voltage source a shown in Figure 3.33.

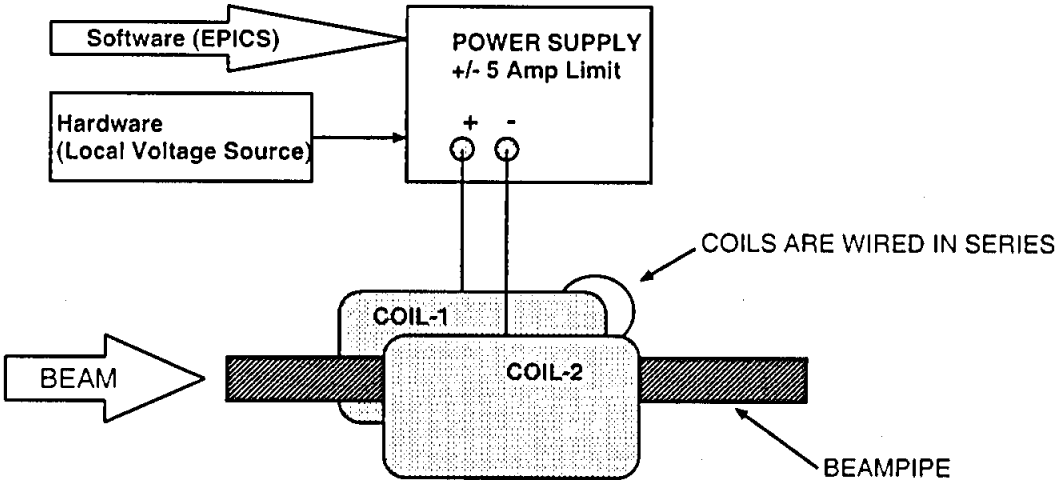

Figure 3.33: The magnet coils are powered by a ±5 A power supply. The power supply is remotely controlled during the experiment to deflect the orbit of the beam in the beampipe.

3.6 Hall C Møller Polarimeter

A Møller polarimeter is used in this experiment to measure the resultant effects of the beam orbit on the beam polarization. The polarimeter is located 40 m upstream

of the target pivot in experimental Hall C. Møller polarimetry is based on the scattering of two polarized electrons ($\vec{e} + \vec{e} \rightarrow e + e$). A scattering asymmetry results from the spin–spin interaction of an incident polarized electron in the beam with a polarized target electron in a magnetized target foil. The Møller cross section is described in Section 3.6.1. A description of the target, spectrometer, and detectors is given in Section 3.6.2. The detector signal and data acquisition electronics are discussed in Section 3.6.3, and the interpretation of the polarimeter data and discussion of important parameters for determining the beam polarization is described in Section 3.6.4.

3.6.1 Physics and Analyzing Power

The cross section for Møller scattering is given by

$$\frac{d\sigma}{d\Omega} = \frac{d\sigma_o}{d\Omega}(1 + \sum_{ij \in x,y,z} A_{ij} P_i^B P_j^T), \tag{3.38}$$

where P_i^B (P_j^T) are components of the beam (target) polarization. A_{ij} are the analyzing powers which depend on the incident electron energy and scattering angle. $\frac{d\sigma_o}{d\Omega}$ is the unpolarized cross section. $\frac{d\sigma_o}{d\Omega}$ and the A_{ij} can be written [Wa86] in center–of–mass frame quantities (denoted by the overbar symbol) of the reaction as

$$\begin{aligned}
\frac{d\sigma_o}{d\Omega} &= \left(\frac{r_0}{2 \cdot \overline{\gamma} \cdot (\overline{\gamma}^2 - 1) \cdot \sin^2 \overline{\theta}}\right)^2 \cdot a_0 \cdot \frac{1}{100} \\
A_{xx} &= -\sin^2 \overline{\theta} \cdot \left((2\overline{\gamma}^2 - 1) + (\overline{\gamma}^4 - 1) \cdot \sin^2 \overline{\theta}\right) / a_0 \\
A_{yy} &= -\sin^2 \overline{\theta} \cdot \left((4\overline{\gamma}^2 - 3) - (\overline{\gamma}^2 - 1)^2 \cdot \sin^2 \overline{\theta}\right) / a_0 \\
A_{zz} &= -\sin^2 \overline{\theta} \cdot \left((2\overline{\gamma}^2 - 1) \cdot (4\overline{\gamma}^4 - 3) - (\overline{\gamma}^4 - 1) \cdot \sin^2 \overline{\theta}\right) / a_0 \\
A_{xz} &= A_{zx} = 2 \sin^2 \overline{\theta} \cdot \overline{\gamma} \cdot (\overline{\gamma}^2 - 1) \cdot \sin \overline{\theta} \cdot \cos \overline{\theta} / a_0 \\
A_{xy} &= A_{yx} = A_{yz} = A_{zy} = 0.
\end{aligned} \tag{3.39}$$

E_0 is the kinetic energy (in MeV) of the incident electron, $m_e = 0.510999\,\text{MeV}$ is the electron rest mass, $\overline{\theta}$ is the center–of–mass scattering angle of the Møller electrons,

$\overline{\gamma} = \sqrt{(E_0 + m_e)/2m_e}$, $a_0 = (2\overline{\gamma}^2 - 1)^2 \cdot (4 - 3\sin^2\overline{\theta}) + (\overline{\gamma}^2 - 1)^2 \cdot (4 + \sin^2\overline{\theta})\sin^2\overline{\theta}$, $r_0 = 2.818$ fermi is the classical electron radius, and $\frac{1}{100}$ is a conversion factor from fm^2 to barn. At ultra-relativistic energies ($\overline{\gamma} \gg 1$) the differential cross section becomes

$$\frac{d\sigma_0}{d\overline{\Omega}} \rightarrow \left(\frac{r_0}{2 \cdot \overline{\gamma}} \cdot \frac{4 - \sin^2\overline{\theta}}{\sin\overline{\theta}}\right)^2, \tag{3.40}$$

and the analyzing powers become essentially energy independent,

$$\begin{aligned} A_{xx} &\rightarrow -\frac{\sin^4\overline{\theta}}{(4 - \sin^2\overline{\theta})} \\ A_{yy} &\rightarrow -A_{xx} \\ A_{zz} &\rightarrow -\frac{\sin^2\overline{\theta} \cdot (8 - \sin^2\overline{\theta})}{(4 - \sin^2\overline{\theta})^2} \\ A_{xz} &\rightarrow 0. \end{aligned} \tag{3.41}$$

A plot of the non-zero analyzing powers are shown in Figure 3.34. All are largest at $\overline{\theta} = 90°$ and the maximum is $A_{zz} = -\frac{7}{9}$.

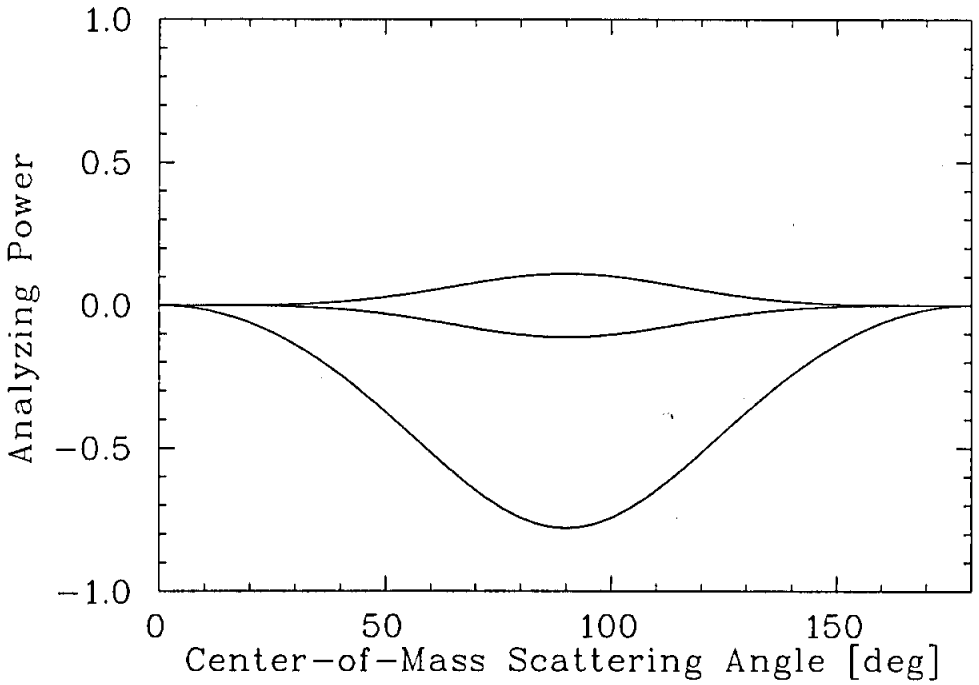

Figure 3.34: Analyzing power for A_{xx}, A_{yy}, and A_{zz} at ultra-relativistic energies ($overline\gamma \gg 1$) as a function of center-of-mass scattering angle $\overline{\theta}$.

The polarimeter used for this experiment uses a target which is polarized along the beam direction ($\hat{z}$) and therefore the only component of beam polarization which is measurable in this high-energy limit is P_z^B corresponding to the maximum analyzing power A_{zz}. Therefore the cross section to consider is

$$\frac{d\sigma}{d\Omega} = \frac{d\sigma_o}{d\Omega}(1 + \overline{A_{zz}} P_z^B P_z^T), \tag{3.42}$$

where $\overline{A_{zz}}$ is the average analyzing power of the polarimeter. By switching the helicity of the polarization at the injector the sign of P_z^B will change at the polarimeter. The coincidence rate changes by an amount $2A_{zz}P_z^B P_z^T$ between the two helicity states. Using Equation 2.26 the experimental asymmetry is written in terms of the measured coincidence rates in each of the two helicity states, $R_{\uparrow\uparrow}$ and $R_{\uparrow\downarrow}$, as

$$\epsilon_{exp} = \frac{R_{\uparrow\uparrow} - R_{\uparrow\downarrow}}{R_{\uparrow\uparrow} + R_{\uparrow\downarrow}} = \overline{A_{zz}} P_z^B P_z^T. \tag{3.43}$$

3.6.2 Design and Layout

A layout of the polarimeter is shown in Figure 3.35. The polarimeter consists of a chamber in which a target foil can be magnetized to saturation in a uniform magnetic field provided by a pair of superconducting Helmholtz coils. Downstream of the target

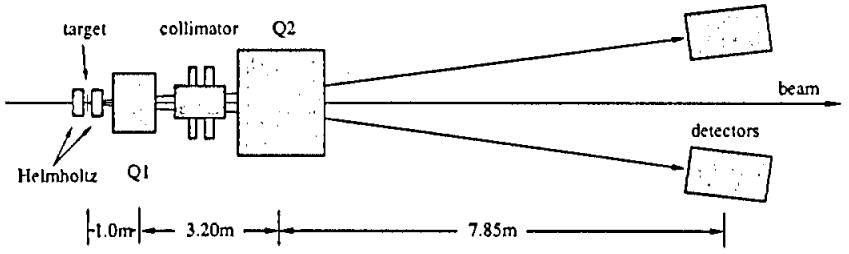

Figure 3.35: Layout of the Hall C Møller polarimeter. A superconducting Helmholtz coil configuration polarizes a target foil into saturation. Quadrupoles Q_1, Q_2, and the detector collimator defines the acceptance of the detectors for measuring the incident and scattered electron in coincidence. Figure courtesy of B. Zihlmann.

location are two quadrupoles separated by a collimation chamber. The quadrupoles

form a magnetic spectrometer for an incident beam energy range of $2 - 6$ GeV (Møller electrons are in the range $1 - 3$ GeV). The quadrupole field strengths are adjusted to maintain a constant acceptance for 90° center–of–mass scattered Møller electrons over this energy range. The optimized setpoints of the quadrupole currents are shown in Figure 3.36. The collimation chamber shown in Figure 3.37 is composed of seven Densimet (tungsten alloy) blocks which can be remotely positioned with actuators. The central block (bored to pass the primary beam to the beam dump) and the two downstream inner blocks mainly reduce detector counts due to multiple-scattering beam growth and forward angle bremsstrahlung radiation resulting from the target. The upstream outer blocks cut off the large angle elastic Mott background where the cross section is larger than Møller scattering. The quadrupole optics and a collimator in front of the detector stacks define the acceptance of the polarimeter. Finally, there are two symmetrical electron detector stacks located in the horizontal scattering plane.

3.6.3 Detecting the Møller Coincidence Signal

A detector stack is depicted in Figure 3.38. The first element is a 16–channel scintillation counter hodoscope for measuring the horizontal position of the scattered Møller electrons. The hodoscope data is used to optimize the tuning of the polarimeter by locating the 90° center of mass Møller pairs to the center of the detector acceptance. The hodoscope is followed by a defining aperture before a total absorption lead glass counter to detect electron events. A Møller event is formed by triggering on a timing coincidence between signals from the left and right lead glass detectors. The accidental background is also measured. This is accomplished by forming a coincidence in exactly the same way, but with one of the detector signals delayed outside of the nominal coincidence.

At a pre–scaled rate (sampled rate of the Møller coincidences) of ~100 Hz, hodoscope events, the lead glass signal, and coincidence timing signal are recorded by an ADC and time–to–digital converter (TDC) to provide diagnostic pulse height spec-

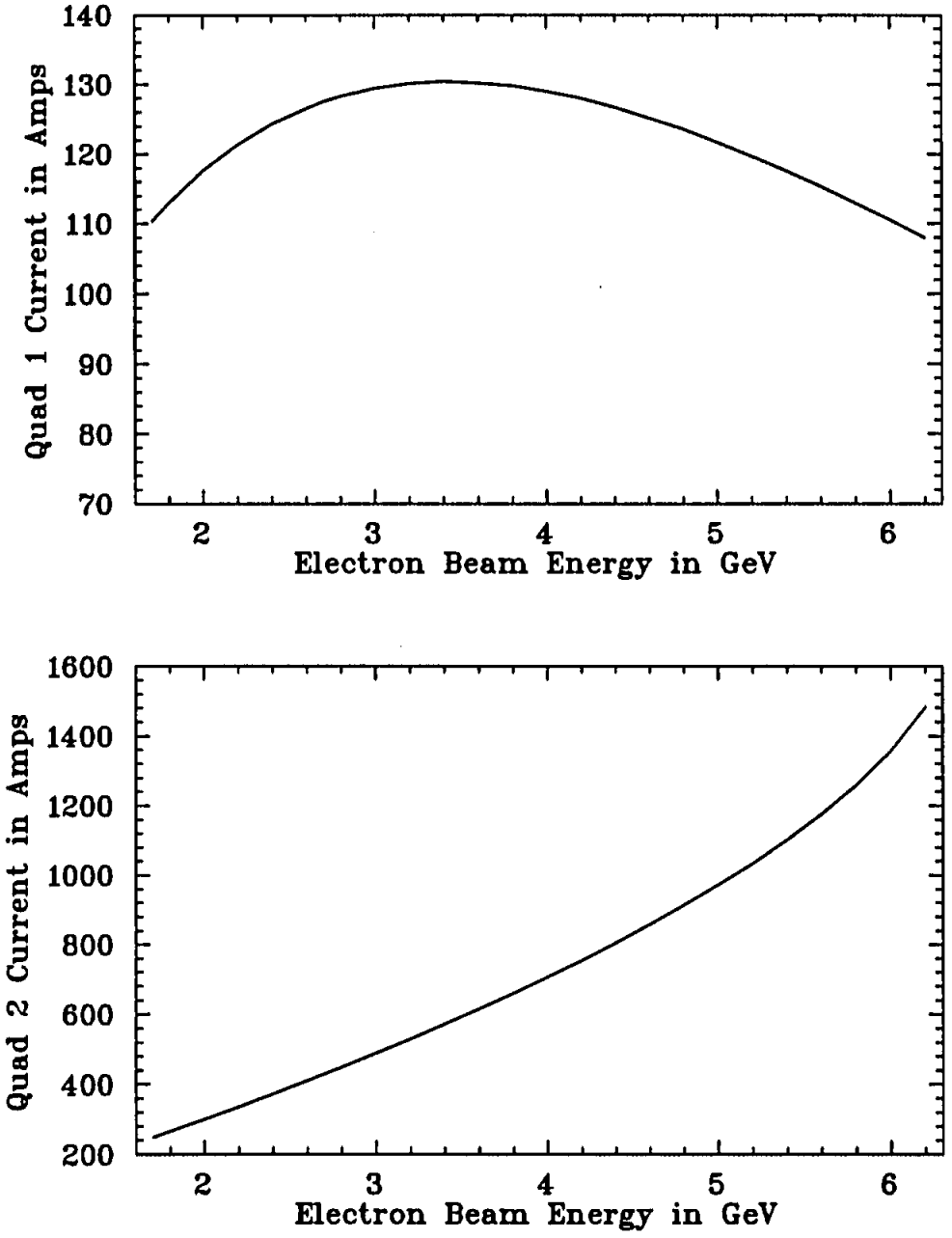

Figure 3.36: Quadrupole magnet setpoints for Q_1 and Q_2 which maintain a constant acceptance for the center-of-mass scattered electrons in the energy range between 2 and 6 GeV. Figure courtesy of B. Zihlmann.

tra. The Møller coincidence event signal, accidental event signal, a signal proportional to the beam current and a 100 MHz clock signal are recorded in two banks of scalers. Each bank is gated with the helicity of the beam in a mutually exclusive way. The

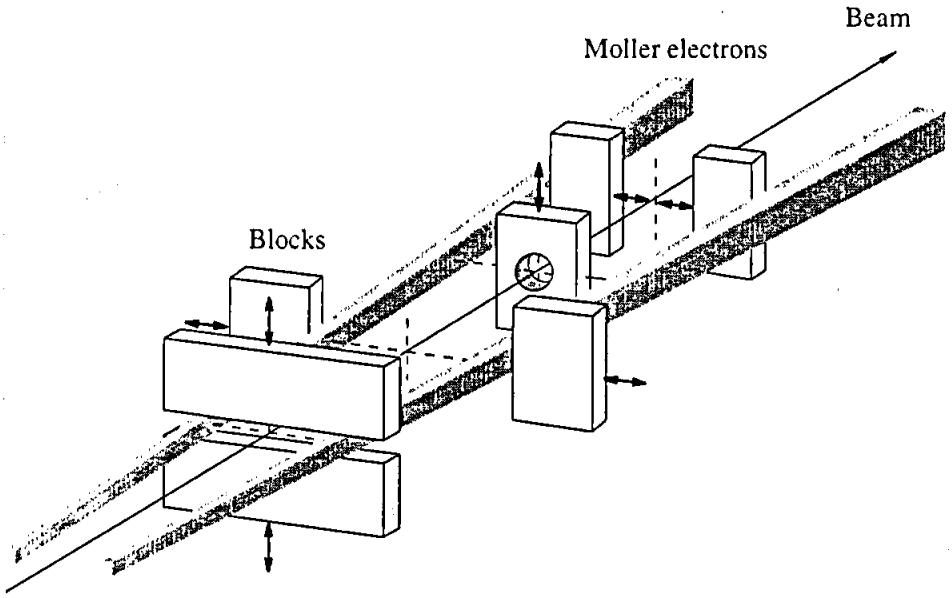

Figure 3.37: The collimator is a set of seven tungsten–alloy blocks which are mounted on linear actuators. The central block is bored to allow the non–interacting beam to pass to a beam dump. The others are paired symmetrically as shown. Figure courtesy of B. Zihlmann.

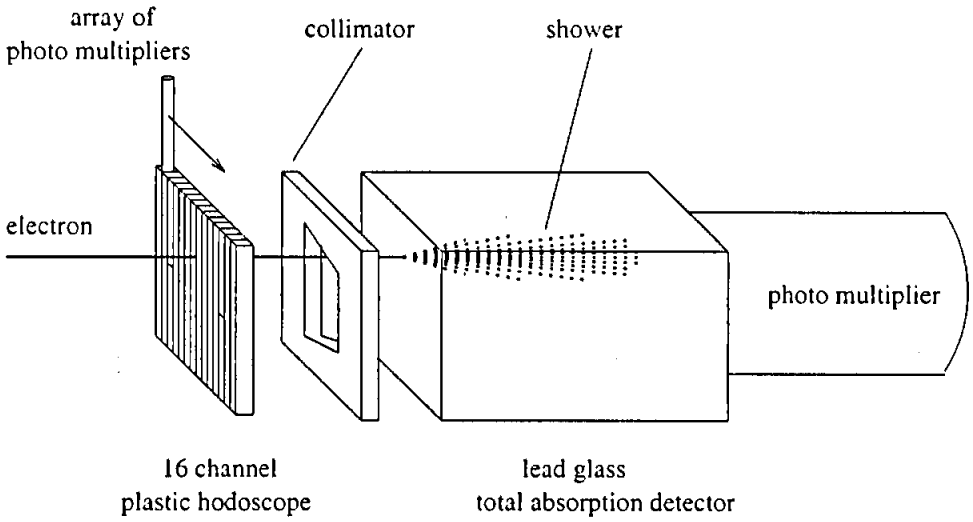

Figure 3.38: One of the two Møller detectors stacks showing the horizontal position sensitive hodoscopes, collimator, lead glass detector, and PMT. Figure courtesy of B. Zihlmann.

experimental asymmetry, ϵ_{exp}, is determined from the scaler data. A schematic of the data acquisition electronics is shown in Figure 3.39. For the experiment conditions

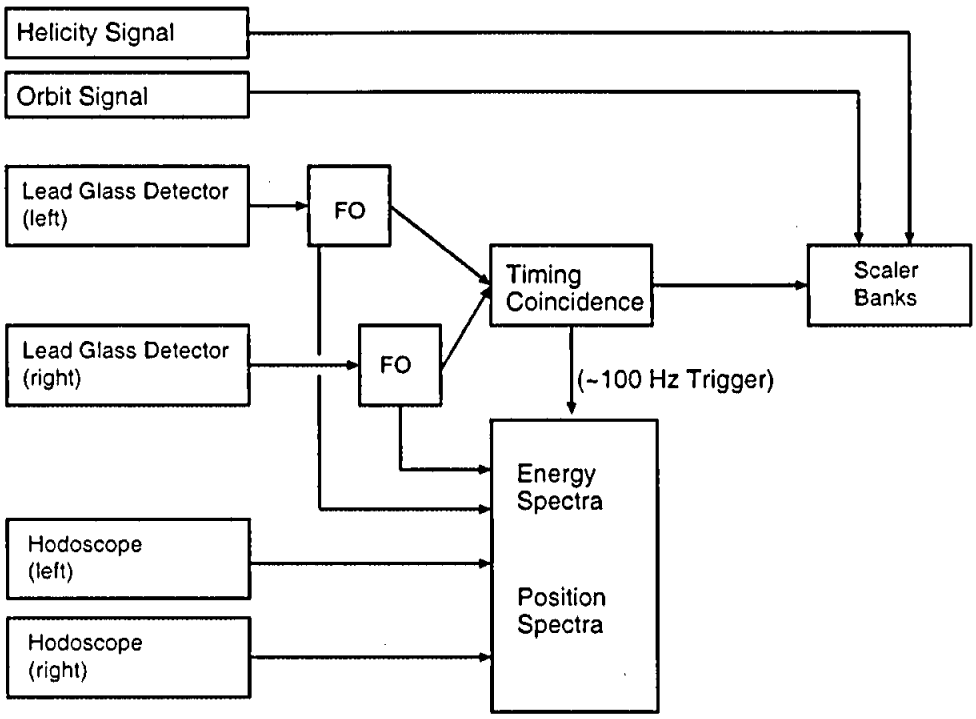

Figure 3.39: Møller polarimeter electronics diagram.

($E_{Moller} \approx 3.4\,\mathrm{GeV}$, $i_{beam} \leq 3.5\,\mu\mathrm{A}$, target thickness $= 4\,\mu\mathrm{m}$) the Møller coincidence rate was $\approx 30\,\mathrm{kHz}$. A statistical uncertainty of $\approx 6 \times 10^{-5}$ is acquired in a 2 hour measurement of the beam polarization.

3.6.4 Interpreting the Polarimeter Results

The first check of the polarimeter is that the quadrupole spectrometer is optimized. A good hodoscope hit distribution is shown in Figure 3.40. The figure shows the hit pattern of the left hodoscope versus right hodoscope channels for coincidences. In this case, the events are centered about $\overline{\theta} = 90^\circ$ and should have a symmetrical angular distribution to the detectors.

The coincidence time–of–flight (TOF) and full energy lead glass pulse height spectra are shown in Figure 3.41. The TOF shows good accidental rejection with a signal to background of 1000:1. The energy spectrum (cut on coincidences) shows a clean energy distribution in the center–of–mass scattering. These diagnostics are used to

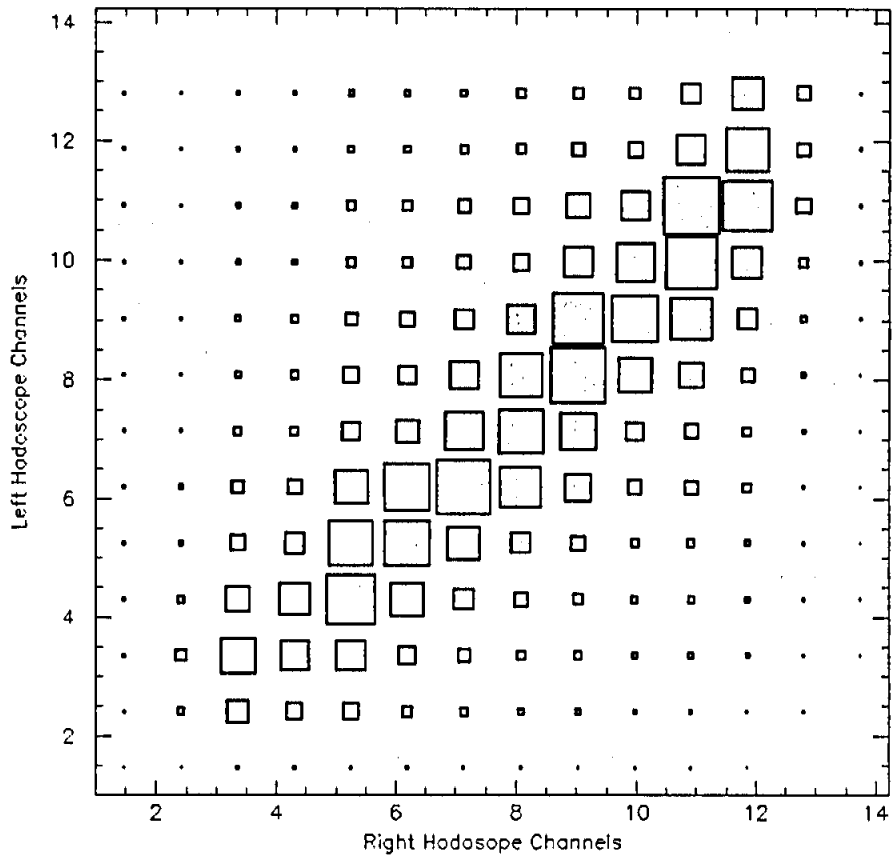

Figure 3.40: Left hodoscope events plotted against right hodoscope events for good optics setup for polarimeter. The size of the squares is proportional to the number of coincidence events recorded at the hodoscope elements indicated. Figure courtesy of B. Zihlmann.

prepare the polarimeter for operation. Once the polarimeter tuning was accomplished the measurement of the beam polarization commenced.

Recall from Equation 3.43 that the measured beam polarization is determined from

$$P_z^B = \frac{1}{\overline{A_{zz}} P_z^T} \cdot \epsilon_{exp}. \tag{3.44}$$

The uncertainty in the polarization is given by

$$\frac{\delta P_z^B}{P_z^B} = \sqrt{\left(\frac{\delta\epsilon}{\epsilon}\right)^2_{stat} + \left(\frac{\delta\overline{A_{zz}}}{\overline{A_{zz}}}\right)^2_{syst} + \left(\frac{\delta P_z^T}{P_z^T}\right)^2_{syst}}. \tag{3.45}$$

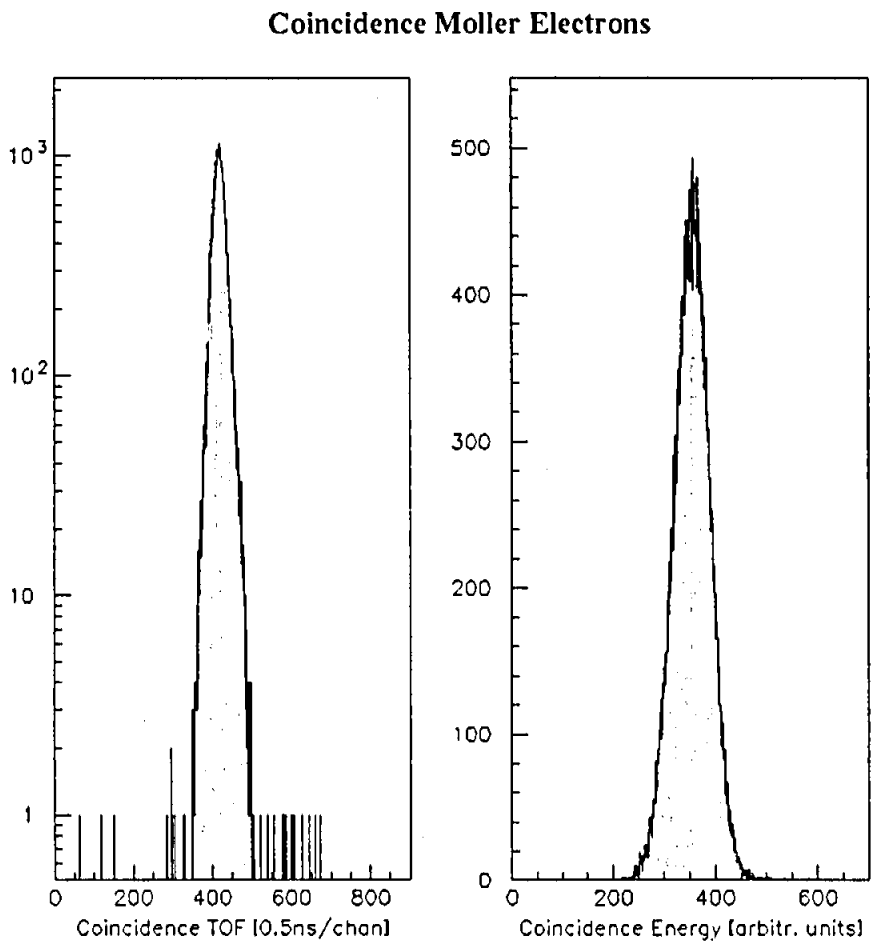

Figure 3.41: Time–of–flight energy pulse height energy spectra for Hall C Møller polarimeter. The ordinate in both plots is the number of recorded Møller events. Figure courtesy of B. Zihlmann.

An absolute measurement of the beam polarization requires good absolute knowledge of both $\overline{A_{zz}}$ and P_z^T. This experiment measures a relative difference in the beam polarization. Therefore, a good measurement of the beam polarization is useful. However, absolute knowledge of the analyzing power and the target polarization is less important. It is necessary, however, that the analyzing power and target polarization do not depend upon the beam orbit. The level to which this is true is discussed further in Chapter 4.

3.7 Accelerator Operation

Feedback systems are typically used when sending beam through the accelerator to maintain beam parameters stable within limits. Feedback systems were used during the experiment to maintain beam delivery and reduce systematic beam orbit and energy related noise. These are described in Section 3.7.1. The extraction of the beam to the Hall C polarimeter is described in Section 3.7.2.

3.7.1 Orbit, Energy, and Master Oscillator Feedback

Orbit locks are a system for maintaining a consistent orbit through the recirculation arcs [Pa99]. When the accelerator is first setup the beam is launched into each recirculation arc with conditions that best match the reference orbit ($x = y = x' = y' = 0$). The recirculation arc optics are then tuned for good transmission to the next linac. Once the orbit locks are running a pair of correction magnets in each transverse direction (spaced $\approx 90°$ apart in betatron phase) are modulated to maintain the orbit. The feedback time for this process is about 5 seconds.

Energy locks are a system for maintaining the absolute energy setup of the accelerator. When the accelerator is first setup the recirculation arc optics are set specifically for an operating energy and a dispersion pattern. A dispersion pattern means the set of beam position readings which depend upon the energy of the beam. When these locks are running groups of beam position monitors sample and compare the orbit with a model of the accelerator. If the absolute energy begins to differ from nominal the dispersion pattern will change in all arcs. The gradients of RF acceleration cavities in the end of each linac are then adjusted to restore the dispersion pattern as determined by the model. The feedback time for this process is about 5 seconds.

The Master Oscillator Modulation Feedback [Ti99] is a system for maintaining the beam bunches on the crest of the linac RF. This feedback system is fast and modulates the phase of all of the RF cavities in the north (south) linac by 0.07 °(0.05 °) at a rate of 383 Hz (397 Hz). The amplitude of this modulation is measured in a high dispersion

region of the subsequent spreader magnet system with a beam position monitor. The system has a resolution adequate enough to measure the RF phase difference between the crest of the accelerating field and the beam bunches (0.3°). The system can then adjust and maintain the overall RF accelerating phase of the linac.

3.7.2 Beam Separation to Experimental Halls

This experiment involved extracting the perturbed beam to the Hall C transport arc after four complete recirculations of the accelerator . Concurrent with this experiment another was performed in the Hall B experimental area using a beam of only three recirculations of the accelerator. The Hall A experimental area was unused for this period. To accomplish this configuration only two of the three 1497 MHz electron bunches were produced at the electron gun (by two of the three lasers). Following three complete recirculations of the accelerator, one of those two electron bunches was deflected out of the accelerator by an RF separator operating at the third subharmonic of the accelerator (499 MHz) to Hall B. The remaining electron bunch, spaced by 499 MHz in the accelerator, continued for a fourth full recirculation to transit the orbit perturbation in arc 7. Since all of the remaining beam in the accelerator at this point was destined for Hall C, the extraction of the beam was accomplished with a DC magnet, rather than by RF separation. For measurement of the beam energy the transport arc optics for Hall C were set to a dispersive mode.

3.8 Beam Controls and Data Acquisition

The beam controls and accelerator data acquisition is managed by the Orbit Run Control (ORC) program written in Tcl/Tix [Ou90] explicitly for this experiment. The ORC communicates to the high level Experimental Physics and Industrial Control (EPICS) [LANL] accelerator controls through the common device interface *cdev* [Cd99]. The ORC controls the beam orbit modulation in arc 7, the laser power level (beam current), data acquisition of accelerator parameters, and provides (through a hard-

ware interface) real-time orbit signals for the polarimeter data acquisition system.

After setting the spin rotators and determining the magnet setpoints for an orbit perturbation, the ORC handles the run control. This run sequence is described in Section 3.8.1. The timing diagram for the controls of the beam helicity, beam orbit, and polarimeter data acquisition is given in Section 3.8.2.

The ORC logs accelerator data to disk using the program *ezlog* [La]. Depending upon the conditions, between 1000 and 4000 accelerator parameters are recorded at rates between 0.2 Hz and 5 Hz. Log files are compressed and saved for off-line analysis.

3.8.1 Sequence of Run

Each measurement is performed in the same sequence. Refer to Figure 3.42 for the communications diagrams of the sub-systems used in the experiment. First, the Wien

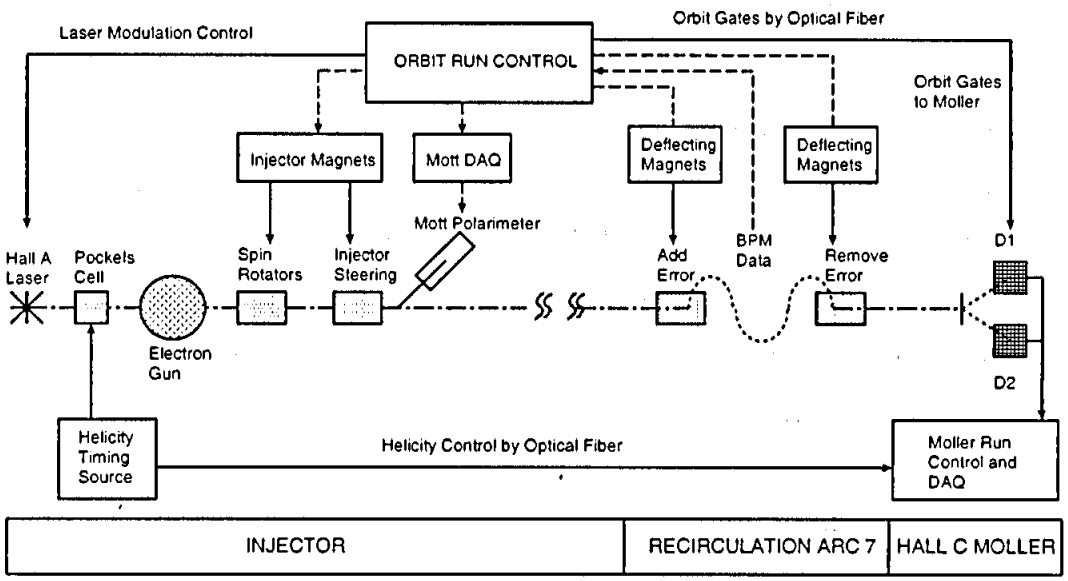

Figure 3.42: Schematic showing software (dotted line) and hardware (solid line) control flow between subsystems of the experiment.

filter and solenoid spin rotator setpoints are adjusted for the specific run conditions. The beam is then steered to minimize transmission loss through the injector and finally sent to the Mott polarimeter to verify the polarization orientation. Next the

beam is transported through the machine to the Møller polarimeter. With the beam in a tune-up mode the magnet setpoints for the two beam orbits to be studied are determined. The high duty factor (CW) beam is restored and the orbit flipping sequence is started to verify good transmission for each of the two orbits. Once checked the ORC program and orbit reversal are started. The polarimeter data acquisition is initiated. Polarimeter runs are typically 20 min in duration and are run successively until adequate statistics are gathered. On-line analysis verifies the quality of the polarimeter data.

3.8.2 Helicity and Orbit Reversal

A timing diagram of the helicity and orbit reversal, and beam and polarimeter gating is shown in Figure 3.43. The beam orbit is changed every 120 seconds. To reverse the

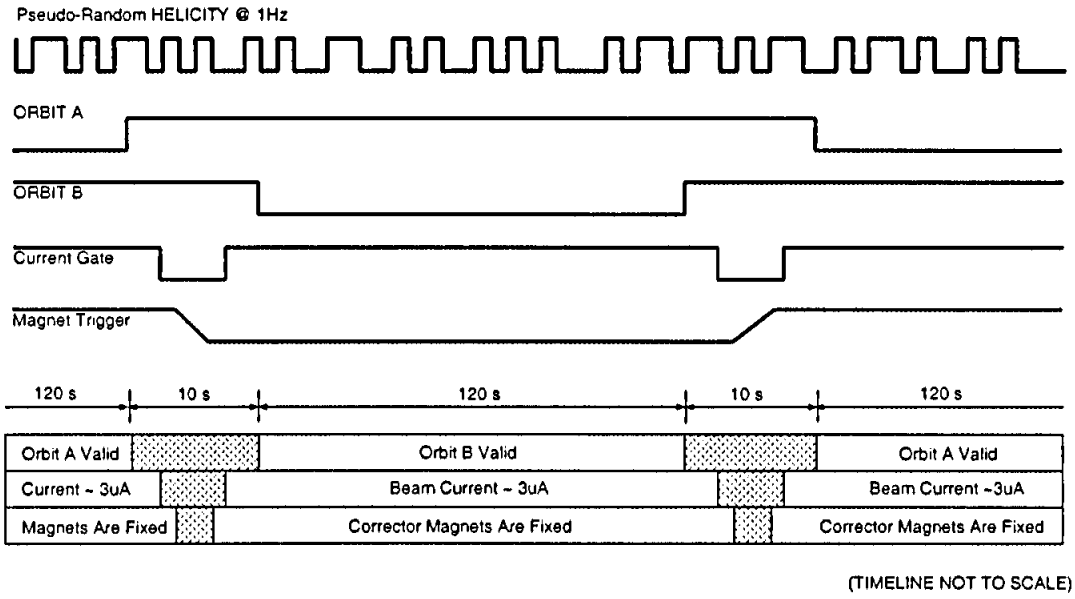

Figure 3.43: Timing scheme shows the beam helicity, orbit, and deflection magnet signals. The hatched areas in the lower part of the figure indicate when the orbit is invalid, the beam current is reduced, or the magnet currents are changing.

beam orbit the ORC first gates the polarimeter data acquisition (DAQ) off. A delay of 500 ms is followed by a control signal to ramp the orbit magnets between their present

and target values. The ramping process is done in a quasi–synchronous manner, stepping each magnet by 10% of the difference between present and final setpoints, pausing for $\approx$ 900 ms between increments, until the target setpoints are reached. A second delay of 500 ms is issued by the ORC before restoring the polarimeter measurement gate. The ramping process takes 10 s and the measurement interval lasts 120 s, totaling 130 s for a full orbit reversal. Therefore, the polarimeter DAQ is accumulating events with an efficiency of 92%.

To measure the final beam polarization the helicity of the injected beam polarization is regularly reversed, or flipped. Typically, the beam helicity at the injector is flipped at 30 Hz, or a subharmonic of the 60 Hz line frequency, so that physical beam properties which vary slowly compared with the flipping frequency are averaged between helicity states. Also, 60 Hz variations are prominent, so 30 Hz flipping averages over these effects. Because of the Pockels cell high voltage driver failure the helicity was flipped at 1 Hz (clocked to the 60 Hz line frequency) for this experiment. Systematics associated with flipping the helicity at this frequency do not present a problem for the asymmetries measured in this experiment. The beam helicities are chosen in random patterns of four ($+--+$ or $-++-$) such that the average time of measurement of each helicity state is the same [Be93].

Chapter 4

Data Reduction Techniques and Analysis

The measurement of the beam polarization sensitivity to the beam orbit is performed at the Hall C Møller polarimeter. However, to interpret the results knowledge of the beam polarization, energy, and orbit in recirculation arc 7 are required. Further, knowledge of the beam profile, position, and intensity at the polarimeter target provide a means to study systematics of the polarimeter which may affect the measurements.

Determining the beam polarization in arc 7 relies on a good measurement of the injector polarization, which is discussed in Section 4.1. Measurements of the beam energy performed during and prior to this experiment, necessary for calculating the average linac energy, are discussed in Section 4.2. Systematics associated with extracting the beam polarization orientation and orbit in arc 7, and systematics of the Møller measurement as a function of beam parameters, are discussed in Section 4.3. Finally, the polarization sensitivity results are presented in Section 4.4 in comparison to simulations using the spin tracking program MURTLE SPIN22.

4.1 Injector Polarization Determination

Knowledge of the beam polarization vector at the injector is necessary to extract three meaningful results for this experiment. First, by comparing the polarization vector measured at the Møller polarimeter with that produced at the injector, the

average linac energy can be extracted to a few parts in 10^3. The average linac energy is used for spin tracking simulations. Second, the sensitivity of the beam polarization to vertical betatron oscillations in the recirculation arc is predicted to scale linearly with the vertical component of the beam polarization, $\sim \sin(\theta)\sin(\phi)$. This results because the interaction is expected to scale according to the factor $P_y \times B_x$, where P_y is the horizontal component of the beam polarization and B_x is the horizontal component of the quadrupole magnetic field (vertically focusing). Accurate knowledge of the injector polarization vector is necessary to determine the angular dependence of this effect. Finally, sign discrepancies are a classic source of error in polarization experiments so verifying the sign of the beam polarization is important.

The spatial orientation (axis) and helicity (sign) of the beam polarization vector is set at the injector. The calibration of the electron beam helicity to the control electronics, which sets the Pockels cell optical helicity, is described in Section 4.1.1. The beam polarization orientations for the experiment are calculated using the calibration data and magnet current readbacks for the injector spin rotators. A comparison of the beam polarization as measured by the Mott polarimeter with the spin rotator settings is made in Section 4.1.2.

4.1.1 Determining the Beam Helicity

The correlation between the electron beam helicity and the electronics which trigger the Pockels cell high voltage was determined at the start of the experiment. This was accomplished by comparing the Mott scattering asymmetry between two symmetrical detectors. The measurement is done for a known Wien filter spin rotator setpoint. The difference in the detector rates, uniquely determined by the kinematics of the scattering and polarimeter design, determine the beam helicity. The polarized beam and the Mott polarimeter configuration is shown in Figure 4.1 for the case $\theta_{Wien} = +90°$. At the beginning of the experiment it was not known whether the sign convention for the helicity control electronics resulted in a positive or negative helicity

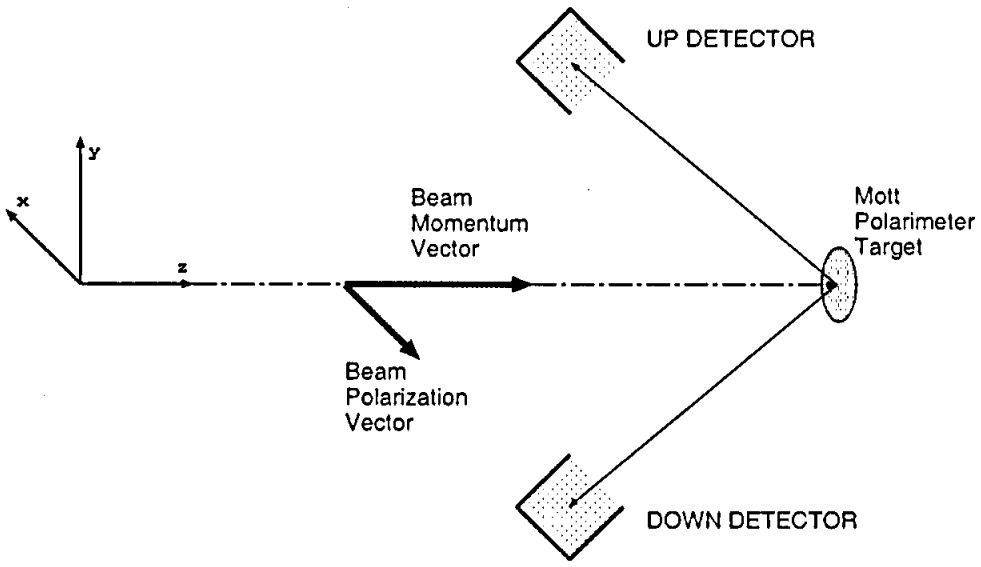

Figure 4.1: Schematic for the Mott scattering geometry and location of the *up* and *down* detectors used to determine the beam helicity.

electron beam from the gun. To determine the convention we make the assumption that the helicity of the beam is positive for one of the two states of the control electronics ($\vec{P}_{Gun} = +P_0\hat{z}$). In this case, $\vec{P}_{Mott} \cdot \hat{x} < 0$ and the Mott elastic rate in the *up* detector is expected to be less than that in the *down* detector ($\sigma_{up} < \sigma_{down}$). If the assumption in the convention was wrong, the inequality in the detector rates would be reversed. The measurement was performed. Consequently, the helicity convention was used to extract the sign of the polarization from the polarimeter data. Neither the helicity generation electronics (logical trigger, Pockels cell, high voltage driver electronics) nor the helicity signal communications (fiber optic or electrical cabling), were modified during the course of the experiment.

4.1.2 Determining the Beam Polarization

Performing this experiment requires setting the beam polarization orientation for the accelerator. A measurement of the beam polarization in the injector is useful, because in all cases the polarization at the injector, recirculation arc 7, and Møller polarimeter are related. The rotations of the spin manipulation system are calculated from

the spin rotator calibration data and current readbacks. Recall the convention of the coordinate system for describing the beam polarization orientation in Figure 2.1. For each measurement (data set) two perturbed orbits with a common polarization orientation (prior to arc 7) were studied. That orientation is therefore based on the injector orientation. The desired orientations at recirculation arc 7 and the corresponding injector spin rotator setpoints used to accomplish them for the 18 data sets are shown in Table 4.1.

After preparing the spin rotators for a specific injector orientation, the beam polarization was measured at the Mott polarimeter. Using the spin rotator setpoints, the polarization orientation expected at the polarimeter can be computed. The injector magnets and spin rotators which precess the reference orbit polarization are shown in Figure 4.2. The transport of the beam polarization to the Mott polarimeter

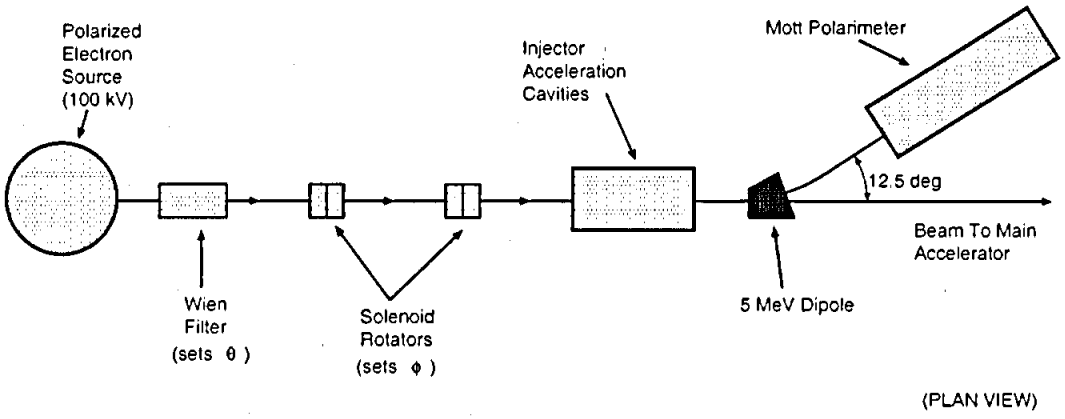

Figure 4.2: A schematic indicating the spin rotation components in the CEBAF injector between the polarized gun (producing a longitudinally polarized beam) and either the Mott polarimeter or the accelerator proper.

can be written as the product of the individual polarization rotation matrices for the 90° dipole bend beneath the polarized gun, the Wien filter, the two solenoid rotators S1 and S2, and the 12.5° dipole bend to the Mott polarimeter beamline. The spin rotation due to each dipole magnet, Ψ, is given by $\frac{g-2}{2}\gamma\theta_{bend}$, where g is the electron gyromagnetic factor, $\gamma = \frac{E}{mc^2}$ is the total energy divided by the electron rest mass, and θ_{bend} is the dipole bend angle. Consequently, the polarization at the Mott

DATA SET	Desired Arc 7 Orientation	θ_{Wien} (deg)	ϕ_{S1} (deg)	ϕ_{S2} (deg)
#1	[-147,+000]	$+31.28 \pm 0.30$	$+1.43 \pm 0.19$	$+0.97 \pm 0.19$
#2	[+090,+090]0:0	-87.56 ± 0.63	$+50.07 \pm 0.44$	$+37.87 \pm 0.30$
#3	[+090,+090]M:M	-87.56 ± 0.63	$+50.06 \pm 0.44$	$+37.88 \pm 0.30$
#4	[+090,+090]$\frac{M}{2}$:$\frac{M}{2}$	-87.56 ± 0.63	$+50.06 \pm 0.44$	$+37.88 \pm 0.30$
#5	[+090,+180]M:M	-27.53 ± 0.29	$+1.42 \pm 0.19$	$+0.97 \pm 0.19$
#6	[+090,+135]M:M	-50.58 ± 0.41	$+50.06 \pm 0.44$	$+16.02 \pm 0.21$
#7	[+090,+225]M:M	-50.58 ± 0.41	-47.16 ± 0.44	-14.11 ± 0.21
#8	[+090,+090]M:M	-89.39 ± 0.64	$+50.06 \pm 0.44$	$+37.87 \pm 0.30$
#9	[+045,+090]M:M	-109.30 ± 0.76	$+50.06 \pm 0.44$	$+0.97 \pm 0.19$
#10	[+135,+180]M:M	$+17.60 \pm 0.25$	$+1.43 \pm 0.19$	$+0.97 \pm 0.19$
#11	[+045,+180]M:M	-72.74 ± 0.54	$+1.43 \pm 0.19$	$+0.97 \pm 0.19$
#12	[+045,+270]M:M	-109.26 ± 0.76	-47.16 ± 0.44	$+0.98 \pm 0.19$
#13	[+090,+090]M:M	-89.39 ± 0.64	$+50.06 \pm 0.44$	$+37.88 \pm 0.30$
#14	[+090,+090]M:0	-89.39 ± 0.64	$+50.06 \pm 0.44$	$+37.88 \pm 0.30$
#15	[+090,+090]0:M	-89.39 ± 0.64	$+50.06 \pm 0.44$	$+37.88 \pm 0.30$
#16	[+090,+090]$\frac{M}{2}$:$\frac{M}{2}$	-89.39 ± 0.64	$+50.06 \pm 0.44$	$+37.88 \pm 0.30$
#17	[+090,+090]0:0	-89.39 ± 0.64	$+50.06 \pm 0.44$	$+37.88 \pm 0.30$
#18	[+135,+180]M:M	$+17.60 \pm 0.25$	$+1.44 \pm 0.19$	$+0.98 \pm 0.19$

Table 4.1: Spin manipulator setpoints for the experiment. The desired orientation is denoted by the prefix [θ,ϕ]A:B. (θ,ϕ) are the necessary spin rotator setpoints and A:B determine whether orbit A or B is M (maximum), M/2 (half-maximum), or 0 (reference orbit).

polarimeter, $\vec{P}_{Mott}$, is related to the polarization at the electron gun, $\vec{P}_{Gun}$, by

$$\vec{P}_{Mott} = R_y(\Psi_{12.5^\circ}) \cdot R_z(\phi_{S1} + \phi_{S2}) \cdot R_y(\theta_{Wien}) \cdot R_x(\Psi_{90^\circ}) \cdot \vec{P}_{Gun}, \qquad (4.1)$$

where $R_i(\theta)$, $i \in x, y, z$, represents a rotation about the i^{th} coordinate axis by an

angle θ.

The beam polarization was verified at the Mott polarimeter following each spin rotator adjustment. Because the polarimeter measures the two transverse components of the beam polarization, the azimuthal rotation angle can be computed directly from the measured experimental asymmetry

$$\phi_{meas} = \arctan\left(\frac{\epsilon_y}{\epsilon_x}\right), \tag{4.2}$$

and then compared with the expected orientation calculated using the spin rotator calibration data

$$\phi_{calc} = \arctan\left(\frac{\vec{P}_{Mott}\cdot\hat{y}}{\vec{P}_{Mott}\cdot\hat{x}}\right). \tag{4.3}$$

A comparison of the two is shown in Figure 4.3, indicating generally good agreement. The uncertainties in the plot result from the uncertainty of the spin rotator setpoint (systematic uncertainty) and the uncertainty of the rotation angle determined from the Mott polarimeter (statistical uncertainty).

4.2 Beam Energy Measurements

The motion of the electron spin in electromagnetic fields depends linearly on the electron energy. The acceleration boosts received by the electrons from the electrostatic field of the electron gun (100 keV), and the injector and linac RF acceleration cavities, determine the beam energy. Consequently, knowledge of the beam energy is required to describe the beam polarization evolution through the accelerator. The average linac energy $\overline{E_{linac}}$ is a useful parameter for this characterization. Extraction of the average linac energy from beam energy measurements is covered in Section 4.2.1.

The measurement of the beam energy using the Hall C transport line as a magnetic spectrometer is described in Section 4.2.2. Alternatively, extraction of the beam energy by measuring the net spin precession in the accelerator is discussed in Section 4.2.3. A series of beam energy measurement techniques, which include spin precession, elastic electron–proton scattering, and magnetic spectrometer measurements

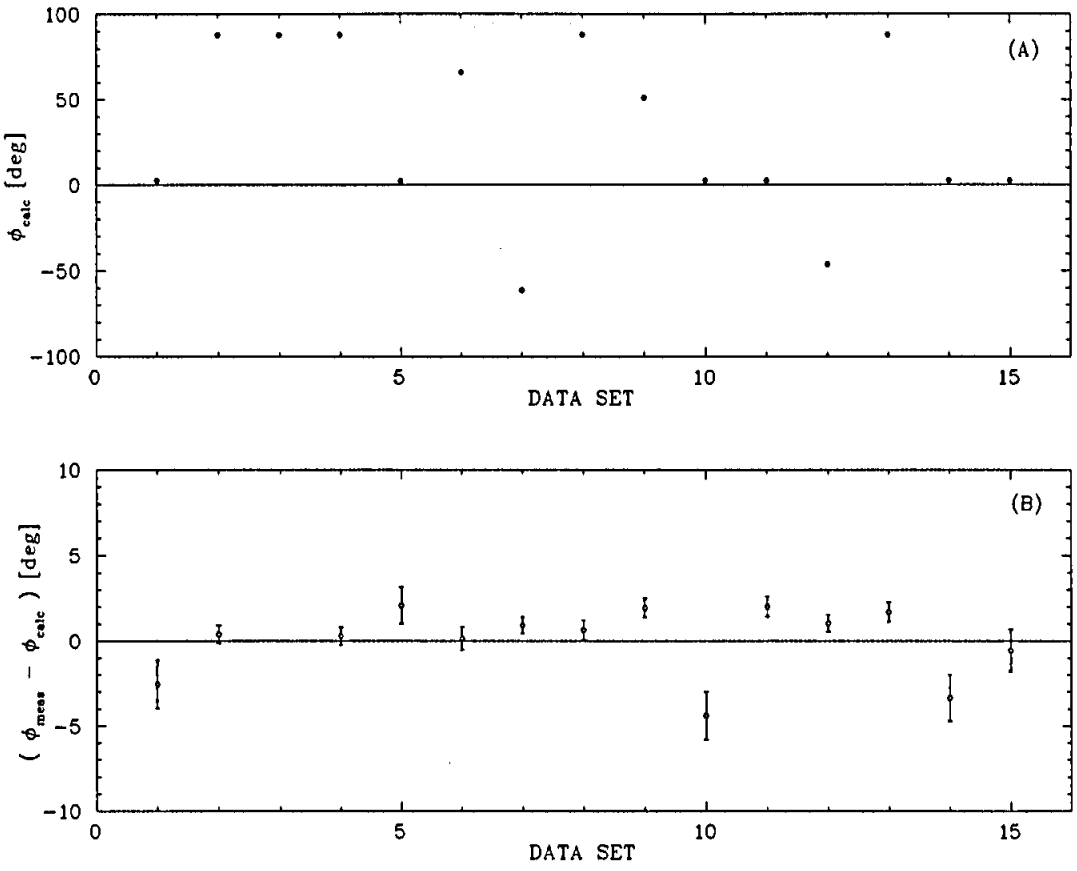

Figure 4.3: The upper plot (A) shows the desired azimuthal orientation expected at the Mott polarimeter for each data set. The lower plot (B) shows the difference between the expected and measured orientation.

are described in Section 4.2.4. Finally, a measurement of the momentum spread of the beam is discussed in Section 4.2.6.

4.2.1 Calculation of Average Linac Energy Gain, $\overline{E_{linac}}$

It is a fair approximation to assume that the North and South linac gains, E_{North} and E_{South}, are equal (at most $\sim 10^{-3}$ different) and that the injector gain, $E_{Injector}$, is scaled to the linac gain for pre–acceleration by a ratio $\alpha = \frac{E_{Injector}}{E_{Linac}} = 0.1125$. This condition is required for matching the momenta of different energy beams during recirculation in the spreader/recombiner geometries. Restating these conditions

$$\overline{E_{Linac}} \;=\; E_{North} = E_{South}$$

$$E_{Injector} = 0.1125 \cdot E_{Linac}, \tag{4.4}$$

the energy for n passes of recirculation, E_{n-Pass}, is

$$\begin{aligned} E_{n-Pass} &= E_{Injector} + n \cdot E_{North} + n \cdot E_{South} \\ &= \alpha \cdot \overline{E_{Linac}} + n \cdot \overline{E_{Linac}} + n \cdot \overline{E_{Linac}} \\ &= (\alpha + 2n)\overline{E_{Linac}}. \end{aligned} \tag{4.5}$$

The average linac energy for a n–pass energy measurement is given as

$$\overline{E_{Linac}} = \frac{E_{Measured}}{(\alpha + 2n)}. \tag{4.6}$$

The error in the extracted linac energy is simply given by

$$\Delta\overline{E_{Linac}} = \frac{\Delta E_{Measured}}{(\alpha + 2n)}. \tag{4.7}$$

4.2.2 Method 1: Hall C Arc Energy Measurement

The transport arc shown in Figure 4.4 is a 41.6 m section of beamline consisting of 8 dipoles, 12 quadrupoles, and 8 pairs of correction magnets (horizontal and vertical) which transport the beam from the accelerator to the experimental end station. The deflection angle of the arc is 34.3 °.

A technique is described [Ya95, Gu99] for measuring the beam momentum p by using the transport arc as a magnetic spectrometer. The beam momentum is determined by

$$p = \frac{e}{\Theta} \int Bdl, \tag{4.8}$$

where $\int Bdl$ is the magnetic field integral over the path of the electron beam and Θ is the bending angle through which the electron beam is deflected. The beam energy is then given by $E = \sqrt{(pc)^2 + (m_e c^2)^2}$; for cases where $\frac{m_e}{p} \ll 1, E \approx pc$.

This energy measurement technique requires de-energizing all of the periodic focusing elements (quadrupoles) in the beamline, thereby leaving the arc in a dispersive mode with only the dipole magnets energized. The 8 dipoles are powered in series

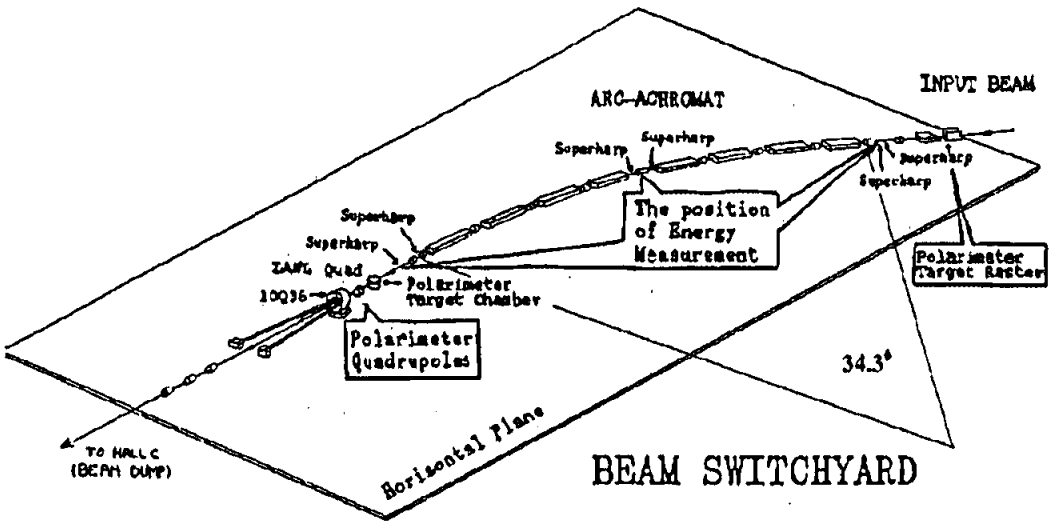

Figure 4.4: Hall C transport arc. Figure courtesy of C. Yan.

by a single calibrated power supply. Each dipole is field-mapped and the correction magnets are set to compensate the effect of the Earth's remnant magnetic field.

By measuring the transverse beam profile at a pair of locations, separated by a suitable distance, the beam centroid and direction can be determined. By performing this measurement at the beginning and end of the transport arc the net deflection angle of the beam is measured. This and the beam profile information provide the the beam momentum (p), energy (E), and momentum spread ($\frac{\Delta p}{p}$). To accomplish this a pair of beam profile diagnostics called *superharps* are located at both the entrance an exit of the arc. Each superharp is a wire scanner capable of measuring the beam intensity profile as a function of position in two orthogonal directions transverse to the beam momentum. The superharp contains a *fork* supporting a $22\,\mu$m diameter tungsten wire that is moved through the beam as shown in the system schematic of Figure 4.5. A secondary electron emission current due to the beam intercepting the tungsten wire is recorded and correlated with the position of the moving wire. In this way the horizontal and vertical beam profiles are measured. The motion of the wire is monitored using an 18–bit absolute shaft encoder with $1.24\,\mu$m resolution. The overall resolution of the superharp provides better than $10\,\mu$m profile and position

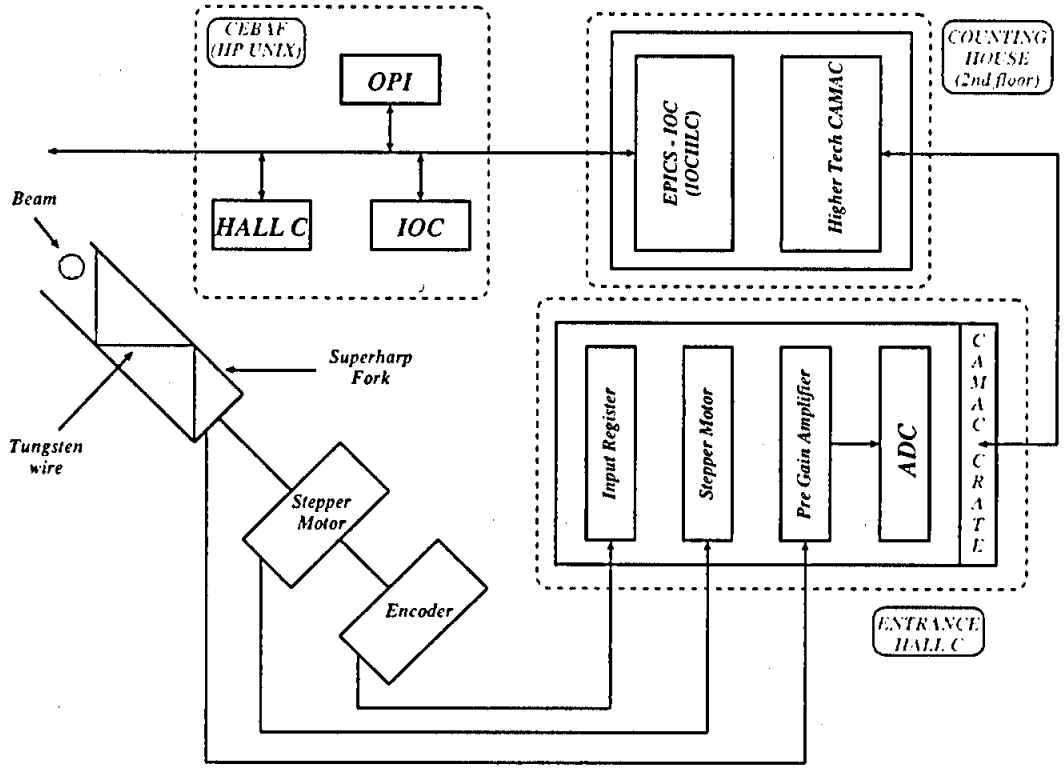

Figure 4.5: Diagram of the superharp beam profile measurement. Figure courtesy of P. Gueye.

resolution. By using the superharps for reference in conjunction with the total field integral for the dipole string used to bend the beam through the arc, absolute beam energy measurements can be performed at the level of 10^{-3}.

This system can be used with continuous (CW) beam currents between $0.1 - 30\,\mu$A. However, because the measurement is destructive to the beam it cannot be performed parasitically. Rather, a dedicated measurement was performed to determine the electron beam momentum. The results for the measurement are listed in Table 4.2. The beam energy and average linac energy are calculated using Equations 4.8 and 4.6.

Date	Beam Momentum MeV/c	Beam Energy MeV	$\overline{E_{Linac}}$ MeV
March 6, 1999	3411.37 ± 0.85	3411.37 ± 0.85	420.51 ± 0.11

Table 4.2: Results of the Hall C arc energy measurement.

4.2.3 Method 2: Spin Precession Technique

As the electron beam propagates through the accelerator the polarization precesses about the magnetic fields it encounters. The net polarization precession from the nine recirculation arcs and transport arcs can be written

$$\begin{aligned}
\Psi &= \sum_{bends} \Psi_i \\
&= \tfrac{g-2}{2m_e} \cdot [(E_I + E_N)\theta_1]_{Arc1} + [(E_I + E_N + E_S)\theta_2]_{Arc2} + \\
&\quad [(E_I + 2E_N + E_S)\theta_1]_{Arc3} + [(E_I + 2E_N + 2E_S)\theta_2]_{Arc4} + \\
&\quad [(E_I + 3E_N + 2E_S)\theta_1]_{Arc5} + [(E_I + 3E_N + 3E_S)\theta_2]_{Arc6} + \\
&\quad [(E_I + 4E_N + 3E_S)\theta_1]_{Arc7} + [(E_I + 4E_N + 4E_S)\theta_2]_{Arc8} + \\
&\quad [(E_I + 5E_N + 4E_S)\theta_1]_{Arc9} + [(E_I + 5E_N + 4E_S)\theta_h]_{Hall}. \qquad (4.9)
\end{aligned}$$

The precession for n passes of the accelerator is more compactly written as

$$\begin{aligned}
\Psi_n &= \tfrac{g-2}{2m_e} \textstyle\sum_n [(E_I + nE_N + (n-1)E_S)\theta_1 + \\
&\quad ((1 - \delta_{1,n})E_I + (n-1)(E_N + E_S))\theta_2 + \\
&\quad (E_I + n(E_N + E_S))\theta_h], \qquad (4.10)
\end{aligned}$$

where $\delta_{1,n}$ is the Kronecker delta. By performing the sum over n passes and making use of Euler's formula, $\sum_{i=1}^{N} i = \frac{N(N+1)}{2}$, the sum can written

$$\begin{aligned}
\Psi_n &= \frac{g-2}{2m_e} \cdot (n\theta_1 + (n-1)\theta_2)\, E_I + \frac{n}{2}\left((n+1)\theta_1 + (n-1)\theta_2\right) E_N \\
&\quad + \frac{n(n-1)}{2}(\theta_1 + \theta_2)E_S + (E_I + n(E_N + E_S)\theta_h)\,. \qquad (4.11)
\end{aligned}$$

By making the transformations

$$\begin{aligned} E &= E_I + n(E_N + E_S) \\ \delta E &= E_N - E_S \\ \theta_t &= n\theta_1 + (n-1)\theta_2 + \theta_h \\ \delta\theta &= \theta_1 - \theta_2, \end{aligned} \tag{4.12}$$

the total precession between the injector and an experimental hall is written in terms of quantities which are sensible for describing the accelerator configuration. For example, it is useful to speak of the beam energy, E, the imbalance in the linac energies, δE, or the difference in the recirculation arc transport bend angle, $\delta\theta$. Finally, the total polarization precession through the accelerator from the injector to an experimental hall is written as

$$\Psi_n = \frac{g-2}{2m_e}\left[E_I\left(\frac{\theta_t - \theta_h}{2}\right) + E\left(\frac{\theta_t + \theta_h}{2}\right) + \frac{n\delta E}{2(2n-1)}\left(\theta_t - \theta_h + (n-1)\delta\theta\right)\right]. \tag{4.13}$$

The beam energy can then be extracted from measuring the total precession of the polarization in the accelerator

$$E = \frac{\frac{4m_e\Psi}{g-2} - E_I(\theta_t - \theta_h) - \frac{n\delta E}{2(2n-1)}[\theta_t - \theta_h + (n-1)\delta\theta]}{\theta_t - \theta_h}. \tag{4.14}$$

The uncertainty in this measurement includes the uncertainty in the accelerator parameters. The error terms from the beam energy measurement are determined by taking appropriate derivatives

$$\begin{aligned} \frac{dE}{d\Psi} &= \frac{4m_e}{g-2}\cdot\left(\frac{1}{\theta_t + \theta_h}\right) \\ \frac{dE}{dE_I} &= -\frac{\theta_t - \theta_h}{\theta_t + \theta_h} \\ \frac{dE}{d(\delta\theta)} &= -\frac{n(n-1)\delta E}{2n-1}\cdot\left(\frac{1}{\theta_t + \theta_h}\right) \\ \frac{dE}{d\theta_t} &= [-E - E_I - \frac{n\delta E}{2n-1}]\cdot\left(\frac{1}{\theta_t + \theta_h}\right) \\ \frac{dE}{d\theta_h} &= [-E - E_I - \frac{n\delta E}{2n-1}]\cdot\left(\frac{1}{\theta_t + \theta_h}\right) \end{aligned}$$

$$\frac{dE}{d(\delta E)} = -\frac{n}{2n-1}[\theta_t - \theta_h + (n-1)\delta\theta] \cdot \left(\frac{1}{\theta_t + \theta_h}\right). \quad (4.15)$$

This experiment used a fourth pass ($n = 4$) to the Hall C Møller polarimeter. The precession of the beam polarization in the accelerator is determined by comparing the measured polarization at the injector Mott and Hall C Møller polarimeters. This Møller polarimeter is only sensitive to the $\hat{z}$ component of the beam polarization. As the polarization is rotated to different orientations in the injector, θ_{inj}, the orientation of the polarization will rotate at the experimental hall by the same amount. The polarimeter then measures an experimental asymmetry which is proportional to $R_y(\Psi_n) \cdot \vec{P}_{injector} \cdot \hat{z}$, which varies as $\cos(\theta_{injector} + \Psi_n)$.

Although the measurable component of the polarization is in the accelerator bend plane, 4 of the 7 data sets used to extract the precession are oriented out of the bend plane. Consequently, to extract the precession the following method is used:

1. Calculate the orientation of the polarization vector, $\vec{P}(\theta, \phi)$, at the injector using the spin rotator setpoints. Next, calculate the projection of the beam polarization into the bend plane to determine the corrected injector angle, θ_{cor}. The spin rotator setpoints and the corrected injector angle, θ_{cor}, are given in Table 4.3.

2. Compute the experimental asymmetry for the Møller runs for these data sets. Because the polarimeter is only sensitive to the $\hat{z}$ component of the beam polarization, the measured experimental asymmetries must also be corrected to determine the bend plane phase angle. This is accomplished by dividing each of the experimental asymmetries by the calculated opening angle between the $\hat{y}$-axis and the beam polarization (as determined at the injector) to produce the corrected experimental asymmetries.

3. The experimental Møller asymmetries are plotted as a function of the corrected injector phase, θ_{cor}, and the data is fit using $P_0 \cos(\theta_{cor} + \Psi_n)$. This fit was performed and the data and resultant curve are shown in Figure 4.6. The total

Data Set	θ_{Wien} (deg)	ϕ_{S1+S2} (deg)	θ_{cor} (deg)
# 5	$-27.53 \pm .29$	$2.39 \pm .27$	$1.10 \pm .01$
# 6	$-50.58 \pm .41$	$66.08 \pm .49$	$44.92 \pm .46$
# 7	$-50.58 \pm .41$	$-61.27 \pm .49$	$-42.64 \pm .32$
# 9	$-109.30 \pm .76$	$51.03 \pm .45$	$47.20 \pm .32$
# 10	$17.60 \pm .25$	$2.40 \pm .27$	$0.72 \pm .01$
# 11	$-72.74 \pm .54$	$2.40 \pm .27$	$2.29 \pm .01$
# 12	$-109.26 \pm .76$	$-46.18 \pm .48$	$-42.93 \pm .37$

Table 4.3: Spin rotator settings and corrected polarization phase for the component of the beam polarization in the accelerator bend plane.

precession was determined from the fit to be $\Psi_4 = 329.2° \pm 3.3°_{fit} \pm 1.0°_{sys}$.

The measured phase and error estimates listed in Table 4.4 are combined to determine the beam energy at the Møller polarimeter. The beam energy determined by this

Description	Quantity	Value	Error
Number of Passes	n	4	0
Precession Angle	Ψ	4649.20°	3.3°
Wien Filter Angle	θ_{Wien}	$-110° < \theta < +110°$	$< 1.0°$
Injector Energy	E_{Inj}	47.25 MeV	2.36 MeV
Linac Imbalance	δE	≤ 0.5 MeV	–
Arc Bend Angle	θ_{arc}	180.00°	0.01°
Hall Bend Angle	θ_{hall}	−37.52°	0.01°

Table 4.4: Estimates of error in accelerator parameters for determining the beam energy from the total polarization precession between the injector and Hall C at $n = 4$ passes.

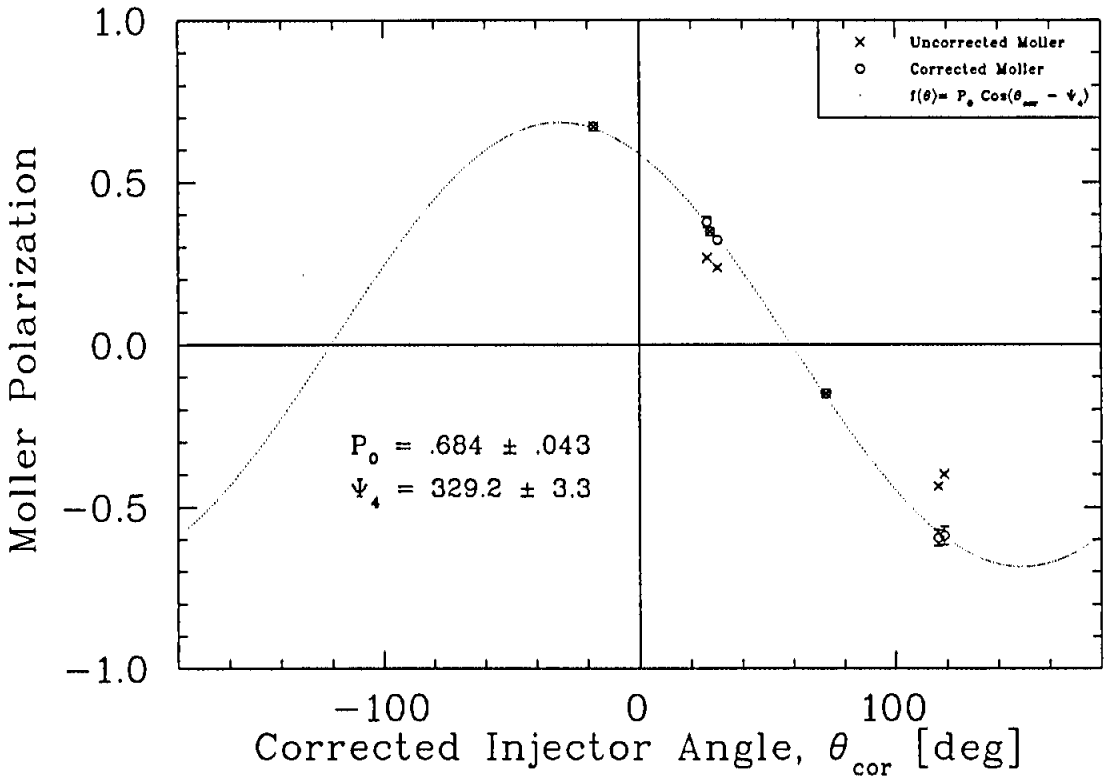

Figure 4.6: Uncorrected and corrected polarization as measured by the Hall C Møller polarimeter.

method is $E_{n=4} = (3407.23 \pm 4.08)$ MeV. The uncertainty in the measurement is due to the fit uncertainty of the total accelerator precession and uncertainties indicated in Table 4.4 and computed using Equations 4.15. The average linac energy is then computed to be $\overline{E_{linac}} = (420.00 \pm 0.50)$ MeV.

4.2.4 Method 3: The "Energy Festival"

During the 2 days prior to this experiment a series of measurements, known as the *energy festival*, were performed to determine the final beam energy in the three experimental halls. A complete discussion is given elsewhere [Mi99]. However, it is useful to report the results for comparison. The beam energy was measured by three distinct techniques. All techniques combined yield an average linac energy of 420.19 ± 0.39 MeV. A brief description for each of the measurement techniques of the

beam energy is given:

1. *Injector and End Station Spin Precession.* The precession of the beam polarization is measured between polarimeters at different passes using the technique described above.

2. *Hall A Arc and Hall C Arc Energy Measurement.* The Hall A and Hall C experimental areas are located at the end of transport arc of definite bend angle from the accelerator switchyard. With accurate knowledge of the total the bending dipole field in the transport arc and the beam trajectory, the beam momentum is measured.

3. *Hall A Electron–Proton Scattering.* This method determines the beam energy by measuring the opening angle kinematics between a scattered electron and a recoil proton. This measurement system is a part of standard Hall A hardware. The detector is designed to measure the scattering in two locations symmetrically located with respect to the beamline. By averaging the two results, extraction of the beam momentum (and beam energy) is independent of the beam trajectory to first order.

A summary plot for the energy festival is given in Figure 4.7. All of the results listed are extrapolated from spin precession calculations based on polarimetry at the injector and experimental halls except for the three cases noted. The energy measurements were performed for two beam delivery configurations, "initial" and "final", between the three halls. The final configuration was used for this experiment.

4.2.5 Average Linac Energy: In Conclusion

A synopsis of the three methods for quoting the beam energy are shown in Table 4.5. The value for all three are in very good agreement. The value used for the remainder of the analysis is the average of the two methods used during the experiment, $\overline{E_{linac}} = (420.26 \pm 0.26)$ MeV.

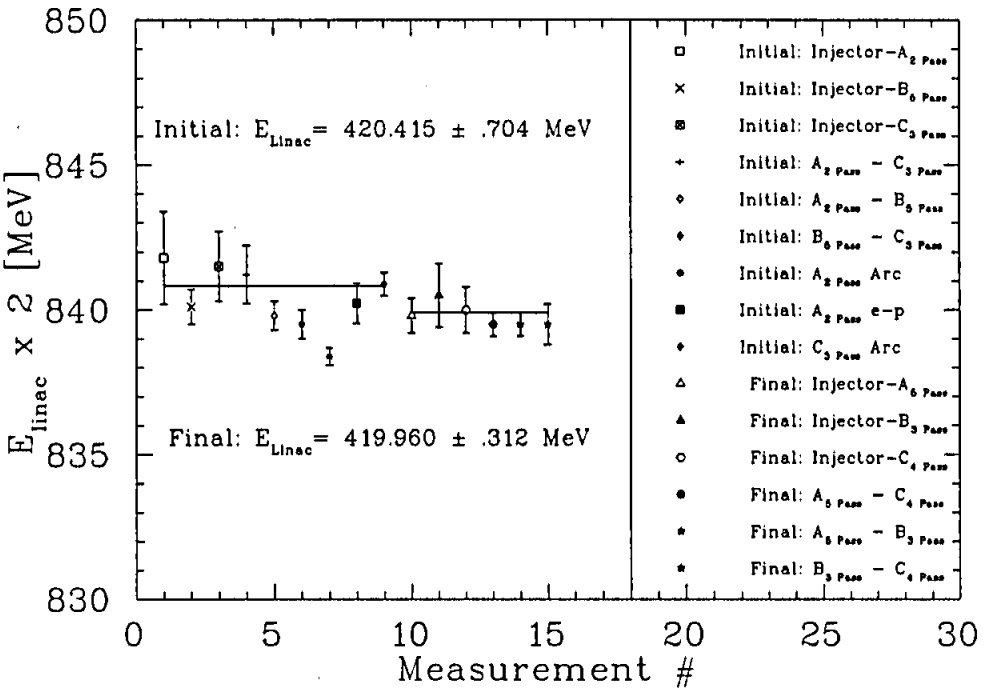

Figure 4.7: Results of the *energy festival* are shown.

Description	$\overline{E_{linac}}$ (MeV)
Hall C Arc Method	(420.51 ± 0.11) MeV
Spin Precession	(420.00 ± 0.50) MeV
Energy Fest (for comparison)	(420.19 ± 0.39) MeV

Table 4.5: Summary of the average linac energy ($\overline{E_{linac}}$) determined during the experiment compared to the *energy festival* result.

4.2.6 Measurement of the Momentum Spread, $\frac{\Delta p}{p}$

To estimate the momentum spread, $\frac{\Delta p}{p}$, beam profile scans were performed with the Hall C beamline in a dispersive mode. The dispersion of a beam is defined as the transverse beam position dependence upon the momentum spread of the beam. The analogy to a prism is identical. The path of a monochromatic energy beam passing through a dispersive magnetic system will be the same for all particles in the beam with the same initial conditions. However, the trajectory of particles within

a beam with a spread in beam energy, or momenta, passing through a dispersive magnetic system will follow different paths. The dispersion in the beamline can be calculated from the optics of the magnetic elements. At the location of the superharp approximately 200 cm upstream of the polarimeter target the dispersion is $\eta_x = 12.5$ meters. Therefore, for example, a point–like beam with a momentum spread of $\frac{\Delta p}{p} = 1 \times 10^{-3}$ at the location of the first superharp would have a transverse width of 12.5 mm at the last superharp in the dispersive mode.

Scans of the horizontal beam profile used for the Hall C arc energy measurement are shown in Figure 4.8. The scanning tungsten wire has a finite thickness (22 μm)

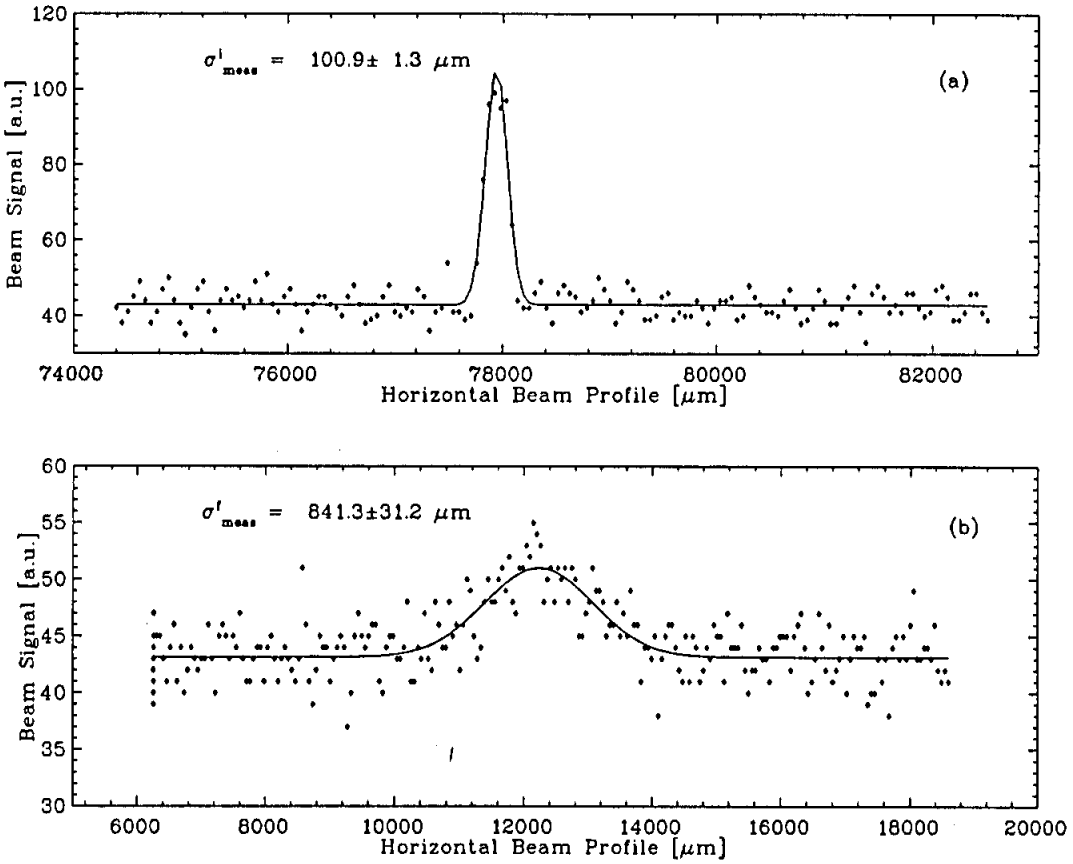

Figure 4.8: Plot (a) shows the horizontal wire scan profile at the first superharp location. Plot (b) shows the effect on the beam profile, for a similar horizontal wire scan profile, for transporting the beam to a location with horizontal magnification $M_x = 3$ and dispersion $\eta_x = 12.5m$.

and because the size of the wire is comparable with the size of the beam in the first

scan the resultant profile is increased. In other words, an infinitesimally thin wire would resolve a narrower beam profile. The measured profile is then the convolution of the true beam profile with that of the wire. If the wire is modeled with having a Gaussian interception profile $\sigma_{wire} = 22\mu m$ then the relationship between the true beam profile σ_{true} and the measured beam profile σ_{meas} is

$$\sigma^2_{meas} = \sigma^2_{true} + \sigma^2_{wire}, \tag{4.16}$$

where the true beam profile $\sigma_{true} = 98.5\mu m$.

The same approach is used to calculate the effect on the beam profile as measured at the final superharp. However, in this case, the final measured beam profile depends upon the convolution of the magnification of the original beam, the dispersion of the transport arc, and the wire thickness,

$$\sigma_{final}{}^2 = (M_x\sigma_{true})^2 + (\eta_x\frac{\Delta p}{p})^2 + \sigma^2_{wire}. \tag{4.17}$$

Using the result from the first superharp scan and from the Hall C transport optics where the magnification $M_x = 3$ and the dispersion $\eta_x = 12.5$ meters, each with a 5% error, the one sigma $\frac{\Delta p}{p} = (1.48 \pm 0.15) \times 10^{-4}$.

Another approach, which validates the assumption that it is acceptable to model the wire with a Gaussian interception profile $\sigma_{wire} = 22\mu m$ is to simply associate a systematic error of 22 μm with each harp profile measurement. A calculation of $\frac{\Delta p}{p}$ proceeds exactly the same except that the σ^2_{wire} term in both Equations 4.16 and 4.17 are omitted. In this case the one sigma result is $\frac{\Delta p}{p} = (1.47 \pm 0.14) \times 10^{-4}$.

4.3 Systematic Effects in Measuring the Beam Polarization Sensitivity

Measuring the beam polarization sensitivity depends on how well the beam polarization and orbit can be determined in the accelerator, and the extent to which parameters such as the beam intensity and profile at the Møller polarimeter change during a measurement. A measure of the quality for setting the desired polarization

orientation at arc 7 is given in Section 4.3.1. Section 4.3.2 discusses the beam orbit measurement in the accelerator and the beam position stability at the polarimeter. The effects of the beam quality on the polarimeter systematics are described in Section 4.3.3. Results are presented for both non–rastered and rastered beam profiles at the Møller target in Sections 4.3.4 and 4.3.5, respectively. The effect of the beam quality on the polarimeter analyzing power, A_{zz}, and to the target polarization, P_z^T, are estimated in Section 4.3.6 and Section 4.3.7, respectively. Finally, the uncertainties in these quantities correlated with the beam orbit perturbation are summarized in Section 4.3.8.

4.3.1 Defining Beam Polarization at Recirculation Arc 7

The effect of the beam orbit on the polarization is predicted to depend upon the angular orientation of the polarization in the recirculation arcs. The injector spin rotators define the initial angular orientation of the beam polarization prior to injection into the accelerator. The nominal spin transport model, using the measured average linac energy, $\overline{E_{linac}}$, then determines the angular orientation at the entrance to arc 7. Comparing this orientation with the desired orientation indicates how well the polarization orientation is prepared for the experiment.

To make the comparison, the desired spin vector is denoted by $\vec{s}_7$. The propagated spin vector, based upon the measurements, is denoted by $\vec{s}_p$. A program named LAUNCHV8 was written to calculate and interpret the spin transport results for this experiment. $\vec{s}_p$ is calculated by starting with the injector spin vector for each data set. Then, the injector spin vector is rotated by the nominal spin transport matrices for 3.5 passes of the accelerator using the average linac energy. The comparison is made by determining the inclusive angle, $\theta_{misalign}$, between the desired and propagated spin vectors at arc 7

$$\theta_{misalign} = \frac{\vec{s}_7 \cdot \vec{s}_p}{|\vec{s}_7||\vec{s}_p|}. \tag{4.18}$$

A plot of $\theta_{misalign}$ for the 18 data sets is shown in Figure 4.9. The reasonable agreement

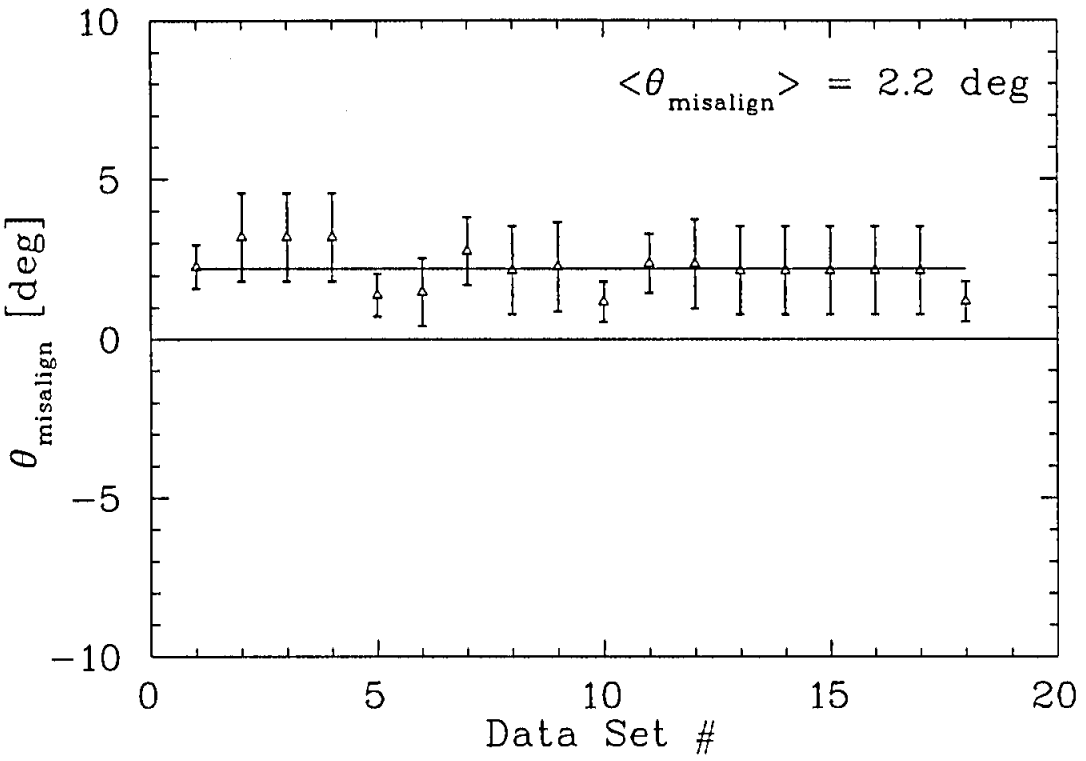

Figure 4.9: The inclusive angle $\theta_{misalign}$ between the desired spin vector $\vec{s}_7$ and the propagated spin vector $\vec{s}_p$ at recirculation arc 7.

indicates that the desired angular regions of the study were reached. There is no impact on the experiment in that $\theta_{misalign}$ is small. For the analysis, the spin direction based on the injector spin rotators and average linac energy measurements, $\vec{s}_p$, are used in any event.

4.3.2 Beam Orbit Stability

The stability of the beam orbit is an important factor. A typical data set involves between 50 and 80 orbit perturbations. Each orbit is one of two types, denoted by O_1 or O_2. The orbit perturbations are interleaved (O_1, O_2, O_1, O_2, etc.). The two orbits are meant to be symmetrical to one another in the vertical plane. The measured beam position indicates that the two orbits are generally symmetrical, but not perfect reflections of one another. This point is discussed later in the analysis

sections. Beam orbit stability is distinguished by three cases; (a) reversal of the beam orbit in recirculation arc 7; (b) isolation of the perturbed orbit to within the arc; and (c) correlation of the beam position at the polarimeter target to the orbit perturbations.

An orbit reversal, $O_1 \rightarrow O_2$ or $O_2 \rightarrow O_1$, occurs once every 120 seconds. The horizontal and vertical beam position is sampled by beam position monitors (BPMs) in the accelerator. Beam position readbacks (from data set # 3) for a monitor near the center of the arc are shown in Figure 4.10. The plots clearly show the orbit reversal, apparent in both planes of the beam orbit. It is also clear that the amplitude of

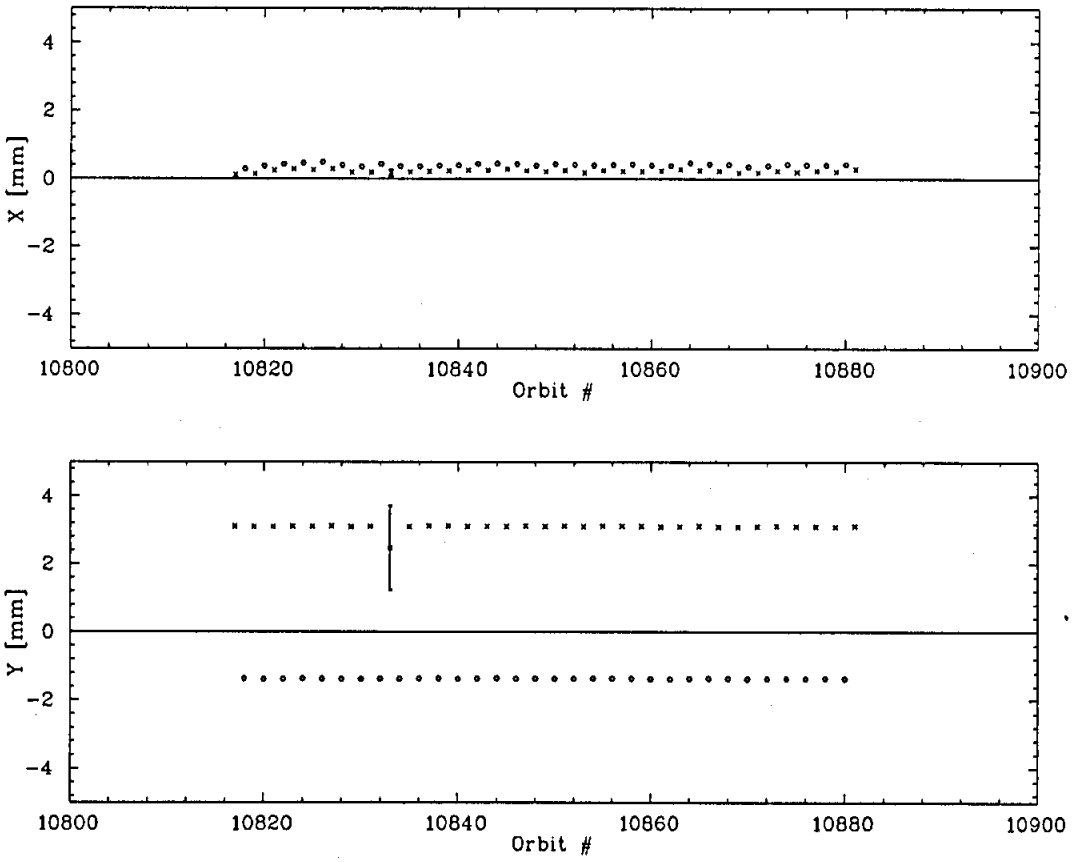

Figure 4.10: The horizontal (vertical) beam position at the center of the recirculation arc is shown in the upper (lower) plot. One of the two interleaved orbits O_1 (O_2) is denoted by the symbol x(o).

the beam orbit in both planes is not measured to be symmetrical about the origin

as described by the beam position monitor. Although the perturbing magnets only deflect the beam vertically, mis-alignment of the magnets is suspected to cause the minor horizontal motion correlated with the orbit perturbation. From the figure the ratio of the vertical to horizontal orbit amplitude is $\approx \frac{4.4\,\mathrm{mm}}{0.2\,\mathrm{mm}}$, or 22 : 1. Similar results for all 18 data sets are shown in Figure 4.11. The upper two plots of the figure

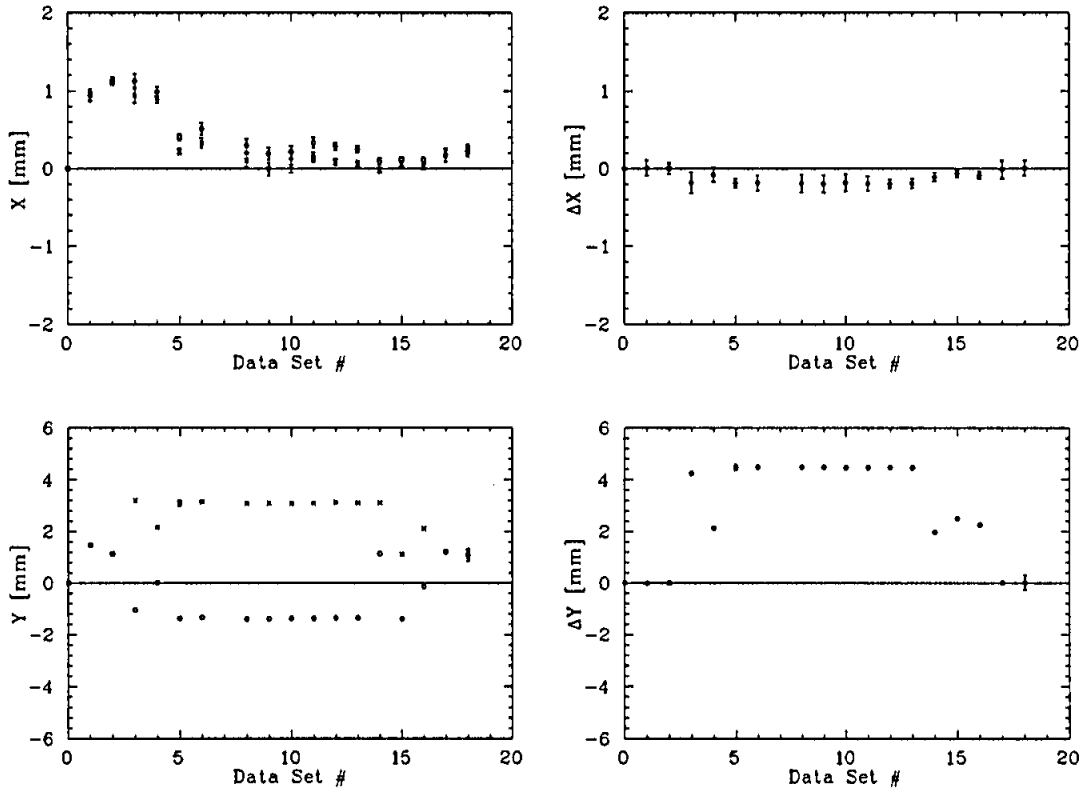

Figure 4.11: The average horizontal (vertical) beam position at the center of the recirculation arc is shown in the upper (lower) plot. The plots show the results for the 18 data sets.

show the horizontal position (averaged over the course of data set #3) for each orbit (O_1 and O_2) and their *difference* ($O_1 - O_2$). The lower two plots show similar results for the vertical beam position. The amplitude of the horizontal and vertical beam orbit are proportional in all cases. The upper left plot of the figure indicates that the absolute horizontal position of the reference orbit changed after data set # 4. However, the difference orbit data in the upper right plot indicate that the correlated horizontal motion is generally bounded by $\approx 250\,\mu$m for the entire experiment. This

is an important point, and indicates that the position stability of the beam orbit is generally not correlated to the absolute beam position measured. The lower right plot indicates the relative orbit amplitude being studied for the data sets.

Next, the isolation of the orbit perturbation is considered. The beam orbit perturbations are meant to be executed in the vertical plane of arc 7 proper. To show this, the *difference* between the two orbits $(O_1 - O_2)$ from the beginning of arc 7 and ending at the Hall C polarimeter is shown in Figure 4.12. The upper plot shows the

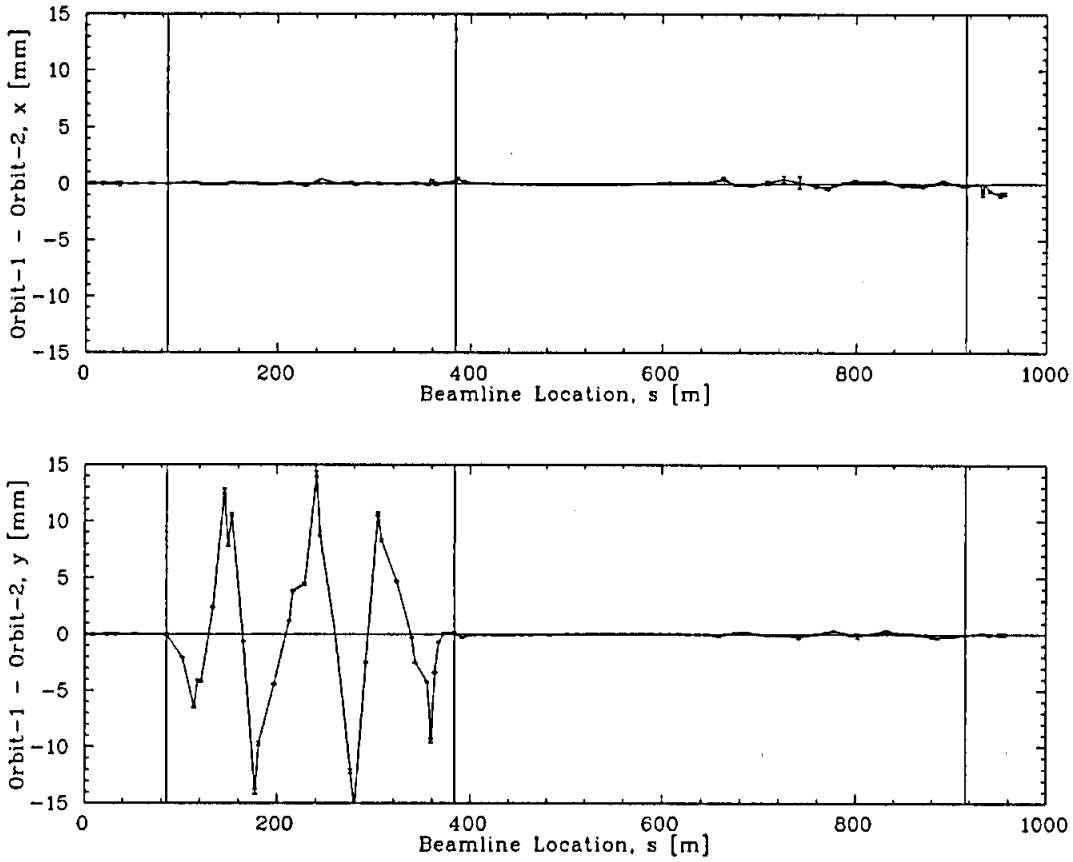

Figure 4.12: The horizontal (vertical) difference in beam orbit is shown along the length of the recirculation arc in the upper (lower) plot. The 3 vertical bars delineate the arc proper and the remaining transport to the Møller polarimeter.

difference between the horizontal position of both orbits. The lower plot shows the result for the vertical beam motion. The three vertical bars indicate the start of arc 7, the end of arc 7, and the polarimeter location, respectively. The orbit perturbations

are clearly isolated to the vertical plane of arc 7. Isolation of the orbit perturbations shown is typical for the experiment.

Finally, the absolute beam position at the Møller target foil is considered. The horizontal and vertical beam position is measured approximately 100 cm upstream of the target. Measurements are shown in Figure 4.13 for data set # 3. Again, the

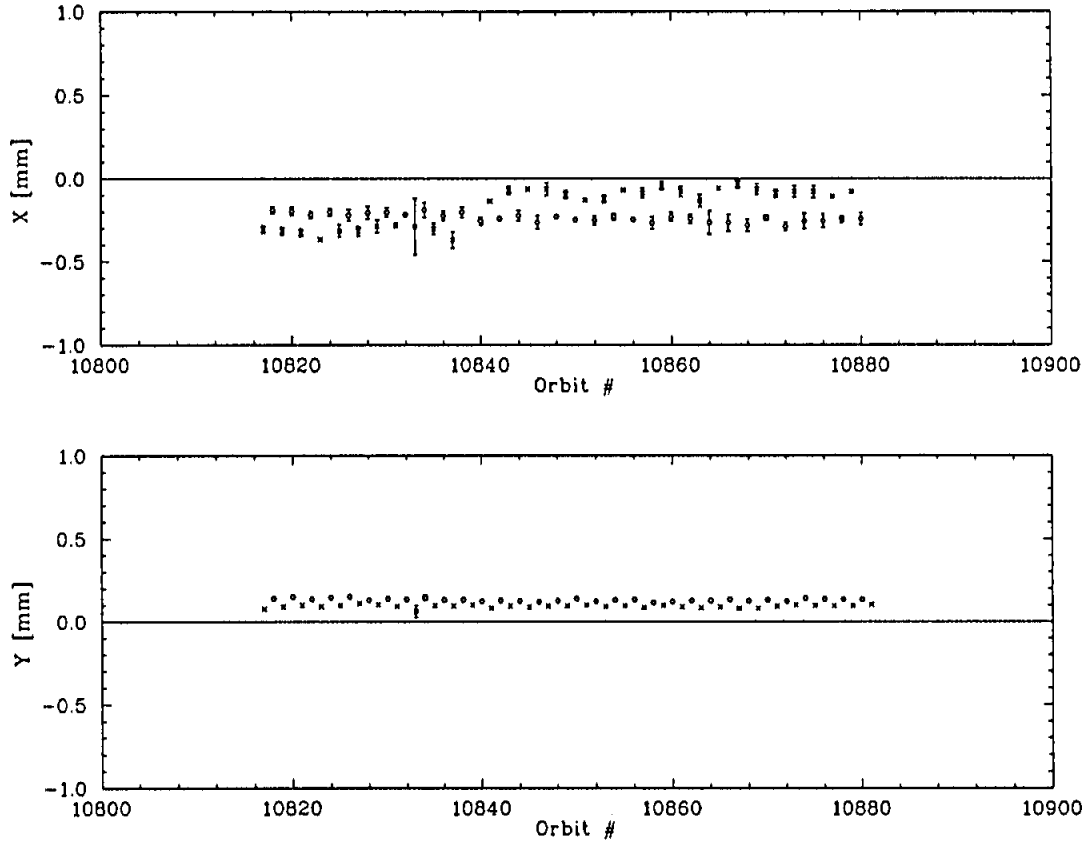

Figure 4.13: The horizontal (vertical) beam position just prior to the Møller polarimeter target foil is shown in the upper (lower) plot. The x (o) symbol represents the two interleaved orbit O_1 (O_2).

vertical beam position is typically more stable. This results because only vertical deflection magnets control the orbit perturbations; there are no horizontal deflection magnets correlated with the orbit perturbations. The *difference* of the beam position correlated to the orbit perturbation is plotted for all 18 data sets in Figure 4.14. The upper two plots show the average horizontal beam position for each orbit (O_1 and O_2) and their *difference* ($O_1 - O_2$). The lower two plots show similar results for the vertical

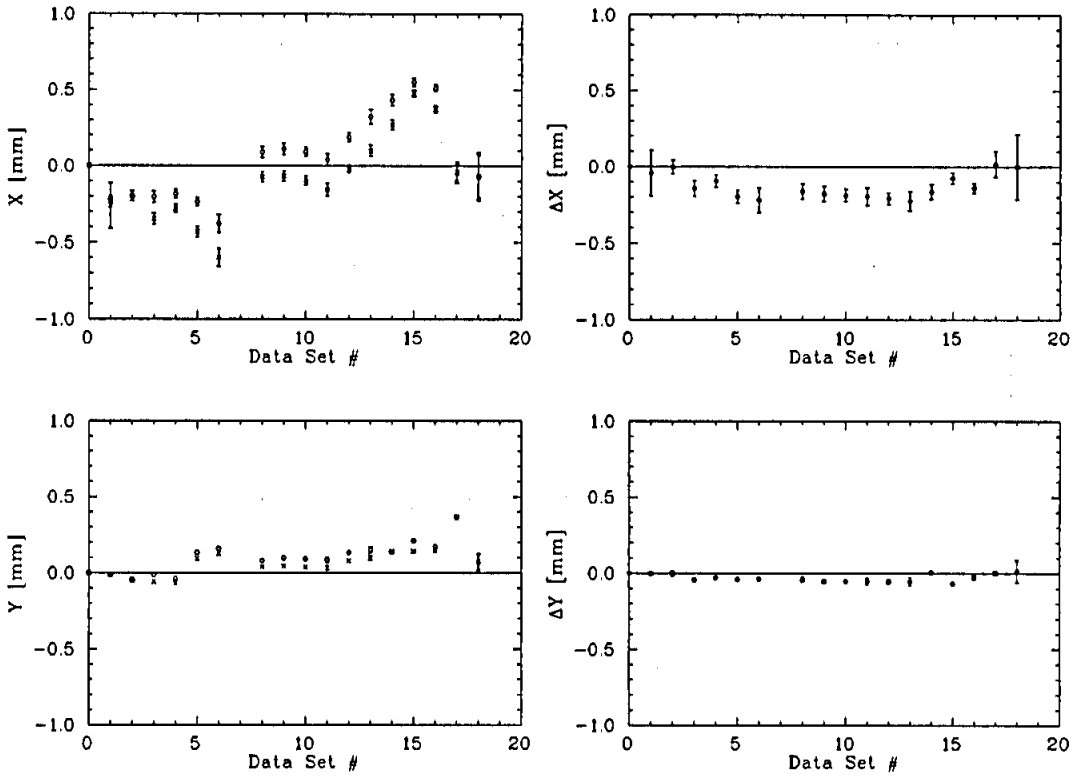

Figure 4.14: The average horizontal (vertical) beam position upstream at the Møller polarimeter target foil is shown in the upper (lower) plot. The plots show the results for the 18 data sets.

beam position. It is useful to notice that although the absolute beam position may differ for each data set, the difference between the beam orbits is essentially constant at the polarimeter target for all of the data sets. In our case, the control of the beam position at the target is $\Delta x \leq 200\,\mu$m and $\Delta y \leq 50\,\mu$m.

4.3.3 Beam Parameters at the Møller Polarimeter

The beam parameters are meaningful to determine the accuracy of the Møller polarimeter results. The beam current (I), beam profile (σ_x or σ_y), beam energy (E), and momentum spread ($\frac{\Delta p}{p}$) may affect the result. The extent to which these parameters are important for this experiment is determined by the impact each has to a sensitivity of the polarimeter correlated with the orbit perturbation. If the beam current it too large then the target polarization P_z^T can be reduced by heating of the

target by the beam. Alternatively, the effective analyzing power $\overline{A_{zz}}$ of the polarimeter depends to some extent on the beam profile and beam position at the target. These factors certainly affect the absolute measurement of the beam polarization. However, this experiment is only sensitive to parameters that change with the orbit perturbation.

Beam rastering is a common technique to reduce target heating by increasing the area over which the beam strikes the target. A rastering system was used in this experiment except for three early data sets (#2, #3, #4). Therefore, the non–rastered and rastered data sets are presented separately.

4.3.4 Non–Rastered Beam Profile in Achromatic Mode

The results of this section describe the beam profile at the polarimeter target without the use of beam rastering. The optics of the arc were in their nominal achromatic mode (focusing elements energized). The non–rastered data sets are #2, #3, and #4. These correspond to the orbit conditions 0:0, M:M, and $\frac{M}{2}$:$\frac{M}{2}$ using a transverse polarization orientation. These conditions were repeated later in the experiment with the use of beam rastering. This was done to ensure no loss of data due to the un–rastered beam and to improve the statistics of the measurement.

The beam position and profile for data set # 3 were measured using a superharp. The beam profile was measured approximately 200 cm upstream of the target by the last superharp before the polarimeter. Although the beam position resolution of the superharp is better than the beam position monitors in the transport arc, the superharp is destructive to the beam. Therefore, only periodic scans were made of the beam profile. The horizontal and vertical beam profiles for each orbit, O_1 and O_2, are shown in Figure 4.15. The beam centroid and width are extracted from the data by fitting the measured profiles. The difference in the beam centroid between the two orbits is calculated using a systematic position uncertainty for the superharp of 10 μm per profile scan. The difference in the beam centroid for the horizontal and ver-

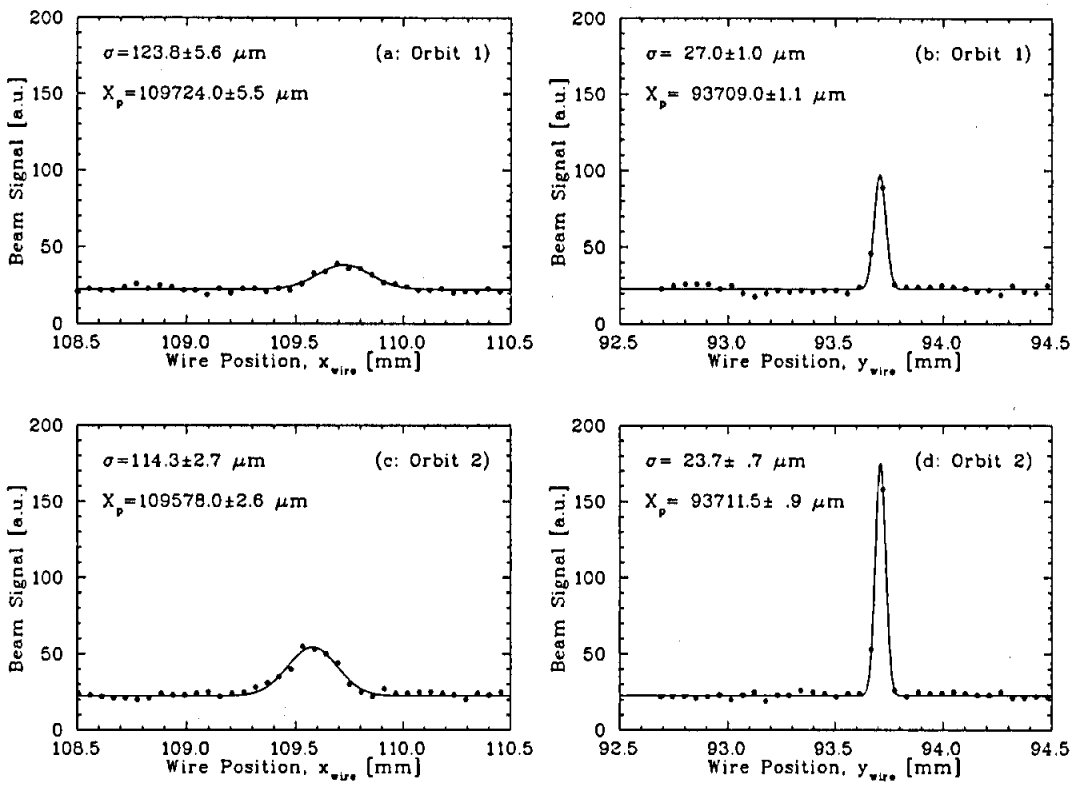

Figure 4.15: Profiles for the non-rastered beam were measured for both orbit perturbations O_1 and O_2.

tical profiles are $\Delta x = (150 \pm 21)\,\mu$m and $\Delta y = (5 \pm 16)\,\mu$m, respectively. Both are consistent with the upper bounds as determined by the relative BPM results for the entire data set. Again, the horizontal beam position correlated to the orbit perturbation is stronger because the orbit deflection magnets cannot correct the horizontal orbit.

The beam widths extracted from the profiles are $\sigma_x = (119.0 \pm 13.1)\,\mu$m and $\sigma_y = (25.4 \pm 10.4)\,\mu$m. In this case, the horizontal profile is large enough so that it can be corrected as done in Section 4.2.6. However, the vertical beam width is narrow enough that the wire is almost entirely intercepting the beam at one or two positions in the scan. In this case, the measured width only provides an approximate measure of the vertical beam width. The corrected horizontal width is calculated to be $\sigma_x = (117.0 \pm 16.5)\,\mu$m.

The aspect ratio of the transport between the first and last superharp is then $\frac{\sigma_x}{\sigma_y} \approx 4.7$. The beam profile was separately measured to be round entering the transport arc. These results are used later to determine the sensitivity of the polarimeter analyzing power and target heating effects for data sets #2, #3, and #4.

4.3.5 Rastered Beam Profile in Achromatic Mode

The effects of target depolarization due to target heating by ionization energy loss of the beam in the target material can be problematic. This occurs when the beam intensity is too large or the beam spot is too small. Since it is not desirable to reduce the beam intensity (it increases the time required to measure the effect) a common technique is to raster the beam over the target area thereby dissipating the beam power over a larger area and, for a thermally conductive target, reducing the peak target temperature. This target is located in a vacuum chamber so convective heat transfer is essentially zero and radiative heat transfer is also shown to be insubstantial.

The Møller raster system consists of a pair of magnets to deflect the beam in the two transverse directions, respectively. To accomplish this, one magnet is rotated by 90° with respect to the other about the beampipe. Each magnet is powered by a function generator and power amplifier operating with a frequency $f = 10.25\,\text{kHz}$. A constant phase delay of 90° exists between the power supplies for the two magnets. Therefore, the magnets deflect the beam orbit in a circle at 10.25 kHz. As determined earlier, the magnification for the orbit motion in the two transverse planes is in ratio $\frac{M_x}{M_y} \approx 5$.

The horizontal and vertical beam profiles for each orbit, O_1 and O_2, were measured. The profiles for are shown in Figure 4.16. Notice that in all four plots the wire scan exhibits a regular baseline signal, apparently interleaved with the true beam intensity signal. This zero is an artifact of the method by which the superharp system samples the beam intensity. The true intensity profile is bounded by the envelope of the data in each scan. This was checked by performing a simulation to determine the

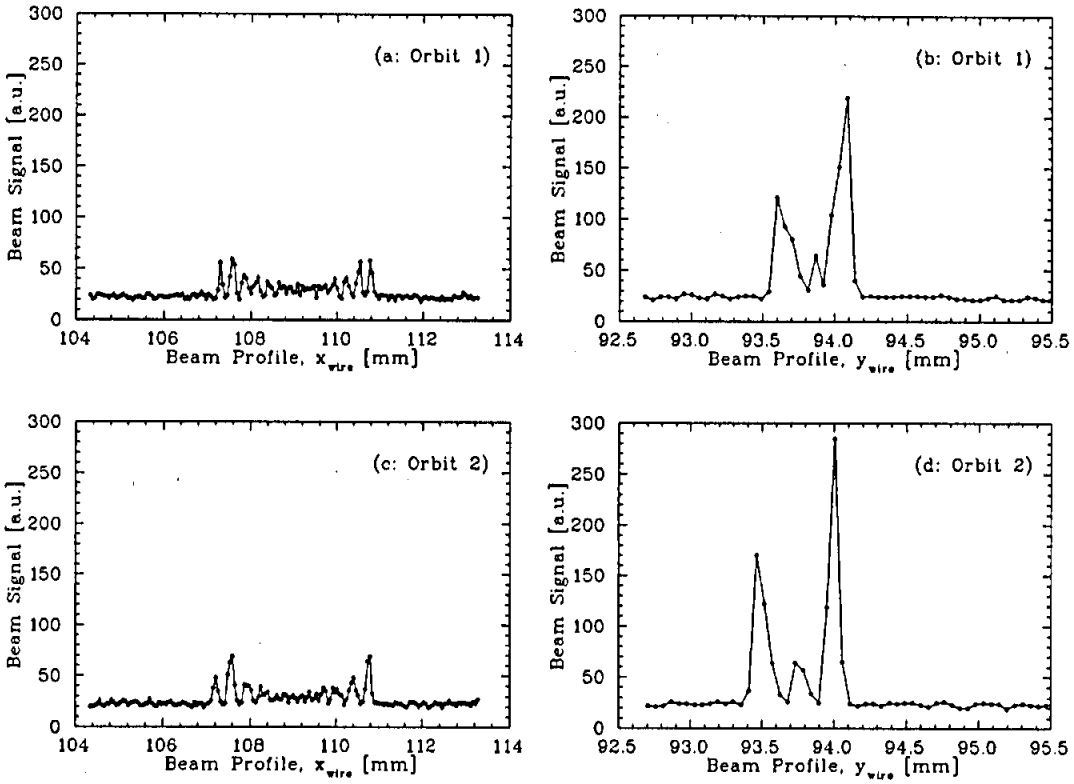

Figure 4.16: Profiles for the rastered beam were measured for both orbit perturbations O_1 and O_2.

rastered beam envelope.

A simulation was performed to reproduce the envelope of the superharp scan. The raster pattern was simulated by distributing the nominal beam profile along an elliptical curve with major axis a and minor axis b. For the case shown in Figure 4.16 the values for the simulation are $a = 1.80\,\text{mm}$ and $b = 0.25\,\text{mm}$. The results of the simulation are shown in the projection near the target plane in the upper left plot of Figure 4.17. The horizontal and vertical projections indicate general agreement with the *size* of the raster pattern. However, the profiles between the simulation and measurement indicate that the actual *profile* may not be purely elliptical. The important feature to extract from the result is that the elliptical raster pattern can be used to approximate the overall shape and size of the rastered beam. A more detailed description of the rastered beam could be constructed, however, this descrip-

tion is useful enough for bounding the effects of the rastered beam to the polarimeter systematics (which are themselves shown to be small).

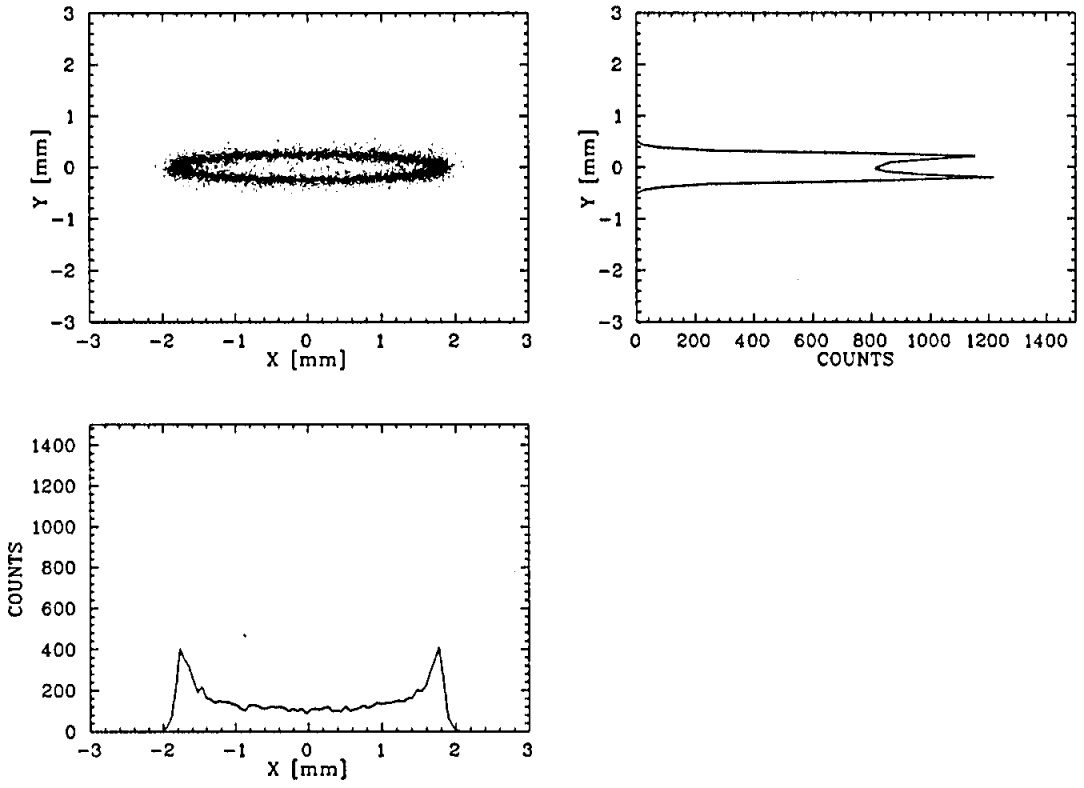

Figure 4.17: The simulation of the rastered beam at the Møller target foil is shown with the projections of the beam onto the horizontal and vertical axes.

4.3.6 Simulation Results for $\overline{A_{zz}}$

The Hall C Møller polarimeter described in Section 3.6 is modeled using a Monte Carlo simulation program. The program was originally developed for characterizing a single–arm Møller polarimeter at SLAC [Sw95]. The version running at CEBAF has been modified for the two–arm coincidence Møller polarimeter in Hall C. The program includes the calibration data for the magnetic spectrometer and the spatial geometry of the collimators and detectors. The simulation program was used to determine the effect of the beam profile and position at the polarimeter target to the average analyzing power $\overline{A_{zz}}$.

The average analyzing power $\overline{A_{zz}}$ is determined from the simulated coincidence rate in the program. Simulation options include multiple scattering, radiative corrections (inclusive and exclusive processes), and a correction for the momentum of the target electrons. This final effect was realized by Levchuk [Le92]. He reasoned that the asymmetries measured in Møller scattering could be diluted or enhanced by the intrinsic momenta of the target electrons. The size of this effect depends mainly on the center–of–mass detector acceptance and is calculated by using the known target atomic electron momentum distributions in the simulation code. The correction to the analyzing power is approximately +3% for the acceptance of this polarimeter. The detector collimators and spectrometer optics determine the coincidence acceptance for the detectors. The lead glass detectors are designed to have an angular acceptance of 83° to 97° in the center–of–mass. The program then calculates the analyzing power from the simulated cross section (coincidence rate)

$$\overline{A_{zz}} = \frac{\int A_{zz}\sigma d\Omega}{\int \sigma d\Omega}. \tag{4.19}$$

Simulations were performed to determine the sensitivity of the effective analyzing power $\overline{A_{zz}}$ to the beam conditions. The simulations were performed for a beam energy of 3.409 GeV using the quadrupole setpoints and collimator geometry of the polarimeter. The first set of simulations were performed to determine the relative change in $\overline{A_{zz}}$ from the theoretically calculated value. These results are shown in Table 4.6 for a nominal beam spot at the polarimeter; $\sigma_x = 200\,\mu$m and $\sigma_y = 100\,\mu$m. The simulation code was run for multiple cases to determine the sensitivity of $\overline{A_{zz}}$ to the beam conditions of the experiment. In all cases, multiple scattering at the target, radiative corrections, and the Levchuk effort were included. The number of events processed in each simulation was 10^8. The results are shown in Table 4.7. The results for cases #1 and #2 show little difference between the smallest beam profile measured for this experiment and the typical beam profile at the Møller target. Cases #2 and #3 compare the effect of turning the rastering system on. Cases #3 and #4 compare moving the raster pattern to consider the spot motion correlated to the orbit

Case	$\overline{A_{zz}}$
QED Exact $(-\frac{7}{9})$	-0.7778 ± 0
Simulation (I)	-0.7756 ± 0.0003
Simulation (M+R+L)	-0.7951 ± 0.0029

Table 4.6: $\overline{A_{zz}}$ calculated by Monte Carlo when considering different simulation conditions; (I)deal case, (M)ultiple Scattering, (R)adiative corrections, and the (L)evchuk effect.

Case	x_0 (mm)	y_0 (mm)	σ_x (μm)	σ_y (μm)	r_{minor} (mm)	r_{major} (mm)	$\overline{A_{zz}}$
# 1	0.0	0.00	117.0	25.4	0.00	0.00	-0.7952 ± 0.0029
# 2	0.0	0.00	200.0	100.0	0.00	0.00	-0.7951 ± 0.0029
# 3	0.0	0.00	200.0	100.0	1.80	0.25	-0.7951 ± 0.0030
# 4	0.5	0.25	200.0	100.0	1.80	0.25	-0.7951 ± 0.0029
# 5	-0.5	-0.25	200.0	100.0	0.00	0.00	-0.7948 ± 0.0029

Table 4.7: Monte Carlo simulation results of the Møller polarimeter for various beam conditions relevant to the 18 data sets. (x_0, y_0) are the beam centroid, (σ_x, σ_y) are the beam widths, (r_{minor}, r_{major}) represent the minor and major axis for the rastering pattern, and $\overline{A_{zz}}$ is the effective analyzing power.

perturbations. In this comparison the beam spot was moved ≈ 2 times larger than observed in the experiment. Cases #4 and #5 considers moving the entire beam away from the target center. This was checked to determine if the rastering decreases the overall sensitivity of the effective analyzing power to the beam position, by averaging over a larger area of the target foil. Indeed, the simulation code indicates this may be the case. The effective analyzing power is predicted by the simulation code to be largely insensitive to the beam profiles and beam motion associated with the orbit perturbations. The value used for all of the data sets is $\overline{A_{zz}} = -0.7951 \pm 0.0030$.

4.3.7 Target Temperature Effects

The Møller scattering asymmetry depends upon both the beam and target electron being, on average, oriented with respect to one another. To measure the beam polarization the target electrons, therefore, must be polarized. To accomplish this a ferromagnetic material is chosen for the target. Ferromagnetism is essentially a quantum mechanical effect. It is described by an interaction which aligns the atomic dipole moments of neighboring atoms to one another. This is despite the randomizing tendency by the thermal motion of the atoms to break the alignment. Magnetization results when the atomic electron spins of the foil are aligned in an external field. However, as the temperature of the ferromagnet increases mis–alignment of the electron spins by thermal motion reduce the magnetization. Above a point, called the Curie temperature T_c, the ferromagnetism abruptly ceases; the material becomes paramagnetic (linear magnetization with applied field). Below this point, the magnetization, M_s, varies with temperature according to the law

$$\frac{M_s(T)}{M_s(T=0K)} \approx 1 - k \cdot T^{\frac{3}{2}}, \tag{4.20}$$

where k is a constant of the material.

The target for this polarimeter is a pure iron foil. Iron does not have the largest polarizability of all ferromagnets. However, it has the most well understood polarizability, thereby minimizing systematic uncertainty in determining the foil magnetization. Further, iron has the largest ratio of polarizable electrons to total atomic electrons, thereby making the material a suitable choice for a high–precision polarized solid target. The foil is positioned by a target ladder and oriented normal to the beam direction. The foil is polarized by immersing it in a strong magnetic field. A pair of superconducting Helmholtz coils produce a uniform field of 3 Tesla. The saturation magnetization is defined at zero magnetic field and zero temperature. For pure iron this value is $M_s(T=0, B=0) = 2.216\mu_B$, where μ_B is a Bohr magneton. The corrections for pure iron at room temperature and in a 3 Tesla magnetic field have been computed [Lo96]. The increased temperature *reduces* the magnetization 2%. The

large magnetic field *increases* the magnetization 0.5% by the paramagnetic effect. The resulting magnetization is $M_s(T = 294°K, B = 3T) = 2.181\mu_B$. This represents the contribution of both the electron spin and the electron orbital magnetization due to the electron motion (current) in the iron atom,

$$M_s = M_{spin} + M_{orbit}. \tag{4.21}$$

The orbital magnetization for iron is $M_{orbit} = 0.0918\mu_B$. Consequently, the magnetization due to spin is extracted; $M_{spin} = 2.0911\mu_B$. Finally, the polarization of the iron is determined by the ratio of the spin magnetization of an iron atom to the total number of electrons in an iron atom (Z=26). The value has been calculated in the same reference [Lo96] to be $(8.043 \pm 0.015)\%$.

The effect of the beam current on the foil is now considered. The beam deposits energy in the target through collision and radiative losses. These losses are characterized by the energy loss per unit length, dE/dx, usually expressed in the units of (MeV-cm^2)/g. The target used for the experiment is a pure iron foil 4 μm thick. The density of iron at 300° K is $\rho = 7.87\,\mathrm{g/cm^3}$, therefore the target thickness is $\rho t = 3.15\,\mathrm{mg/cm^2}$. The average ionization energy loss at $E_{beam} \approx 3\,\mathrm{GeV}$ is $\frac{dE}{dx} \leq 2\,(\mathrm{MeV} - \mathrm{cm^2})/\mathrm{g}$. The power deposited in the target by the beam is given by

$$P_{target} = \frac{dE}{dx} \cdot \rho \cdot t \cdot i_{beam}, \tag{4.22}$$

where i_{beam} is the beam current in microamperes. The beam current varied between $2 - 4\,\mu$A for all data sets as demonstrated in Figure 4.18. For maximum beam current ($4\,\mu$A) the power dissipated in the target by the beam is then $P_{target} = 25.2\,\mathrm{mW}$.

Two points relevant to the experiment are to be made about target heating. The first point is that the deposited power heats the target material. The equilibrium temperature of the target depends upon the target thermal conductivity, geometry, environment, and the beam current and profile (size). The Curie temperature for iron is 770° C. These factors are extremely important to an absolute polarization measurement. The second point is that this experiment does not require an absolute

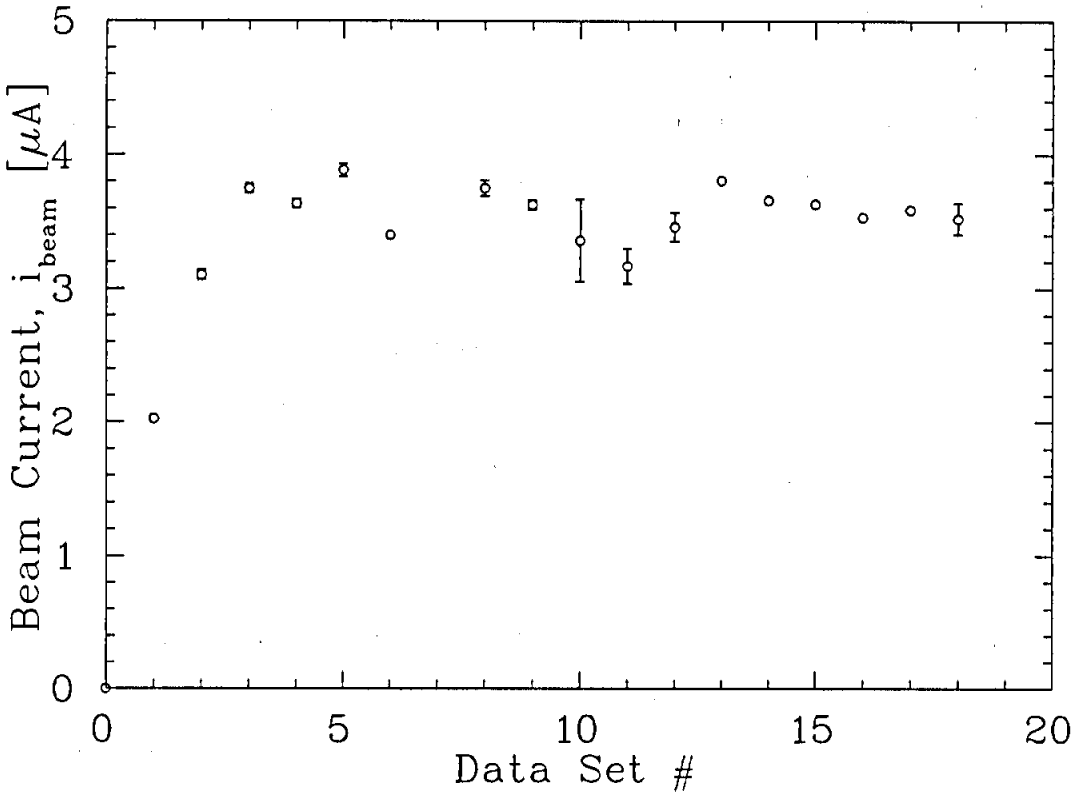

Figure 4.18: Average beam current i_{beam} for the 18 data sets.

measure of the beam polarization. The important factors are whether the beam current or beam profile change significantly with the orbit perturbation in arc 7. The target geometry and environment are assumed to be fixed. The thermal conductivity, although temperature dependent, is only weakly temperature–dependent above 70° K.

To address the first point, the equilibrium target temperature due to energy deposited of dE/dx loss is considered. The area over which the beam is distributed affects the final target temperature. For this reason the beam spot size is increased at the target location. To do this we used a beam rastering system (except for data sets #3, #4, and #5). The rastering system substantially increases (by 10^2) the interception area of the target by the beam. This greatly suppresses target heating effects, enabling a better absolute measure of the beam polarization. But more importantly, it decreases the sensitivity to the beam current and position fluctuation at the target. As the equilibrium target temperature depends on the interception area of

the electron beam, the non-rastered and rastered cases are treated separately. Recall that the non-rastered data sets were repeated with beam rastering. Therefore, conclusions of the polarization sensitivity can be based from a consistent set of operating conditions. The case for the rastered beam is treated first.

The current distribution for the rastered beam is elliptical ($\frac{M_x}{M_y} \approx 5$). The solution of the equilibrium target temperature is determined by solving Laplace's equation with a steady-state heat source (power deposited by the beam). Although, the current distribution is elliptical, the approach to this problem is readily (and more easily) solved for the circular case. An upper bound for the target temperature can be made by making this approximation. A heat source by a circular rastered beam contained in an annular region of the target defined at the beam radius r_b can be approximated by,

$$P(r)_{target} = P_{beam}\frac{\delta(r - r_b)}{2\pi r}. \tag{4.23}$$

The solution of Laplace's equation satisfying this condition [Pi58] is given by

$$T(r,t) = \left(\frac{P_{beam}}{\pi r_t^2 \kappa l}\right) \cdot \sum_{m=1}^{\infty} \frac{J_0(\beta_m r) \cdot J_0(\beta_m r_b)}{\beta_m^2 J_1^2(\beta_m r_t)} \cdot (1 - e^{-\alpha\beta_m^2 t}), \tag{4.24}$$

where P_{beam} is the deposited beam power (Watts), l is the target thickness (cm), $r_t = 1.3\,\text{cm}$ is the radius of the target before contacting the target ladder (large thermal mass), and $\kappa = 0.753\,\text{W/(cm°K)}$ is the thermal conductivity of iron at 300° K. β_m corresponds to the m^{th} zero of the Bessel function $J_0(\beta_m r_t)$. The equilibrium temperature is defined by the geometry of the target and the material,

$$\alpha = \frac{\kappa}{c_p \rho}, \tag{4.25}$$

where $c_p = 0.453\,\text{J/g°K}$ is the specific heat capacity and $\rho = 7.9\,\text{g/cm}^3$ is the density of iron. The first three zeros of $J_0(\beta_m r_t)$ are given by $\beta_1 = 2.41\,\text{cm}^{-1}$, $\beta_2 = 5.52\,\text{cm}^{-1}$, and $\beta_3 = 8.65\,\text{cm}^{-1}$. Consequently, the equilibrium temperature is dominated by β_1. For the time dependent factor to contribute less than 5% (e^{-3}), a duration of 2.46 seconds is required.

To bound the case of the real rastered beam current distribution the circular solution is applied for the minimum ($r_b = r_{min}$ minor axis) and maximum ($r_b = r_{max}$ major axis) radii of the real distribution as determined in Section 4.3.5. This approach is depicted in Figure 4.19. The solution of Equation 4.24 for the two cases are shown

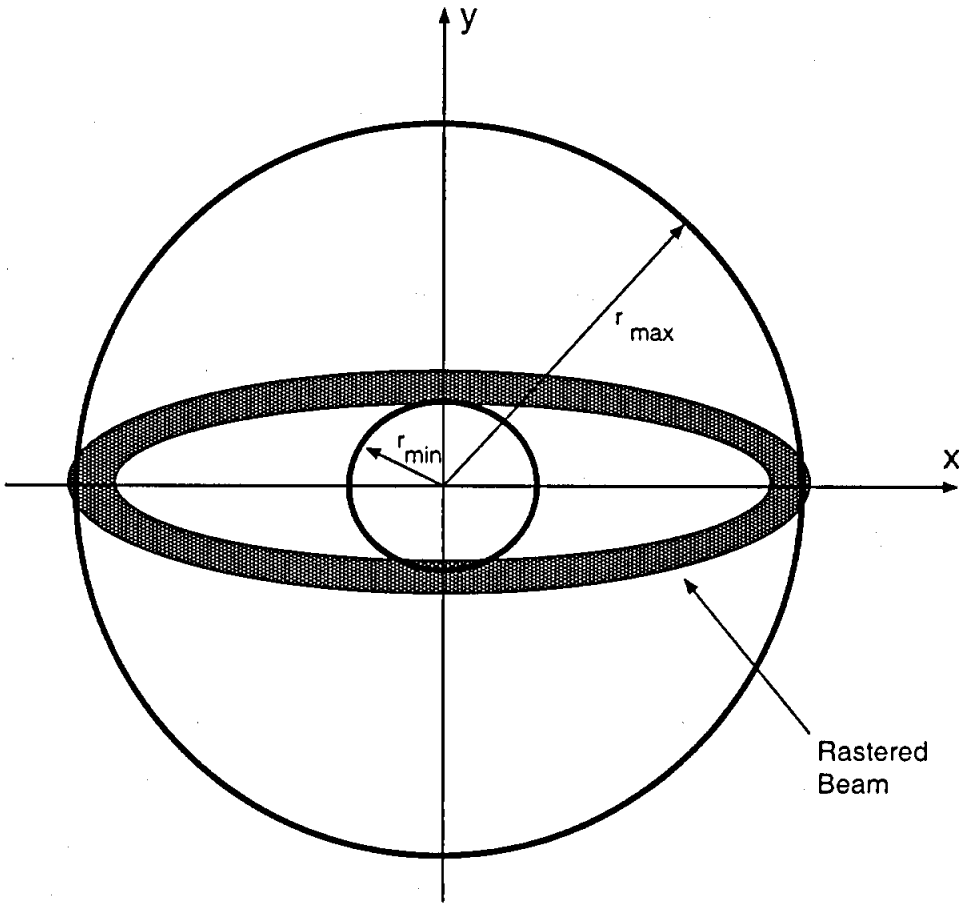

Figure 4.19: The diagram indicates the two circular hoop beams at radii r_{min} and r_{max} that bound the actual beam intensity profile near the target.

in Figure 4.20. The central target temperature within the rastered circle is constant and falls quadratically beyond the rastering radius. The temperature rise ΔT and the equilibrium temperature T_{final} ($T_{initial} = 27°$ C) are shown in Table 4.8. It is reasonable that the central target temperature is uniform because of the cylindrical symmetry of the circular raster model. Indeed, the result of this case bears the same dependence for a uniformly distributed current distribution of the same radius. The

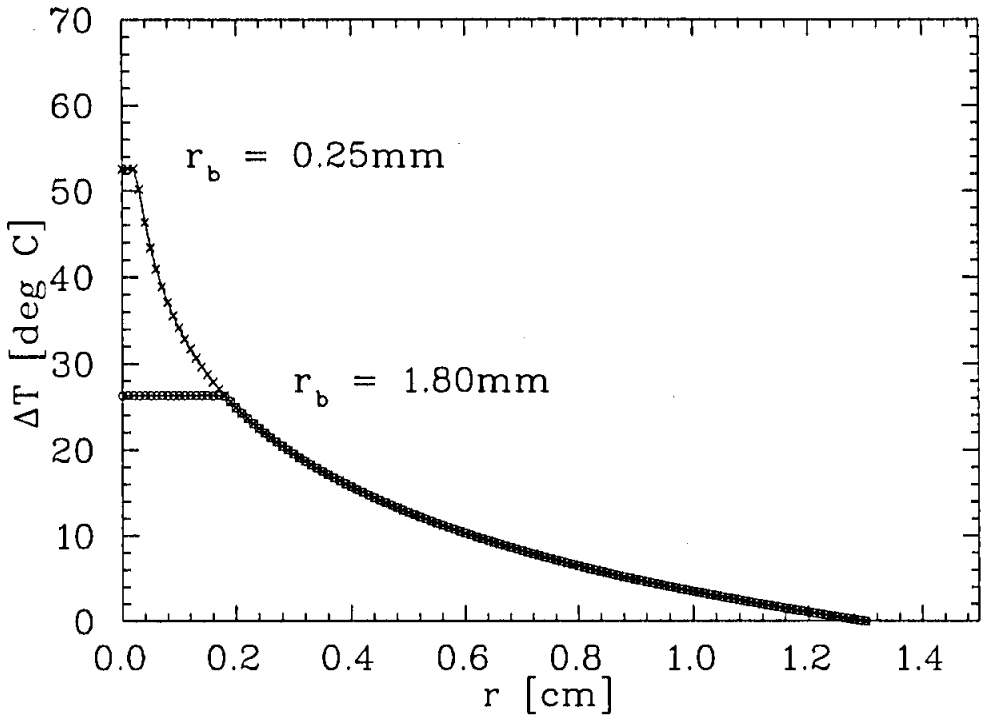

Figure 4.20: The increase in the iron target foil temperature as a function of the radial position of the target is shown. This case is for a circular hoop raster pattern, a 4 μA beam current, and a 4 μm thick iron foil. The increase in temperature has the cylindrical symmetry of the circular raster pattern.

Beam Radius	ΔT	T_{final}
$r_b = 0.025$ cm	52.6° C	79.6° C
$r_b = 0.180$ cm	26.3° C	53.3° C

Table 4.8: The increase (ΔT) and equilibrium (T_{final}) temperature of the iron target foil for the two cases of a circular hoop beam that bound the actual beam intensity profile near the target.

temperature rise for a disk source of heat is calculated to be

$$\Delta T_{disk} = \left(\frac{P_{beam}}{2\pi\kappa t}\right) \cdot \ln\left(\frac{r_t}{r_b}\right). \tag{4.26}$$

Either solution can then be used to consider the case for the non-rastered beam. The non-rastered beam is considered for the case where it deposits the collisional

energy within the 1-σ radius of the beam spot. The measured horizontal and vertical beam are take from the results of Section 4.3.4. Again, the beam profile has an elliptical shape and the real case is considered by bounding the ellipse by a smaller and larger radius beam size. The results are given in Table 4.9

Beam Radius	ΔT	T_{final}
$r_b = \sigma_x = 0.0117\,\text{cm}$	62.7° C	89.7° C
$r_b = \sigma_y = 0.0025\,\text{cm}$	83.3° C	110.3° C

Table 4.9: The increase (ΔT) and equilibrium (T_{final}) temperature of the iron target foil for the two cases of a circular disk beam that bound the actual beam intensity profile near the target.

To return to the second point we consider the correlation of the beam current to the orbit perturbation. The beam current is sampled about 24 times over the duration of each orbit perturbation (120 sec). In this way, the fluctuation in beam current from $O_1 \rightarrow O_2$ or $O_2 \rightarrow O_1$ can be determined. The result for data set #3 is shown in Figure 4.21. The upper plot shows the average beam current during ≈ 60 successive orbit perturbations. The downward slope in the average beam current is likely an artifact of slow beam motion in the injector which increases interception with defining beam apertures and results in beam loss. The cause for the semi-periodic oscillation in the beam current which occurred every 6-8 orbit cycles (12 minutes) is unknown, however, it is likely correlated to injector beam interception. There is no obvious correlation of the beam current to the beam orbit, as expected. The lower plot reinforces this point. The plot shows the difference in the average beam current between successive orbit perturbations. The important points to extract is that (a) there is no correlation in the beam current to the orbit perturbation; (b) the average current difference in size between successive orbits $< 50\,\text{nA}$; and (c) the differences are statistically consistent with zero.

Extending this to all the data sets, the difference between the average beam current

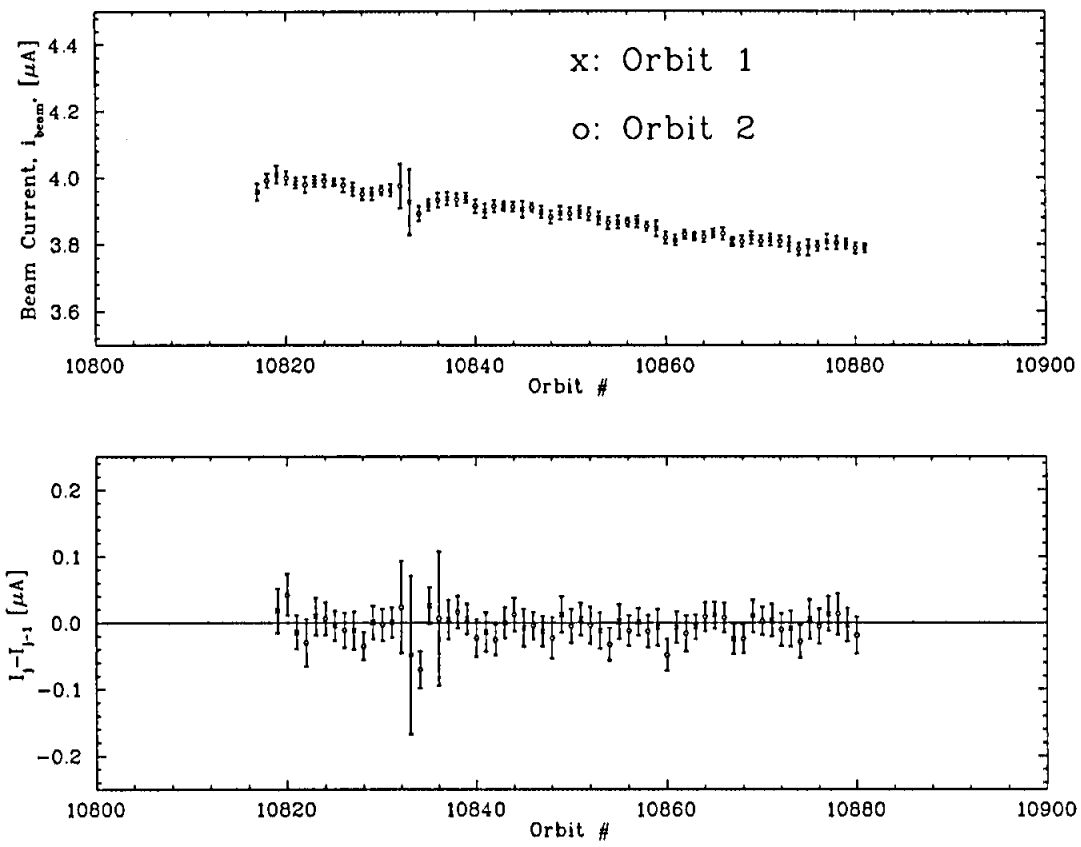

Figure 4.21: The beam current versus orbit perturbation type is shown in the upper plot for both orbits O_1 and O_2. The difference in beam current between successive orbits is shown in the lower plot. The results are from data set #3.

of both orbits is computed, and is shown in Figure 4.22. The relatively large error bars are due to overestimating the orbit-to-orbit difference by considering the difference of the *average* beam current for both orbits for each data set (lasting approximately 2 hours). The particularly large error bar in data set #10 is explained by an increase in the beam current from 3 μA to 4 μA approximately two-thirds of the way through the measurement to increase the data rate. In conclusion, the beam current for the experiment is stable from orbit to orbit at the level of $\leq 2\%$ and is *not* correlated to the orbit perturbation.

The equilibrium polarization and sensitivity to the beam current and profile is considered. The dependence of the saturation magnetization of iron on temperature is shown in Figure 4.23. The plot shows the results of a measurement [Lo96] compared to

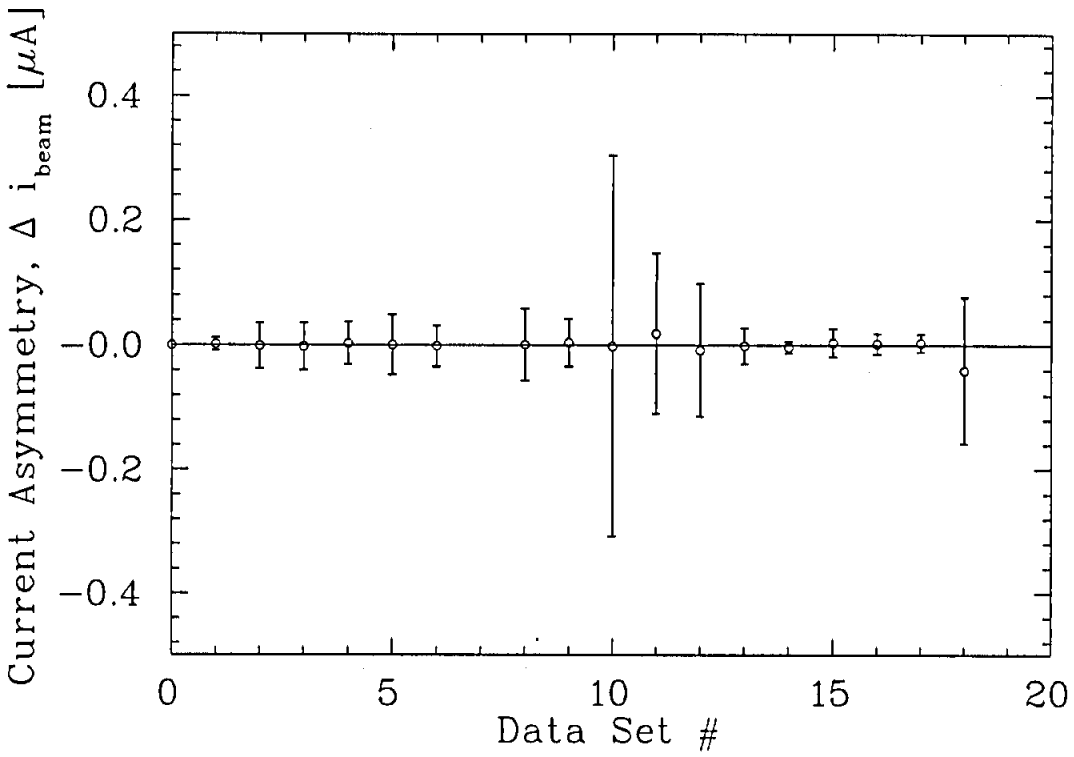

Figure 4.22: Beam current difference between O_1 and O_2 for all 18 data sets.

world data for iron. The slope of the plot is increasingly negative at larger temperature so we consider the larger equilibrium temperature (greatest depolarization) for the rastered and non-rastered cases. The reduction in polarization from the no-beam configuration ($P_z^T = 8.043 \pm 0.015\%$) for the two cases is estimated in Table 4.10.

Case	Relative Depolarization	Target Polarization P_z^T
Rastered	$(-2.5 \pm 0.1)\%$	$(7.842 \pm 0.016)\%$
Non-Rastered	$(-2.9 \pm 0.1)\%$	$(7.810 \pm 0.016)\%$

Table 4.10: Estimate of the relative depolarization due to the rastered and non-rastered beam profiles.

Finally, the beam position at the target is considered. The beam motion at the polarimeter target is estimated to be $d = \sqrt{\Delta x^2 + \Delta y^2} \leq 210\,\mu$m. This motion is small compared to the size of the target covered by the rastered beam. However, it is

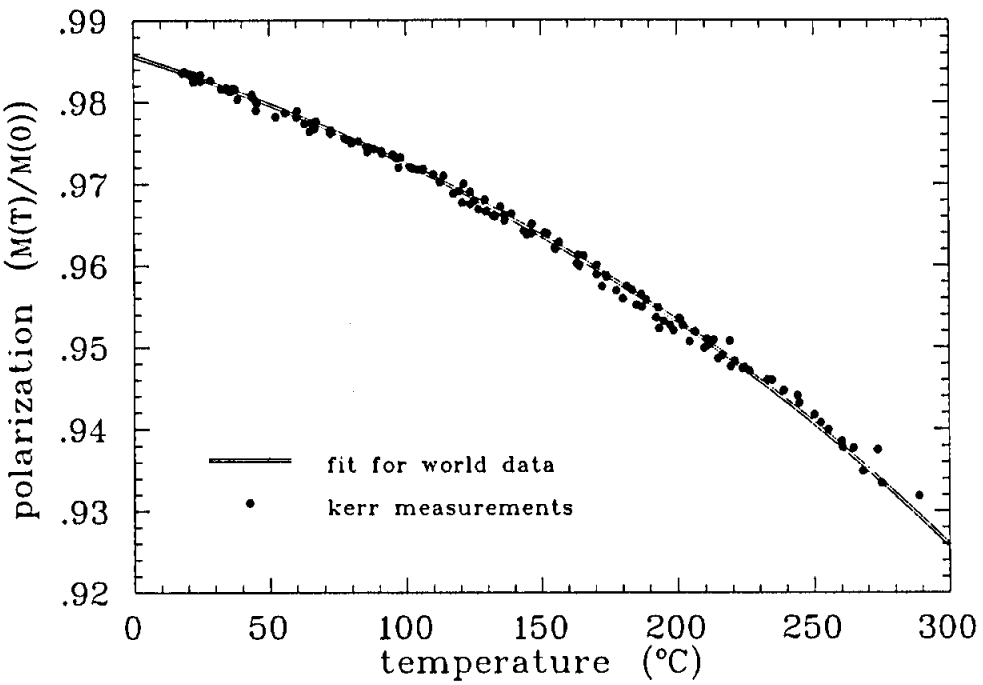

Figure 4.23: The temperature dependence of the magnetization of iron with temperature. The results of a measurement [Lo96] are compared with world saturation data for iron.

comparable to the size of the non-rastered beam. In this case, the beam may physically move by more than one spot size of the beam at each orbit reversal. The time constant for the equilibrium temperature to be reached for this target is estimated to be ≤ 3 seconds. Therefore, the equilibrium temperature is reached in less than 2.5 % of each measurement interval (120 seconds), and more importantly, affects both orbits equally.

4.3.8 Conclusion of Systematic Polarimeter Effects

The two main effects considered as a source of systematic uncertainty correlated to the beam orbit perturbation are the modification of the effective analyzing power $\overline{A_{zz}}$ and the depolarization of the polarimeter target with, and without, beam rastering. The relative uncertainty in each of these is listed in Table 4.11. Referring to Equation 3.45 the estimated systematic relative error contribution to the difference in measured

Polarimeter Parameter	Relative Uncertainty
$\left(\frac{\delta\overline{A_{zz}}}{\overline{A_{zz}}}\right)$	0.38 %
$\left(\frac{\delta P_z^T}{P_z^T}\right)_{Rastered}$	0.20 %
$\left(\frac{\delta P_z^T}{P_z^T}\right)_{Non-Rastered}$	0.20 %

Table 4.11: The maximum relative uncertainties in the polarimeter systematics for the effective analyzing power and target polarization correlated with the orbit perturbation type is shown.

polarization is small

$$\frac{\delta P_z^B}{P_z^B} = \sqrt{\left(\frac{\delta\overline{A_{zz}}}{\overline{A_{zz}}}\right)^2_{syst} + \left(\frac{\delta P_z^T}{P_z^T}\right)^2_{syst}} = 0.43\%. \tag{4.27}$$

4.4 Results and Analysis for Polarization Sensitivity Measurements

The extraction of the experimental asymmetries and calculation of the beam polarization are discussed in Section 4.4.1. The interpretation of the data for determining the sensitivity of the beam polarization angular dependence and orbit amplitude dependence is given in Section 4.4.2. Simulation results for the angular and orbit amplitude dependencies are compared with measurements in Section 4.4.3. Finally, a hypothesis for the discrepancy between the measurements and simulation results is discussed in Section 4.4.4.

4.4.1 Extracting the Experimental Asymmetries

The measurement of the beam polarization at the Møller polarimeter is determined by measuring the coincidence scattering rate for two helicity states of the beam. The difference in these rates, divided by their sum, gives the measured experimental asymmetry, ϵ. This asymmetry is directly proportional to the longitudinal component of the beam polarization at the polarimeter target.

Measuring the coincidence scattering rate is a scaler measurement. The coincidence events between the two arms (detectors) of the polarimeter are recorded for a given helicity state. The helicity is reversed at 1 Hz, and it is necessary to bin the coincidence events separately for each helicity. Further, the overall rate depends upon the number of electrons in the beam which reach the polarimeter target. Because the coincidence events are being separated by helicity, it is then necessary to normalize the number of events in each helicity cycle to the total number of electrons striking the target during the same cycle. Therefore, the beam current and measurement duration for each helicity are recorded in scalers too. One final level of separation must be performed. A polarimeter measurement spans many orbit reversals. Therefore, to determine the polarization for each orbit separately the coincidence events must also be categorized by orbit perturbation, O_1 or O_2. All levels of separation were accomplished in the scaler banks used to record the coincidence rate data. Each polarimeter run lasted approximately 20 minutes, at a coincidence rate of ≈ 30 kHz.

Extracting the experimental asymmetries for both orbits was performed using an off-line data analysis program written for the polarimeter. The program calculates the total experimental asymmetry for each orbit (ϵ_1 or ϵ_2) from each polarimeter run. The experimental asymmetries for the entire experiment are plotted versus *Run #* in Figure 4.24. The run numbers are grouped into their respective data sets and combined to produce an experimental asymmetry for each of the two orbit perturbations. A summary of the polarimeter data for each of the 18 data sets is given in Table 4.12. Lastly, the measured component of the beam polarization (P_z^B) is calculated using the effective analyzing power $\overline{A_{zz}}$ determined in Section 4.3.6, and the target polarization determined in Section 4.3.7. The polarization for both orbits (P_1 and P_2) and their difference ($\Delta P = P_1 - P_2$), are plotted in Figure 4.25. Indicated in the upper plot, nearly the maximum beam polarization ($P_0 = 68.4\%$) was observed for data set #15 and data set #18. The data sets with nearly zero polarization correspond to the orientations which are transverse to the accelerator bend plane (and the target polarization). The calculated difference in polarization (ΔP) between the

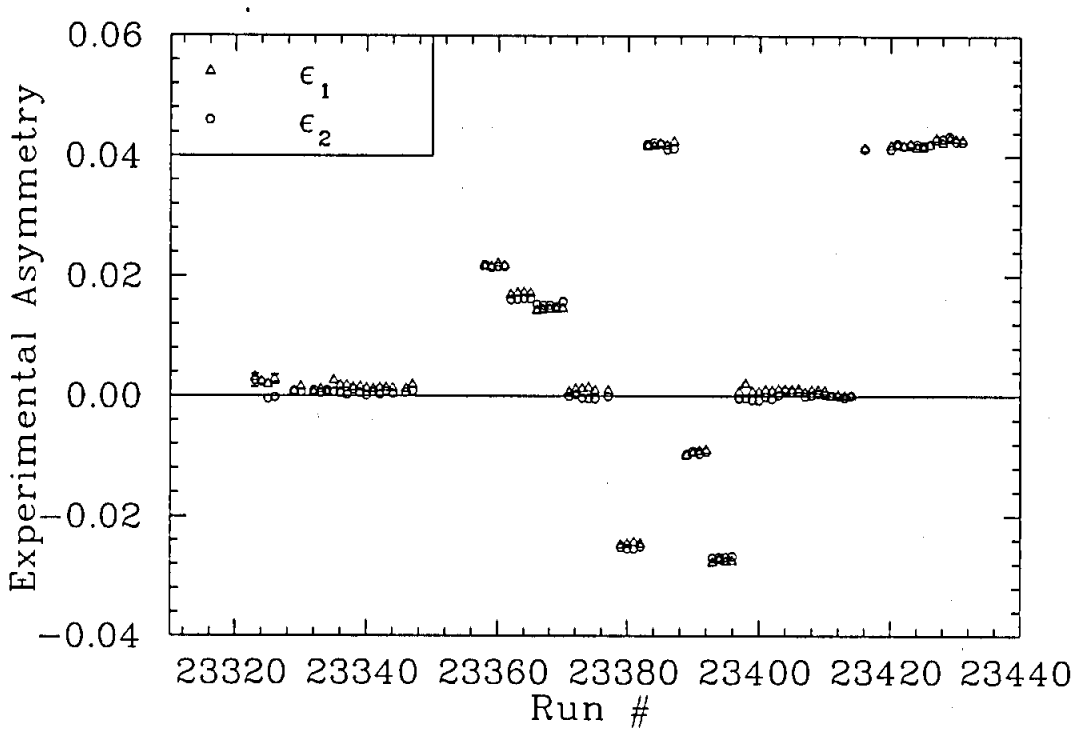

Figure 4.24: The calculated experimental asymmetries ϵ_1 and ϵ_2 for each Møller polarimeter run for the duration of the experiment are shown.

two orbits is the component of the effect measured at the polarimeter. The size of this component is $\approx 3\%$ of the maximum beam polarization ($\sim 10^{-2}$ effect).

4.4.2 Interpretation of Polarization Results

To describe the sensitivity of the beam polarization to the beam orbit we describe the effect in terms of the spin transport matrix formalism discussed in Chapter 2. Each of the two perturbed orbits can be described by a spin transport matrix,

$$S_{O1} = \begin{pmatrix} S_{xx} & S_{xy} & S_{xz} \\ S_{yx} & S_{yy} & S_{yz} \\ S_{zx} & S_{zy} & S_{zz} \end{pmatrix}_{O1} \tag{4.28}$$

DATA SET	Desired Arc 7 Orientation	Run # Start : End	ϵ_1 $\times 10^{-2}$	ϵ_2 $\times 10^{-2}$
#1	[-147,+000]	23323:23323	0.3019 ± 0.0641	0.2556 ± 0.1058
#2	[+090,+090]0:0	23329:23334	0.0873 ± 0.0094	0.0747 ± 0.0094
#3	[+090,+090]M:M	23335:23342	0.1581 ± 0.0079	0.0498 ± 0.0080
#4	$[+090,+090]\frac{M}{2}:\frac{M}{2}$	23343:23347	0.1350 ± 0.0102	0.0645 ± 0.0102
#5	[+090,+180]M:M	23358:23361	2.1766 ± 0.0084	2.1628 ± 0.0083
#6	[+090,+135]M:M	23362:23365	1.7109 ± 0.0086	1.6207 ± 0.0086
#7	[+090,+225]M:M	23366:23370	1.4451 ± 0.0080	1.5231 ± 0.0079
#8	[+090,+090]M:M	23371:23378	0.1041 ± 0.0080	-0.0147 ± 0.0078
#9	[+045,+090]M:M	23379:23382	-2.4572 ± 0.0088	-2.5256 ± 0.0089
#10	[+135,+180]M:M	23383:23388	4.1862 ± 0.0079	4.1816 ± 0.0080
#11	[+045,+180]M:M	23389:23392	-0.9373 ± 0.0088	-0.9474 ± 0.0089
#12	[+045,+270]M:M	23393:23396	-2.7504 ± 0.0088	-2.6809 ± 0.0087
#13	[+090,+090]M:M	23397:23403	0.1038 ± 0.0066	-0.0326 ± 0.0065
#14	[+090,+090]M:0	23404:23406	0.1102 ± 0.0097	0.0794 ± 0.0098
#15	[+090,+090]0:M	23407:23408	0.0726 ± 0.0112	0.0040 ± 0.0113
#16	$[+090,+090]\frac{M}{2}:\frac{M}{2}$	23409:23410	0.0927 ± 0.0120	0.0350 ± 0.0120
#17	[+090,+090]0:0	23411:23414	0.0025 ± 0.0087	-0.0010 ± 0.0086
#18	[+135,+180]M:M	23416:23422	4.1668 ± 0.0086	4.1580 ± 0.0088

Table 4.12: Summary of the experimental asymmetries measured for O_1 and O_2 for the 18 data sets indicating the respective polarization orientation at arc 7. The run numbers can be referenced in Figure 4.24.

and

$$S_{O2} = \begin{pmatrix} S_{xx} & S_{xy} & S_{xz} \\ S_{yx} & S_{yy} & S_{yz} \\ S_{zx} & S_{zy} & S_{zz} \end{pmatrix}_{O2} . \tag{4.29}$$

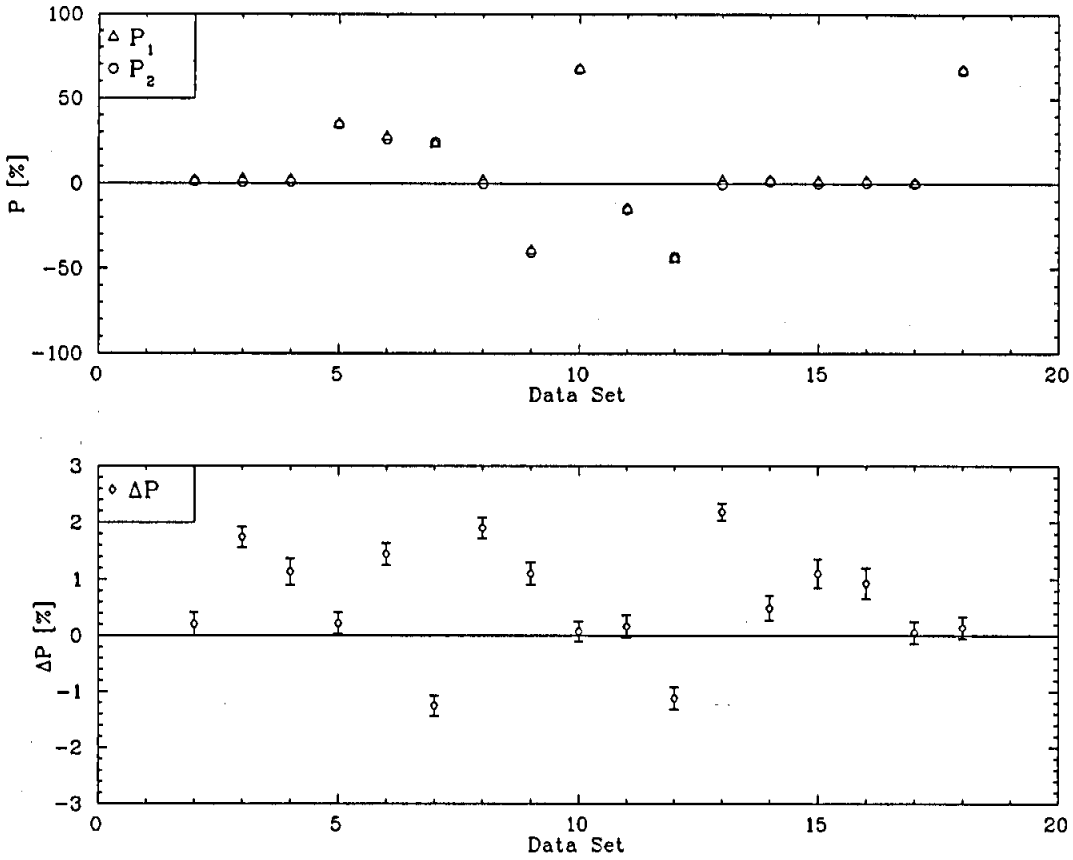

Figure 4.25: The extracted polarization P_1 and P_2 for both orbits are shown for each data set in the upper plot. The difference, $\Delta P = P_1 - P_2$, is shown in the lower plot.

Both beam orbits act on the same initial spin orientation at arc 7 defined by two polar angles, $\vec{s}_7 = \vec{s}_7(\theta, \phi)$. In general, the final spin orientations for the two beam orbits at some later location will be different; this is the effect being studied. The difference in the final spin orientations can be written as

$$\delta\vec{s} = S_{O1} \cdot \vec{s}_7 - S_{O2} \cdot \vec{s}_7 = (S_{O1} - S_{O2}) \cdot \vec{s}_7. \tag{4.30}$$

For this experiment the difference between the spin vectors would ideally be measured at the end of arc 7. However, there is no simple means to do this, so the beam polarization is transported to one of the nearest polarimeters for analysis. In doing so, the beam polarization associated with each orbit precesses; the difference in the beam polarization therefore precesses equally. The polarimeter design only analyzes the longitudinal component of the beam polarization, so the measurable effect is

finally described,

$$\delta\vec{s}_{meas} = (R_y(\Psi_{7C}) \cdot \delta\vec{s}) \cdot \hat{z}, \tag{4.31}$$

where $R_y(\Psi_{7C})$ describes the nominal spin transport precession between the end of arc 7 and the Hall C Møller polarimeter. The expression for $\delta\vec{s}_{meas}$ can be explicitly written as

$$\delta\vec{s}_{meas} = A_{31}\sin(\theta)\cos(\phi) + A_{32}\sin(\theta)\sin(\phi) + A_{33}\cos(\theta), \tag{4.32}$$

where

$$\begin{aligned} A_{31} &= -\sin(\Psi_{7C})\Delta S_{xx} + \cos(\Psi_{7C})\Delta S_{zx} \\ A_{32} &= -\sin(\Psi_{7C})\Delta S_{xy} + \cos(\Psi_{7C})\Delta S_{zy} \\ A_{33} &= -\sin(\Psi_{7C})\Delta S_{xz} + \cos(\Psi_{7C})\Delta S_{zz}. \end{aligned} \tag{4.33}$$

The ΔS_{ij} are the differences between the spin transport matrices for the two orbits, $(S_{ij})_{O1} - (S_{ij})_{O2}$. It is important to note that the term which dominates Equation 4.32 is proportional to A_{32}. This is simply because of the condition where

$$|A_{31}| \approx |A_{33}| < 10^{-2} \cdot |A_{32}|. \tag{4.34}$$

This results because ΔS_{ij}, where neither i nor j represent $\hat{y}$, is nearly zero. Consider the results of Section 2.3.5 as an example. The physical interpretation is that the bend plane spin precession for both orbits are essentially equal. This result is expected because both orbits encounter essentially the same bending dipole magnetic fields (responsible for the bend plane precession).

Consequently, the measurable component of the effect at the polarimeter can be written to good approximation as

$$\delta\vec{s}_{meas} = [-\sin(\Psi_{7C})\Delta S_{xy} + \cos(\Psi_{7C})\Delta S_{zy}] \cdot \sin(\theta)\sin(\phi). \tag{4.35}$$

As noted in Chapter 2, this implies the expected dependence of the effect on the initial vertical component of the beam polarization. The orbit dependence is represented

through ΔS_{xy} and ΔS_{zy}. The precession angle Ψ_{7C} has a practical significance in determining *how much* of the effect is finally measurable at the polarimeter.

To understand the sensitivity of the beam polarization to the beam orbit the experimental results are therefore divided into two groups. The first group represents the angular dependence of the sensitivity. In this case, the two orbit perturbations, O_1 and O_2, were repeated for different polarization orientations. The orbit perturbations were set to have large amplitudes ($|O_1| \approx |O_2| \approx 7\,\mathrm{mm}$) to maximize $|A_{32}|$. The polarization orientations were chosen to be initially on a cone of opening angle θ about the momentum direction at the beginning of arc 7. This was done to decouple the $\sin(\theta) \cdot \sin(\phi)$ dependence and to simplify the analysis. The orientations are therefore described on either of two surfaces, $\theta = 45°$ or $\theta = 90°$. The polarimeter beam raster was used for all of the angular dependence measurements.

The measured sensitivity ΔP for the angular dependence is shown in Figure 4.26, separate for both surfaces defined by the polar angle θ. The data are listed in Table 4.13. The ideal and measured angular polarization orientations are shown in the table. The measured polarization difference ΔP is given by

$$\Delta P = \frac{\Delta\epsilon}{\overline{A_{zz}} \cdot P_z^T} \cdot \frac{\sin(\theta_{ideal})}{\sin(\theta_{meas})}. \tag{4.36}$$

The final factor in Equation 4.36 is necessary to compare polarization orientations of the same ideal surface in θ ($\theta = 45°$ and $\theta = 90°$). The ϕ dependence, however, does not require correction and can be interpreted directly. The polarization sensitivity for both cases were then fit using the functional form $\Delta P = \Delta P_\theta \sin(\phi)$, where ΔP_θ gives the amplitude of the effect on the corresponding surface in θ. The fit results are listed in Table 4.14. A few conclusions can be drawn from the data and the fit. For a given surface in θ the dependence on ϕ is nearly as predicted, indicating that it is the focusing component of the quadrupole field which dominates the effect. The amplitude of the fit measures the strength of the polarization sensitivity and is expected to have a $\sin(\theta)$ dependence. For the cases being studied the ratio of the

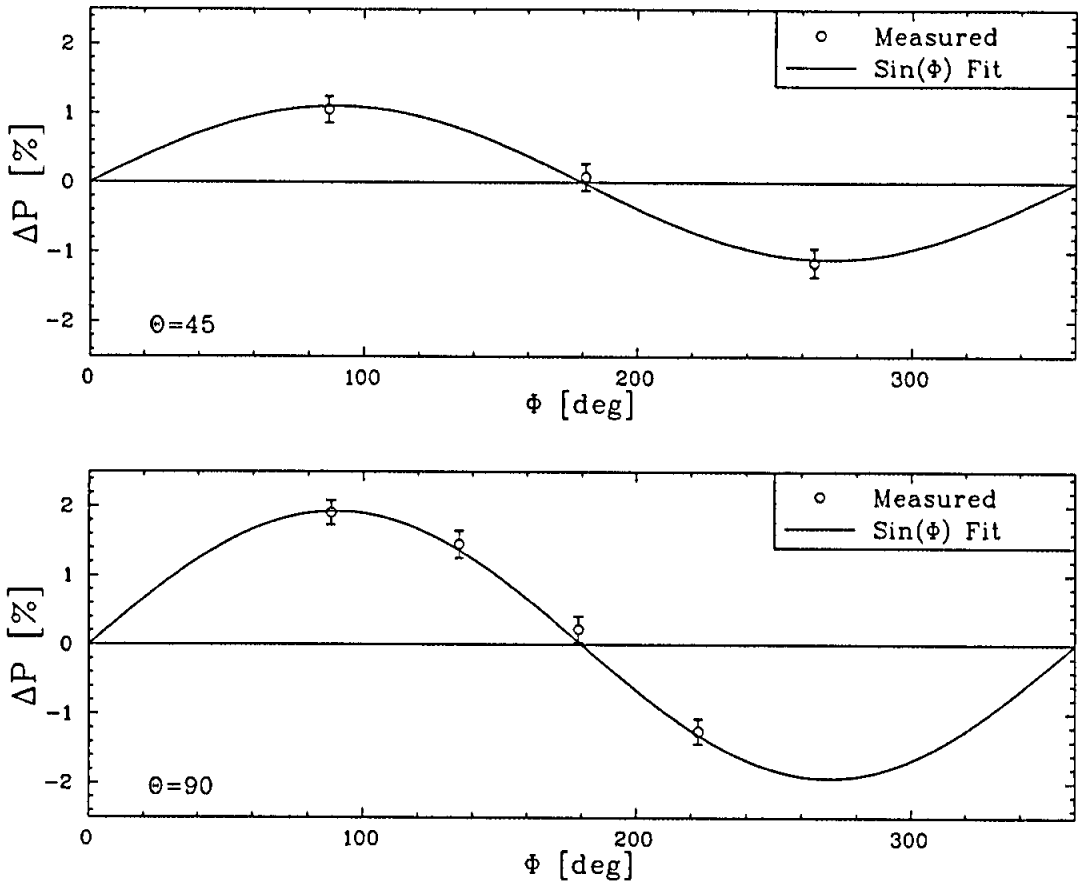

Figure 4.26: Angular dependence of the measured sensitivity ΔP for the two surfaces $\theta = 45°$ and $\theta = 90°$ at maximum orbit amplitudes.

amplitudes should be

$$\frac{\sin(45°)}{\sin(90°)} = \sqrt{2}/2 \approx 0.707, \tag{4.37}$$

however, the experimentally determined ratio is (0.58 ± 0.04).

The second group of data represents the dependence of the beam polarization sensitivity to the orbit amplitude. The polarization orientation for this group was set to be transverse to the bend plane ($\theta = +90°, \phi = +90°$) to maximize the expected angular dependence. For orbits which are simply a multiple of one another, the amplitude dependence is predicted to be linear. This is because the horizontal component of the quadrupole magnetic field varies linearly with vertical displacement from the axis of the magnet. For example, to the extent that the effect is indeed lin-

Data Set #	$(\theta, \phi)_{ideal}$ Ideal	$(\theta, \phi)_{meas}$ Measured	$\Delta\epsilon$ $\times 10^{-4}$	ΔP %
9	45 , 90	47.3, 87.3	6.84 ± 1.26	1.06 ± 0.19
11	45 , 180	49.4, 177.0	1.00 ± 1.26	0.15 ± 0.19
12	45 , 270	43.2, 264.4	-6.95 ± 1.23	-1.15 ± 0.20
4	90 , 90	89.6, 86.8	11.9 ± 1.12	1.91 ± 0.18
6	90 , 135	85.9, 134.9	9.01 ± 1.22	1.45 ± 0.20
5	90 , 180	85.5, 178.9	1.38 ± 1.18	0.22 ± 0.19
7	90 , 225	88.7, 222.7	-7.80 ± 1.13	-1.25 ± 0.18

Table 4.13: The raw and corrected data for the angular measurements are shown. The second column gives the expected angular orientation of the beam polarization at the beginning of arc 7. The third column gives the measured angular orientation based upon the injector spin rotator setpoints and average linac energy. The fourth column gives the difference in the longitudinal asymmetry between the perturbed orbits. The fifth column gives the computed difference in polarization between the perturbed orbits. For all angular measurements the Møller raster was operational.

Angular Cut	ΔP_θ	χ^2/dof
$\theta = 45°$	$(1.11 \pm 0.06)\%$	0.17
$\theta = 90°$	$(1.93 \pm 0.09)\%$	1.90

Table 4.14: Amplitude of polarization sensitivity, ΔP_θ, for the two surfaces $\theta = 45°$ and $\theta = 90°$.

ear, comparing two equal, yet opposite, beam orbits of amplitude A_0 should produce the same effect as that of a single beam orbit with amplitude $2A_0$ about the central orbit. This point is important because by comparing orbits in this way the effect on the beam polarization can be doubled, and made easier to observe.

The two orbits were selected in some cases to be identical to one another ($O_1 = O_2$ = unperturbed orbit). The measurement of the beam polarization was simply

made without energizing the deflection magnets. In other cases, the orbits were selected to be opposing one another. In these cases the deflection magnets were energized to produce an orbit O_1, and the opposing orbit O_2 was determined by reversing the polarity of the two initial deflection magnets. The final two deflection magnets were adjusted in all cases to best remove the orbit perturbation. The size of each beam orbit was referenced by a beam position monitor located at the mid-point of arc 7 to measure the vertical beam position, y_1 or y_2. Note that neither y_1 nor y_2 measure the amplitude of the orbit, but simply provide a measure of the relative orbit displacement. The orbit-dependent polarization sensitivity can therefore be referenced by their difference, $\Delta y = y_1 - y_2$. Results are shown for both rastered and non-rastered beams in Figure 4.27. The data for the measurements is shown in Table 4.15. Fitting the results using the linear function $\Delta P = M_0 \cdot \Delta y + N_0$, yield

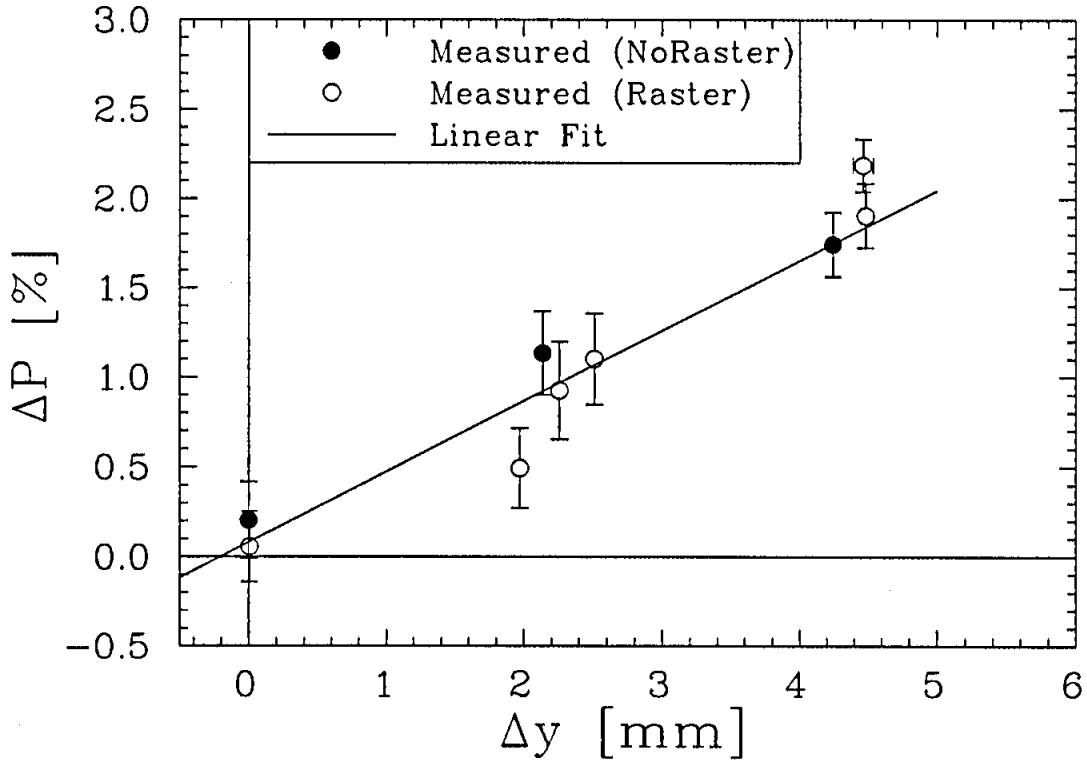

Figure 4.27: Orbit amplitude dependence of the polarization sensitivity ΔP. In this case the beam polarization direction is transverse to the accelerator bend plane ($\theta = +90°, \phi = +90°$).

Data Set #	$(\theta, \phi)_{meas}$ Measured	Δy (mm)	$\Delta\epsilon$ $\times 10^{-4}$	ΔP %
2†	89.5 , 86.8	0.00 ± 0.13	1.26 ± 1.33	0.20 ± 0.21
3†	89.5 , 86.8	4.24 ± 0.15	10.8 ± 1.12	1.74 ± 0.18
4†	89.5 , 86.8	2.14 ± 0.13	7.04 ± 1.45	1.13 ± 0.23
8	88.6 , 88.4	4.48 ± 0.13	11.9 ± 1.12	1.91 ± 0.18
13	88.6 , 88.4	4.46 ± 0.26	13.6 ± 0.92	2.19 ± 0.15
14	88.6 , 88.4	1.97 ± 0.16	3.08 ± 1.38	0.49 ± 0.22
15	88.6 , 88.4	2.51 ± 0.13	6.87 ± 1.59	1.10 ± 0.26
16	88.6 , 88.4	2.26 ± 0.18	5.77 ± 1.70	0.92 ± 0.27
17	88.6 , 88.4	0.01 ± 0.14	0.35 ± 1.22	0.06 ± 0.20

Table 4.15: The raw and corrected data are shown for the orbit amplitude measurements. The second column gives the measured angular beam polarization orientation at arc 7. The third column gives the difference in the orbit amplitude measured at the reference BPM, the fourth column gives the difference in the longitudinal asymmetry between the perturbed orbits, and the fifth column gives the computed difference in polarization between the perturbed orbits. The symbol † indicates measurements without the Møller raster. The other measurements shown used the Møller raster.

the best-fit parameters $M_0 = (0.39 \pm 0.04)$ %/mm and $N_0 = (0.08 \pm 0.11)$ %.

A more practical statement of the effect is in terms of the sensitivity observed for a single beam orbit. To determine this conversion factor, the difference between O_1 and O_2 (see Figure D.1 for instance) was considered. The amplitude constructed from $O_1 - O_2$ is described by Y_0. The relationship between Y_0 and the relative vertical orbit displacement at the reference BPM, Δy, was determined to be

$$Y_0 = (3.5 \pm 0.4) \cdot \Delta y. \tag{4.38}$$

Using this conversion, the sensitivity for this configuration described by a single comparable orbit is

$$\Delta P = (0.11 \pm 0.02)\%/mm \cdot Y_0 + (0.08 \pm 0.11)\%. \tag{4.39}$$

For example, if the nominal orbit were to acquire a 2 mm amplitude, then the measurable effect would be $\Delta P = (0.30 \pm 0.15)\%$. It is clear from the size of N_0 that the uncertainty in the extracted result is comparable to an uncertainty of approximately 1 mm in the comparable single orbit.

4.4.3 Simulation Results for Experiment

A series of simulations were performed to determine if the experimental results could be reproduced. The simulation of all 18 data sets was performed using the same method. First, the injector spin rotator setpoints were used to calculate the injector spin direction, $\vec{s}_{inj}$. Next, the injector spin orientation was rotated by the nominal accelerator precession, assuming a *flat* reference orbit for the accelerator and the average linac energy, $\overline{E_{linac}} = (420.26 \pm 0.26)\,\mathrm{MeV}$. This determines the spin orientation at arc 7, $\vec{s}_7$. To calculate the effect of the beam orbit on the spin motion the spin tracking code MURTLE SPIN22 was used.

The model for the spin tracking code is based upon the design model of the accelerator. The design model is defined in terms of the beam optics definitions for use with the beam tracking program OPTIM [Le99]. This model includes the sequence of dipole and quadrupole magnets along the arc. The magnetic field values used for the dipole magnets were determined by scaling their values at the nominal arc 7 momentum (2.845 GeV/c) to the momentum extracted from beam energy measurements from the experiment (2.987 GeV/c) for arc 7. The magnetic field values used for the quadrupole magnets were determined from quadrupole readbacks and calibration data recorded during the experiment. The deflection magnets were modeled by impulsive deflections to the unperturbed beam orbit. Simulations using OPTIM were performed to reproduce measured beam orbit data which were collected from the beam position monitors.

A first series of simulation results were performed assuming that the reference orbit for the accelerator was identically flat. In other words, a zero BPM value is

coincident with the magnetic axis of the quadrupoles. The results, shown in Appendix D, indicate that this model of the accelerator does not best represent the flat orbit of arc 7. Further analysis of the numerical spin tracking model revealed two interesting points. The first reveals that the difference between the model and measured reference orbit are different, and affect the absolute prediction of the spin motion. The second reveals that other possible effects in the description or model of the accelerator during the experiment contribute to an underestimate of the simulation results by 13%. These two points are discussed here and in the final section of the chapter.

While considering the validity of the spin tracking model an interesting observation was made regarding the reference orbit of the accelerator. The observation was that the measured absolute orbit data does not reflect the symmetrical perturbations to the beam orbit which were introduced by the deflection magnets (see Figure D.1). This point, at first, does not appear to make a difference, because no matter which orbit is physically measured, a reproduction (even approximate) of the orbit should (with the assumption of linearity) lead to the correct observed result when the differences of the simulations for individual orbits are calculated. However, there is an incongruity in this assumption when applied generally to the numerical spin tracking model. It assumes that the reference orbit is either zero, or simply a multiplicative factor of both perturbed orbits. The reference orbit (unperturbed orbit) in our case was measured only a few times during the experiment. However, it is neither zero, nor a multiplicative factor of either orbit. The initial and final measured reference orbits are shown in Figure 4.28. The lack of symmetry between the orbits, noted earlier in Figure D.1, is a consequence of the reference orbit(s) shown. When a reference orbit, O_{ref}, is subtracted from the measured orbit perturbations (for data set #3), the corrected orbits are formed accordingly,

$$\begin{aligned} O_1' &= O_1 - O_{ref} \\ O_2' &= O_2 - O_{ref}. \end{aligned} \tag{4.40}$$

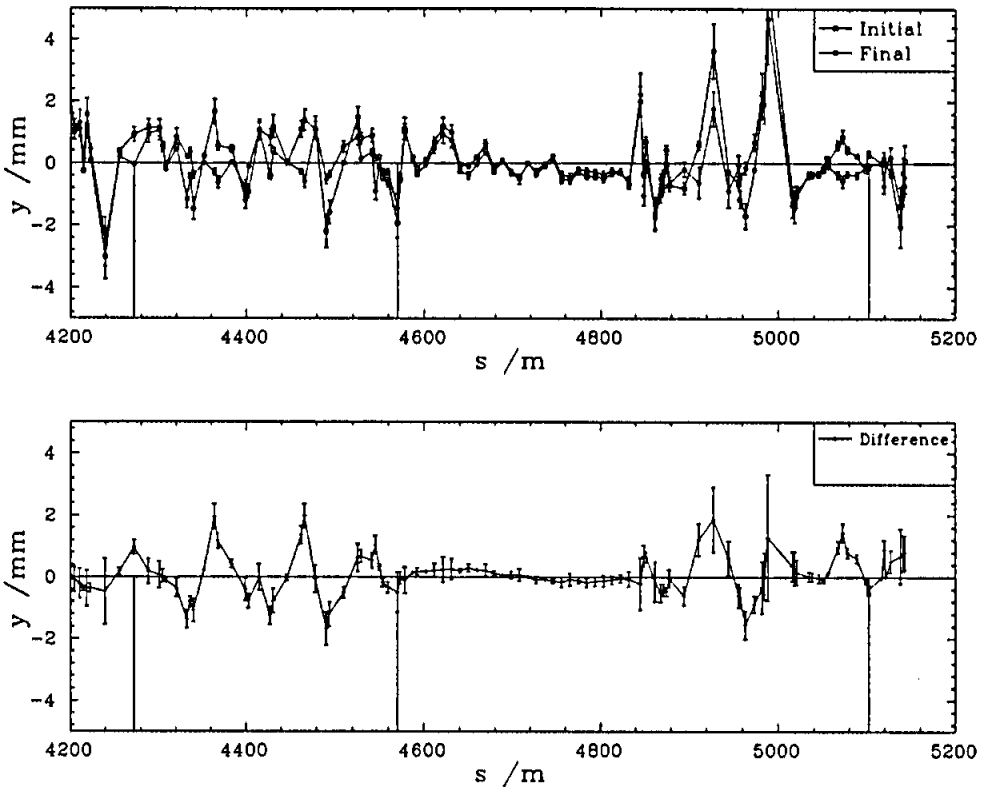

Figure 4.28: The upper plot shows the initial and final reference orbits measured during the experiment (over a 4 day period). The lower plots shows that their difference is comparable to each of the individual reference orbits.

The uncorrected (O_1, O_2) and corrected (O_1', O_2') orbits are shown in Figure 4.29. The corrected orbits clearly show the reversal of the deflection magnet strengths. An overlay of O_1' with $-O_2'$ is shown in the upper plot of Figure 4.30. The lower plot of the same figure indicates that their sum $(O_1' + O_2')$ is nearly zero, or that to a high degree are multiplicative factors of one another. Two important points result. First, the initial conditions to simulate both orbits are identical $(y = y' = 0)$ in this description. They do not require independent initial conditions which effectively contribute to both the reference orbit and also the perturbed orbit. Second, and more importantly, the reference orbit, normalized to zero, is consistent with the model used for the spin tracking simulations. The corrected beam orbits were described using the beam optics program OPTIM. The deflection magnet values which best reproduce the corrected orbits were determined. In this case, they are opposite to one another.

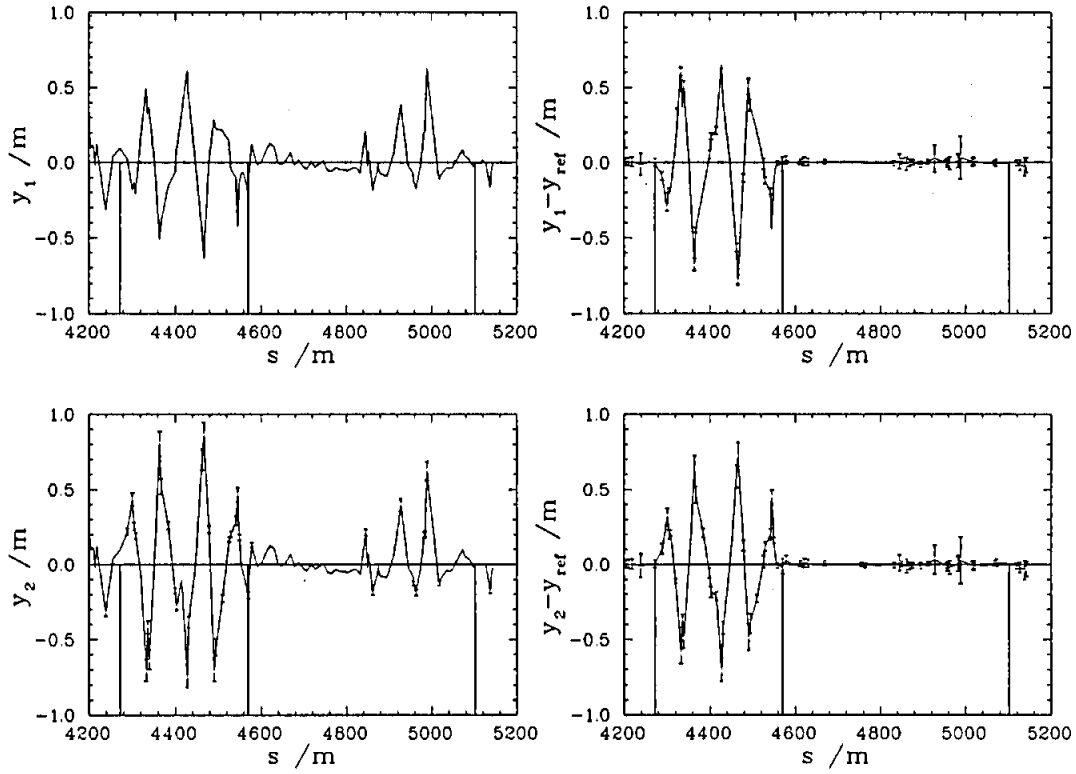

Figure 4.29: The uncorrected orbits (O_1, O_2) are shown in the two leftmost plots. The corrected orbits (O_1', O_2') are shown in the two rightmost plots. The results are from data set #3.

Best fits of the corrected orbit data are shown in Figure 4.31 for data set #3.

Using this orbit correction scheme a reference orbit was subtracted for all of the data sets. Note, however, that reference orbit data was only measured on three occasions over the 4 day experiment. As indicated in Figure 4.28, the reference orbit changed in a substantial way over this time. Unfortunately, more reference orbit data was not measured. The approach taken was to subtract the reference orbit measured closest in time to the data set. After applying the orbit corrections, simulations of the spin tracking were performed.

The spin tracking program numerically integrated the spin motion for the simulated orbits. The initial spin direction in each case was given by $\vec{s}_7$ at the beginning of arc 7. Results from the spin tracking simulations for data set #3 are shown in Figure 4.32. This case describes the simulated spin difference between two maximum

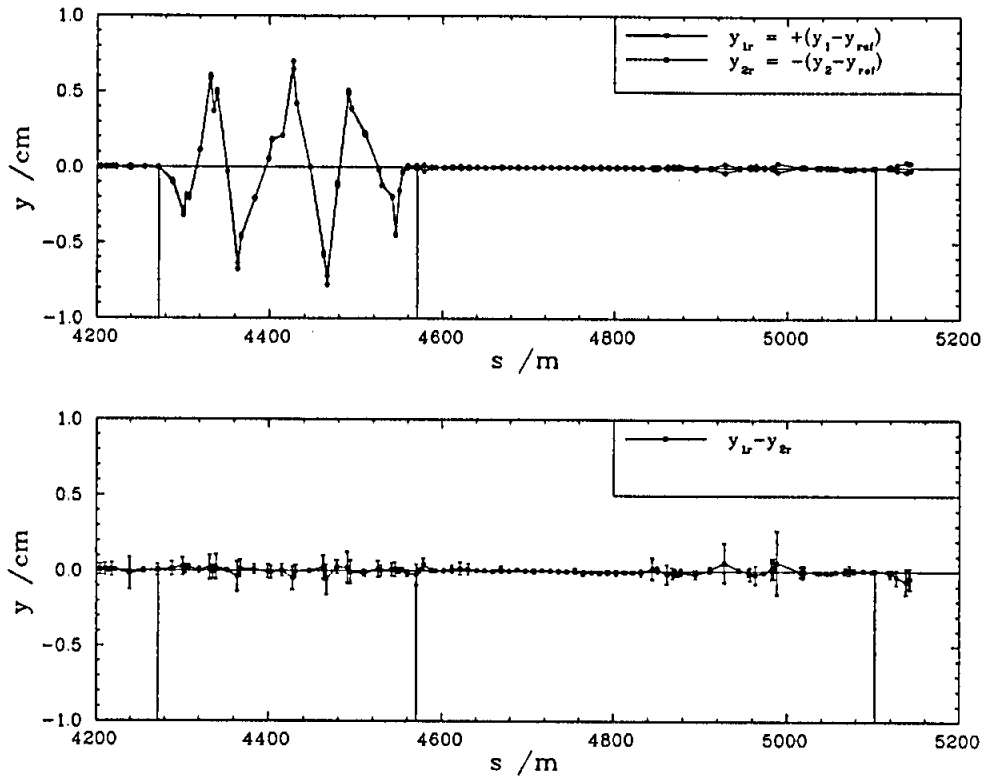

Figure 4.30: The upper plot overlays the corrected orbits O_1' with $-O_2'$ for data set #3. The lower plots is their sum, indicating that $O_1' \sim O_2'$ to a high degree.

(yet, opposing) beam orbit perturbations for an initial spin direction transverse to the accelerator bend plane ($\theta = +90°, \phi = +90°$). The three plots show the *differences* between the three components of the spin orientation between the two orbit perturbations. The plot for δs_y shows the difference in the vertical component of the spin vectors between O_1' and O_2'. The difference increases gradually along the arc. This is because the amplitudes of the two simulated orbits are unequal. Consequently, the spin vectors are rotating away from the vertical direction at different rates from one another. For ideally opposite orbit perturbations this would not be expected. At the quadrupole magnet locations δs_y changes. The horizontal magnetic field in the vertical mid-plane of the quadrupole magnets rotate the two spin vectors in opposing directions. The largest rotations occur at the largest vertical beam displacement along the arc. Although the changes in δs_y are difficult to notice (because they are

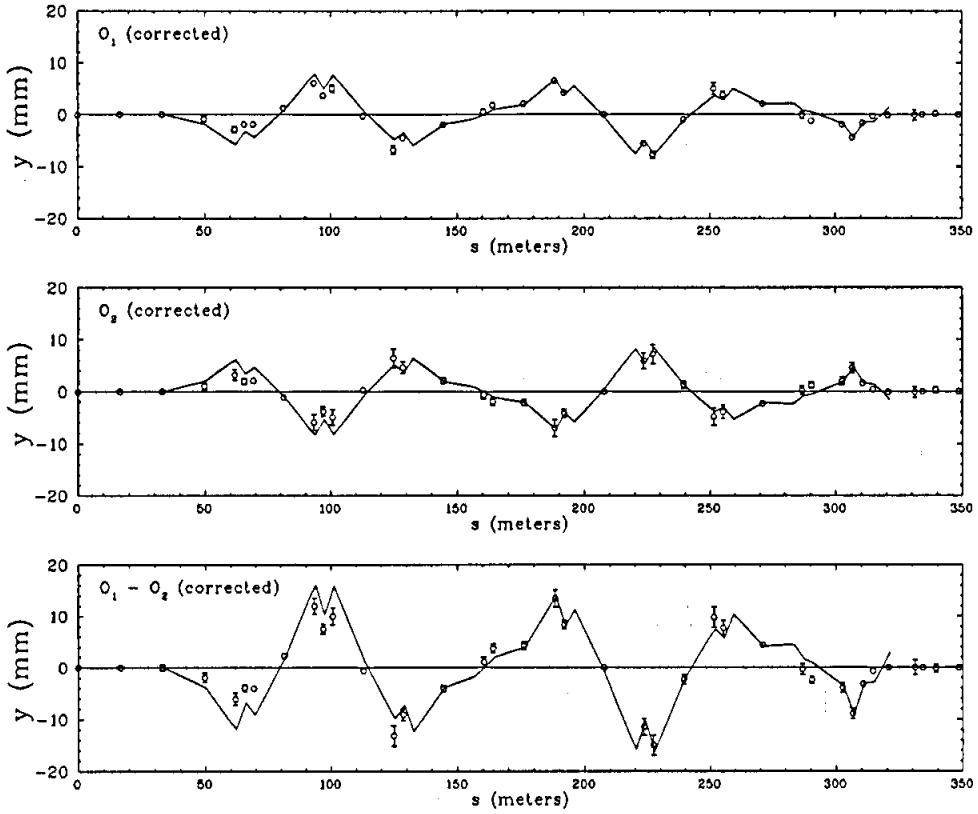

Figure 4.31: Reproducing the corrected orbits for O_1' and O_2' are shown in the upper two plots. The accuracy of the model in reproducing the absolute beam orbit is in this case better than Figure D.1.

both rotating away from the vertical direction similarly), the corresponding change in a bend plane spin component, δs_z, indicates the quadrupole rotations more clearly. Note the scale of the plot for δs_z is larger by a factor of ten. As the two spin vectors precess in the dipole magnets, the difference also rotates. This is apparent in the plot for δs_z as a growth in the amplitude of the difference. Consequently, the effect appears in the plot of δs_x as the difference rotates in the bend plane. However, the quadrupole rotations are not directly apparent because the spin cannot rotate from $\hat{y}$ to $\hat{x}$ by this interaction. Finally, note the zeroes in the amplitude of the oscillations for δs_x and δs_z. These locations in the beamline do not represent cancellations of the effect. Rather, they are simply the locations where the difference in the spin vectors have rotated to a direction transverse to the component being plotted. This can be

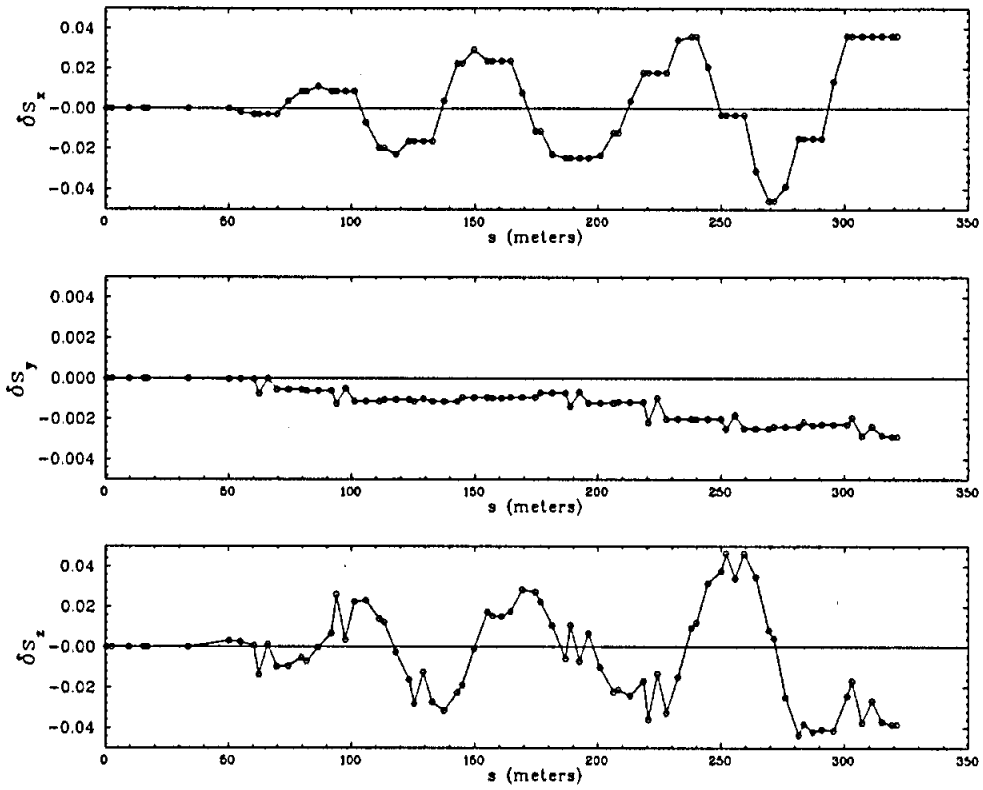

Figure 4.32: Each plot shows the *difference* between the spin component between the two orbit perturbations.

seen as the amplitude of the effect is shifted back and forth between δs_x and δs_z.

The simulation comparison to the measured effect on the beam polarization proceeds as described earlier. First, the polarization orientation at the entrance to arc 7 is calculated for all data sets,

$$\vec{s}_7(\theta, \phi) = R_y(\Psi_{I7}) \cdot \vec{s}_{inj}, \tag{4.41}$$

where $\vec{s}_{inj}$ is the injector spin orientation defined by the polarized gun and spin rotators. The polarization precession angle between the injector and arc 7 is

$$\Psi_{I7} = \left(\frac{g-2}{2}\right)\left(\frac{7.1125 \cdot \overline{E_{linac}}}{m_e}\right) 180^\circ = +3720.9^\circ. \tag{4.42}$$

The resulting difference between spin orientations between the two orbits is given by $\delta\vec{s}$. The resulting difference is then rotated by the polarization precession angle

between the end of arc 7 and the polarimeter, given by

$$\Psi_{7C} = \left(\frac{g-2}{2}\right)\left(\frac{8.1125 \cdot \overline{E_{linac}}}{m_e}\right)(-37.517°) = -290.3°. \tag{4.43}$$

Finally, the longitudinal component of the effect is analyzed at the polarimeter. This result multiplied by the extracted magnitude of the beam polarization, P_0, gives

$$\Delta P_{sim} = P_0 \cdot (R_y(\Psi_{7C}) \cdot \delta\vec{s}) \cdot \hat{z}, \tag{4.44}$$

the simulated effect. The results of the simulation are shown in Figure 4.33. The simulation results underestimate the measured effect by approximately 25%. Comments of the simulation results are described in the final section of this chapter.

4.4.4 Comments on Simulation Results

A satisfying result of the previous section is that a consistent approach of the nominal spin transport model and numerical spin tracking model provide a good starting point to quantifying the *absolute* spin motion (beam orbit) in the accelerator. Still, the final simulation results underestimate the measured effect. This underestimate, though a discrepancy, reveals the systematic uncertainties which were incorporated in the simulation. These are described here for comparison.

Foremost, the greatest sensitivity of the simulation results depend upon a consistent model of the beam orbit motion in the accelerator. The results of the previous section indicate that perhaps the measured reference orbit better describes the average magnetic center of the quadrupoles than do the absolute beam position data for the ideal central orbit. Or perhaps the extent to which the reference orbit is *orthogonal* to the perturbed orbit is the contributing factor. In either case, prediction of the absolute beam orbit (relative to the numerical spin tracking model) provides approximately a 1 mm uncertainty in the beam position. Added linearly to the measured effect, this provides at 10–15% systematic uncertainty in the results.

Another important related factor is the uncertainty in the beam position for larger orbit amplitudes. At larger beam orbit amplitudes (> 2.5 mm) a non–linearity in the

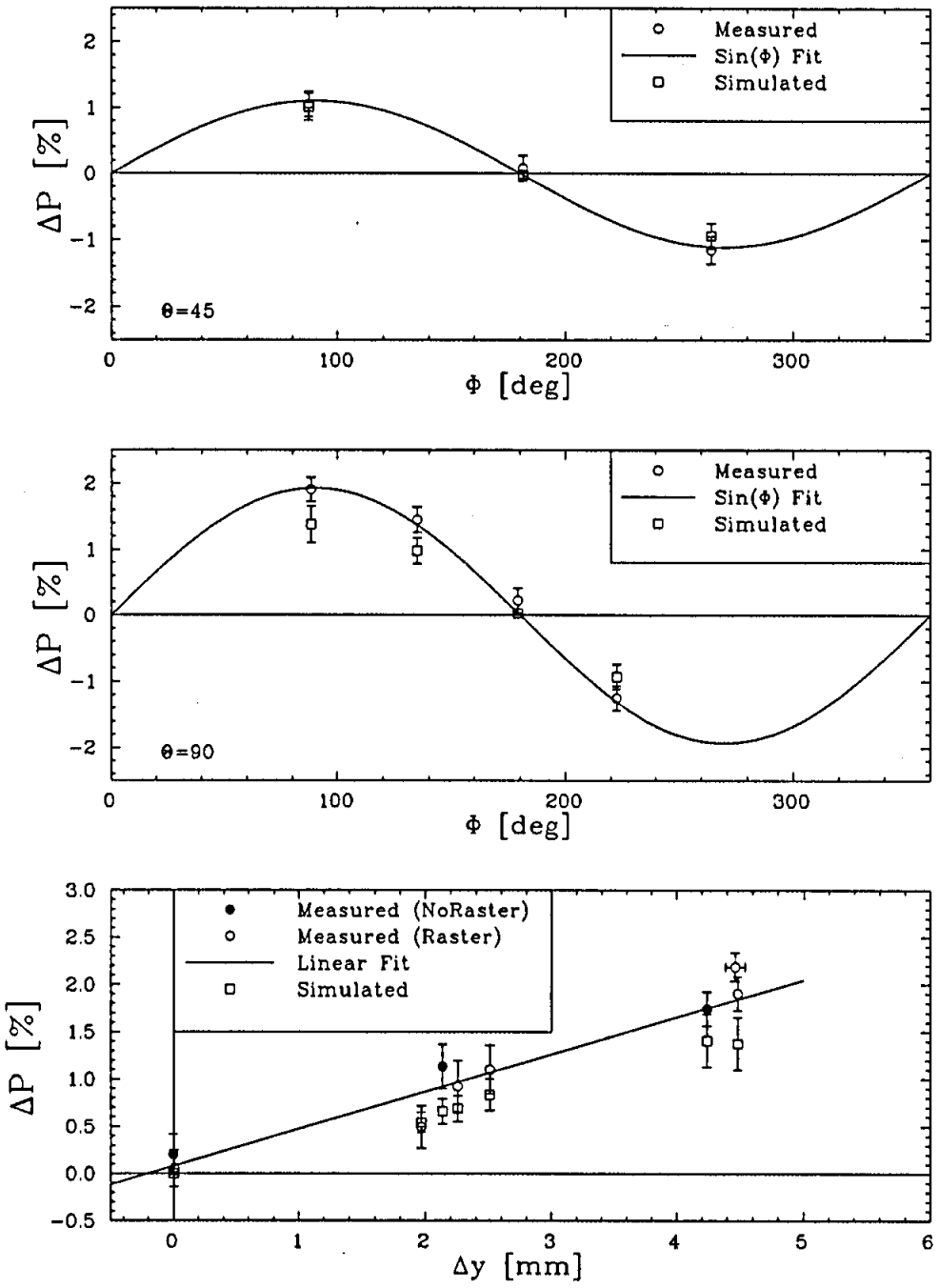

Figure 4.33: The final simulation results are shown alongside the measured effect and the initial simulation results.

response signal of the beam position monitors *underestimates* the beam position. The non-linearity is quadratic on the vertical mid-plane of the BPMs and may underestimate the displacement of the beam position by as much as 5% [De99] (per orbit) at

the largest beam displacements (7 mm). This effect, of course, contributes most when the beam position is near an extrema in its orbit. In the cosine–like approximation, considering the quadratic nature of the underestimate, the effect contributes $< 5\%$ per orbit; or $< 7\%$ when comparing two orbits.

Next, the spin tracking program was considered. Simulations performed of the reference orbit and simple orbit perturbations using the ideal accelerator model agree well with analytic calculations for the nominal spin transport. This is indicative of the capability for the spin tracking program to numerically simulate the spin transport. Although the quadrupole and dipole magnets are included in the numerical spin tracking model, two effects are not treated; edge focusing due to non–normal entry of the dipole magnets and the fringe field effects of the quadrupole magnets.

Edge focusing of the main dipole magnets was considered first. The non–normal entrance to a rectangular dipole magnet (as exists in the arc) results in a vertical focusing of the electron beam. This focusing is geometrically similar to the vertical quadrupole focusing which is predicted to contribute largest to the spin sensitivity effect. The vertical focusing is given by

$$\frac{1}{f_y} = \frac{\tan(\frac{\theta_0}{2})}{\rho_0}, \tag{4.45}$$

where $\theta_0 = 5.625°$ is the nominal non–normal entrance angle to the arc 7 dipole magnets, $\rho_0 = 30.57\,\mathrm{m}$ is the bend radius for the arc 7 dipole magnets, and f_y is the resulting vertical plane focal length. For the CEBAF arc 7 dipole magnets $f_y = 622.3\,\mathrm{m}$. If the beam were displaced to the pole face of the magnet ($y \approx 1.27\,\mathrm{cm}$) the vertical deflection angle would be $\theta_{bend} = 0.0012°$. The resulting precession of the spin would be $\theta_{spin} = a\gamma\theta_{bend} = 0.0081°$. Adding both faces for the 32 dipole magnets in the arc gives no more than 0.52° of precession to the beam polarization. For comparison, a single typical quadrupole in the arc has a field gradient $G \approx 0.50\,\mathrm{kG/cm}$ and a length $l_{quad} = 0.30\,\mathrm{m}$. Assuming the beam were offset $\Delta y = 1\,\mathrm{cm}$ the corresponding deflection angle would be $\theta_{bend} = Gl_{quad}\Delta y = 0.086°$. The corresponding precession for the single quadrupole is $\theta_{spin} = 0.58°$. The dipole edge

focusing is therefore an unlikely candidate, and contributes $< 1\%$ to the total focusing.

The fringe field of a quadrupole magnet is considered next. The spin tracking program treats the quadrupole magnet as hard-edged, so the fringe field is not taken into account. However, an important point here is that that although the quadrupole magnet induces a deflection of beam particles, the extent to which the beam changes position within the magnet is small; this is left to the moment arm of the following drift space. Therefore, to good approximation, the fringe field of a quadrupole magnet simply adds to its *effective length*. For the arc 7 quadrupole magnets ($l = 30\,\text{cm}$) the effective length is approximately one bore radius (1.43 cm) longer. Consequently, the spin tracking program may underestimate the quadrupole focusing by $< 5\%$.

There are other factors, although they are far less significant. For example, the quadrupole field profile is not purely quadrupole. This is because the poles of the magnet are not perfect hyperbolic surfaces. The other contributing *multipole fields* have been measured [Ka99] and contribute to $< 0.5\%$ of the total field as seen by the beam. Another effect, which is small at these beam energies, is due to synchrotron radiation losses. The result is that the beam radiates energy electromagnetically when deflected; largest in the dipole arc bending magnets. Consequently, the spin tune is reduced. However, an estimate of this effect for an entire arc gives the reduction in spin tune to be $< 10^{-3}\%$.

In conclusion, the factors which effect the sensitivity of the beam polarization studied here are those which have the largest impact on the vertical beam focusing. These include the model of the absolute vertical orbit and an accurate description of the vertical focusing EM fields.

Chapter 5

Conclusions

5.1 Summary of Experiment

This experiment studied the sensitivity of the beam polarization to the beam orbit in the recirculation arcs of the CEBAF accelerator. Simulations predict the sensitivity to be due to an interaction of the vertical component of the beam polarization with the horizontal magnetic fields in the vertical plane of quadrupole magnets along the arc. This interaction causes the beam polarization to rotate by an amount calculated to be $\leq 0.05°$ at each quadrupole. A coherence condition results when the interaction of the spin precession frequency (ν_s) and the oscillation frequency of the vertical component of the beam orbit (ν_y) are similar. With this condition satisfied, the rotations of the beam polarization add, generating a larger net effect. Specifically, arc 7 was chosen for the study because near the nominal design energy for arc 7 ($E_{Arc7} = 2.845\,\mathrm{GeV}$) $\nu_s \approx \nu_y = 3$. Simulations predict a 1% effect to the beam polarization for the experiment described.

To perform the experiment a modification and calibration was made to the injector spin rotators to increase the polarization orientation range to $\geq 2\pi$. A injector Mott polarimeter in the 5 MeV region of the accelerator measured two components of the electron beam polarization before it was transported to the main accelerator. A set of deflecting magnets to create, and subsequently remove, an isolated perturbation to the vertical beam orbit in arc 7 were installed. The magnet controls

interleaved two different orbit perturbations in 120 second intervals for many hours reliably. Mis-alignments of the deflection magnets kept coupling of the perturbation into the horizontal orbit suppressed by a factor better than 20:1. A Møller polarimeter was used to measure the longitudinal component of the beam polarization of the electron beam following arc 7, after it was extracted from the accelerator. Correlated position motion of the beam near the polarimeter target to the orbit perturbations was kept within $\Delta x \leq 200\,\mu$m and $\Delta y \leq 50\,\mu$m. This was verified with beam position monitoring sampled during each 120 second interval, and separately by an independent measurement of the beam profile using a beam wire scanner. Experimental asymmetries were measured using Møller scattering to determine the longitudinal component of the beam polarization. To measure the predicted polarization sensitivity a relative difference in the beam polarization was measured between the two orbit perturbations. Measurements of the beam position and profile near the polarimeter target were made. These led to estimates of polarimeter systematics which may affect the results of the experiment. An absolute measure of the beam polarization was not required for this experiment. False asymmetries due to target depolarization by target heating, or the sensitivity of the polarimeter analyzing power due to beam profile or orbit variation, are shown to be small. A beam rastering system was used at the polarimeter target to suppress the target depolarization. Estimates indicate that the target depolarization was absolutely reduced by at most 3%. The variation with orbit perturbation was determined to be $\leq 0.1\%$. Simulations were performed using a Monte Carlo program used for the polarimeter design to estimate the dependence of the effective analyzing power $\overline{A_{zz}}$ to the beam orbit perturbations. Results indicate that the relative effect for target rastering and correlated spot motion is $\leq 0.4\%$. Total systematic uncertainties correlated to the orbit perturbations are $< 0.5\%$.

The experiment measures two effects. First, the polar angles of the beam polarization at arc 7 were varied. The $\sin(\phi)$ dependence agreed reasonably well with the model. However, the expected $\sin(\theta)$ dependence was not accurately predicted (using only one type of reference orbit for both surfaces in θ) by the the simulation. The

experimental disagreement of the $\sin(\theta)$ dependence is approximately 17%. Although the $\sin(\phi)$ dependence describes the angular polarization orientation, the $\sin(\theta)$ dependence describes both the angular orientation and orbit amplitude sensitivities. Because the dependence of the polarization sensitivity is correlated strongly to the absolute knowledge of the beam position for the orbit perturbations, it is more likely that the average reference orbit during the $\theta = 45°$ and $\theta = 90°$ measurements are different. However, without more reference orbit data it is not possible to confirm this hypothesis. The angular polarization orientation is fairly well understood at arc 7, particularly from the spin rotator calibration data and the consistent results from the spin precession energy measurement. If the polarization orientation at arc 7 were largely mis-understood a $\sin(\phi)$ dependence would also be observed, and this is not the case.

Second, the dependence upon the amplitude of the orbit perturbation was measured for a fixed transverse polarization orientation. The measurement of the small polarization effect was determined to increase with orbit amplitude. The scaling is consistent with the linear model predicted for the ideal accelerator. The measurable component of the effect for the conditions in this experiment indicate that the sensitivity of the polarization to the beam orbit is (0.11 ± 0.02) %/mm with an uncertainty of (0.08 ± 0.11)%. For the conditions of this experiment this corresponds to a 1–2 % of the total polarization being projected into the longitudinal direction at the experimental hall.

5.2 Spin Transport Prediction Capability

The spin transport for the accelerator was described in terms of an analytic spin transport model and a numerical spin tracking model. Measurement of the total precession in the accelerator, using the analytic spin transport model, determined the beam energy to be (3407.23 ± 4.08) MeV. Measurement of the beam energy by an independent method (Hall C spectrometer method) determined the beam energy

to be (3411.37 ± 0.85) MeV, providing excellent agreement with the analytic spin transport model.

The spin tracking program MURTLE SPIN22 was used to simulate the spin motion of the electron beam orbit in recirculation arc 7. Simulations performed of the reference orbit and simple orbit perturbations using an ideal accelerator model agree well with analytic calculations for the analytic spin transport calculation. This is indicative of the capability for the spin tracking program to numerically simulate the spin transport.

Spin tracking simulations were performed using a model of the accelerator for comparison with the measured effects. Indeed, a predicted weak sensitivity of the beam polarization to the beam orbit was observed. The accelerator model provided only approximate reproducibility of the absolute measured beam orbit. However, the model does provide a much better description for corrected beam orbits. This point, not expected in the first stage of the analysis, led to a poor simulation reproduction of the measured beam orbits, and spin tracking predictions different by a factor of 2 from what was measured (see Appendix D). Subsequent analysis included an orbit correction scheme, subtracting the best–known measured reference orbit from the measured perturbed orbit. This final description yielded a consistent approach to applying the accelerator model. Consequently, the predictive power of the numerical spin tracking simulations improved. The final simulation results underestimate the measured effect by only 20–30%. However, estimates of the model indicate that the simulation results may be expected to underestimate the effect by 13%. Further, the simulation limit for reproducing the measured beam orbit by better than 1 mm in some locations along arc 7 incurs a systematic uncertainty in the simulation result by approximately 10–15%.

Lastly, spin tracking simulations were performed to estimate the depolarization phenomenon due to the finite emittance of the beam. Using the ideal accelerator model, the predictions indicate the depolarization to be entirely negligible at the present accelerator energies. To the extent that such a small loss in polarization

cannot be measured absolutely between the injector and experimental end station, no such loss in polarization was found.

5.3 Considerations for Accelerator Energy Upgrade

Although no discernible loss in beam polarization was identified in the CEBAF accelerator at the present operating energies, this issue may be more seriously questioned when the accelerator energy is upgraded.

The simulations for the accelerator design were performed for a maximum accelerator energy of 4.045 GeV. However, the maximum energy has already exceeded 5.5 GeV and plans to upgrade the design energy of the accelerator to 12 and then finally 24 GeV already exist. Synchrotron radiation losses of the electron beam grow like E^4/ρ where E is the beam energy and ρ is the bending radius. For the CEBAF accelerator the bending radius remains constant, and at 24 GeV the synchrotron radiation losses increase by more than 10^3 from what they are presently. Consequently, the beam quality (emittance, beam optics) may be different and issues for depolarization phenomena should be considered in more detail.

Finally, the nominal precession of the accelerator would increase substantially. For example, at 24 GeV the first recirculation arc would have a spin tune $\nu_s = 2.99$, almost identical to the present vertical betatron tune $\nu_y = 3.0$. The precession for the entire accelerator at this energy would increase to more than 150 revolutions. Consequently, beam energy measurements (perhaps even for the energy stability) will have an improved resolution due to the increase in γ.

5.4 Suggestions for Future Work

This was an interesting experiment; the first opportunity to study the weakest regime of a polarization "resonance". The experiment revealed that the predictive capability for such accelerators can clearly be made, however, an accurate absolute model is

required to do so. It would be an interesting pursuit to determine the parameter(s) in the present model of the CEBAF accelerator which better describe both the absolute beam orbit and consequently, the polarization sensitivity. With such a model, spin tracking could readily be employed to improve present, or design future, accelerators, carefully optimizing the maximum required beam polarization. If a similar experiment were again undertaken more emphasis would be placed on characterizing the beam orbit (and reference orbit) with a better absolute model. A more modest emphasis would be placed on the systematics for this particular polarimeter. A further minor reduction in the target polarization, for instance, with an increased beam current would only increase the figure of merit. The improvement in the statistics of the measurement would allow for more study of different beam orbits. Practically, this may be complicated due to the radiation background generated downstream of the polarimeter with increased beam current, *however*, it may reveal more about the accelerator.

Appendix A

Total Accelerator Precession

The spin transport model and experience at the CEBAF accelerator indicate the precession of the beam polarization remains in the bend plane of the accelerator to a large extent (within a few degrees). The precession in the bend plane of the accelerator can then be written as the sum of three terms; (a) a Wien filter spin rotation θ_{Wien}; (b) the precession in the first N recirculation arcs ψ_N due to the deflection of the beam momentum in each; (c) and the final precession in a transport arc ψ_{Hall} due to the deflection of the beam momentum to an experimental hall. The total precession is then

$$\psi_{Total} = \theta_{Wien} + \psi_N + \psi_{Hall}. \tag{A.1}$$

The Wien filter is simply a spin rotator and for the rest of this discussion $\theta_{Wien} = 0$ arbitrarily. The precession terms for recirculation and extraction simply depend upon the beam energy and bending angle of each recirculation and transport arc. The steps to do this are simple algebra, yet pedantically shows how the entire machine is summed-up. The energy in the n^{th} recirculation arc (in MeV) is

$$E_n = E_{injector} + n \cdot E_{linac}, \tag{A.2}$$

where $E_{injector}$ is the energy of the injector and is always set to a specific fraction of the linac energy, i.e., $E_{injector} = \alpha E_{linac}$ ($\alpha = 0.1125$). E_{linac} is the average energy of both linacs. Combining these yield

$$E_n = (\alpha + n) \cdot E_{linac}. \tag{A.3}$$

The bend angle of each recirculation arc is $\theta_{bend} = \pi$. By applying Equation 2.6 repeatedly the precession in the first N recirculation arcs is given by

$$\begin{aligned} \psi_N &= \sum_{n=1}^{N} a \left(\frac{E_n}{m_e c^2} \right) \pi \\ &= \frac{a \pi E_{linac}}{m_e c^2} \sum_{n=1}^{N} (\alpha + n). \end{aligned} \tag{A.4}$$

By using the Euler's relation, $\sum_{n=1}^{N} n = \frac{N(N+1)}{2}$, the precession is compactly written as

$$\psi_N = \frac{a \pi E_{linac}}{m_e c^2} \left(\alpha N + \frac{N(N+1)}{2} \right). \tag{A.5}$$

When the beam is extracted after the N^{th} recirculation arc ($N = 1, 3, 5, 7, 9$) a final pass of the south linac increases the beam energy prior to an extraction transport arc to

$$E_{Hall} = (\alpha + N + 1) \cdot E_{linac}. \tag{A.6}$$

The bending angles for the three experimental halls are given in Table A.1 in units of degrees and units of π, that is, $\theta_{Hall} = \hat{\theta}_{Hall} \pi$. The precession in the transport arc

θ_{Hall}	Hall A	Hall B	Hall C
(deg)	$+37.50\,^\circ$	$+0\,^\circ$	$-37.52\,^\circ$
(rad)	$+0.2083\,\pi$	$+0\,\pi$	$-0.2084\,\pi$

Table A.1: The bending angle for the three experimental halls. Halls A and C are symmetrical to one another about Hall B.

to a given experimental hall is,

$$\begin{aligned} \psi_{Hall} &= a \left(\frac{E_{Hall}}{m_e c^2} \right) \theta_{Hall} \\ &= \frac{a \pi E_{linac}}{m_e c^2} (\alpha + N + 1) \cdot \hat{\theta}_{Hall}. \end{aligned} \tag{A.7}$$

By summing ψ_N and ψ_{Hall},

$$\psi_{Total} = \frac{a \pi E_{linac}}{m_e c^2} \left[N\alpha + \frac{N(N+1)}{2} + (\alpha + N + 1)\hat{\theta}_{Hall} \right]. \tag{A.8}$$

Since the beam can only be extracted after full circuits, or passes, of the accelerator it is more convenient to write this result in terms of the pass number p. It is easy to convince oneself that the last recirculation arc, N, seen by the beam for p passes is given by the relationship $N = 2p - 1$. Making this substitution we have finally

$$\psi_{Total} = \frac{a\pi E_{linac}}{m_e c^2}\left[2p^2 - p(1 - 2\hat{\theta}_{Hall} - 2\alpha) - \alpha(1 - \hat{\theta}_{Hall})\right]. \qquad \text{(A.9)}$$

Appendix B

Calculation of Injector Spin Rotator Angles

The product of the rotations of the three spin manipulators transforms the polarization vector at the electron gun, $\vec{P}_{Gun}$, to a polarization vector exiting the spin manipulation system, $\vec{P}_{SM}$,

$$\vec{P}_{SM} = R_z(\phi_{Solenoid_2}) \cdot R_z(\phi_{Solenoid_1}) \cdot R_y(\theta_{Wien}) \cdot \vec{P}_{Gun}, \tag{B.1}$$

The rotation matrices about the i_{th} $(i \in x, y, z)$ axis are given by $R_x(\theta)$, $R_y(\theta)$, and $R_z(\theta)$. A positive rotation

$$R_x(\theta) = \begin{pmatrix} 1 & 0 & 0 \\ 0 & \cos\theta & \sin\theta \\ 0 & -\sin\theta & \cos\theta \end{pmatrix},$$

$$R_y(\theta) = \begin{pmatrix} \cos\theta & 0 & \sin\theta \\ 0 & 1 & 0 \\ -\sin\theta & 0 & \cos\theta \end{pmatrix},$$

$$R_z(\theta) = \begin{pmatrix} \cos\theta & -\sin\theta & 0 \\ \sin\theta & \cos\theta & 0 \\ 0 & 0 & 1 \end{pmatrix}. \tag{B.2}$$

angle is given by the right-hand rule. Because the rotations in the two solenoid magnets are about the same axis and are in series they commute, where $\phi_{S_{12}} =$

$\phi_{Solenoid_1} + \phi_{Solenoid_2}$, giving,

$$\begin{aligned}
\vec{P}_{SM} = & \quad R_z(\phi_{S_{12}}) \cdot R_y(\theta_{Wien}) \cdot \vec{P}_{Gun} \\
= & \begin{pmatrix} \cos\theta_{Wien}\cos\phi_{S_{12}} & -\sin\phi_{S_{12}} & \sin\theta_{Wien}\cos\phi_{S_{12}} \\ \cos\theta_{Wien}\sin\phi_{S_{12}} & \cos\phi_{S_{12}} & \sin\theta_{Wien}\sin\phi_{S_{12}} \\ -\sin\theta_{Wien} & 0 & \cos\theta_{Wien} \end{pmatrix} \cdot \vec{P}_{Gun}. \qquad \text{(B.3)}
\end{aligned}$$

For the case $\vec{P}_{Gun} = (0, 0, \pm P_0)$ we find the trivial solution,

$$\begin{pmatrix} P_x \\ P_y \\ P_z \end{pmatrix}_{SM} = P_0 \begin{pmatrix} \sin\theta_{Wien}\cos\phi_{S_{12}} \\ \sin\theta_{Wien}\sin\phi_{S_{12}} \\ \cos\theta_{Wien} \end{pmatrix}, \qquad \text{(B.4)}$$

because the Wien filter and solenoids produce simple rotations in the standard spherical coordinate system. The condition for setting the rotation angles of the spin manipulator involves choosing $(\theta_{Wien}, \phi_{S_{12}})$ such that a final polarization, $\vec{P}_{final}$, is reached in an experimental area. The final polarization is determined by all of the intervening spin rotations (about 3 possible axes) of the accelerator. The final polarization can be written as the product of N additional rotations,

$$\vec{P}_{final} = \prod_{j=1}^{N} \left(R_{ij}(\theta_j) \right) \cdot \vec{P}_{SM}, \qquad \text{(B.5)}$$

where the j^{th} rotation is due some precession θ_j about the i^{th} axis. If the simple spin transport model for the accelerator is correct then this product of rotations due to the recirculation and transport arcs are all about the same $\hat{y}$ axis. In this case, all of the rotations commute and add simply giving,

$$\begin{aligned}
\vec{P}_{final} = & \quad R_y(\Theta) \cdot \vec{P}_{SM}, \\
= & \quad P_0 \begin{pmatrix} \cos\Theta & 0 & \sin\Theta \\ 0 & 1 & 0 \\ -\sin\Theta & 0 & \cos\Theta \end{pmatrix} \cdot \begin{pmatrix} \sin\theta_{Wien}\cos\phi_{S_{12}} \\ \sin\theta_{Wien}\sin\phi_{S_{12}} \\ \cos\theta_{Wien} \end{pmatrix}, \\
= & \quad P_0 \begin{pmatrix} \sin\theta_{Wien}\cos\phi_{S_{12}}\cos\Theta + \cos\Theta\sin\theta_{Wien} \\ \sin\theta_{Wien}\sin\phi_{S_{12}} \\ -\sin\theta_{Wien}\cos\phi_{S_{12}}\sin\Theta + \cos\Theta\cos\theta_{Wien} \end{pmatrix}, \qquad \text{(B.6)}
\end{aligned}$$

where $\Theta = \sum_{j=1}^{N} \theta_j$ is the net sum of bending angle through which the beam momentum was deflected in the accelerator. These equations and the conditions that $|\vec{P}_{final}| = 1$ determine $(\theta_{Wien}, \phi_{S_{12}})$.

The most trivial solution is for the case where the final polarization is to be longitudinal at the experimental area ($\vec{P}_{final} = \pm P_0 \hat{z}$). The solution then gives that $\phi_{S_{12}} = 0$ (polarization in bend plane and $\theta_{Wien} = -\Theta$ (modulo 2π).

Appendix C

Solenoid Magnets: Focusing and Spin Rotation

Because the beam transport through the injector should remain constant it is necessary to find a solution that allows the focal lengths of the two solenoid spin rotators to remain constant (maintaining the injector optics) while the spin rotation angle Θ_{spin} of each can be varied.

Consider the halves of the solenoid magnet. Each half contains a coil; the first (second) coil referred to as A (B). The wiring of the coils is such that the longitudinal magnetic field, B_z, produced by each coil for positive current, point in opposite directions. As an example, consider the longitudinal magnetic field profile for this situation in the upper plot of Figure C.1. The lower plot of the same figure shows the square of the magnetic field profile, B_z^2, which determines the focal length of the magnetic. Because the magnetic field profile due to each coil scales linearly with the peak magnetic field (or coil current) the total spin rotation of the magnet can be written as

$$\begin{aligned}
\Theta_{spin} &= \frac{ge}{2mv\gamma} \cdot \int B_z dl \\
&= \frac{ge}{2mv\gamma} \cdot \int (B_{zA} + B_{zB}) dl \\
&= \frac{ge}{2mv\gamma} \cdot (\int B_{zA} dl + \int B_{zB}) dl \\
&= \widetilde{B_A} \cdot G_1 + \widetilde{B_B} \cdot G_2, \qquad \text{(C.1)}
\end{aligned}$$

where $\widetilde{B_A}$, $\widetilde{B_B}$ are the peak magnetic fields of each solenoid profile and G_1, G_2 absorb

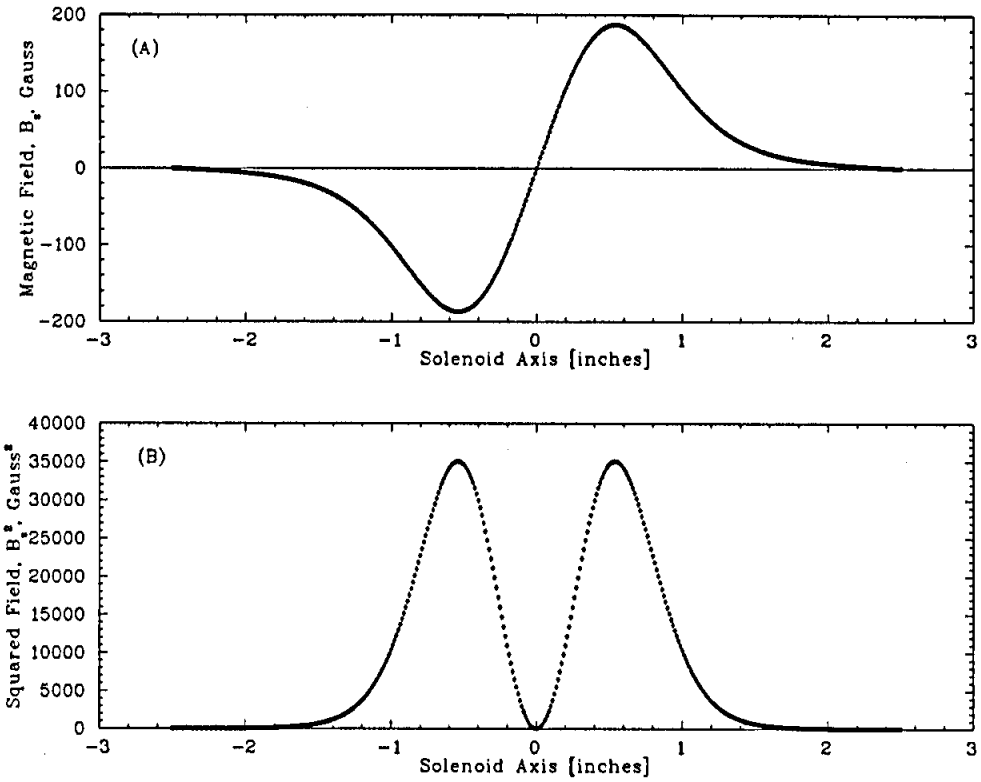

Figure C.1: Magnetic field orientation profile for one of the injector solenoid spin rotators with positive current in each of the two coils.

the field integral of the magnet.

Similarly, an expression for the inverse focal length can be written as

$$\begin{aligned} F_{focus} &= \frac{e^2}{(2mv\gamma)^2} \cdot \int B_z^2 dl \\ &= \frac{e^2}{(2mv\gamma)^2} \cdot \int (B_{zA} + B_{zB})^2 dl \\ &= \frac{e^2}{(2mv\gamma)^2} \cdot (\int B_{zA}^2 dl + 2\int B_{zA}B_{zB} dl \int B_{zB}^2 dl) \\ &= H_1 \cdot \widetilde{B_A}^2 + 2H_{12} \cdot \widetilde{B_A}\widetilde{B_B} + H_2 \cdot \widetilde{B_B}^2, \end{aligned} \tag{C.2}$$

where $\widetilde{B_A}^2$, $\widetilde{B_B}^2$ are the peak magnetic field squared of each solenoid profile and H_1, H_2 absorb the field integral of the magnet. However, because the total integral adds the field profiles in quadrature a cross-term exists relating them. This non-linear overlap provides the condition for meeting both the constant focal length and

variable spin rotation requirements. The results of the two equations can be solved to determine the the two peak fields $\widetilde{B_A}$ and $\widetilde{B_B}$ in terms of the fixed focal length strength. The coefficients are found by using a field map of the solenoid magnet or simulating the profile using a codes like POISSON / SUPERFISH [Me87].

Using the design focal length for each of the two spin rotators in the injector the set of peak fields (and magnet currents) are calculated in terms of the possible spin precession in each magnet. Simulation plots of Θ_{spin} as a function of the current in each half of the solenoid magnet are shown in Figure C.2 for both solenoid spin

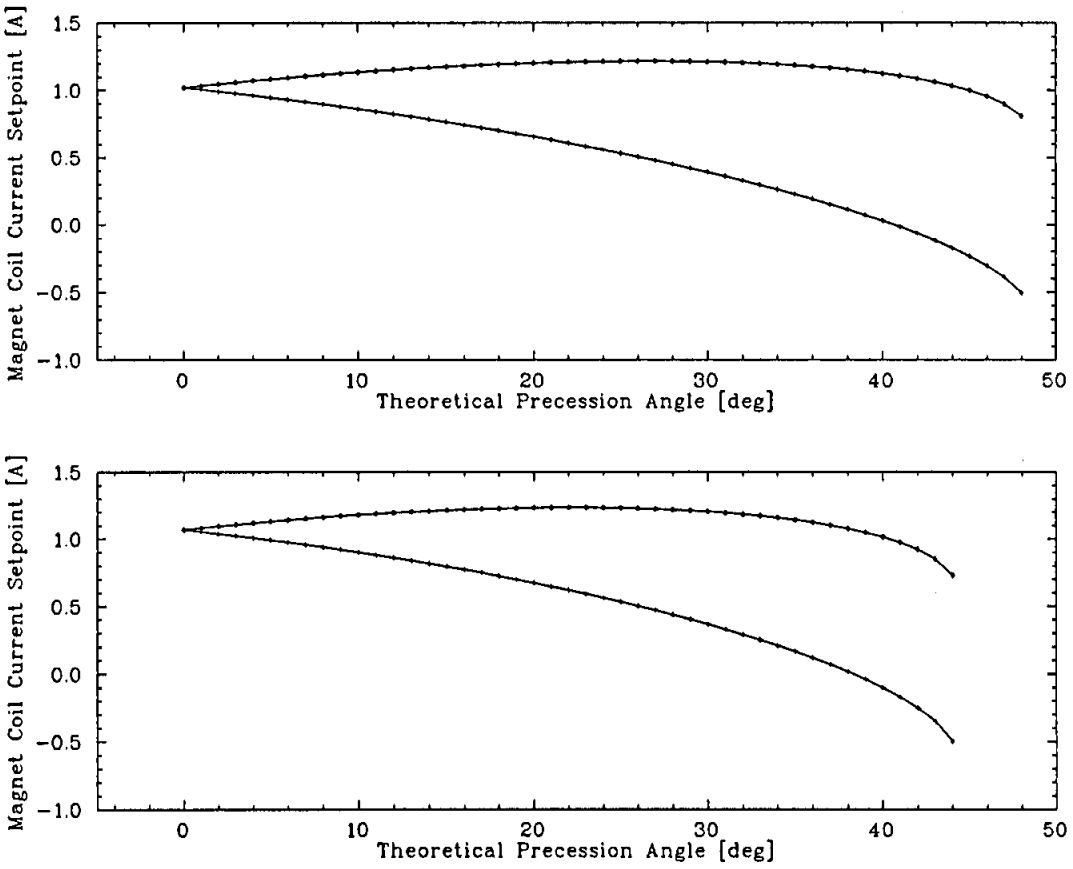

Figure C.2: Current setpoints for S_1 (upper) and S_2 (lower) solenoid spin rotators. In each plot the upper curve is for the first coil (A) and the lower curve is for the second coil (B) in the magnet.

rotators. The coefficients for the first solenoid rotator (S_1) are $G_1 = -G_2 = 1.2166$, $H_1 = H_2 = 0.308$, and $H_{12} = -0.1506$. The coefficients for the second rotator (S_2) are

$G_1 = -G_2 = 3.2066$, $H_1 = H_2 = 2.1036$, and $H_{12} = -0.1052$. It is clear that the spin rotation angle is zero when the coil currents are equal (coils drive current in opposing directions). Again, refer to Figure C.1 for an example of this case. The integral of the asymmetrical curve in the upper plot is clearly zero, and determines Θ_{spin}, yet the integral of the lower plot is non-zero, and determines the magnet focusing. Finally, upper bound of the spin rotation in each magnet is limited to the extent that the geometry of the magnet overlaps the two field profiles. For this magnet design that maximum precession angle is $\approx 45°$.

Appendix D

Simulation Results for the Flat Reference Orbit

Reproducing the absolute measured beam orbit proved difficult. By varying the vertical position and angle of the beam orbit at the entrance to arc 7 (y_0, y_0') beam optics simulations improved reproducing the beam position data. Nevertheless, the overall reproducibility of the measured beam orbit indicates that the optics model used for describing the arc does not reproduce the absolute beam orbit very well. An uncertainty of approximately $1 - 2\,\mathrm{mm}$ is associated with this method.

To perform spin transport simulations the OPTIM model description was converted to a TRANSPORT description for use with the spin tracking program. A simulation result for reproducing both orbits (O_1 and O_2) is shown in Figure D.1. Also shown in their calculated difference $(O_1 - O_2)$. Two points are are clear. First, the initial beam conditions entering the arc which best describe the individual beam orbits are artificial. That is, they are different from one another which physically is not true. However, these initial conditions best describe the absolute orbit within the arc and were pursued during this stage of the analysis. Second, the difference plot indicates that the betatron phase between the simulated and measured orbit is not constant. This may indicate that the focusing description of the model does not entirely describe the real condition. Note particularly that there are locations where the simulated and measured position of the beam fall on opposite sides of the bend plane $(y = 0)$. In sum, these two points affect the simulated spin rotations for both orbits.

Using the analysis technique described in Section 4.4.3 and Section 4.4.2 a com-

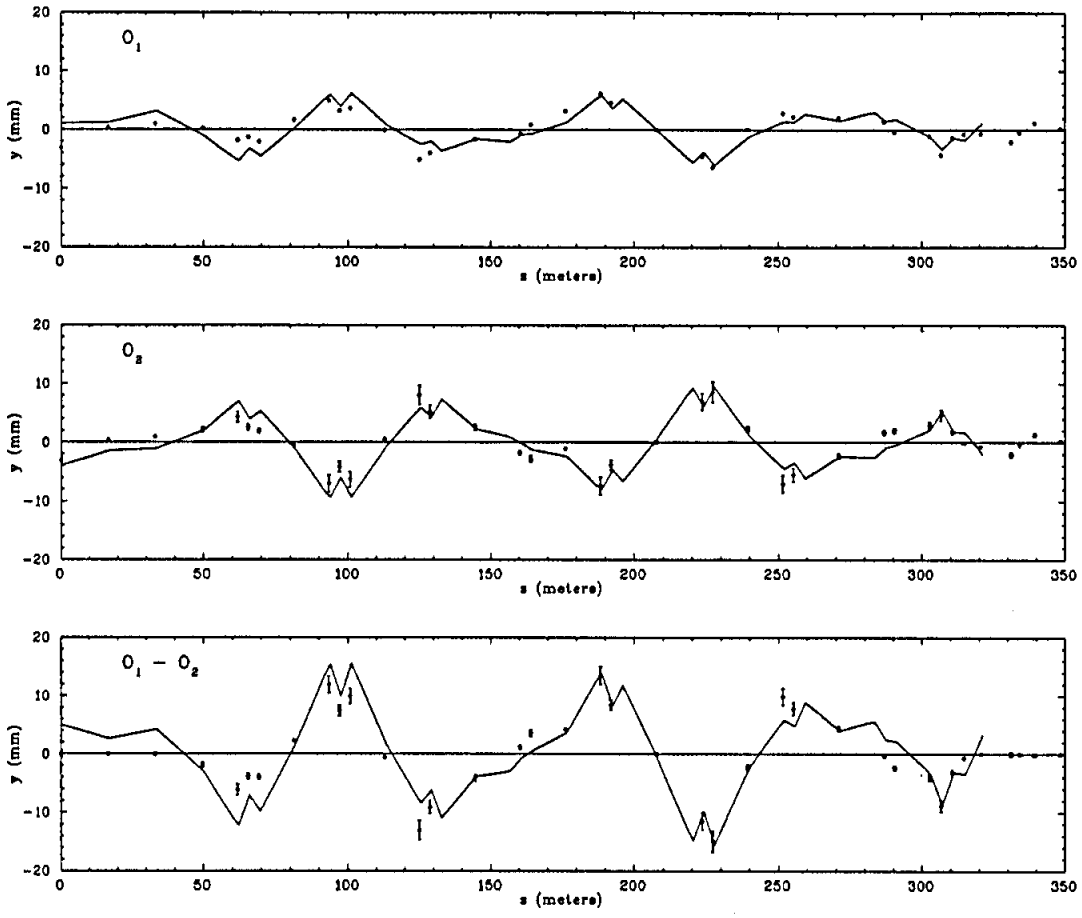

Figure D.1: Reproducing the absolute orbits for O_1 and O_2 are shown in the upper two plots. The accuracy of the model in reproducing the absolute beam orbit is approximately $1 - 2\,\mathrm{mm}$.

parison between the experiment and simulation is made for the ideal *flat* reference orbit. The results are shown in Figure D.2. The simulations underestimate the magnitude of the effect by approximately a factor of 2 in most cases. The expected $\sin(\phi)$ angular dependence is correctly given, however, the $\sin(\theta)$ dependence (which measures the strength of the effect) also gives an underestimate. The discrepancy of the simulation with the experiment was, at first, surprising.

The initial approach to distinguish the source of the underestimate began by separating the nominal transport model from the numerical spin tracking model. An observation made of the initial spin transport model is that only a component of the

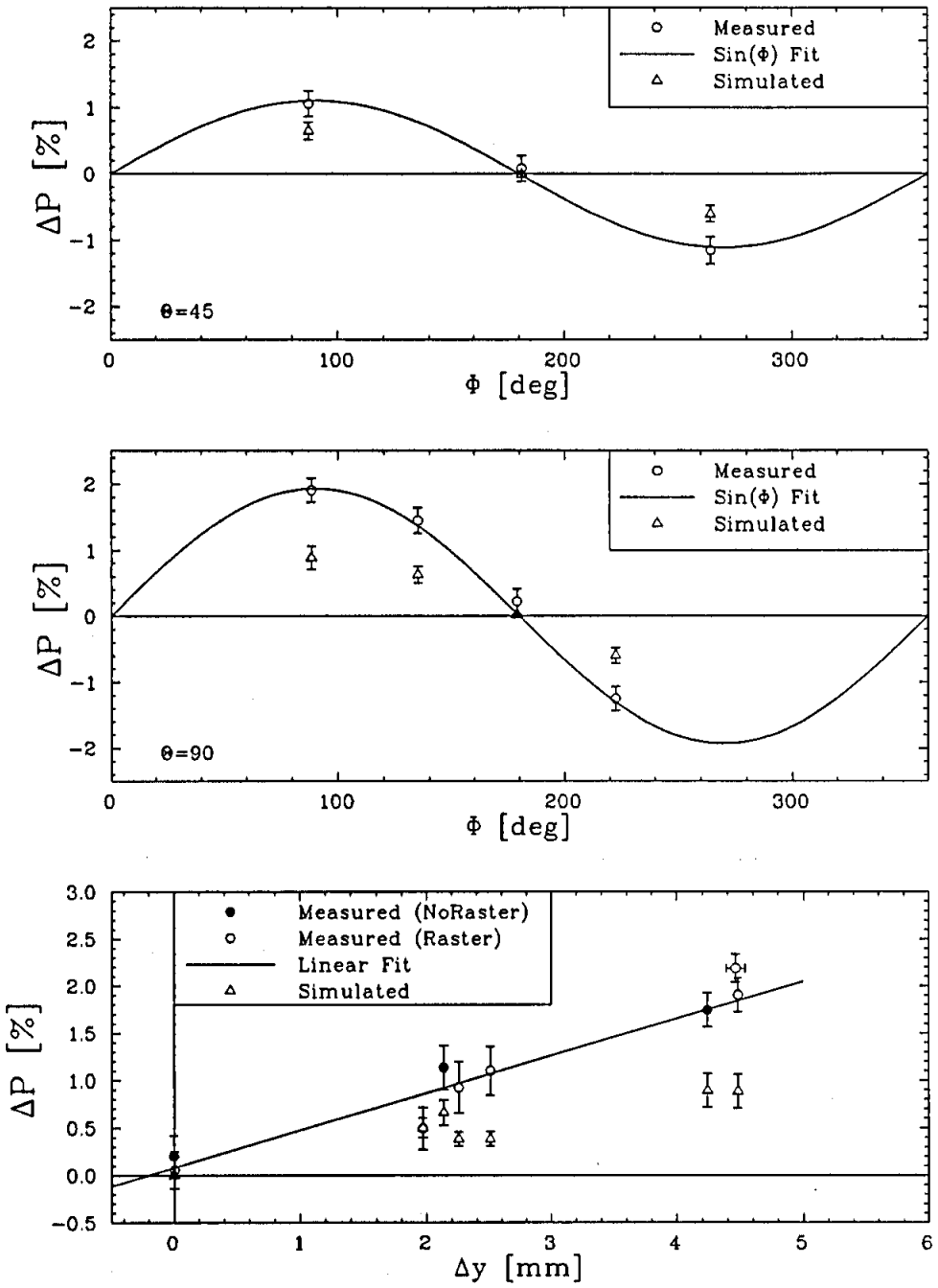

Figure D.2: The measured polarization sensitivity is shown alongside the simulation results for all of the experiment data.

simulation effect is resolved at the polarimeter. In other words, $|\delta\vec{s}| > |\delta\vec{s}_{meas}|$. To make this point three quantities are compared; (a) the *magnitude* of the simulation effect, $|P_{sim}|$; (b) the *measurable component* of the simulation effect, $|P_{sim}|_{Møller}$; (c)

and the data for the experiment $|\Delta P|$. The three quantities are plotted in Figure D.3. Although the measurable component of the simulation is smaller than the experimen-

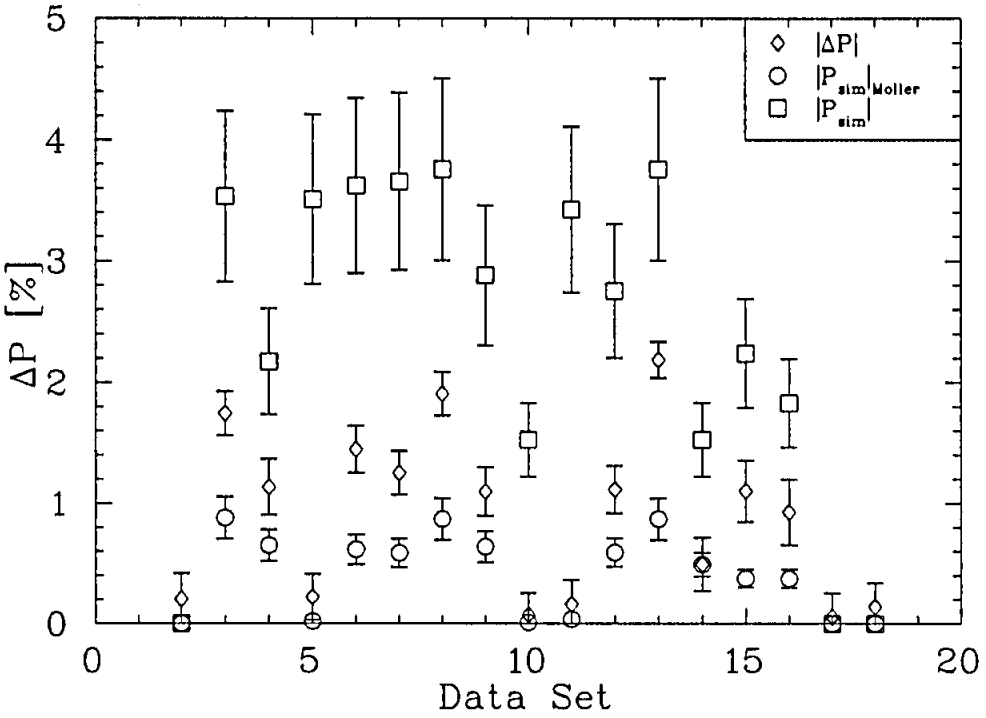

Figure D.3: Comparison of the relative size of the total, $|P_{sim}|$, and projected, $|P_{sim}|_{Møller}$, simulation effect with data for the experiment.

tal results, it is clear that the magnitude of the total simulation effect is largest in all non–zero cases. For the null effect, the results are comparable with the uncertainty of the measurement.

This observation is consistent with a geometrical scale factor. In other words, a rotation of the simulation effect, $\delta\vec{s}$, can increase or decrease the measurable effect. Consequently, calculations were performed to determine if a single rotation (simplest case) of the simulation results could account for the discrepancy. A rotation in the accelerator bend plane was considered foremost because the factor would need to be large, approximately a factor of 2. It was determined that a single rotation of $\approx +14°$, applied finally to all simulations results, improved the prediction of the measurement substantially. A comparison is made in Figure D.4 where the rotation has already

been applied to all of the simulation results.

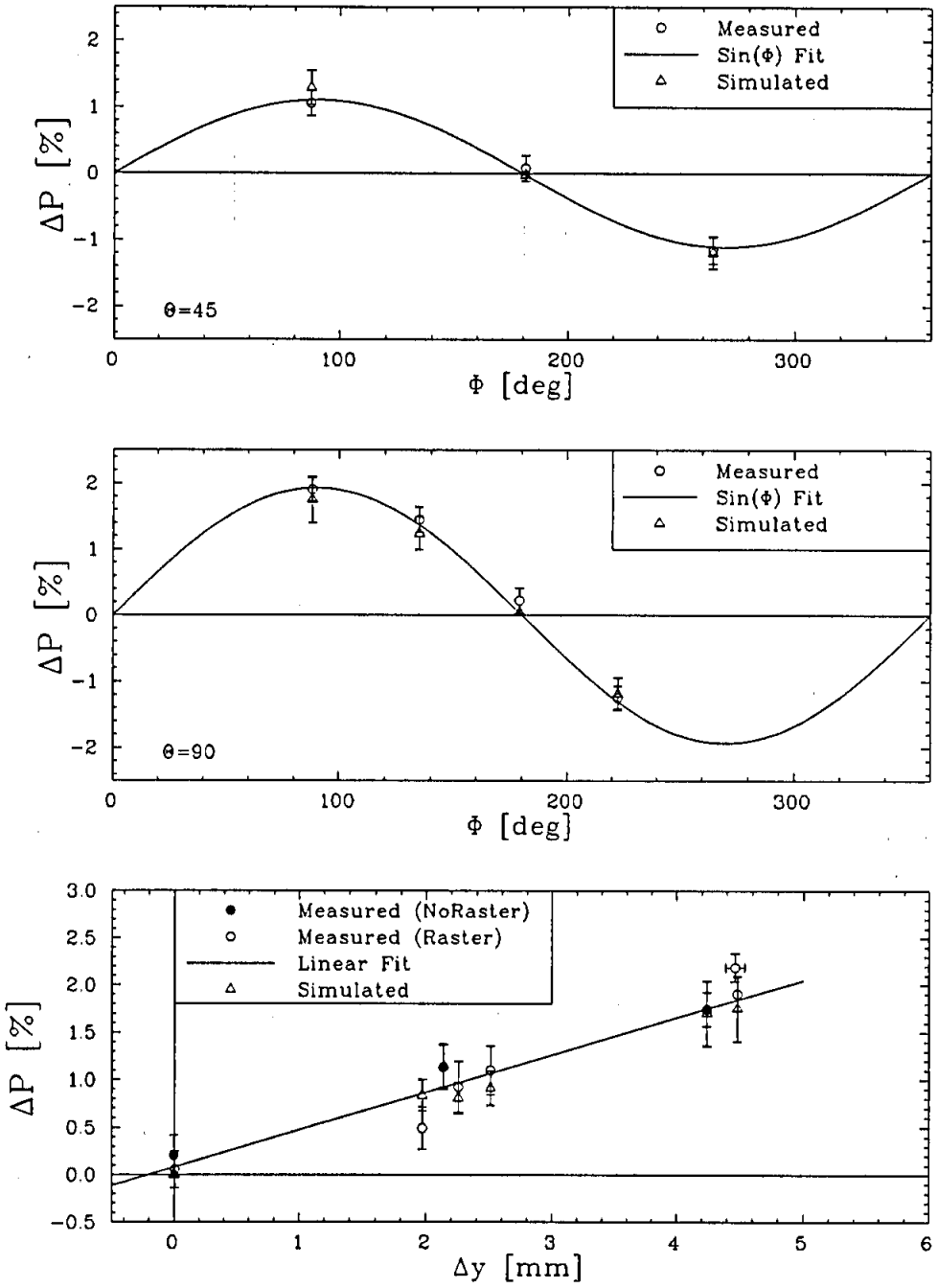

Figure D.4: The measured polarization sensitivity is shown alongside the simulation results (rotated by $\approx +14°\hat{z}$) for all data sets.

The important point to consider is whether the nominal spin transport model

of the accelerator is consistent with this explanation. If the nominal spin transport model is considered as the source of the discrepancy, the most likely explanation requires that the precession of the accelerator was different by the rotation angle, +14°. Accounting for a +14° precession difference of the nominal spin transport, even at the greater arc beam energies (larger γ), in the CEBAF accelerator is difficult. The effect would have to appear following the orbit perturbations in arc 7, as the result depends upon the difference. If the excess precession were gained gradually through the earlier part of the accelerator, then the spin direction at the beginning of arc 7 would have been different than expected. The $\sin(\phi)$ dependence would then be modified, and this was not observed in the data. Further, simulations were performed to vary the spin orientation at arc 7 by amounts comparable with a +14° rotation. No substantial improvement was found. Consequently, this is an unlikely cause of the discrepancy.

The alternative is that the excess precession would appear following the orbit perturbations. For example, the corresponding dipole deflection angle required to explain the rotation in arc 7 (2.989 GeV) is an additional +1.81°. In the Hall C arc (3.409 GeV) an additional +2.06° deflection angle is required. Both explanations represent more than a 1% correction to the transport arc bend angle. Similarly, more than a 1% correction to the beam energy is required to generate the +14° precession for the given bend angles. Such large corrections are simply inconsistent with the operation of the accelerator. Perhaps an even more satisfying result, of the nominal spin transport model, is the excellent agreement of the final beam energy determined by the spin precession technique with alternative methods used during the experiment. Such a result is in direct conflict with the explanation being a discrepancy of the nominal spin transport model. The conclusions of Chapter 4, rather, do indicate that the absolute knowledge of the beam orbit relays the information required to consistently describe the absolute spin motion of the beam polarization.

References

[Ba59] V. Bargmann, L. Michel, V.L. Telegdi, Phys. Rev. Lett, **2**, 435–436 (1959).

[Ba78] T. Baumeister, Editor–in–Chief, *Marks' Standard Handbook for Mechanical Engineers, Eighth Edition*, McGraw–Hill Book Company, New York, NY (1978).

[Be93] D.H. Beck, *G0 Technical Design Report*, University of Illinois at Urbana–Champaign, (1993).

[Br77] K.L. Brown, F. Rothacker, D.C. Carey, and Ch. Iselin, TRANSPORT, A Computer Program for Designing Charged Particle Beam Transport Systems, SLAC Report No. 91 (1977).

[Br85] K.L. Brown, D. Douglas, R.V. Servranckx, L. Schachinger, Users Guide to the Program Dimad, SLAC Report 285 UC-28 (A), May, 1985.

[Ca92] L.S. Cardman, *Polarized Electron Sources for the 1990's*, Nuclear Physics A**546**, 317c-336c (1992).

[Car92] D.C. Carey, *The optics of charged particle beams.*, Harwood Academic Publishers, United Kingdom (1992).

[Ch82] A. Chao, *Polarized Beams in High Energy Circular Accelerators*, PEP Note 301, Stanford Linear Accelerator Center, Stanford, CA (1979).

[Co87] E. Cohen, *The 1986 Adjustment of the Fundamental Physical Constants*, Rev. Mod. Phys., Vol.59, No. 4, 1121 (1987). g_e reported by van Dyck, Schwinberg, and Dehmelt (1984) at the University of Washington.

[Cd99] The Common DEVice interface. CEBAF internal document.

[De99] J.C. Denard, private communication.

[Du93] B.M. Dunham, *PhD Thesis*, University of Illinois at Urbana-Champaign (1993).

[En93] D.A. Engwall, B.M. Dunham, L.S. Cardman, D.P. Heddle, and C.K. Sinclair, *A spin manipulator for electron accelerators*, Nuclear Instruments and Methods in Physics Research, **A324** (1993) 409-420.

[LANL] *Experimental and Physics Industrial Control System (EPICS)* was developed jointly by LANL, ANL, CEBAF, LBL, BNL, and DESY.

[Fi95] T.H. Fieguth, private communication.

[Fr60] M. Froissart, R. Stora, Nuclear Instruments and Methods, **7** (1960) 297.

[Ga92] T.J. Gay, F.B. Dunning, *Mott electron polarimetry*, Rev. Sci. Instrum., 63(2), 1635-1651 (1992).

[Gue96] A. Guerra, private communication.

[Gue97] A. Guerra, private communication.

[Gu99] P. Gueye, private communication.

[He90] E. Hecht, *Optics, 2nd Edition*, Addison-Wesley Publishing Company, (1990).

[Ja75] J.D. Jackson, *Classical Electrodynamics*, Wiley, New York, (1962).

[Ka99] J. Karn, private communication, and L. Harwood *et. al, Magnet Design and Performance for the CEBAF Beam Transport System*, Internal CEBAF Technical Note.

[Ke41] D. W. Kerst, R. Serber, Phys. Rev. **60**, 53 (1941).

[Ki81] T. Kinoshita and W.B. Lindquist, *Eighth-Order Anomalous Magnetic Moment of the Electron*, Phys. Rev. Let., Vol. 47, No. 22, 1573 (1981).

[La] C. Larrieu, *ezlog, version 1.2*, a program for logging EPICS channel data to disk at slow rates ($< 1Hz$), based on a code *kalog* written by Kurt Brown.

[La77] J.D. Lawson, *The Physics of Charged Particle Beams*, Oxford University Press, (1977).

[Le92] L. Levchuk, *The Intra-Atomic Motion of Bound Electrons as a Possible Sourcfe of a Systematic Error in Electron Beam Polarization Measurements by Means of a Møller Polarimeter*, (1992); Nucl. Instr. and Meth. **A311** 496 (1994).

[Le99] V. Lebedev, author of OPTIM.

[Li63] S. Lin, N. Sherman, and J.K. Percus, *Elastic Scattering of Relativistic Electrons by Screened Atomic Nuclei*, Nuclear Physics **45** (1963) 492-504.

[Lo96] M. Loppacher, PhD Thesis, University of Basel, Switzerland (1996).

[Li93] T. Limberg, P. Emma, R. Rossmanith, *The North Arc of the SLC as a Spin Rotator*, SLAC-PUB-6210, Stanford Linear Accelerator Center, Stanford, CA (1993).

[Me87] M.T. Menzel, H.K. Stokes, *User's Guide for the* POISSON / SUPERFISH *Group of Codes*, Los Alamos Accelerator Code Group, LA-UR-87-115 (1987).

[Mi99] J.M. Mitchell, *Beam Energy Determination from Spin Precession Measurements at JLab*, internal document, June 8, 1999.

[Mo29] N.F. Mott, Proc. Roy. Soc. (London) **A135**, 429 (1932); **A124**, 426 (1929).

[Mo84] B.W. Montague, *Polarized Beams in High Energy Storage Rings*, PHYSICS REPORTS (Review Section of Physics Letters), 113, No. 1 (1984) 1-96. North-Holland Physics Publishing Division.

[Ou90] J. Ousterhoust, author of Tcl (Tool Command Language).

[Pa99] C. Payne, private communication.

[Pi58] L. A. Pipes, *Applied Mathematics for Engineers and Physicists*, 2nd Edt., McGraw-Hill, New York (1958).

[Pi76] D.T. Pierce and F.Meier, Phys. Rev. B **13**, 5484 (1976).

[Pi96] P. Piot, K. Assamagan, J-C. Denard, J. Grames, J. Price, C. Sinclair, *OTR Viewer in the CEBAF 5 MeV Mott Polarimeter for on-line Beam Profile Measurement*, CEBAF TN-96, Jefferson Laboratory, Newport News, VA (1996).

[Po95] M. Poelker, Appl. Phys. Lett., Volume 67, Issue 19, 2762 (1995).

[LM] LaserMetrics/Fast Pulse Technology model number G-1059-PFW, 750–950.

[PDG98] Particle Data Group, particle properties, 184 (1998).

[Pr97] J.S. Price, *et al.*, *5 MeV Mott Polarimeter Development at Jefferson Lab*, Proceedings of the VII. International Workshop on Polarized Gas Targets, Polarized Beams, University of Illinois at Urbana-Champaign, 446-450 (1997).

[Pr92] W.H. Press, S. A. Teukolsky, W.T. Vetterling, B.P. Flannery, *Numerical Recipes in ForTran 77, Second Edition*, Cambridge University Press (1992).

[Ro94] S. Robinson, *PhD Thesis*, University of Basel (1994).

[Sa85] J.J. Sakurai, *Modern Quantum Mechanics*, Addison-Wesley Publishing Company, New York, NY 1985).

[Sa77] M. Salomaa and H.A. Enge, *Velocity Selector for Heavy Ion Separation*, Nuclear Instruments and Methods **145** (1977) 279-282.

[Sh56] N. Sherman, *Coulomb Scattering of Relativistic Electrons by Point Nuclei*, Physical Review, Volume 103, Number 6, 1601-1607 (1956).

[Si81] C.K. Sinclair and R.H. Miller, IEEE Trans. Nucl. Sci., **NS-28**, 2649 (1981).

[Si88] C.K. Sinclair, *Report on Polarized Electron Source and Electron Polarimetry Workshop*, 8th International Symposium on High Energy Spin Physics, AIP Conference Proceedings (1988).

[Si96] C.K. Sinclair, *Accelerator Setups Which Provide Longitudinal Beam Polarization to More Than One Experimental Hall Simultaneously*, CEBAF-TN-96-032, Jefferson Laboratory, Newport News, VA (1996).

[So64] A.A. Sokolov and I.M. Ternov, Kokl. Akad. Nauk. SSR **153**, 1052 (1963) [Sov. Phys. Dokl. **8**, 1203 (1964)].

[Sr97] J. Sromicki, *et al.*, *Spin Dependence in Mott Scattering of 14 MeV Electrons from Heavy Nucleons*, Proceedings of the VII. International Workshop on Polarized Gas Targets, Polarized Beams, University of Illinois at Urbana-Champaign, 326-335 (1997).

[St99] M. Steigerwald, private communication.

[Sw95] M. Swartz, NIM Nucl. Instr. and Meth. A 363 (1995) 526.

[Th26] L.H. Thomas, *Nature* **117**, 514 (1926).

[Ti99] M. Tiefenbach, private communication.

[Uh25] Uhlenbeck, Goudsmidt, Physica, **5** 266 (1925).

[Ug70] P. Ugincius, H. Uberall, and G.H. Rawitscher, *Nuclear Size Effects in the Polarization of Elastically Scattered Electrons*, Nuclear Physics **A158** (1970) 418-432.

[Wa86] B. Wagner, *PhD Thesis*, Mainz Univeristy, 1986.

[Ya95] C. Yan, *et al.*, *Superharp - A wire scanner with absolute position readout for beam energy measurement at CEBAF*, Nuclear Instruments and Methods in Physics Research A **365** (1995) 261-267.

Vita

Joseph Michael Grames was born in Paterson, New Jersey, on July 24, 1970. He and his younger sister, Janis Grames, were raised in Clifton, New Jersey, by their mother Diane Grames. He received a Bachelor of Science (B.S.) degree with High Honor in the field of Physics and a minor concentration in Mathematics from the Stevens Institute of Technology in May, 1992. He then attended the University of Illinois at Urbana-Champaign and received the Master of Science (M.S.) degree in 1994. His thesis research continued at the Thomas Jefferson National Accelerator Facility in Newport News, Virginia. He received the Doctor of Philosophy (Ph.D.) degree from the University of Illinois in January, 2000. He won the Alfred M. Mayer physics Prize in 1992 while at Stevens. He is a member of the American Physical Society since 1992.

Publications:

OTR Viewer in the CEBAF 5 MeV Mott Polarimeter for On-Line Beam Profile Measurement, P. Piot *et al.*, Thomas Jefferson National Accelerator Facility, TN-96, 1996.

Presented Talks:

Measurement of a Weak Polarization Sensitivity to the Beam Orbit of the CEBAF

Accelerator, J.M Grames *et al.*, International Workshop on Polarized Sources and Targets, Erlangen, Germany, 1999.

Polarized Beam Transport at the TJNAF Accelerator: Simulations and Preliminary Measurements, J.M. Grames *et al.*, Seventh Internationl Workshop on Polarized Gas Targets and Beams, Urbana, Illinois, 1997.

Contribution to Talks:

5 MeV Mott Polarimeter Development at Jefferson Lab, J.S. Price *et al.*, Seventh Internationl Workshop on Polarized Gas Targets and Beams, Urbana, Illinois, 1997.

Beam Polarization Measurement at TJNAF, B. Zihlmann *et al.*, 1997 Joint April Meeting of the American Physical Society and American Association of PHysics Teachers, Washington, D.C., April 1997.

5 MeV Mott Polarimeter Development for Rapid Precise Electron Beam Polarization Measurements, J.S. Price *et al.*, Workshop on Polarized Electron Sources and Low Energy Polarimeters, NIKHEF, Amsterdam, Netherlands, 1996.